

Transient sources with LST-1: study of novae, supernovae, and gamma-ray bursts

Arnau Aguasca i Cabot



Aquesta tesi doctoral està subjecta a la llicència <u>Reconeixement- CompartIgual 4.0. Espanya</u> de Creative Commons.

Esta tesis doctoral está sujeta a la licencia <u>Reconocimiento - Compartirlgual 4.0. España de Creative Commons.</u>

This doctoral thesis is licensed under the <u>Creative Commons Attribution-ShareAlike 4.0. Spain License.</u>

PHD THESIS

TRANSIENT SOURCES WITH LST-1: STUDY OF NOVAE, SUPERNOVAE, AND GAMMA-RAY BURSTS

ARNAU AGUASCA I CABOT

SUPERVISORS Dr. Pol Bordas Coma Dr. Marc Ribó Gomis





Arnau Aguasca i Cabot, *Transient sources with LST-1: study of novae, supernovae, and gamma-ray bursts*, PhD Thesis Barcelona, 22 de maig de 2025

Transient sources with LST-1: study of novae, supernovae, and gamma-ray bursts

Memòria presentada per optar al grau de doctor per la Universitat de Barcelona

Programa de doctorat en Física

AUTOR Arnau Aguasca i Cabot

DIRECTORS
Dr. Pol Bordas Coma
Dr. Marc Ribó Gomis

TUTOR
Dr. Alberto Manrique Oliva

DEPARTAMENT DE FÍSICA QUÀNTICA I ASTROFÍSICA Barcelona, 22 de maig de 2025



I hereby declare that this Thesis represents my own work which has been done after registration for the degree of PhD at Universitat de Barcelona, and has not been previously included in a Thesis or dissertation submitted to this or any other institution for a degree, diploma or other qualifications.

Arnau Aguasca i Cabot Barcelona, 22 de maig de 2025

La branca de l'astrofísica que estudia els fenòmens transitoris permet l'exploració de fonts astronòmiques que mostren variabilitat temporal que pot estendre's des d'unes poques fraccions de segon fins escales tan llargues com desenes d'anys. Aquests esdeveniments transitoris poden donar lloc a una gran varietat de fenòmens observats en tot l'espectre electromagnètic. En alguns casos, aquests esdeveniments poden fins i tot estar associats a la detecció d'ones gravitacionals o a l'emissió de neutrins. La detecció d'emissió electromagnètica transitòria i molt energètica, en el rang dels raigs gamma (amb energies per sobre de 100 MeV) sol estar relacionada amb canvis dràstics en l'entorn del sistema que emet aquesta radiació. En alguns casos, aquests fenòmens transitoris poden ser produïts a causa de la seva destrucció parcial o total. Durant aquests episodis, la font pot esdevenir extremadament lluminosa, arribant a ser una de les més brillants del cel, inclús si es troba a distàncies cosmològiques. Malgrat els avenços en aquest camp d'investigació en els darrers anys, els mecanismes que produeixen l'emissió de raigs gamma provinents de fonts transitòries continuen sent enigmàtics, amb independència de la naturalesa de la font que els produeix.

Els raigs gamma en el rang d'energies de desenes de GeV fins a centenars de TeV poden ser detectats des de terra amb els telescopis Txerenkov. Aquesta Tesi s'emmarca precisament en l'estudi de les fonts transitòries utilitzant el primer prototip de la nova generació de telescopis Txerenkov, que formarà part del futur *Cherenkov Telescope Array Observatory* (CTAO). El CTAO estarà constituït per diferents tipus de telescopis distribuïts al llarg d'una gran superfície, formant una matriu de telescopis Txerenkov per tal de detectar raigs gamma en un rang ampli d'energies. Els telescopis més grans del CTAO, anomenats *Large-Sized Telescopes* (LST), estan optimitzats per detectar raigs gamma d'energies relativament baixes, d'algunes desenes de GeV. El primer d'aquests telescopis (LST-1) es troba en fase de posada en servei tot i que paral·lelament ja està començant a donar els primers resultats científics. A més a més, actualment hi ha tres LSTs en construcció.

Aquesta Tesi se centra en l'estudi de fonts transitòries en el rang de raigs gamma de molt alta energia ($100 \,\text{GeV} < E < 100 \,\text{TeV}$). S'ha realitzat un estudi detallat de les explosions de noves i supernoves (SNe) i dels esclats de raigs gamma (en anglès gamma-ray bursts, GRB).

• Hem estudiat l'emissió produïda en la font RS Ophiuchi, la primera explosió de nova mai detectada en el rang de molt alta energia. Hem analitzat dades obtingudes contemporàniament amb LST-1 i el telescopi *Fermi*-LAT durant aquest esdeveniment. Hem modelitzat la seva emissió fent servir l'espectre de raigs gamma més complet mai obtingut per un esdeveniment d'aquestes característiques, que inclou a més a més de les observacions preses amb LST-1 i *Fermi*-LAT, les dades obtingudes amb els telescopis Txerenkov MAGIC i H.E.S.S. L'emissió de raigs gamma de RS Ophiuchi es pot explicar correctament en un escenari en hadrònic. També hem avaluat les perspectives per a futures deteccions d'explosions de noves amb el CTAO, ressaltant les

excel·lents capacitats dels LSTs per detectar aquest tipus d'esdeveniments i restringint els paràmetres físics rellevants implicats en l'emissió de raigs gamma.

- Hem cercat emissió de raigs gamma de molt alta energia en dues supernoves properes produïdes durant el col·lapse d'un estel molt massiu, etiquetades SN 2023ixf i SN 2024bch. Aquestes explosions de supernova varen ser observades amb el LST-1 i els telescopis MAGIC poques setmanes després del seu descobriment. Tot i que cap de les dues fonts ha estat detectada, hem pogut obtenir límits superiors al seu possible flux de raigs gamma de molt alta energia, emfatitzant els punts forts i les limitacions que les observacions en aquest rang poden oferir per la comprensió dels fenòmens físics que donen lloc a aquest tipus d'explosions.
- Hem estudiat l'emissió de raigs gamma de molt alta energia del GRB 221009A, conegut com el GRB més brillant de tots els temps. Les observacions obtingudes amb el LST-1 mostren un excés de raigs gamma amb una significació estadística de 4.1σ durant les primeres observacions. Hem restringit la seva emissió de raigs gamma de molt alta energia i l'hem comparada amb diversos models teòrics que poden explicar d'una manera consistent les dades multilongitud d'ona obtingudes amb diferents telescopis per aquest esdeveniment. Els nostres resultats poden ajudar a resoldre l'actual degeneració existent entre alguns d'aquests models teòrics compatibles amb l'emissió de banda ampla d'aquest esdeveniment.

Els resultats obtinguts per aquests tres tipus de fonts posen en relleu les excel·lents capacitats dels LSTs per a l'estudi de fonts de raigs gamma transitòries. A més, aquests resultats proporcionen un primer tast del potencial del CTAO per estudiar aquests tipus d'esdeveniments.

Títol: Fonts transitòries amb LST-1: estudi de noves, supernoves i esclats de raigs gamma

Paraules clau: Astronomia de raigs gamma, noves (estels), supernoves, esclats de raigs gamma.

Time-domain astronomy enables the study of transient sources whose emission vary over time, from fractions of seconds to years. Transient events produce rich phenomena across the electromagnetic spectrum and may also emit gravitational waves or neutrinos. The detection of transient, energetic gamma-ray emission (above 100 MeV) is connected to drastic changes in the surrounding environment of an astrophysical object or even its partial or total destruction. During these episodes, the source can become extremely luminous and one of the brightest sources in the sky even if it is located at cosmological distances. Despite recent advances, the mechanisms driving the production of gamma rays in transient sources remain poorly understood, indistinctly of the source nature.

Energetic gamma rays, from tens of GeV to hundreds of TeV, can be detected with imaging atmospheric Cherenkov telescopes (IACTs) from the ground. This Thesis is framed on studying transient sources with the next generation of IACTs that will form the Cherenkov Telescope Array Observatory (CTAO). CTAO consists of different telescope types distributed in an array across a large area to detect gamma rays in a broad range of energies. The Large-Sized Telescopes (LSTs) are the largest telescopes of CTAO. Optimised to detect gamma rays of energies as low as tens of GeV, the first LST (LST-1) is in commissioning and starting to produce scientific results. Three more LSTs are under construction.

This Thesis is focused on transient sources with a fast-evolving spectrum at very-high-energy gamma rays (VHE; $100 \, \text{GeV} < E < 100 \, \text{TeV}$). A detailed study of novae, supernovae (SNe), and gamma-ray bursts (GRBs) is conducted.

- We studied the emission of RS Oph, the first nova detected at VHE gamma rays. We analysed contemporaneous LST-1 and *Fermi*-LAT data from this event. We modelled its gamma-ray emission with the most complete gamma-ray spectrum to date, including *Fermi*-LAT, LST-1, Major Atmospheric Gamma-ray Imaging Cherenkov (MAGIC), and High Energy Stereoscopic System (H.E.S.S.) spectral information. The RS Oph gamma-ray emission can be properly explained in a hadronic scenario. We also assessed the prospects for future nova detections with CTAO, emphasising the excellent capabilities of LSTs to detect such events and constrain the involved relevant physical parameters.
- We searched for VHE gamma-ray emission on two close core-collapse SNe, SN 2023ixf and SN 2024bch, observed with LST-1 and MAGIC within weeks of their discovery. Although none of the sources were detected, we derive upper limits to constrain their VHE gamma-ray emission. We discuss the strengths and weaknesses of gamma-ray data to constrain the physical parameters involved in the gamma-ray emission.
- We studied the VHE gamma-ray emission of GRB 221009A, dubbed as the brightest-of-all-time GRB. LST-1 observations yielded an excess of gamma rays at a statistical significance of 4.1σ during the earliest IACT observations of

this GRB. We constrained its VHE gamma-ray emission and compared it with theoretical models that are consistent with the published multi-wavelength data. Our results can help disentangle the degeneracy among models that are consistent with the broad-band emission of this event.

The results obtained on these three source types stress the excellent capabilities of LSTs for the study of transient and fast-evolving soft gamma-ray sources. Moreover, these results provide a first taste of the potential of CTAO to study transient sources.

CONTENTS

1	Introduction 1
	1.1 The gamma-ray sky 1
	1.2 Transient gamma-ray sources 2
	1.3 Thesis overview 3
2	Particle acceleration and gamma-ray emission 5
	2.1 Particle acceleration and energy losses 5
	2.2 Non-thermal emission mechanisms 7
	2.3 Gamma-ray absorption mechanisms 16
3	Gamma-ray detectors 19
	3.1 Space-borne detectors 19
	3.2 Ground-based detectors 22
4	IACT data calibration, processing and high-level analysis 37
1	4.1 General description of the data analysis flow 37
	4.2 Data levels in CTAO 48
	4.3 LST-1 data analysis 48
	4.4 MAGIC+LST data analysis 56
	III IIII TOTO LEGI dada didayota
5	Novae 59
	5.1 Introduction 59
	5.2 RS Oph 60
	5.3 Observations and data analysis 61
	5.4 Modelling 63
	5.5 Results 65
	5.6 Robustness tests of the model fitting 75
	5.7 Discussion 80
	5.8 Studying novae with LSTs and CTAO 84
	5.9 Conclusions 91
6	Core-collapse supernovae 93
U	6.1 Introduction 93
	6.2 SN 2023ixf 95
	6.3 SN 2024bch 100
	6.4 Discussion 103
	6.5 Conclusions 108
7	Gamma-ray bursts 109
	7.1 Introduction 109
	7.2 GRB 221009A 110
	7.3 Observations 111
	7.4 Data analysis 112
	7.5 Results 115

	7.6	Discussion 121
	7.7	Conclusions 125
8	Gen	eral conclusions 127
A	Tem	poral Resolution Estimator for Transient Sources 129
	а.1	
	A.2	Application to observational data 131
	А.3	Conclusions and future work 136
В	Obs	ervations of classical novae with LST-1 139
		V1405 Cas 139
	в.2	V1674 Her 140
	в.3	U Sco 140
		LST-1 data analysis 142
	в.5	Fermi-LAT data analysis 142
		Results 143
	в.7	Summary 146
C		e developments in the context of IACTs 149
Ac	rony	ms 151
Bił	oliogi	raphy 155
Lis	st of I	Figures 185
Lis	st of T	Tables 187
Pu	blica	tions 189
Μe	embe	rship in collaborations 191
Ac	knov	vledgments 193

INTRODUCTION

1.1 THE GAMMA-RAY SKY

The violent universe can be unveiled thanks to the information provided by several, independent messengers, which include gamma rays, neutrinos, gravitational waves (GWs), and cosmic rays (CRs). Gamma rays have been one of the most successful of such messengers, revealing a rapidly-changing Universe. This effectiveness proceeds from two main factors. Firstly, gamma rays unambiguously pinpoint their origin. This contrasts with CRs, which are deflected by magnetic fields during their propagation and consequently arrive at Earth with an isotropic distribution. Secondly, gamma rays are detectable through gamma—matter interactions, simplifying their observation (e.g. Blümer et al. 2009; Bose et al. 2022). Conversely, neutrino and GW astronomy have historically been limited by the small number of detected events, although significant advances have been made in recent years (e.g. Kurahashi et al. 2022; Abbott et al. 2020).

Gamma rays (which are defined in this Thesis as photons with energies greater than the electron rest-mass energy, \sim 511 keV) can be divided into different ranges according to their energy. This Thesis focuses on energetic gamma rays above 100 MeV, which are in turn typically grouped into three bands: high energy (100 MeV < E < 100 GeV) (HE), very-high energy (100 GeV < E < 100 TeV) (VHE), and ultra-high energy (E > 100 TeV) (UHE). Extremely efficient non-thermal processes are responsible for the production of such energetic gamma rays. Observing the HE–UHE gamma-ray sky provides therefore a privileged view of a rapidly evolving, violent (non-thermal) Universe. Moreover, energetic gamma rays offer relevant information about CRs and fundamental physics. For instance, gamma rays can be used to study the CR propagation and spatial distribution of particle accelerators, as gamma-ray are the result of CR interaction with radiation fields and interstellar gas (e.g. Acero et al. 2013). Furthermore, gamma rays can be used for probing Lorentz invariance violation, axion-like particles, and dark matter (e.g. Bolmont et al. 2022; Abe et al. 2024a; Abe et al. 2024d, 2025c).

The first detections in each of these HE, VHE and UHE gamma-ray bands and the following consolidation as new astronomical windows has occurred at different times. HE gamma-ray astronomy was the first window unveiled thanks to the development of rocket technologies in the 1950s–1960s and subsequent space-borne observatories (see Fig. 1.1). HE gamma-ray astronomy lead the advances in the field, setting the observational basis for gamma-ray astronomy. On the contrary, the discovery of astrophysical phenomena yielding VHE and UHE gamma-ray fluxes had to await significant advances in ground-based gamma-ray detector techniques. The milestone marking the establishment of VHE and UHE gamma-ray observational astronomy was achieved only recently, in the 2000s and 2020s, respectively (see Fig. 1.1). The great success of VHE gamma-ray astrophysics is mostly attributed to the development of the imaging atmospheric Cherenkov

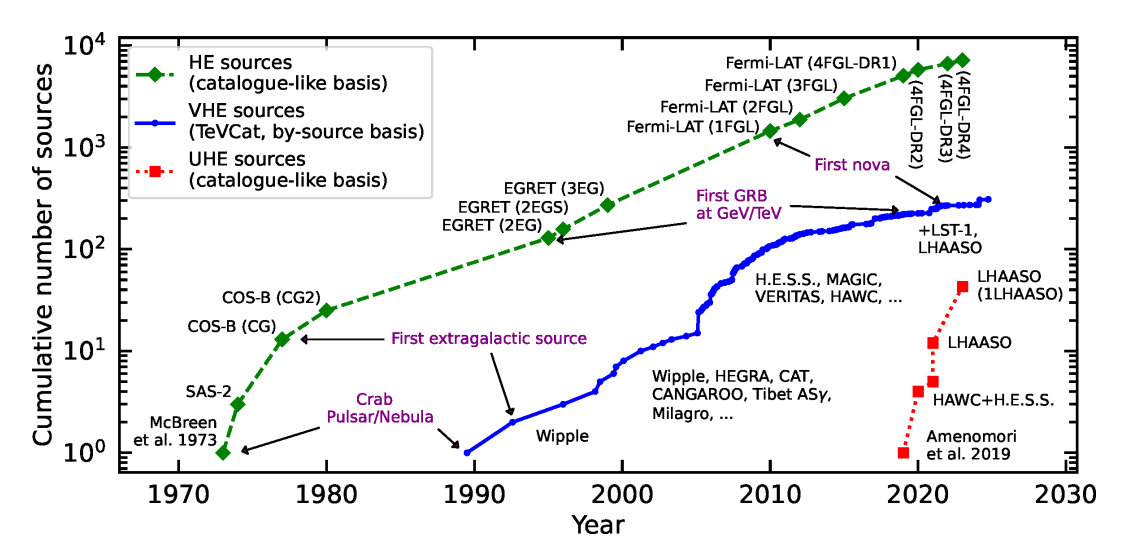


Figure 1.1: Cumulative number of sources discovered at gamma rays as a function of time (also known as Kifune plot) for the HE (green; McBreen et al. 1973; Kniffen et al. 1974; Thompson et al. 1974, 1977; Hermsen et al. 1977; Swanenburg et al. 1981; Thompson et al. 1995, 1996; Hartman et al. 1999), VHE (blue; Wakely and Horan 2008), and UHE (red; Amenomori et al. 2019; Abeysekara et al. 2020; Abdalla et al. 2021; Cao et al. 2021, 2024) gamma-ray bands.

telescope (IACT) technique, while wide field of view (FoV) gamma-ray detectors (particle detector arrays) have been key in revolutionising the field at UHE gamma rays.

The current number of sources emitting in the HE, VHE and UHE gamma ray bands is of the order of a few thousands (Ballet et al. 2023), a few hundreds (Wakely and Horan 2008), and a few tens (Cao et al. 2024), respectively (see Fig. 1.1). At HE/VHE gamma rays, multiple source classes populate this band (both galactic and extragalactic). Among the galactic sources, one can find supernova (SN) remnants, novae, pulsars, pulsar wind nebulae and halos, gamma-ray binaries, and microquasars, among others; starburst Galaxies, blazars, or gamma-ray burst (GRB) afterglows are a few examples of extragalactic sources. Such a diversity of sources and the corresponding associated physics makes them excellent laboratories to test for particle acceleration, emission, and absorption processes under extreme conditions.

VHE gamma-ray astronomy is moving into a new era with the construction of the major ground-based IACT facility, the Cherenkov Telescope Array Observatory (CTAO). CTAO will drive the TeV astrophysics in the following decades. It will boost the detection of VHE gamma-ray sources with its enhanced sensitivity and spatial resolution. Additionally, it will allow for the first time the study of an almost unexplored domain related to short (sub-minute) timescale variability phenomena.

1.2 TRANSIENT GAMMA-RAY SOURCES

Multiple sources exhibit variable emission, being it periodic, aperiodic, or episodes of eruptive events in which their emission increases across the electromagnetic spectrum in a distinct and sometimes unpredictable manner. These episodes can

last for a broad range of timescales, from milliseconds to years. Observationally, a variable and transient source differ in that the former always remains detectable, whereas the latter exhibits periods whose emission drops below the detection threshold. Transient phenomena are known at HE or VHE gamma rays from sources in our Galaxy and at cosmological distances, e.g., in the case of gamma-ray binaries, microquasars, galactic novae, colliding wind binaries, blazars, and GRBs, among others. Notably, galactic novae and GRBs have been detected as VHE gamma-ray emitters very recently, further enlarging such an heterogeneous class list.

Transient VHE gamma-ray emission stands as a fundamental probe of the underlying physical processes in these sources, additionally providing stringent constraints on the underlying gamma-ray emission processes and the emission region (e.g. Rees and Mészáros 1992; Wehrle et al. 1998; Rieger and Volpe 2010; Aydi et al. 2020; Zhang et al. 2024). VHE gamma-ray transients also serve as excellent laboratories for particle physics and multi-messenger astrophysics. However, the occurrences and properties of these events are largely unknown. To this end, sensitive detectors at short timescales, together with wide FoV surveys, will be crucial for detecting and further understanding these sources and discovering new types of VHE transient gamma-ray emitters, e.g., tidal disruption events or SN explosions.

1.3 THESIS OVERVIEW

This Thesis is focused on deepening our understanding of three different types of transient sources in the gamma-ray band: galactic novae, SN explosions, and GRBs. Our aim is to shed new light on the physical mechanisms leading to the observed HE/VHE gamma-ray emission from these sources. Although they are three distinct source classes, their phenomenology is partially connected to some extent. The same acceleration mechanisms are thought to occur in nova eruptions, in the early phases of SN explosions, and in SN remnants. Furthermore, the shocks in novae develop under similar density conditions as in interacting core-collapse SN (CCSN) explosions. In turn, long GRBs are known to typically originate from certain types of CCSNe.

The characterisation of novae, SN explosions and GRBs at gamma rays not only allows us to constrain the physics of particle acceleration and non-thermal emission but also provides a complementary view of such systems for their study, as gamma rays can escape regions where the emission at other wavelengths is absorbed. To achieve this goal, it is required to understand the mechanisms that accelerate particles to relativistic energies, the mechanisms leading to the emission of gamma rays and their interaction mechanisms with our detectors. Finally, inference analysis is required to characterise the unknown properties and physics of the sources from the recorded data with the detectors.

This Thesis is organised as follows. Chapter 2 reviews the particle acceleration and non-thermal emission and absorption processes. Chapter 3 introduces the detectors used in the gamma-ray band. Chapter 4 describes the data analysis of IACTs. Chapters 5, 6, and 7 present the results of the work on novae, CCSNe, and GRBs, respectively. Finally, conclusions are provided in Chapt. 8. The appendices provide information about additional work conducted in the framework of this Thesis. In Appendix A, we describe a dedicated algorithm to obtain a variable light

4 INTRODUCTION

curve with the shortest temporal resolution. The study of classical novae followed up with LST-1 is provided in Appendix B. In the end, Appendix $\mathbb C$ lists the code developments on open-source software packages.

2

PARTICLE ACCELERATION AND GAMMA-RAY EMISSION

Electromagnetic radiation is the main channel of information with which we can study astrophysical sources. A profound understanding of the processes that imprint the electromagnetic spectrum is essential for studying the physical processes in act on these sources and for characterising their unknown properties, such as the magnetic field, density, etc.

HE–VHE gamma rays are produced through non-thermal emission processes involving the acceleration of relativistic particles and their interaction with other particles, photons and magnetic fields. The gamma-ray emitting particle population is accelerated to VHEs through mechanisms that typically yield to power-law particle energy distributions. Particles can then transform a fraction of their energy into gamma-ray radiation via several emission processes. In this chapter, a summary of the mechanisms involved in particle acceleration and energy losses by radiative processes are provided in Sect. 2.1. The intrinsic non-thermal emission of these processes is discussed together with the effect of gamma-ray absorption mechanisms in Sects. 2.2 and 2.3, respectively.

2.1 PARTICLE ACCELERATION AND ENERGY LOSSES

Particles can achieve relativistic energies through various processes, including Fermi acceleration mechanisms, magnetic reconnection, and stochastic shearing, among others (Longair 2011; Lemoine and Pelletier 2015; Rieger 2019). For detailed reviews discussing particle acceleration in astrophysical sources, the reader is refereed to Drury (e.g. 1983), Kirk et al. (1994), and Rieger et al. (2007). The most widely considered acceleration mechanism in the context of gamma-ray emission is the diffusive shock acceleration (first order Fermi acceleration).

Diffusive shock acceleration (DSA) is based on the idea of particles obtaining energy through multiple shock front crossings, which occur as a result of numerous scatterings with magnetic turbulences present both in the upstream and downstream sides of the shock. In this scenario, a particle with a given energy E in the upstream flow diffuses back and forth across the shock front via interaction with magnetic turbulence scattering centres, which isotropises the particle average velocity with that of the region before crossing the shock front. In each crossing, the particle gains energy, as it encounters the other region of the shock moving towards the shock front. After completing a cycle, the average relative particle energy gain is $\langle \Delta E \rangle / E \propto v_{\rm s}/c$, where $v_{\rm s}$ and c are the shock front velocity and the speed of light, respectively. After multiple crossings, the differential spectrum of the accelerated particles follows a power-law shape. For strong shocks, the spectral index α of this power-law particle energy distribution $(dN/dE \propto E^{\alpha})$ is $\alpha \approx -2$. DSA stands as one of the most efficient mechanisms for energising particles, providing the necessary

particle acceleration in VHE astrophysical sources with a slope similar to the one observed in CRs (Bell 1978).

The maximum energies that particles can attain can be obtained through the balance between the energy gain of a given acceleration mechanism and the energy losses that the particle can undergo, i.e., particle cooling mechanisms (radiative and non-radiative). One can evaluate the efficiency of a given cooling mechanism by specifying the corresponding energy losses per unit time dE/dt (energy-loss rate, hereafter *energy losses*), whose expression will depend on the given processes. For example, the energy radiated in gamma rays per unit time by an incident particle with energy E when interacting with the surrounding particles or photon fields is

$$-\left(\frac{dE}{dt}\right) = c \int d\varepsilon \, n \, \varepsilon \, \frac{d\sigma(\varepsilon, E)}{d\varepsilon} \,, \tag{2.1}$$

where n is the number density of the targets and $\frac{d\sigma(\varepsilon,E)}{d\varepsilon}$ is the differential cross section per unit photon energy ε for an incident particle with energy E. Note that the energy losses depend in general not only on the particle energy E, but also on other physical quantities affecting the interaction of the particle with the surrounding medium. Different processes can in turn dominate at different energy ranges. Particle cooling will modify the original particle energy distribution, which might yield to distinct spectral features given the energy dependence of the considered process. As a result, the time-evolved population will yield a different emission than the original population. For a complete treatment, the diffusion equation considering all energy-loss mechanisms has to be solved to address this temporal evolution (Ginzburg and Syrovatskii 1964).

When comparing multiple energy losses at play, an assessment of the relative relevance for each of them is needed. A commonly used parameter for this purpose is the timescale of energy losses, the *cooling time*:

$$t = E \left| \frac{dE}{dt} \right|^{-1} . {(2.2)}$$

In particular, the cooling times of the competing processes are compared with the dynamical time and the acceleration time to evaluate their efficiency. The acceleration time can be estimated considering the maximum acceleration rate from classical electrodynamics (Hillas 1984):

$$t_{\rm acc} = E \left(\frac{dE_0}{dt}\right)^{-1} = \frac{E}{\eta e c B},\tag{2.3}$$

where B is the magnetic field, c is the speed of light, e is the electron charge, and η is a parameter that characterises the fraction of total energy that goes into accelerating particles, and depends on the nature of the acceleration mechanism. In particular, for DSA, $\eta \sim (\frac{v}{c})^2 f_{\rm sc}$, where v is the shock velocity and $f_{\rm sc}$ is the ratio of the particle mean free path to its Larmor radius (Drury 1983; Begelman et al. 1990). $f_{\rm sc}$ reaches 1 when the particle diffusion length approaches the Larmor radius, which corresponds to the so-called Bohm diffusion regime (Jones and Ellison 1991; Protheroe 1999).

If one knows the parameters involved in Eq. 2.3, the maximum energy of the particle can be estimated and used to predict the intrinsic gamma-ray emission

produced by these relativistic particles. In contrast, if the parameters are unknown, the observed data can be used to constrain them. For example, in this Thesis, the particle acceleration efficiency of the nova RS Oph was constrained (see Chapt. 5), while we also provide stringent observational constrains for GRB 221009A (see Chapt. 7).

2.2 NON-THERMAL EMISSION MECHANISMS

Multiple processes can dominate the gamma-ray emission depending on the physical conditions of the emitting region, occasionally implying some ambiguity when different processes can equally well explain the observed emission. In the following sections, a brief description and the relevant expressions for the main non-thermal emission and absorption processes are provided. For more detailed information, the reader is referred to dedicated reviews and specialised books such as Blumenthal and Gould (1970), Rybicki and Lightman (1979), Aharonian (2004), Longair (2011), and Ghisellini (2013).

In addition to the temporal evolution of the intrinsic emission following the changes on the original particle distribution due to energy losses, as discussed in Sect. 2.1, the emission of a given source of gamma rays might be modified by Doppler boosting or radiation absorption processes. Doppler boosting can increase or reduce the observed flux, depending on the velocity and orientation of the emitter relative to the observer (see, e.g. Rybicki and Lightman 1979; Ghisellini 2013 for further details). On the other hand, absorption processes reduce the observed flux with respect to the intrinsic emission. This flux reduction can be computed by solving the differential equation for the radiative transfer, which can be written as

$$\frac{dI(\varepsilon)}{ds} = j(\varepsilon) - k(\varepsilon)I(\varepsilon), \qquad (2.4)$$

where $I(\varepsilon)$ is the specific intensity*, $j(\varepsilon)$ and $k(\varepsilon)$ are the specific emissivity and absorption coefficients, respectively, and ds is the differential element of length in the radiation path.

Knowing the differential cross section of the processes at play is fundamental for computing the emissivity and absorption coefficients. These coefficients are then used to estimate observable quantities to constrain the source physical properties. While cross sections for electromagnetic processes are known from quantum electrodynamics, cross sections for interactions of hadrons are estimated from experimental data conducted in particle accelerators (e.g. Pacholczyk 1970; Kelner et al. 2006).

While nuclear interactions in heavy nuclei can yield gamma-ray line emission up to several MeV, gamma rays at HEs and VHEs are produced by emission processes rendering a continuum photon spectrum, with distinct spectral features such as specific slopes or energy slopes, arising from both the emission processes themselves or particle energy loss mechanisms. The solution of the radiative transport equation without considering absorption processes is $I(\varepsilon) = I(\varepsilon, s_0) + \int_{s_0}^s ds' j(\varepsilon, s')$, where s_0 is the distance at which the intensity is $I(\varepsilon, s_0)$. Therefore, for a constant

^{*}The term "specific" means here that the quantity is given per photon energy ε . The nomenclature in the text is (ε) . In this case, $I(\varepsilon)$.

emissivity and $I(\varepsilon, s_0) = 0$, one obtains $I(\varepsilon) = j(\varepsilon)s$. In this section, the relevant expressions and dependencies are provided for the radiative processes involved in the production of gamma rays discussed in this Thesis.

2.2.1 Synchrotron radiation

A charged particle radiates when it is accelerated by the presence of a magnetic field \vec{B} following the Lorentz force law. The radiation produced by relativistic particles under the effect of a magnetic field is called synchrotron radiation. The synchrotron emitted power depends, amongst other parameters, on the angle between the particle velocity vector \vec{v} and \vec{B} , the pitch angle θ .

Let the energy of a relativistic particle be $E = \gamma mc^2$, where m and γ are its mass and Lorentz factor, respectively. The latter is defined as $\gamma = \left[1 - \beta^2\right]^{-1/2}$, where β is the ratio between the particle velocity v and the speed of light c (i.e. $\beta = v/c$). The photon energy distribution of the emitted power (specific power or power spectrum, $P(\varepsilon)$, with units of $[\operatorname{erg} \operatorname{s}^{-1} \operatorname{erg}^{-1}]$) from a single, relativistic electron with energy E in a magnetic field B forming a pitch angle θ is (Rybicki and Lightman 1979):

$$P_{\rm e}(\varepsilon, \varepsilon_{\rm c}) = \frac{\sqrt{3}e^3 B \sin \theta}{h m_{\rm e} c^2} F\left(\frac{\varepsilon}{\varepsilon_{\rm c}}\right) , \qquad (2.5)$$

where m_e and e are the electron mass and charge, respectively, h is the Planck constant, and

$$F\left(\frac{\varepsilon}{\varepsilon_{\rm c}}\right) = \frac{\varepsilon}{\varepsilon_{\rm c}} \int_{\frac{\varepsilon}{\varepsilon_{\rm c}}}^{\infty} dx \, K_{5/3}(x) \,, \tag{2.6}$$

where $K_{5/3}(x)$ is the Bessel function of the second kind of order 5/3 and ε_c is the characteristic synchrotron energy defined as

$$\varepsilon_{\rm c} = \frac{3}{4\pi} \frac{he}{m_{\rm e}^3 c^5} B E^2 \sin \theta \,. \tag{2.7}$$

The term $F\left(\frac{\varepsilon}{\varepsilon_c}\right)$ can be approximated with the functional form $F(x) \approx 1.85x^{1/3}\exp\left(-x\right)$, where $x = \varepsilon/\varepsilon_c$. This analytical approximation is accurate within 1% to the numerical result for $x \in [0.1, 10]$ (Aharonian 2004). The function $F\left(\frac{\varepsilon}{\varepsilon_c}\right)$ displays a maximum at $\varepsilon_m \simeq 0.29\varepsilon_c$. For an isotropic pitch angle distribution, Eq. 2.7 can be conveniently expressed as

$$\left[\frac{\varepsilon_{\rm c}}{\rm eV}\right] \approx 5.5 \left[\frac{B}{\rm G}\right] \left[\frac{E}{10 \,{\rm GeV}}\right]^2. \tag{2.8}$$

In the presence of a population of electrons with a number density distribution $n_{\rm e}(E)dE$ in the energy interval E and E+dE, the specific synchrotron emissivity $(j_{\rm sync}(\varepsilon)$, units of $[{\rm erg\,cm^{-3}\,s^{-1}\,erg^{-1}\,sr^{-1}}])$ can be computed by convolving the power spectrum of the emitted photons by a single electron, $P_{\rm e}$, and the electron energy distribution per unit volume per unit solid angle $(n_{\rm e}(E)$, with units of $[{\rm erg^{-1}\,cm^{-3}\,sr^{-1}}]$):

$$j_{\text{sync}}(\varepsilon) = \int_{E_{\text{min}}}^{E_{\text{max}}} P_{\text{e}}(\varepsilon, E) \, n_{\text{e}}(E) \, dE \,. \tag{2.9}$$

For a power-law particle energy distribution with slope p, $n_{\rm e}(E) \propto E^{-p}$, the specific synchrotron emissivity depends on the energy ε as $j_{\rm sync}(\varepsilon) \propto \varepsilon^{-\frac{p-1}{2}}$. Therefore, the observed emission is proportional to $\varepsilon^{-\frac{p-1}{2}}$ in an optically thin medium. In case of an optically thick medium, synchrotron photons will be absorbed by the same emitting electrons or the surrounding thermal plasma. This absorption dominates at low energies in the radio band and has to be considered when accounting for the synchrotron emission at these energies. The characteristic slope of the specific intensity is $I_{\rm sync}(\varepsilon) \propto \varepsilon^{\frac{5}{2}}$. The reader is referred to, e.g., Pacholczyk (1970) and Rybicki and Lightman (1979) for a detailed review of the synchrotron absorption process.

In general, electrons are more prone to cool through synchrotron emission than protons. The total energy loss per unit time (dE/dt, with units of [erg s⁻¹]) radiated by relativistic particles that are isotropically distributed in pitch angle is expressed as (Rybicki and Lightman 1979)

$$-\left\langle \frac{dE}{dt} \right\rangle_{\text{sync}} = \frac{4}{3} \left(\frac{m_{\text{e}}}{m} \right)^2 \frac{c\sigma_{\text{T}}}{m_{\text{e}}^2 c^4} \omega_{\text{mag}} \beta^2 E^2 \approx \frac{4}{3} \left(\frac{m_{\text{e}}}{m} \right)^2 \frac{c\sigma_{\text{T}}}{m_{\text{e}}^2 c^4} \omega_{\text{mag}} E^2, \tag{2.10}$$

where $\sigma_{\rm T}$ is the Thomson cross section, $\sigma_{\rm T} = \frac{8\pi}{3} \left(\frac{e^2}{m_{\rm e}c^2}\right)^2 \approx 6.65 \times 10^{-25} \, {\rm cm}^2$, and $\omega_{\rm mag}$ is the magnetic energy density defined as $\omega_{\rm mag} = B^2/8\pi$, with units of [erg cm⁻³]. On the right-hand side of Eq. 2.10, β has been approximated to 1 since relativistic particles are considered. The dependency of the energy losses with the particle mass $(dE/dt \propto m^{-2})$ makes electrons to radiate more power than protons for the same given energy E.

We can easily obtain the synchrotron cooling timescales by replacing Eq. 2.10 in Eq. 2.2. The synchrotron cooling for electrons can be conveniently expressed as

$$\left[\frac{t_{\text{sync}}}{\text{s}} \right] \approx 400 \left[\frac{B}{\text{G}} \right]^{-2} \left[\frac{E}{\text{TeV}} \right]^{-1} .$$
 (2.11)

2.2.2 Inverse Compton scattering

When electrons and radiation fields are present in the same environment, there is a non-zero probability that a photon and an electron scatter among them. Depending on their relative motion in the laboratory frame, the outcome of this scattering is a positive energy transfer from the photon to the electron or *vice versa*. The former outcome is called Compton scattering and occurs when the incident photon energy ε_0 is higher than the electron energy E, i.e., $\varepsilon_0 > E$. In contrast, the electron transfers energy to the photon if $\varepsilon_0 < E$. This scattering is called inverse Compton (IC).

The total cross section of IC scattering per unit solid angle at the electron rest frame (Ω') requires quantum electrodynamics calculations, and is described by the Klein-Nishina (KN) formula (e.g. Berestetskii et al. 1982; Ghisellini 2013):

$$\frac{d\sigma_{\rm KN}}{d\Omega'} = \frac{3\sigma_{\rm T}}{16} \left(\frac{\varepsilon'}{\varepsilon'_0}\right)^2 \left[\frac{\varepsilon'_0}{\varepsilon'} + \frac{\varepsilon'}{\varepsilon'_0} - \sin^2\theta'\right] \,, \tag{2.12}$$

which depends on the scattering angle and the initial and final photon energies[†] at the electron rest frame, θ' , ε'_0 , and ε' , respectively. Two regimes of scattering can be divided. Firstly, the so-called Thomson regime occurs when the photon energy is lower than the electron rest mass ($\varepsilon'_0 < m_{\rm e}c^2$), i.e., in the laboratory frame $E\varepsilon_0 < m_{\rm e}^2c^4$. In particular, if $E\varepsilon_0 \ll m_{\rm e}^2c^4$, we recover the classical Thomson cross section (Thomson limit). On the contrary, for energies $E\varepsilon_0 > m_{\rm e}^2c^4$, the cross section is reduced with respect to the classical value. In the extreme scenario with $E\varepsilon_0 \gg m_{\rm e}^2c^4$, the KN limit is reached and the cross section decreases as $\propto \sigma_{\rm T}(E\varepsilon_0)^{-1} \ln{(2E\varepsilon_0)}$.

The average energy of the outgoing photon in the Thomson regime is (Ghisellini 2013; Longair 2011):

$$\varepsilon_{\text{av,T}} = \frac{4}{3} \frac{1}{m_e^2 c^4} \varepsilon_0 E^2 \beta^2 \approx \frac{4}{3} \frac{1}{m_e^2 c^4} \varepsilon_0 E^2.$$
 (2.13)

On the right-hand side of Eq. 2.13, relativistic electrons have been considered $(\beta \to 1)$. Let us express $\varepsilon_{av,T}$ in convenient units as

$$\left[\frac{\varepsilon_{\text{av,T}}}{\text{TeV}}\right] \approx 5 \left[\frac{\varepsilon_0}{\text{eV}}\right] \left[\frac{E}{\text{TeV}}\right]^2.$$
(2.14)

Although the photon gains a large amount of energy in the Thomson regime, it still represents a small fraction of the total electron energy since the condition $E\varepsilon_0 \ll m_{\rm e}^2 c^4$ holds in this regime. This is not the case in the KN limit, in which the electron loses a considerable amount of its energy in a single Compton scattering (Blumenthal and Gould 1970).

A convenient simplification of the IC differential cross section occurs when relativistic electrons ($E\gg m_{\rm e}c^2$) interact with low-energy photons ($\varepsilon_0\ll\varepsilon\ll m_{\rm e}c^2$). These conditions are typically satisfied in high-energy astrophysics. In this case, the differential cross-section expression for an isotropic distribution of photons and electrons ($d\sigma/d\varepsilon$, with units of [cm² erg⁻¹]) valid in both the Thomson and KN regimes can be obtained (Aharonian and Atoyan 1981):

$$\left\langle \frac{d\sigma_{\rm IC}}{d\varepsilon} \right\rangle = \frac{3\sigma_{\rm T}}{bE} \left[1 + \frac{z^2}{2(1-z)} - \frac{z}{b(1-z)} + \frac{2z^2}{b^2(1-z)^2} - \frac{z^3}{2b(1-z)^2} - \frac{2z}{b(1-z)} \ln \frac{b(1-z)}{z} \right], \tag{2.15}$$

where the parameter $b=4\varepsilon_0 E/(m_{\rm e}^2 c^4)$ and z is the ratio between the final photon and initial electron energy $(z=\varepsilon/E)$. The energy range of the scattered photon is $\varepsilon\in [\varepsilon_0, Eb/(1+b)]$. Note that the average differential cross section depends on the product ε_0 E. The reader is referred to Jones (1968) and Blumenthal and Gould (1970) for the original derivation of Eq. 2.15 and Aharonian and Atoyan (1981) for a generalised expression of the differential cross section as a function of the scattering angle.

The specific IC emissivity for an isotropic distribution of electrons with energy distribution per unit volume per unit solid angle $n_e(E)$ scattering off an isotropic

[†]In fact, these three quantities are related by the conservation of momentum and energy.

target photon distribution with energy distribution per unit volume $n_{\rm ph}(\varepsilon_0)$ can be computed through

$$j_{\rm IC}(\varepsilon) = \int_0^\infty dE \int_{\varepsilon_0}^{Eb/(1+b)} d\varepsilon_0 \, n_{\rm ph}(\varepsilon_0) \, c \, \varepsilon \, \left\langle \frac{d\sigma_{\rm IC}}{d\varepsilon} \right\rangle \, n_{\rm e}(E) \,. \tag{2.16}$$

Assuming a power-law energy distribution for electrons $n_{\rm e}(E) \propto E^{-p}$ and considering a mono-energetic photon distribution with energy ε_0 , the resulting specific emissivity in the Thomson regime $(b \ll 1)$ is $j_{\rm IC}(\varepsilon) \propto \varepsilon^{-\alpha}$ with a spectral index $\alpha = \frac{p-1}{2}$. Conversely, in the KN regime $(b \gg 1)$, the specific IC emissivity is $j_{\rm IC}(\varepsilon) \propto \varepsilon^{-\alpha} (\ln b + C)$, where $\alpha = p+1$ and C is a constant (Blumenthal and Gould 1970).

For electrons embedded in a mono-energetic photon field with an energy density given by $\omega_{\rm ph}=\int \varepsilon_0 n_{\rm ph}(\varepsilon_0) d\varepsilon_0$ with units of [erg cm⁻³], the IC energy losses per unit time in the Thomson and KN[‡] regimes are (Longair 2011; Blumenthal and Gould 1970):

$$-\left(\frac{dE}{dt}\right)_{\text{IC T}} = \frac{4}{3} \frac{c\sigma_{\text{T}}}{m_{\text{e}}^2 c^4} \,\omega_{\text{ph}} \,\beta^2 \,E^2 \approx \frac{4}{3} \frac{c\sigma_{\text{T}}}{m_{\text{e}}^2 c^4} \,\omega_{\text{ph}} \,E^2 \,, \tag{2.17a}$$

$$-\left(\frac{dE}{dt}\right)_{\rm IC,KN} \approx \frac{3}{8} c\sigma_{\rm T} \, m_{\rm e} c^2 \, \omega_{\rm ph} \, \varepsilon_0^{-2} \left(\ln b - \frac{11}{6}\right) \,. \tag{2.17b}$$

Note that relativistic electrons ($\beta \to 1$) are considered on the right-hand side of Eq. 2.17a. The expressions for the Thomson and KN regimes have remarkably different dependencies with the electron energy. The energy losses in the Thomson regime follows the same energy dependency ($\propto E^2$) as the energy losses for synchrotron emission. Furthermore, Eq. 2.17a is equivalent to Eq. 2.10 by replacing $\omega_{\rm ph}$ with $\omega_{\rm mag}$. In contrast, Eq. 2.17b is only weakly dependent on the electron energy ($\propto \ln E$). A generalised equation for the IC energy losses valid for both regimes is provided in Aharonian and Atoyan (1981).

The expressions in Eq. 2.17 are obtained assuming a mono-energetic radiation field, $\omega_{\rm ph} = \varepsilon_0 n_{\rm ph}$, instead of doing the integral over ε_0 of the product $\varepsilon_0 n_{\rm ph}(\varepsilon_0)$. In the case of a black-body radiation field, we refer the reader to Khangulyan et al. (2014).

The cooling time in the Thomson and KN regime can be approximated as (Aharonian 2004; Khangulyan et al. 2007)

$$\left[\frac{t_{\rm IC,T}}{\rm yr}\right] \approx 3 \times 10^8 \left[\frac{\omega_{\rm ph}}{\rm eV \, cm^{-3}}\right]^{-1} \left[\frac{E}{\rm GeV}\right] \,, \tag{2.18a}$$

$$\left[\frac{t_{\rm IC,KN}}{\rm s}\right] \approx 300 \left[\frac{\omega_{\rm ph}}{\rm erg\,cm^{-3}}\right]^{-1} \left[\frac{E}{\rm TeV}\right]^{0.7} \left[\frac{\varepsilon_0}{\rm eV}\right]^{1.7}.$$
 (2.18b)

Equation 2.18b is a good approximation if the product of electrons and photon energies is $E\varepsilon \in [1, 10^5] \, m_{\rm e}^2 c^4$ (Bosch-Ramon and Khangulyan 2009). More precise approximations for the IC cooling time in the KN regime can be used. The reader is referred to Aharonian and Atoyan (1981) and Moderski et al. (2005).

[‡]The expression for the KN regime is accurate for $b \ge 30$.

In some cases, electrons can IC scatter synchrotron photons present in the emitter region, a process known as synchrotron self-Compton (SSC). Therefore, the synchrotron photon field needs to be considered in the IC emissivity calculations in Eq. 2.16. In these cases, synchrotron and IC losses compete to dominate the particles energy losses.

2.2.3 Relativistic Bremsstrahlung

Charged particles produce electromagnetic radiation when they are accelerated, e.g., when deflected by the presence of Coulomb fields. This radiation is called bremsstrahlung emission. Due to the low inertia of electrons, they are more suited to undergo this process than massive particles when interacting with either ions or electrons. The term "relativistic bremsstrahlung" is used when the velocity distribution of the radiating particles is relativistic, whereas "thermal bremsstrahlung" describes the emission from a thermal particle distribution. Below, bremsstrahlung emission is discussed only for electrons passing through ions at relativistic energies.

The presence of surrounding electrons can screen to some extent the atomic potential that affects the radiating electrons, subsequently modifying the cross section of this process. The screening depends, in addition to the ionisation of the medium, on the energy of the relativistic incident electron, which will undergo a complete screening at the highest incident energies, $E \gg \alpha^{-1} m_{\rm e} c^2 Z^{-1/3}$, where α is the fine structure constant ($\alpha \approx 1/137$) and Z is the atomic number. While, a weak screening and unshielded nucleus will be reached as the energy decreases ($m_{\rm e} c^2 \ll E \ll \alpha^{-1} m_{\rm e} c^2 Z^{-1/3}$; Heitler 1954).

The differential cross section of an electron with energy E interacting with a nucleus with charge Ze that produces a photon with energy ε is (Bethe and Heitler 1934):

$$\frac{d\sigma_{\rm br}}{d\varepsilon} = \frac{3\alpha\sigma_{\rm T}}{2\pi} \frac{Z^2}{\varepsilon} \phi(\varepsilon, E) \,, \tag{2.19}$$

where the function $\phi(\varepsilon, E)$ may be expressed for the full screening case (neutral medium at high energies) as

$$\phi(\varepsilon, E) = \left[1 + \left(1 - \frac{\varepsilon}{E} \right)^2 - \frac{2}{3} \left(1 - \frac{\varepsilon}{E} \right) \right] \ln \left(\frac{183}{Z^{1/3}} \right) - \frac{1}{9} \left(1 - \frac{\varepsilon}{E} \right) . \tag{2.20}$$

In contrast, for the unshielded case, $\phi(\varepsilon, E)$ has the form

$$\phi(\varepsilon, E) = \left[1 + \left(1 - \frac{\varepsilon}{E}\right)^2 - \frac{2}{3}\left(1 - \frac{\varepsilon}{E}\right)\right] \times \left[\ln\left[\frac{2E(E - \varepsilon)}{m_e c^2 \varepsilon}\right] - \frac{1}{2}\right]. \tag{2.21}$$

Note that for an ionised medium, Eq. 2.21 is valid at all energies. Equations 2.19–2.21 are derived for electrons going through heavy nuclei material without considering the contribution of bremsstrahlung with bounded electrons. The factor Z^2 in Eq. 2.19 has to be replaced by Z(Z+1.3) when atomic electrons are considered (Longair 2011). The reader is referred to Blumenthal and Gould (1970) for a detailed derivation for the case of low Z medium.

Despite the $\propto 1/\varepsilon$ form of the differential cross section, its distribution is quite flat until $\varepsilon \sim E$. An electron is likely to emit a substantial part of its energy through

the production of a high-energy photon. The electron will lose its energy in discrete instants in time (Blumenthal and Gould 1970).

The specific emissivity for electrons with an energy distribution per unit volume per unit solid angle $n_e(E)$ going through a medium with atomic number density n is

$$j_{\rm br}(\varepsilon) = \int_{\varepsilon}^{\infty} dE \, c \, n \, \varepsilon \, \frac{d\sigma_{\rm br}}{d\varepsilon} \, n_{\rm e}(E) \, . \tag{2.22}$$

Note that the target particles are at rest since the cross section in Eq. 2.19 is obtained in the reference frame of the target particles. For the case of an electron energy distribution of the form $n_{\rm e}(E) \propto E^{-p}$, the specific bremsstrahlung emissivity recovers the spectral index of the electron energy distribution, i.e., $j_{\rm br}(\varepsilon) \propto \varepsilon^{-p}$ (Blumenthal and Gould 1970).

The energy loss rate for a single electron may be written for the full screening case as (Bethe and Heitler 1934)

$$-\left(\frac{dE}{dt}\right)_{\text{brs}} = \frac{3c\alpha\sigma_{\text{T}}}{2\pi} Z^2 n \left[\ln\left(183Z^{-1/3}\right) + \frac{1}{18}\right] E. \tag{2.23}$$

For the unshielded case, it may be expressed as

$$-\left(\frac{dE}{dt}\right)_{\text{br.u}} = \frac{3c\alpha\sigma_{\text{T}}}{2\pi} Z^2 n \left[\ln\left(2\frac{E}{m_{\text{e}}c^2}\right) - \frac{1}{3}\right] E.$$
 (2.24)

Although a relativistic electron likely loses most of its energy in discrete instants of time, it is also convenient to define the average energy losses for the case of a neutral hydrogen gas at high energies as (e.g. Aharonian 2004)

$$-\left(\frac{dE}{dt}\right)_{\rm br} = \frac{c\,m_{\rm p}\,n}{X_0^{\rm H}}E\,,\tag{2.25}$$

where X_0^H is the radiation length of hydrogen[§]. The approximately linear energy dependency of the bremsstrahlung energy losses[¶] compared with the approximately quadratic dependency for synchrotron and IC energy loss makes bremsstrahlung emission dominant at energies $E < E_0$, where E_0 is the energy at which the two processes have equal energy losses.

The cooling time corresponding to bremsstrahlung emission can be derived from Eq. 2.25:

$$\left[\frac{t_{\rm br}}{\rm yr}\right] = \frac{X_0^{\rm H}}{c \, m_{\rm p} \, n} \approx 3.94 \times 10^7 \left[\frac{n}{\rm cm}^{-3}\right]^{-1}.$$
 (2.26)

Alternatively, one could compute the bremsstrahlung cooling time using Eqs. 2.24 and 2.23. For the unshielded case, the cooling time has a weak dependence on the electron energy (through the term $\propto \ln E$ in Eq. 2.24).

For typical interstellar medium (ISM) number density values ($n_{\rm ISM} \leq 1 \, {\rm cm}^{-3}$; Ferrière 2001), the cooling time for this process is long compared with other

[§]The radiation length is defined as the average distance over which the electron loses 1/e of its energy. The value depends on the material. For hydrogen, $X_0^{\rm H} \approx 63\,{\rm g\,cm^{-2}}$ (De Angelis and Pimenta 2018; Navas et al. 2024).

[¶]Either from Eqs. 2.25, 2.23, or 2.24.

processes mediated by electrons at these densities. However, bremsstrahlung can be relevant at gamma rays above 100 MeV in astrophysical sources near dense regions such as molecular clouds if the energy density of photons and magnetic fields are relatively low (e.g. Munar-Adrover et al. 2013; Ackermann et al. 2013).

2.2.4 Pion decay

Relativistic protons or nuclei can produce gamma rays when they inelastically collide with other hadrons present in the ambient medium. These collisions produce particles such as pions, kaons, and hyperons. The heavy particles decay fast into multiple pions, which subsequently decay, concluding in the generation of gamma rays and other particles like neutrinos, electrons and positrons (e.g. Stecker 1971). The last two can contribute to the overall gamma-ray emission through the processes explained above. However, the main source of gamma rays is the decay of neutral pions, $\pi^0 \rightarrow 2\gamma$ (Kelner et al. 2006).

The minimum energy for an inelastic proton-proton collision to produce neutral pions is $E_{\rm kin}^{\rm th} \approx 286\,{\rm MeV}$ (e.g. Stecker 1971). Neutral pions mainly decay (98.8%) into a pair of photons. Proton-proton collisions produce neutral and charged pions with roughly equal probability at high energies. The latter decays mainly (99.9%) into a muon and neutrino, subsequently decaying into an electron and neutrinos (Gaisser 1991). However, the spectral distribution of pions is dominated by a few leading particles, which carry most of the kinetic energy of the collision (Aharonian 2004).

To compute the gamma-ray emissivity, one has to account for the neutral pion spectrum and compute the kinematics of two-body decay. The specific emissivity of gamma rays with energy ε can be written as (e.g. Aharonian 2004; Stecker 1971)

$$j_{\rm pp}(\varepsilon) = 2 \int_{E_{\pi}^{\rm min}}^{\infty} dE_{\pi} \, \varepsilon \, \frac{q_{\pi}(E_{\pi})}{\sqrt{E_{\pi}^2 - m_{\pi}^2 c^4}} \,,$$
 (2.27)

where m_{π} is the rest mass of the pion, E_{π}^{\min} is the lowest energy that pions can have and still produce gamma rays (defined as $E_{\pi}^{\min} = \varepsilon + \frac{m_{\pi}^2 c^4}{\varepsilon}$), and $q_{\pi}(E_{\pi})$ is the specific pion number emissivity with units of $[\text{cm}^{-3}\,\text{s}^{-1}\,\text{erg}^{-1}\,\text{sr}^{-1}]$. Computing $j_{\pi}(E_{\pi})$ requires integrations over multiple differential cross sections from experimental data (e.g. Stecker 1971). However, a simple formalism, known as the δ -function formalism (Aharonian and Atoyan 2000), provides accurate results under the assumption of a broad, smooth proton energy distribution. This approach considers that protons transfer a fraction κ of their kinetic energy $E_{\rm kin}$ to the leading pion. Then, the specific neutral pion number emissivity between relativistic protons with energy distribution per unit volume per unit solid angle $n_{\rm p}(E_{\rm p})$ and target protons with number density n can be expressed as

$$q_{\pi}(E_{\pi}) = cn \int dE_{p} \, n_{p}(E_{p}) \, \delta(E_{\pi} - \kappa E_{kin}) \, \sigma_{pp}(E_{p})$$

$$= \frac{cn}{\kappa} \, n_{p} \left(m_{p}c^{2} + \frac{E_{\pi}}{\kappa} \right) \, \sigma_{pp} \left(m_{p}c^{2} + \frac{E_{\pi}}{\kappa} \right) , \qquad (2.28)$$

where m_p is the proton mass and σ_{pp} is the total cross section of the proton-proton interaction (with units of [mb]). Equation 2.28 implies that the pion spectrum is

shifted κ times the proton spectrum, keeping the same spectral shape. Experimentally, $\kappa \sim 0.17$ and σ_{pp} may be approximated in the GeV–TeV energy range as (Aharonian and Atoyan 2000)

$$\left[\frac{\sigma_{\rm pp}}{\rm mb}\right] \approx 30 \times \left(0.95 + 0.06 \ln \left[\frac{E_{\rm kin}}{\rm GeV}\right]\right). \tag{2.29}$$

This approximation is valid at energies $E_{\rm kin} \geq 1\,{\rm GeV}$ because at lower energies, the energy dependency of the cross section is not logarithmic. Instead, it increases fast with increasing energy up to 30 mb. The reader is referred, e.g., to Kelner et al. (2006) for a refined cross section parametrisation valid close to $E_{\rm kin}^{\rm th}$.

The emitted gamma-ray differential energy spectrum, $d\phi/dE$ (with units of $[\text{cm}^{-2}\,\text{s}^{-1}\,\text{erg}^{-1}]$), from a population of pions with different energies always peaks at half of the rest mass energy of the neutral pion, independently of their energy distribution. $d\phi/dE$ is symmetric with respect to this maximum (Stecker 1971). At energies beyond the maximum, it is similar to the relativistic proton spectrum but shifted $\sim (\kappa/2)E_{\rm p} \sim 0.1E_{\rm p}$. Therefore, the emission of pion decay provides direct information on the energy distribution of the relativistic protons (Aharonian 2004).

More sophisticated parametrisations for the energy spectra of gamma rays and secondary particles exist, which are valid in a wide energy range and provide accurate results even if abrupt spectral features are present in the proton energy distribution, e.g., pileups or cutoffs (Kelner et al. 2006; Kafexhiu et al. 2014).

A relativistic proton undergoing proton-proton collisions loses about 50% of its energy in a single interaction (e.g. Gaisser 1991). Therefore, the energy losses can be written as

$$-\left(\frac{dE}{dt}\right)_{\rm pp} = c\,\sigma_{\rm pp}\,n\,f\,E\,,\tag{2.30}$$

where f is the coefficient of inelasticity, i.e. $f \approx 0.5$ as stated above. The cooling time of protons through inelastic proton-proton interactions takes the form (Begelman et al. 1990):

$$t_{\rm pp} = (c \, \sigma_{\rm pp} \, n \, f)^{-1} \,.$$
 (2.31)

Similar to relativistic bremsstrahlung, $t_{\rm pp}$ is weakly energy dependent ($\propto 1/\ln E$). For TeV protons, and adopting $\sigma_{\rm pp} \sim 40~{\rm mb}^{-1}$, Eq. 2.31 might be written as (Aharonian 2004):

$$\left[\frac{t_{\rm pp}}{\rm yr}\right] \approx 5.28 \times 10^7 \left[\frac{n}{\rm cm}^{-3}\right]^{-1}.\tag{2.32}$$

Dense regions with high number densities will be more efficient to produce gamma rays through proton-proton interactions, e.g., in SN remnants interacting with molecular clouds or nova eruptions (Ackermann et al. 2013; Acciari et al. 2022).

¹¹ A reasonable assumption given the mild dependency of σ_{pp} with the energy (see Eq. 2.29).

2.3 GAMMA-RAY ABSORPTION MECHANISMS

If absorption processes are present, the radiative transfer equation (see Eq. 2.4) can be solved for the case in which one has emission and absorption, or for the case in which only absorption is present. The solution of Eq. 2.4 in the first case leads to:

$$I(\varepsilon) = \frac{j(\varepsilon)}{k(\varepsilon)} \left(1 - e^{-\tau(\varepsilon)} \right) , \qquad (2.33)$$

where $\tau(\varepsilon)$ is the optical depth, which depends on the cross section of the absorption process, σ , and the number density of particles in the medium, n, along the line of sight as follows:

$$d\tau = n \,\sigma \,ds \,. \tag{2.34}$$

When $\tau \lesssim 1$, photons can pass through the absorber medium without being absorbed since the medium is optically thin. The opposite occurs for an optically thick medium ($\tau > 1$). Equation 2.33 is valid for the case of synchrotron self-absorption at radio wavelengths, for which the specific intensity $I(\varepsilon) \propto \varepsilon^{\frac{5}{2}}$ when $\tau \gg 1$, as mentioned in Sect. 2.2.1.

On the other hand, if only absorption mechanisms are present $(j(\varepsilon) = 0)$, an emitter with an initial specific intensity $I_0(\varepsilon)$ will be observed with a specific intensity $I(\varepsilon)$ after traversing an absorber medium as

$$I(\varepsilon) = I_0(\varepsilon) e^{-\tau(\varepsilon)}. \tag{2.35}$$

This is the situation at gamma rays above 100 MeV once they are created by the processes described in Sect. 2.2.

The main absorption processes at gamma rays above 100 MeV is electron-positron pair creation. In this process, a pair can be created by the interaction of gamma rays with a magnetic, photon, or Coulomb field. In this Thesis, we will be mainly concerned by gamma-ray absorption in intense photon fields, as it is the case of the bright photospheres of a nova and SN (see Chapts. 5 and 6, respectively). A detailed description of absorption processes due to high values of the magnetic field in the acceleration/emission region, or in very dense particle environments, can be found in Aharonian (2004).

2.3.1 *Photon-photon pair production*

Electron-positron pairs can be efficiently created from gamma rays interacting with an intense photon field, e.g., the radiation emitted by a massive companion star in a binary system (e.g. Bednarek 1997). Conversely, this process can also be relevant in low-photon fields, such as the extragalactic background light (EBL), when the gamma-ray source is at cosmological distances, because the chances of interaction between the emitted gamma-ray and the EBL increase (Gould and Schréder 1967a). In this situation, a gamma-ray horizon is actually present at a given redshift beyond which all gamma rays are absorbed.

The total cross section of pair production from two photons with energies ε_{γ} and ε_0 colliding at an angle θ in the laboratory frame is (Gould and Schréder 1967b):

$$\sigma_{\gamma\gamma} = \frac{3}{16}\sigma_{\rm T}(1-\xi^2) \left[(3-\xi^4) \ln\left(\frac{1+\xi}{1-\xi}\right) - 2\xi(2-\xi^2) \right] , \qquad (2.36)$$

where

$$\xi = \left[1 - \frac{1}{s}\right]^{1/2} \,, \tag{2.37}$$

and

$$s = \frac{\varepsilon_{\gamma}\varepsilon_0(1 - \cos\theta_{\gamma\gamma})}{2m_{\rm e}^2c^4} \,. \tag{2.38}$$

Photon-photon pair production occurs ($\sigma_{\gamma\gamma} > 0$) only if there is enough energy to produce an electron-positron pair, that is, if $s \ge 1$, i.e.,

$$\varepsilon_{\gamma} \, \varepsilon_0 \, (1 - \cos \theta) \ge 2m_{\rm e}^2 c^4 \,. \tag{2.39}$$

The cross section reaches a maximum value of $\sigma_{\gamma\gamma}^{\rm max} \approx 0.2\sigma_{\rm T}$ at $s \sim 3.5$ –4 and decays at large s, similar to the IC cross section in the KN regime (Aharonian 2004).

The specific pair-creation optical depth for a gamma ray travelling along a length l in a photon field with energy distribution per unit volume per unit solid angle $n(\varepsilon_0, l)$ is

$$\tau(\varepsilon_{\gamma}) = \int_{0}^{l} dl \left[1 - \cos \theta_{\gamma \gamma}(l) \right] \int_{\varepsilon_{0,\text{min}}}^{\infty} d\varepsilon_{0} \, n(\varepsilon_{0}, l) \, \sigma_{\gamma \gamma}(\varepsilon_{\gamma}, \varepsilon_{0}, \theta_{\gamma \gamma}(l)) \,, \tag{2.40}$$

where

$$\varepsilon_{0,\min} = \frac{2m_{\rm e}^2 c^4}{\varepsilon_{\gamma} (1 - \cos \theta_{\gamma\gamma})} \tag{2.41}$$

is the initial minimum energy of the low-energetic target photon for pair production to occur. The optical depth of photon-photon pair creation can change with time if the relative position between the gamma-ray emitting region and the low-energy photon emitting region changes with time. Moreover, changes with time in the energy or the number density of the low-energy photons can also affect the optical depth. These situations are discussed in Chapts. 5 and 6.

It is worth noting that the created pair might produce synchrotron radiation or undergo IC scattering if the synchrotron or IC losses are high enough. In the case of VHE gamma-ray emission this reprocessing can lead to a net redistribution of the emission towards lower energies, in the GeV band.

3

GAMMA-RAY DETECTORS

The Earth atmosphere is optically thick at the sea level for a wide range of energies across the electromagnetic spectrum. Luckily for life, the gamma rays are not an exception. When they fall upon Earth, gamma rays interact with the matter in the atmosphere. The two main processes of gamma-ray-matter interaction are Compton scattering and pair creation in the presence of a Coulomb field (also known as Bethe-Heitler pair production). Compton scattering dominates at energies from $\sim 0.1 \, \text{MeV}$ to $\sim 10 \, \text{MeV}^*$. At higher energies, Bethe-Heitler pair production is the dominant process (Knoll 2000).

The result of Compton scattering and Bethe-Heitler pair production are energetic charged particles (electrons and positrons) that will dissipate their energy in the atmosphere. The height above sea level (a.s.l.) where these interactions initially occur depends on the energy of the incident gamma ray, ranging from $\sim 50\,\mathrm{km}$ to $\sim 30\,\mathrm{km}$ for MeV and GeV vertical-incident gamma rays, respectively (Siegert et al. 2022). It is convenient to use the depth[†] of the material as a function of the radiation length (see definition in Sect. 2.2.3). The total atmospheric depth at sea level is $X^{\mathrm{atm}} \approx 1030\,\mathrm{g\,cm^{-2}}$. The radiation length by bremsstrahlung of electrons in the Earth atmosphere is $X_{\mathrm{e}} \approx 37\,\mathrm{g\,cm^{-2}}$, while photons have a radiation length through pair creation of $X_{\gamma} = \frac{9}{7}X_{\mathrm{e}}$. Therefore, the atmosphere thickness at sea level is equivalent to ~ 28 and ~ 21 radiation lengths for electrons and photons, respectively.

Gamma rays can only be *directly* detected using satellites above the Earth atmosphere (or high-altitude balloons). This method is effective for gamma rays up to hundreds of GeV due to technological limitations. For energies exceeding a few tens of GeV, *indirect* detection of gamma rays from the ground becomes feasible.

This chapter provides an overview of both space-borne and ground-based gammaray detectors. Section 3.1 describes the methods and current satellites used to directly detect HE gamma rays. Section 3.2 focuses on indirect methods for detecting VHE and UHE gamma rays, along with current instruments operating in this energy range.

3.1 SPACE-BORNE DETECTORS

Direct detection of gamma rays is based on making the gamma-ray interact with matter, i.e., the detector, which is designed according to the dominant interaction mechanism in the studied energy range. Detectors in the MeV band rely on Compton scattering effects, whereas GeV detectors employ the electron-positron pair created in the Bethe-Heitler pair production. Additionally, photo-electric absorption is used to detect soft gamma rays below hundreds of keV and X-rays. The exact energy of transition between the relevant processes depends on the detector material (Knoll

^{*}The values stated are specific to air.

[†]The amount of matter per unit area that a particle encounters along its path.

2000). This section focuses on GeV detectors (hereafter pair-creation detectors). The reader is referred, e.g., to Kierans et al. (2022) and Goldwurm and Gros (2022), for detectors designed to conduct observations of gamma rays below tens of MeV, such as the imaging Compton telescope (COMPTEL) detector onboard the *Compton Gamma Ray Observatory (CGRO)*, the two instruments on the INTErnational Gamma-Ray Astrophysics Laboratory (*INTEGRAL*) satellite, Imager on Board *INTEGRAL* Satellite (IBIS) and SPectrometer on *INTEGRAL* (SPI), or the future mission *Compton Spectrometer and Imager (COSI)*.

The first interaction of a gamma ray with the detector takes place in the converter, a high-Z material that enhances the probability of Bethe-Heitler pair production. Following this interaction, the pair-creation detector aims to estimate key properties of the incoming gamma ray: its direction, energy, and arrival time. The gamma-ray direction is estimated by reconstructing the trajectory of the by-product (secondary) particles from the pair-production process. Tracker detectors are employed for this task. The electrons and positrons have to be tracked immediately after they are created because they undergo multiple Compton scatterings and bremsstrahlung processes, deflecting them. These effects become particularly relevant at low photon energies (below 100 MeV; e.g. Atwood et al. 2009). As a consequence, the angular resolution typically degrades as the energy of the incident gamma ray decreases. The gamma-ray energy is estimated by calorimeters, which measure the total energy of the by-products. Calorimeters are optically thick, high-Z materials where the secondary particles dissipate their energy by developing electromagnetic showers (see Sect. 3.2.1) and are completely absorbed. Finally, the arrival time is estimated based on the clock time at which the detector produces an event trigger from a particle interaction.

Although space telescopes elude the atmosphere, they still have to deal with a large background induced by charged particles from solar origin, CRs, etc. These particles can mask the signal of a gamma ray. Additionally, these particles can produce gamma rays as by-products of their interaction with local material or the Earth atmosphere. To effectively detect astrophysical gamma rays, which are a small fraction compared with the background, suppressing the background is essential. For this task, an anti-coincidence detector is placed around the trackers to detect and veto charged particles producing background signals while providing minimal absorption to gamma rays. Additional methods are used nowadays to discriminate the background from the gamma rays (e.g. Atwood et al. 2009).

Since gamma rays cannot be reflected or refracted, the effective area of these instruments is the detector size (see definition in Sect. 4.1.5). However, the detector size and mass are restricted by the payload rocket capabilities and the cost of launching heavy instrumentation to low Earth orbit. As a result, the capabilities of space detectors are limited at gamma-ray energies above hundreds of GeV because (1) the probability of detecting VHE gamma rays is low, as the effective area of the detector is limited to $\sim 1~\text{m}^2$ and the intrinsic VHE gamma-ray flux at these energies is low. For example, the integral Crab flux above 1 TeV is $\approx 2 \times 10^{-7}~\text{cm}^{-2}~\text{s}^{-1}$ (Aharonian et al. 2006). (2) The calorimeter dimensions should be thick enough to absorb the secondary particles to properly estimate the energy of the incident gamma ray.

Initial pair-creation detectors had a poor angular resolution and did not reconstruct the traces of the secondaries, as the gamma-ray telescope on the *Orbiting Solar Observatory 3* (*OSO-3*) (Kraushaar et al. 1972). Subsequently, imaging pair-creation detectors reconstructing the traces of the secondaries were designed. They can be grouped into three generations. Key members of the first generation are the *Second Small Astronomy Satellite* (*SAS-2*) and the *Celestial Observation Satellite B* (*COS-B*) (Fichtel et al. 1975; Swanenburg et al. 1981, and references therein), while the most successful detector of the second generation is Energetic Gamma Ray Experiment Telescope (EGRET) onboard *CGRO* (Thompson 2008). Currently, the most known pair-creation detectors (third generation) are the Large Area Telescope (LAT) on the *Fermi Gamma-ray Space Telescope* (hereafter *Fermi-LAT*) and the Gamma Ray Imaging Detector (GRID) onboard the *Astro-Rivelatore Gamma a Immagini Leggero* (*AGILE*) satellite (Atwood et al. 2009; Tavani et al. 2008). Figure 1.1 shows the number of sources detected with *SAS-2*, *COS-B*, EGRET and *Fermi-LAT*. Below a description of *Fermi-LAT* is provided.

3.1.1 Fermi-LAT

Fermi-LAT is the most sensitive instrument nowadays operating in the GeV band. Since its launch on 11 June 2008, Fermi-LAT has been the flagship telescope at HE gamma rays. At an altitude of about 550 km, the Fermi Gamma-ray Space Telescope orbits the Earth every 96 min. It primarily operates in survey mode, enabling the monitoring of the entire sky every \sim 3 h with an exposure time on each sky pointing of 30 min (Atwood et al. 2009).

Fermi-LAT is arranged in 16 modular units, setting up a 4x4 array. Each unit consists of a tracker-converter module placed on top of the calorimeter. The 16 tracker-converter units are covered by an anti-coincidence detector. The tracker-converter is divided into two regions (front and back) where the thickness of the converter material (foils) have different thicknesses. A thin converter in the front region allows a better point spread function (see Sect. 4.1.5) at low energies, while a thicker converter in the back region increases the effective area at high energies. The total vertical thickness of the calorimeter is 8.6 radiation lengths (Atwood et al. 2009). A schematic view of Fermi-LAT is shown in Fig. 3.1.

The total effective area of the 16 modules is $0.95\,\mathrm{m}^2$ at nominal incident angles. The half opening angle is 70° (FoV of 2.4 sr). The energy range extends from 20 MeV to 300 GeV with an energy resolution on-axis below 15% at 100 MeV, reaching the best energy resolution of about 6% at a few tens of GeV. The angular resolution is reduced from <3.5° at 100 MeV to <0.15° at $E > 10\,\mathrm{GeV}$ (Atwood et al. 2009)‡.

The continuous scan of the sky with *Fermi*-LAT has provided the deepest all-sky map at HE gamma rays up to date, impacting on the physical understanding of both galactic and extragalactic sources. *Fermi*-LAT has detected more than 7,200 sources at energies between 50 MeV and 1 TeV (see Fig. 1.1; Abdollahi et al. 2022; Ballet et al. 2023).

[‡]Further information about the *Fermi*-LAT performance can be found in https://www.slac.stanford.edu/exp/glast/groups/canda/lat_Performance.htm.

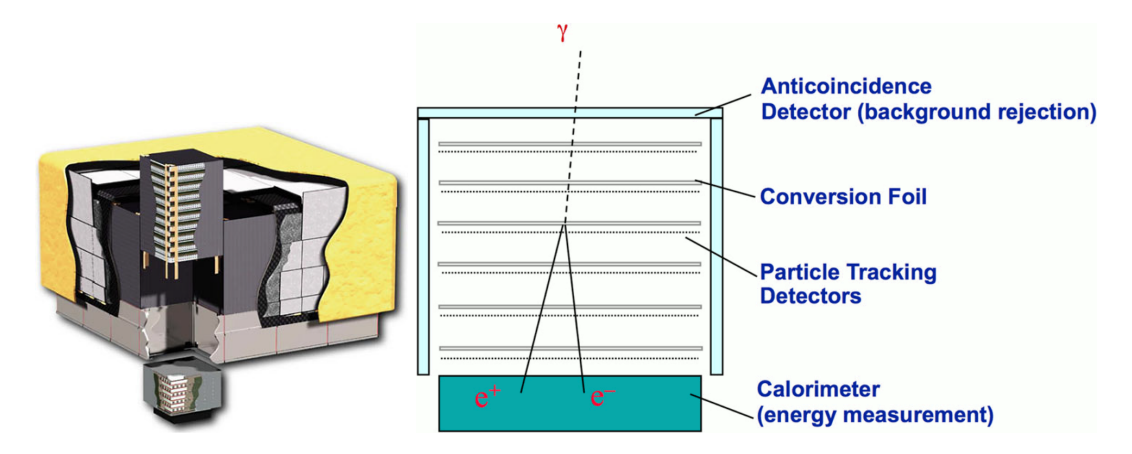


Figure 3.1: Sketch of LAT. Left: Schematic cutout view of LAT. Credit: Baldini (2014). Right: Schematic view of the components of LAT. Credit: Thompson (2015).

3.2 GROUND-BASED DETECTORS

The atmosphere acts as a calorimeter that dissipates the energy of the incident gamma rays. When a gamma ray interacts with the atmosphere, it generates a cascade of secondary particles known as an extensive air/atmospheric shower (EAS) (Auger et al. 1939). The properties of the incident gamma ray can be inferred by characterising the main properties of the EAS. However, CRs also produce EASs, which constitute a large background that ground-based detectors have to subtract. In particular, CRs outnumber the GeV-TeV gamma rays by more than a thousand times (e.g. Maier and Knapp 2007), making the background rejection a key point in GeV-TeV astrophysics.

Ground-based detectors may characterise the EAS either indirectly or directly. The first group relies on the emission induced by the EAS, while the second detects the tail of EAS secondary particles that reach the ground. The main detectors using the first technique are called atmospheric Cherenkov telescopes (ACTs) because they utilise the Cherenkov emission produced by the EAS particles as a calorimetric measurement. If ACTs can spatially resolve the EAS through an image, they are known as Imaging ACTs (IACTs). On the other hand, the tail of secondary particles is detected with particle detector arrays§.

Each technique has its own performance limitations. IACTs are sensitive to gamma rays with energies ranging from tens of GeV to hundreds of TeV. In contrast, particle detector arrays have a higher gamma-ray energy threshold of about (sub-)TeV energies. However, they can be sensitive to gamma-ray energies up to the PeV range. The development of EASs and the emission of Cherenkov radiation are explained in Sects. 3.2.1 and 3.2.2, respectively. Details on IACT and particle-detector-array techniques are provided in Sect. 3.2.3 and 3.2.4, respectively.

[§]This type of detectors is referred to differently according to the reference. A collection of names includes air shower particle detectors, particle samplers, particle arrays, particle detector arrays, air shower arrays, and surface detectors. In this Thesis, they are named particle detector arrays.

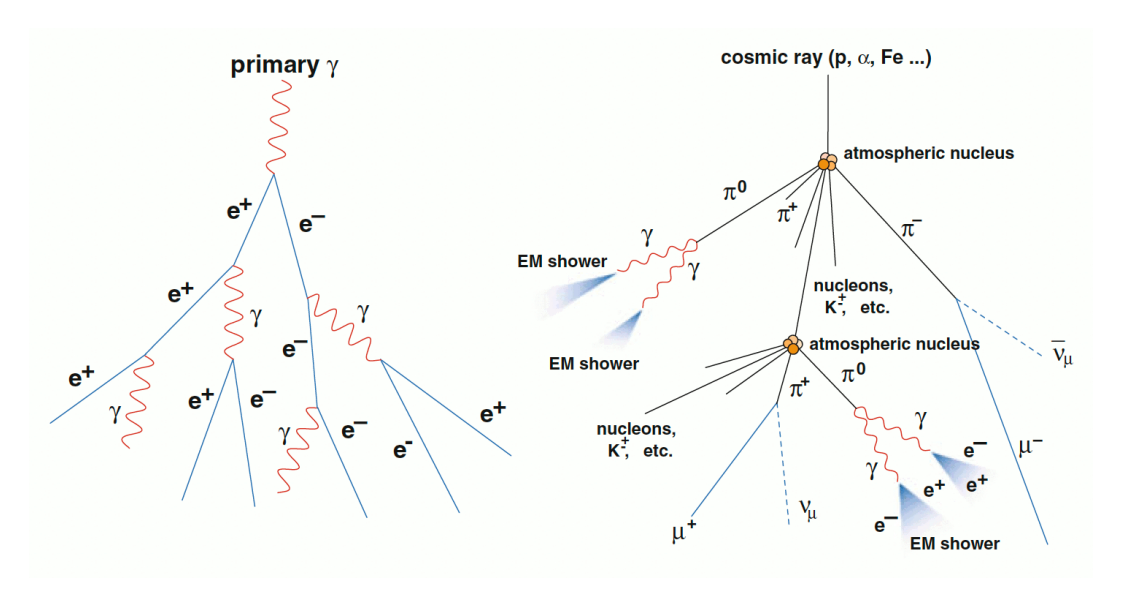


Figure 3.2: Schematic view of an EAS induced by a gamma ray (left) and a CR (right). Credit: Wagner (2006).

3.2.1 Extensive air shower

The secondary particles from a gamma-ray-matter interaction will radiate most of their energy through bremsstrahlung losses. This mechanism rules the energy losses until the charged particles reach the energy where ionisation losses dominate. This energy is called critical energy (in air, $E_c \approx 86 \,\mathrm{MeV}$; e.g. De Angelis and Pimenta 2018). While the radiating secondary electrons and positrons are above this critical energy, they will produce secondary gamma rays that will subsequently create further electron-positron pairs. The average particle energy after each interaction decreases accordingly. As a result, a cascade of particles develops until the ionisation losses dominate. Compton scattering dominates over Bethe-Heitler pair production at low photon energies (~10 MeV). Showers formed by gamma rays, electrons, and positrons are called electromagnetic showers (see left panel of Fig. 3.2). These particles are distributed longitudinally following the axis of motion of the initial gamma ray and extend laterally due to Coulomb scattering between the particles (Gaisser and Hillas 1977; Hillas 1982a). The maximum number of particles is obtained when $E = E_c$. A rough estimate of the number of particles at the maximum particle development is $N \propto E_0/E_c$. The maximum occurs at a height $H_{\rm max} \propto$ $\ln^{-1}(E_0/E_c)$ (e.g. Heitler 1954; Gaisser 1991). EASs from gamma rays of tens of GeV to a few TeV have an order of magnitude $H_{\rm max}$ value between 12 km and 8 km, respectively (de Naurois and Mazin 2015).

The collision of a CR[¶] with a nucleus of the atmosphere results in the production of multiple pions, kaons and light baryons moving predominantly in the initial proton direction (see Sect. 2.2.4). These particles will collide again, leading to the development of an EAS. The fast decay time of neutral pions will promptly produce gamma rays that will create electromagnetic sub-showers. Charged pions will produce muons, a fraction of which will reach the ground due to their relatively large

[¶]We consider in this case only particles made of hadrons. Electrons (about 1% of the CR particles) are omitted because they initiate an electromagnetic shower.

lifetime and relativistic effects without suffering Coulomb scattering. Meanwhile, the other fraction will decay into neutrinos, electrons, positrons. The latter two producing additional electromagnetic sub-showers. As a result, a heterogeneous EAS will develop, called hadronic shower (see right panel of Fig. 3.2). CR-induced EASs are characterised by a longer lifetime than electromagnetic EASs (the latter lasting a few ns compared with $\sim\!10\,\mathrm{ns}$ for hadronic showers due to the muon component). Notably, another difference with respect to electromagnetic EASs is the wider lateral dispersion produced by the relatively large momentum that the charged pions impart in the collisions (e.g. Aharonian et al. 2008). In contrast, the typical interaction in electromagnetic showers transfers a transverse momentum to the secondary particles proportional to the electron mass, which is 270 times smaller than the pion mass.

Despite the differences between CR- and gamma-ray-induced EASs, several effects can make their classification difficult. Firstly, the hadronic showers can mimic gamma-ray-induced EASs if the leading particle of the collision is a neutral pion that produces a sub-electromagnetic shower (Maier and Knapp 2007). EASs with low pion multiplicity and a large fraction of energy into neutral pions produce an irreducible background to gamma-like-induced EASs (Sitarek et al. 2018). Secondly, the geomagnetic field has a large influence on low-energy gamma rays. This effect widens the transversal EAS development in the E–W direction as the e^- and e^+ are deflected in opposite directions, resulting in a more hadron-like-induced EAS appearance (Bowden et al. 1992; Commichau et al. 2008; Szanecki et al. 2013).

3.2.2 Cherenkov emission

A charged particle with velocity v crossing a dielectric medium with refraction index n will produce Cherenkov radiation if it moves faster than the speed of light c in the medium, i.e, $v > \frac{c}{n}$. The emission arises from the constructive interference of the retarded potentials of the electromagnetic fields of the charged particle while they expand at velocity c/n (Frank and Tamm 1937; Longair 2011). This superposition of multiple contributions from different retarded times forms a shock-wave-like cone surface with the apex at the moving particle and with an opening angle Θ_c relative to the particle axis of motion (see left panel of Fig. 3.3). Therefore, Cherenkov radiation is produced by the medium under the effect of the field of the moving particle (Landau and Lifshitz 1984).

Alternatively, Cherenkov emission can be explained qualitatively by the reaction of the medium with refraction index n to the passage of a charged particle. If its velocity is $v < \frac{c}{n}$, its crossing will symmetrically polarise the medium by its electromagnetic field. In the opposite situation, $v > \frac{c}{n}$, the particle will produce a non-symmetric polarisation field in the axis of motion because it travels faster than the field that induces this polarisation (see right panels in Fig. 3.3). The Cherenkov radiation will arise when the polarised medium relaxes.

The Cherenkov emission opening angle Θ_c satisfies the relation (Čerenkov 1937):

$$\cos\Theta_{\rm c} = \frac{c}{vn}.\tag{3.1}$$

¹¹The term "multiplicity" refers to the number of produced pions.

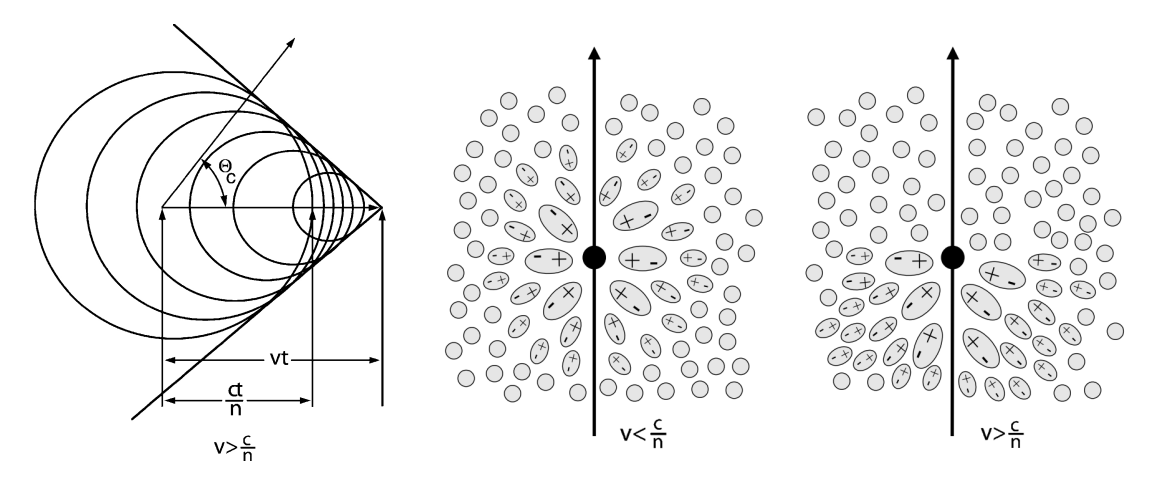


Figure 3.3: Left: Schematic view of the wavefront and the Cherenkov opening angle. Credit: Tavernier (2010). Middle and right: Schematic view of how a medium is polarised when a particle passes with a velocity below or above the speed of light in the medium. Credit: Adapted from de Naurois and Mazin (2015).

The spectral distribution of Cherenkov light per unit length is (Frank and Tamm 1937):

$$\frac{d^2N}{dxd\lambda} = 2\pi\alpha Z^2 \frac{\sin^2\Theta_c}{\lambda^2}.$$
 (3.2)

Relativistic particles in the EAS produce Cherenkov emission**. This emission can be used to characterise the EAS or detect relativistic particles, subsequently deriving properties of the primary particle.

The observed Cherenkov emission from the ground produced by an EAS will be the emission from all the EAS secondary particles. Additionally, since the atmosphere is not homogeneous, the refraction index will change with the height a.s.l. and Cherenkov emission accordingly. Dedicated reviews on the Cherenkov emission from EASs can be found in Hillas (1982b), Rao and Sinha (1988), Aharonian et al. (2008), de Naurois (2012), and de Naurois and Mazin (2015). Below, the main properties important for this Thesis are provided.

The Cherenkov emission from

acspEAS is a brief emission flash that lasts few ns, peaking at UV-blue wavelengths ($\lambda \approx 300\text{--}350\,\text{nm}$). A vertical incident gamma ray produces a flat-ish lateral distribution^{††} of photons centred on the gamma-ray incident direction with a radius of $\sim 120\,\text{m}$. At larger radii, the number of photons decreases. The exact angular distribution depends on the energy and height a.s.l. However, non-statistical fluctuations in the light density appear when the gamma-ray energy decreases (Chitnis and Bhat 1998).

CR-induced EASs produce non-uniform photon distributions with irregular and wider timing profiles than gamma rays because the irregularities in the EAS are propagated into the Cherenkov emission (see, e.g. Fig. 3.4 and Oser et al. 2001). The Cherenkov emission mainly originates from the superposition of multiple

^{**}The energy losses through Cherenkov radiation can be considered negligible compared with bremsstrahlung and ionisation losses since they are about 0.1% relative to ionisation.

⁺⁺The projection on the ground of this flat-ish part is called light pool.

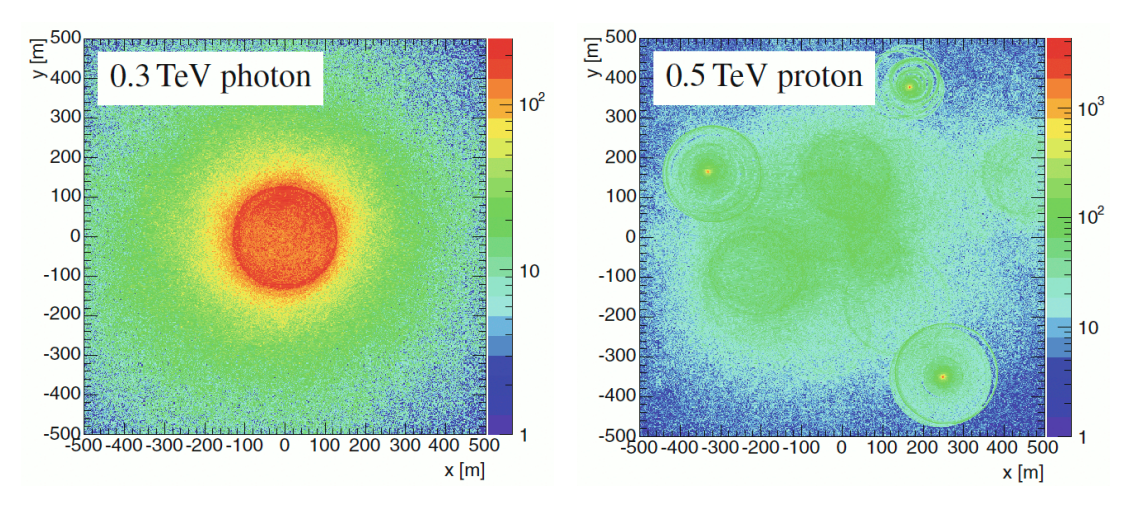


Figure 3.4: Angular distribution of Cherenkov photons from a gamma ray (left) and a proton (right). Credit: Errando and Saito (2024).

electromagnetic sub-showers produced by the gamma rays from neutral pion decays (Chitnis and Bhat 1998).

The Cherenkov emission is a measurable signal to estimate the energy of the incident gamma ray because the total number of Cherenkov photons is proportional to the number of secondaries^{\ddagger}, which is also a quantity proportional to the incident gamma ray energy. For example, a vertical-incident 1 TeV gamma ray produces about 180 photons m⁼² at 1.7 km a.s.l. within 125 m of the EAS axis, but only about 50 photons m⁼² for a 100 GeV gamma ray (Oser et al. 2001).

3.2.3 Imaging Atmospheric Cherenkov Telescopes

IACTs are designed to detect the Cherenkov emission produced by a gamma ray entering the atmosphere. IACTs are characterised by large collection areas that focus the light into the focal plane where the camera digitalises the images. As a result, the images are snapshots of the total longitudinal development of the EAS. IACTs aim to resolve the Cherenkov image of the EAS to reconstruct the properties of the primary event that induced it.

The technical requirements for detecting the brief Cherenkov emission of 10–100 photons m $^{-2}$ inside a circular surface of radius \sim 120 m and resolving the image are (Errando and Saito 2024):

- Large collection mirrors (\sim 100 m²) to collect as many photons as possible.
- Relative large FoV to observe the gamma rays inside the Cherenkov pool^{§§}. Current values are $\gtrsim 3^{\circ}$.

^{‡‡}Note that the Cherenkov emission from EASs is not an ideal calorimeter for protons or heavier particles as fewer particles yield Cherenkov light than gamma-ray initiated cascades, and some particles such as muons are not fully absorbed in the atmosphere (see Wagner 2006; Oser et al. 2001).

^{§§}The usual operation mode of IACT places the source of interest shifted with respect to the telescope pointing for background subtraction (see Sect. 4.1.6.1). This mode implies that a larger FoV is required than the one needed only from the light pool restrictions.

- Fast and sensitive cameras are required to record the brief Cherenkov light over the night sky background (NSB). Photomultiplier tubes (PMTs) with high quantum efficiency are usually used.
- To resolve the Cherenkov image of the EAS, the angular resolution, the pointing accuracy and the camera pixel sizes must be $\leq 0.1^{\circ}$.

IACTs should be placed at an altitude that optimises their performance by ensuring (1) the EASs have sufficiently developed to allow for effective calorimetric measurements and (2) the atmosphere has high transparency to Cherenkov light (de Naurois and Mazin 2015). At the lowest energies, their performance is marred by the limited number of photons detected. Consequently, IACTs suffer from a higher energy threshold at lower altitudes. At the highest energies, IACTs are limited by the number of gamma rays. Despite these limitations, IACTs can study a broad energy range that spans the energy from tens of GeV to hundreds of TeV. Furthermore, they are well suited for the study of non-thermal emission phenomena down to sub-second time-scale (Aharonian et al. 1997b).

IACTs can detect the Cherenkov emission inside the light pool, meaning that the effective area of IACTs is the same light pool size, i.e., $\sim 5 \times 10^4$ m². Nevertheless, the typical collection area of a single telescope is small compared with the light pool area. Therefore, the information recorded is limited to sampling bias and intrinsic fluctuations of the Cherenkov emission by fluctuations in the EAS development (Hofmann 2006). The current energy resolution of IACTs is about 15%.

IACTs are limited by a low duty cycle of about 15% because the sensitive cameras require operation in astronomical darkness or moderate moonlight conditions (e.g. Ohm et al. 2023). The cameras are triggered when multiple pixels exceed a set discrimination threshold. However, in addition to gamma rays, other sources can exceed the discrimination threshold to trigger the camera, such as fluctuations in the NSB and Cherenkov light from CRs. These background events outnumber gamma rays by orders of magnitude and must be suppressed. Additional conditions, such as temporal and topological coincidence of multiple pixels, are applied to suppress accidental events from random triggers. Gamma-ray events are then separated from CR events by exploiting their intrinsic Cherenkov emission differences (see Sect. 3.2.2).

Placing multiple telescopes inside the light pool enables (1) to record the EAS from different locations to reduce the sampling bias and (2) to geometrically reconstruct the EAS from different viewing angles (Aharonian et al. 1997a). Thus, multi-instrument observations improve the EAS reconstruction and reduce the background level by removing events triggered randomly by a single telescope. This approach is called stereoscopic mode and is widely used in current observatories (see Fig. 3.5).

Initial Cherenkov telescopes were small counting-rate detectors. With them, no robust detection of a gamma-ray source was achieved. The first detection was accomplished with the second generation of IACTs. In particular, the first detection was the Crab Nebula with the Whipple telescope (see Fig. 1.1; Weekes et al. 1989). Nowadays, a transition between the third and fourth IACT generations is ongoing. The third generation is formed by the mature Major Atmospheric Gamma-ray

 $[\]P\P$ Astronomical darkness is defined as the conditions when the Sun is 18° below the horizon.

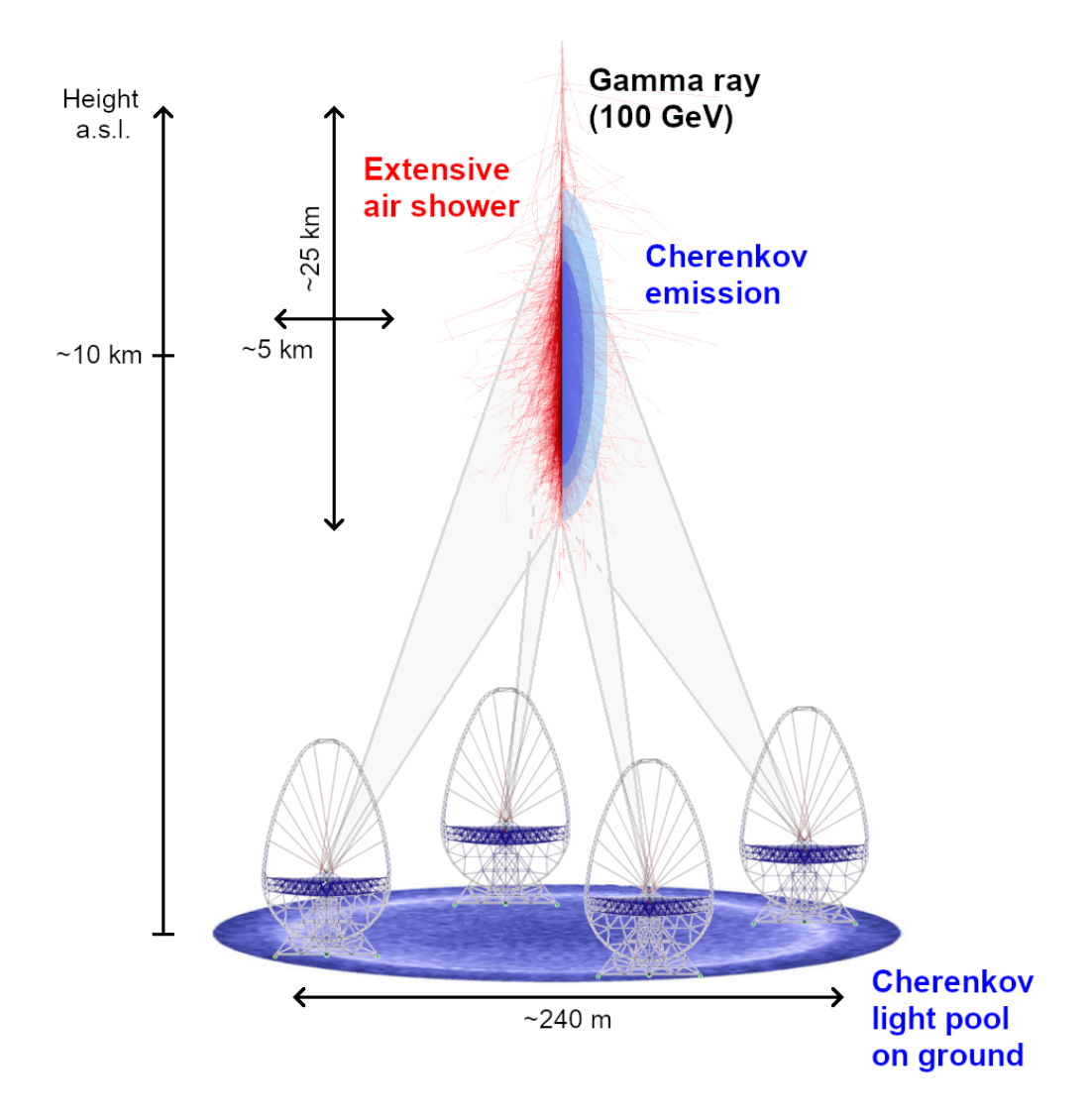


Figure 3.5: Sketch not to scale of the stereoscopic view of a gamma-ray-induced EAS using multiple telescopes. Each telescope views the EAS from different positions inside the Cherenkov pool.

Imaging Cherenkov (MAGIC), the High Energy Stereoscopic System (H.E.S.S.), and the Very Energetic Radiation Imaging Telescope Array System (VERITAS) experiments, among others. The upcoming fourth generation will constitute CTAO. Currently, the first telescope of CTAO is under commissioning, and more are under construction. The reader is referred to Aharonian et al. (2008), Chadwick (2021), Bose et al. (2022), and Mirzoyan (2023) for historic reviews on IACTs. The following sections describe the MAGIC telescopes, CTAO, and LSTs.

3.2.3.1 MAGIC Telescopes

The Major Atmospheric Gamma-ray Imaging Cherenkov (MAGIC) telescopes are two 17 m diameter telescopes separated by 85 m working jointly in stereoscopic mode (see Fig. 3.6). MAGIC is located at 2,200 m a.s.l. in the Roque de los Muchachos observatory in the Canary Island of La Palma, Spain.



Figure 3.6: The MAGIC telescopes. Credit: Aleksić et al. (2016a).

The MAGIC telescopes are designed to achieve a low energy threshold and fast repositioning speed to observe fast transient sources as GRBs. The close distance between both telescopes enables the approximately simultaneous detection of the Cherenkov light produced by the EAS that develops when a gamma ray interacts with the atmosphere. The first telescope, called MAGIC I (M1), started data taking in 2004 in stand-alone mode, while the second telescope, called MAGIC II (M2), joined operations in 2009 (Aliu et al. 2009; Borla Tridon et al. 2010). Since then, both telescopes operate in stereoscopic mode. Between 2011 and 2012, the systems were upgraded to improve and homogenise the performance of both telescopes (Aleksić et al. 2016a).

MAGIC operates in the energy range from about 50 GeV to several tens of TeV. In particular, its sensitivity (see Sect. 4.1.6.3) above 220 GeV for 50 h of mid-zenith angle observations is about 0.7% of the Crab Nebula flux (Aleksić et al. 2016b). This value is valid for point-like sources with a Crab-like spectrum. Despite achieving the best performance in astronomical darkness, MAGIC can operate under moonlight observing conditions with an increased energy threshold and lower sensitivity (Ahnen et al. 2017a).

3.2.3.2 Cherenkov Telescope Array Observatory

The future of the VHE astrophysics requires a facility with improved sensitivity and angular resolution. The Cherenkov Telescope Array Observatory (CTAO) is the result of a worldwide collaboration from the VHE astrophysics community after the experience gained in decades of developments and operation of IACTs (Acharya et al. 2013). Conceived to operate in the energy range between 20 GeV and 300 TeV, CTAO*** is the next-generation IACT facility. It will be located in two different sites. They are referred as CTAO-North (CTAO-N) and CTAO-South (CTAO-S) according to the hemisphere where the site is. CTAO-N is located in the Roque de los Muchachos Observatory, Spain, while CTAO-S is close to the Paranal Observatory, Chile.

The wide energy coverage of CTAO, spanning four orders of magnitude, is achieved by combining telescopes of three different sizes distributed across the CTAO-N and CTAO-S sites. The three telescope types are the Large-Sized Telescope

^{***}The official webpage of CTAO is https://www.ctao.org/.

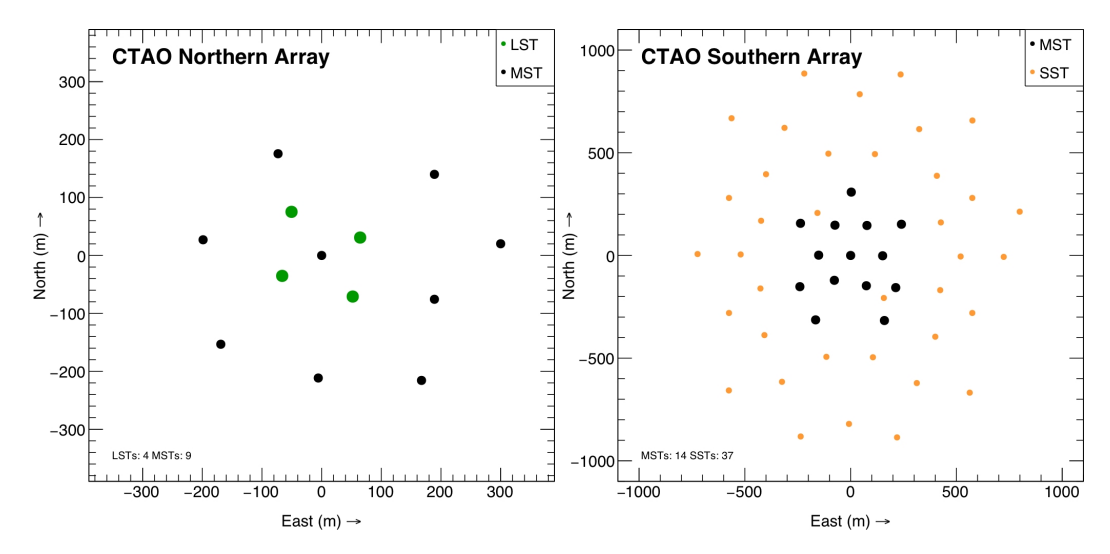


Figure 3.7: Layout of telescopes of CTAO in the Alpha configuration. Left: Array of telescopes in CTAO-N (4 LSTs and 9 MSTs). Right: Array of telescopes in CTAO-S (14 MSTs and 37 SSTs). Credit: Cherenkov Telescope Array Observatory and Cherenkov Telescope Array Consortium (2021).

(LST), Medium-Sized Telescope (MST) and Small-Sized Telescope (SST) (Acharya et al. 2013).

The layout of CTAO-N and CTAO-S is arranged according to the sources of interest visible in each site. CTAO-N focuses on low and mid energies to observe extragalactic sources such as GRBs, active galactic nuclei (AGNs), etc. In contrast, CTAO-S has an improved sensitivity in the high energy range of CTAO, as the primary goal of CTAO-S are galactic sources and sources that can emit up to PeV energies. The key science projects of CTAO are described in more detail in Cherenkov Telescope Array Consortium et al. (2019). To achieve these goals, the current official layout is called Alpha configuration and it considers 4 LSTs and 9 MSTs in the CTAO-N array, while 14 MSTs and 37 SSTs will form CTAO-S. This configuration will be the layout during the first stage of the CTAO construction. However, there are plans to increase the number of telescopes in CTAO-S with two LSTs in the centre of the array (Antonelli 2023). Figure 3.7 shows the telescope layout for CTAO-N and CTAO-S in the Alpha configuration. Note that the LSTs are placed close together to detect the faint gamma rays whose Cherenkov emission density is low and peaks towards the EAS axis. The SSTs are distributed in a wide surface area to increase the effective area and detect more photons in the high-energy range of CTAO.

Figure 3.8 shows the differential flux sensitivity for CTAO-N and CTAO-S. The sensitivity curves can be compared with the sensitivity of current and future instruments. Notably, CTAO will have an improved sensitivity at 1 TeV by an order of magnitude with respect to current facilities (see Acharyya et al. 2019; Gueta 2021, for further information), unveiling dimmer sources that cannot be detected with current instruments. CTAO will have an improved angular resolution than current IACT facilities that will play a role in improving the detection significance of point-like sources and resolving the morphology of extended sources (Hofmann 2006).

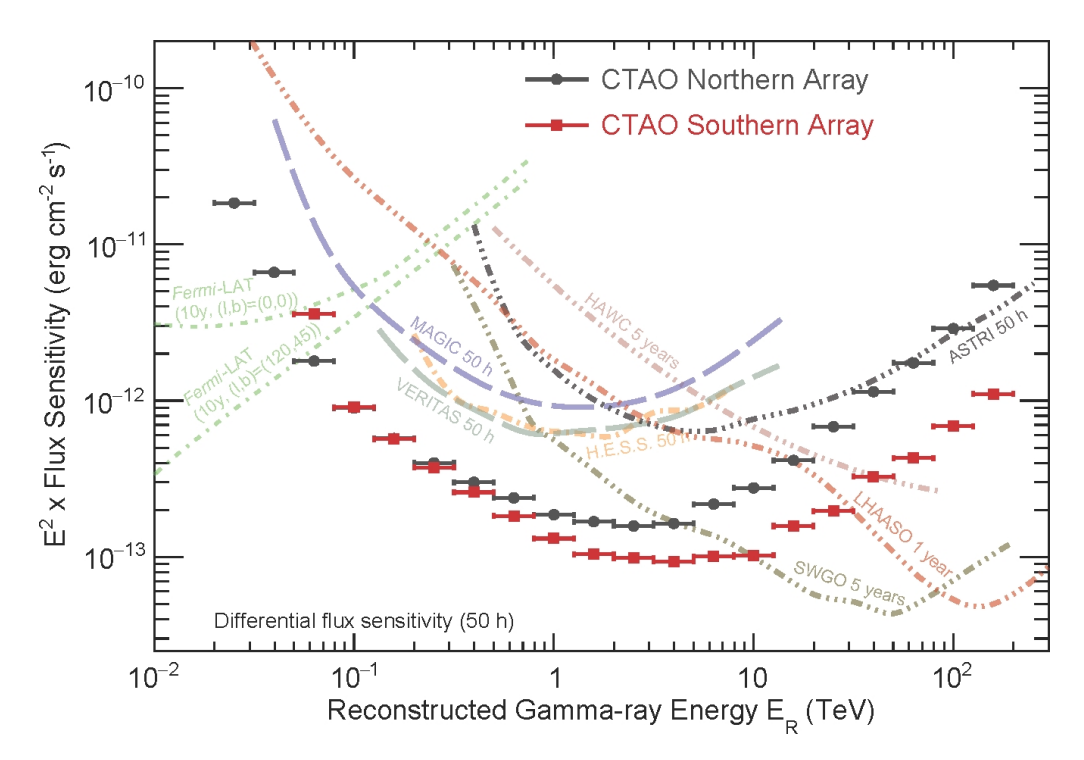


Figure 3.8: Comparison between the CTAO differential flux sensitivity for a Crab-Nebulalike spectrum in 50 h of observations with other experiments (see definition of sensitivity in Sect. 4.1.6.3). Credit: Cherenkov Telescope Array Observatory and Cherenkov Telescope Array Consortium (2021).

CTAO is sensitive to gamma rays that overlap with energies accessible with Fermi-LAT, between a few tens and hundreds of GeV. The observation of gamma-ray sources with CTAO and Fermi-LAT will provide complementary capabilities for emission studies. While Fermi-LAT has a wide FoV, CTAO is extremely sensitive to gamma-ray emission at short timescales. Figure 3.9 compares the differential sensitivity between CTAO-N and Fermi-LAT as a function of time for certain energies accessible for both instruments. The better performance of CTAO over Fermi-LAT is important not only for an improved detectability of transient sources, but also for better spectral constraints in an energy range where spectral features such as breaks and cutoffs appear. Note, however, that long exposures of transient sources with IACTs may be challenging for several reasons. The low duty cycle of IACTs, the source visibility, and the relatively small FoV makes it difficult to continuously observe the same source and achieve a total observation time of more than a few hundred hours per year at most.

3.2.3.3 Large-Sized Telescopes

The Large-Sized Telescopes (LSTs), with a 23 m diameter mirror dish (area \sim 400 m²), are the largest IACTs in CTAO. They are designed to cover the low-energy band of the CTAO energy range. LSTs collect the light using a single parabolic dish constituted by 198 segmented mirrors that focus the light in the focal plane at a distance of 28 m, where the camera is placed (focal ratio f/D=1.2; see Fig. 3.10). The camera is composed of 1,855 high quantum-efficiency (\sim 40% at 350 nm) PMTs grouped into 265 modules of 7 PMTs each. The camera FoV is about 4.5°, and each

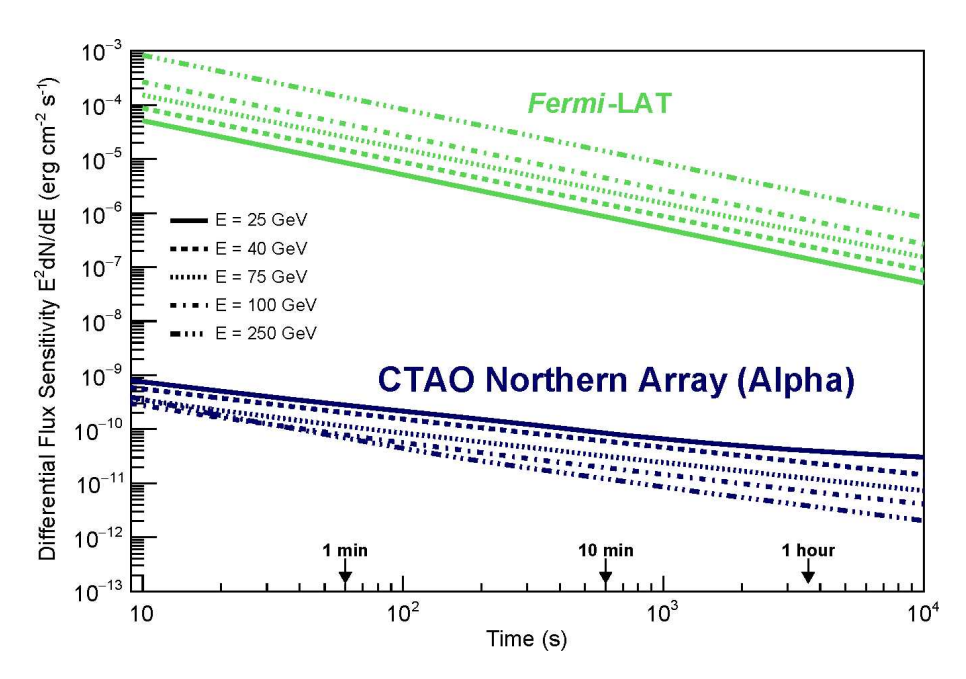


Figure 3.9: CTAO and *Fermi*-LAT differential flux sensitivity as a function of time (see definition of sensitivity in Sect. 4.1.6.3). Credit: Cherenkov Telescope Array Observatory and Cherenkov Telescope Array Consortium (2021).

pixel covers about 0.1°. More information about the camera specifications can be found in Saito et al. (2021).

Each PMT module is connected to a readout board that processes the signals from the PMTs. To increase the dynamical range from 1 to 3,000 photoelectrons (p.e.), the signal is amplified using two gain levels. The two channels are called low gain (LG) and high gain (HG). The signals in these channels are sampled at 1 GHz using Domino Ring Sampler 4 (DRS4) chips embedded in the readout board. The chips store the analogue information in a ring buffer, which is composed of 1,024 sampling cells (known as capacitors; Bitossi et al. 2016). Subsequently, the analogue signals are digitalised by an analog-to-digital converter (ADC) at 33 MHz. For further information on the readout system, the reader is referred to Nozaki et al. (2020) and Masuda et al. (2015), as well as to references therein.

The Cherenkov light is recorded if it produces a signal in the PMTs that satisfies a trigger criterion: the combination of summed-up signals from neighbour modules has to exceed a certain discriminating threshold. Moreover, a multi-telescope trigger is possible when the Cherenkov emission is detected simultaneously within a certain time window by several telescopes.

The mirrors and camera are mounted on a light alt-azimuth mount of carbon-fiber tubes. Motors in each axis move the structure of about 100 tones. The pointing accuracy requirement by design is below 14" (Cortina and Teshima 2015), which is obtained after a post-calibration of the data (Foffano et al. 2021).

LSTs are suited for the detection of gamma-ray sources at energies from tens to hundreds of GeV because of two important factors: (1) The large reflective surface of about 400 m² and (2) the trigger threshold optimised to achieve the lowest gamma-ray energy threshold of 20 GeV (Abe et al. 2023b). Additionally, LSTs are ideal for follow-up observations of transient sources (Inoue et al. 2019;



Figure 3.10: LST-1 in April 2024.

Cherenkov Telescope Array Consortium et al. 2019) thanks to the fast slewing of 180° between coordinates above the horizon in about 20 s (Cortina and Teshima 2015). Furthermore, the relatively wide 4.5° FoV camera allows for the coverage of broad sky regions, which is beneficial in the search for transient sources with a localisation uncertainty of a few degrees.

The first LST (LST-1), see Fig. 3.10, was inaugurated in October 2018 in the Roque de los Muchachos observatory in La Palma, Spain. LST-1 is the first out of four LSTs that will constitute the CTAO-N array. By the time this Thesis is written, LST-1 is in the commissioning phase and has been taking scientific data regularly since the end of 2019 (Moralejo 2021; Abe et al. 2021), which is used to assess the performance of the telescope and debug the different subsystems during regular operations. Over 2,800 h of observation time has been taken with LST-1 until April 2025. The first scientific results of these observations were already published (e.g. Abe et al. 2023). The three remaining LSTs (LST-2–4) in CTAO-N are currently under construction and expected to be integrated and commissioned by 2026–2027 (Abe et al. 2023).

3.2.4 Particle detector arrays

Particle detector arrays detect the particles that form the EAS. They sample the distribution of particles on the Earth surface. Multiple particle detectors are placed in a large area constituting an array to maximise the effective area at the highest energies. Experiments using this technique have to be placed at high altitudes to maximise particle detection and lower the energy threshold down to (sub-)TeV energies. Particle detector arrays are typically sensitive to gamma-ray energies from about TeV to several hundred of TeV, and in some facilities, they can reach PeV energies.

Depending on the technique employed to detect these particles, particle detector arrays can be classified into two main categories: measures through particle

counting or calorimetry. The former technique uses scintillators or resistive plate counters, while calorimetric measures are performed with water Cherenkov detectors (WCDs).

Scintillators or resistive plate counters track the charged particles passing through the detectors. Tibet AS γ and ARGO-YBJ are two experiments that used scintillators or resistive plate counters, respectively (Amenomori et al. 1999; Bartoli et al. 2013). Additionally, underground detectors can be used to detect penetrating muons produced in hadronic showers. This capability, for example present in Tibet AS γ , allows for background-free observations of the gamma-ray sky at energies above \sim 100 TeV, facilitating the study of astrophysical sources that can accelerate particles up to PeV energies (Amenomori et al. 2019). WCDs, on the other hand, are composed of tanks of water in which the charged particles of the EAS are absorbed, while producing Cherenkov radiation. This emission is detected with photocathodes inside the tank. WCDs are used, e.g., in the High-Altitude Water Cherenkov (HAWC) Observatory (Abeysekara et al. 2023).

The limited sampling capabilities of particle detector arrays and the fact that the number of particles detected on the ground strongly depends on the EAS development, which fluctuates from EAS to EAS (see Sect. 3.2.1), result in a degraded energy resolution, typically of \sim 50%. However, they have a large duty cycle (\lesssim 100%) and a wide FoV (\sim sr). These characteristics make particle detector arrays excellent experiments for sky surveys. Their angular resolution improves with energy, reaching the best resolution at \sim 0.1° at the highest energies. Nevertheless, IACTs outperform in angular resolution particle detector arrays at the energy range where they overlap (Sitarek 2022).

The first large-scale dense WCD dedicated to the study of VHE gamma-ray sources was the Milagro Gamma Ray Observatory (Atkins et al. 2000), whose success motivated the construction of the HAWC observatory. Other notable particle detector arrays are the Tibet AS γ experiment, which has been operating since 1990 through multiple phases, and the ARGO-YBJ detectors. The combined experience from ARGO-YBJ, HAWC, and Tibet AS γ laid the foundation for the next generation of experiments that combined multiple detector techniques, culminating in the Large High Altitude Air Shower Observatory (LHAASO), the most extensive and sensitive particle detector array nowadays. LHAASO uses WCDs, scintillators, and wide-field Cherenkov detectors (Cao et al. 2019). LHAASO is a circular detector of about 1.45 km², with its inner region formed by a packed array of WCDs called the water Cherenkov detector array (WCDA) (LHAASO collaboration 2021). WCDA is surrounded by a 1.3 km² array of scintillators and muon detectors (KM2A; Aharonian et al. 2021). Additionally, 18 wide-field Cherenkov detectors are placed next to WCDA. Furthermore, an array of IACTs is under construction (Zhang et al. 2024).

The high duty cycle and wide FoV of particle detector arrays have significantly advanced the study of extended sources and diffuse VHE gamma-ray emission, while also enabling deep surveys at multi-TeV energies of a large fraction of the sky (Bartoli et al. 2014; Abeysekara et al. 2017, 2018; Albert et al. 2020; Amenomori et al. 2021). Moreover, these instruments offer an unbiased view of variable sources and facilitate the serendipitous detection of bright transient sources (Bartoli et al. 2011; LHAASO Collaboration et al. 2023; LHAASO Collaboration 2023). Notably,

LHAASO has published a catalogue of 43 sources that emit at UHE gamma rays (Cao et al. 2021, 2024), including the Cygnus region (LHAASO Collaboration 2024) (see Fig. 1.1). Sources emitting at UHE gamma rays may be potential hadronic accelerators capable of accelerating particles up to PeV energies (see Sect. 2.2.4). These sources are referred to as hadronic PeVatrons. Identifying such astrophysical accelerators is crucial for addressing the long-lasting question of the origin of Galactic CRs observed at Earth (e.g. Blasi 2013).

4

IACT DATA CALIBRATION, PROCESSING AND HIGH-LEVEL ANALYSIS

The reduction and processing of the raw data obtained with a given IACT into a list of gamma-ray-like events is called low-level data analysis. In contrast, high-level data analysis refers to analysing the gamma-ray-like events to obtain scientific data products (spectra, light curves, sky maps, etc.). In this chapter, the low-level and high-level data analysis of the IACT technique are described, focusing on LST-1 and MAGIC+LST data analysis.

4.1 GENERAL DESCRIPTION OF THE DATA ANALYSIS FLOW

To extract the properties of gamma-ray events from raw IACT data, three key processing steps are required:

- Data calibration.
- Background subtraction.
- Reconstruction of the primary particle properties.

Due to computation limitations and the spatially localised Cherenkov signals in the recorded data, low-level IACT analysis typically relies on a limited set of parameters that describe the data rather than the full dataset to infer the properties of gamma-ray events. As a result, the data analysis includes successive steps to filter out irrelevant information for this characterisation and suppress the background noise while preserving the Cherenkov signals. Different techniques exist to reduce IACT calibrated data. Here we will focus on a multivariate-based particle-property reconstruction (known as Hillas-based method). For alternative particle-reconstruction approaches, the reader is referred to works such as Parsons and Hinton (2014), Shilon et al. (2019), and Abe et al. (2024b).

4.1.1 Calibration

The Cherenkov signal is recorded by a fast GHz readout system. The IACT raw data consists of a sequence of measurements in ADC units sampled at discrete timestamps per pixel per gain channel. These time series are referred to as "waveforms".

To ensure accuracy and the lowest possible level of noise, the waveforms must be corrected for potential systematic effects introduced by the readout system. In addition, the time and charge measures need to be calibrated to physical quantities related to the recorded light, i.e., ADC need to be transformed to p.e. counts. Finally, the camera response is homogenised across all pixels (a process known as flat fielding) to have an isochronous, uniform response in all parts of the camera under the same exposure of light. As the quantum efficiency of pixels varies, these

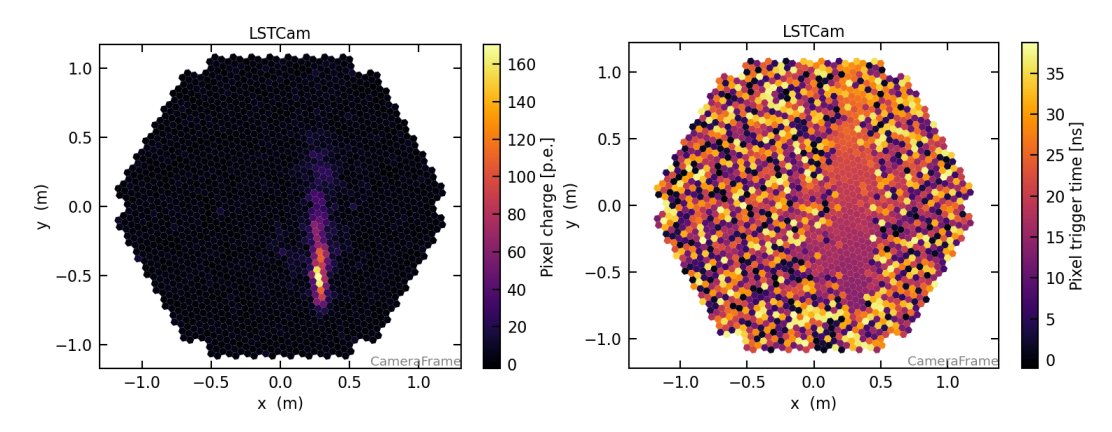


Figure 4.1: Pixel charge and trigger (arrival) time distribution in the LST camera frame for a simulated gamma ray.

processes are done on a pixel-wise basis. The specific corrections and calibration methods depend on the readout system and the camera design (e.g. Holder et al. 2006; Aleksić et al. 2012; Kobayashi et al. 2021).

4.1.2 Charge integration and image cleaning and parametrisation

After calibration, waveforms are integrated over a certain time window positioned along the waveform to extract the total signal associated with the event. This charge integration results in "camera images": a single charge and trigger (arrival) time values per pixel (see Fig. 4.1). Various methods exist for signal integration and arrival time estimation (e.g. Albert et al. 2008a).

The recorded image onto the camera plane from a gamma-ray-induced EAS is a bundled comet-like shape that points its head towards the source direction. Its major axis is related to the projection of the longitudinal development of the EAS, while the transversal axis is connected to the lateral development. As the perpendicular distance between the pointing direction of the telescope and the EAS axis increases (called the *impact parameter*), the image appears more elongated, and its centroid is more displaced from its origin due to parallax (Lessard et al. 2001; Aharonian et al. 2008).

The total charge of the image increases with the primary particle energy. EASs at larger zenith angle (ZA) directions will produce relatively dimmer images because the photons in the light pool are distributed on a larger surface. As a result, the energy threshold will be increased despite the increase in effective area (see definition in Sect. 4.1.5). The opposite occurs as the ZA decreases because the distance between the telescope and the position where the EAS reaches the maximum number of secondary particles is reduced.

The Cherenkov signal in the images presents a time gradient of a few ns (see right panel of Fig. 4.1), which is a critical piece of information for analysing the signal of CR-induced EASs (see Sects. 3.2.1 and 3.2.2). Furthermore, time information breaks the degeneracy between dim close and bright far EASs in single telescope mode (Aliu et al. 2009; de Naurois and Mazin 2015).

The images of CR-induced EASs projected onto the camera plane are more irregular and with wider transversal development than gamma rays (see comparison

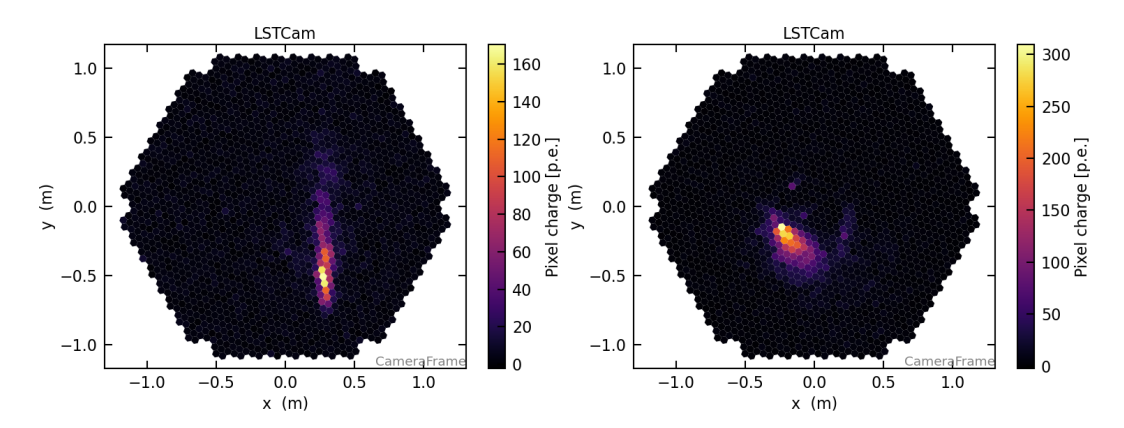


Figure 4.2: Pixel charge distribution in the LST camera frame of a bright simulated gamma ray (left) and proton (right).

in Fig. 4.2 and Sects. 3.2.1 and 3.2.2). Additionally, a single muon event created in a hadronic shower can produce a ring-shaped or arc-shaped image if it passes close or far to the telescope, respectively. Its characteristic shape results from their straight trajectory with a constant Cherenkov cone angle. Muon rings are used as calibrators to assess the absolute optical efficiency of the telescope (e.g. Gaug et al. 2019).

Typically, the Cherenkov signal is confined to just a few tens of pixels (see Fig. 4.2), which is a small fraction of the total number of available pixels of IACT cameras, $\mathcal{O}(1,000)$. The rest of the camera records background noise (NSB, PMT after pulses*, moonlight, electronic noise, etc.). Images are cleaned up to keep only triggers with Cherenkov images and reduce the NSB noise that strongly affects the image parametrisation (see Fig. 4.3). Various cleaning techniques exist that exploit the distinct characteristics of Cherenkov images to discriminate them from signal-less pixels.

Cleaning methods are typically based on a two-level procedure, and can account also for additional conditions, e.g., arrival time coincidence. A widely used method is the "tail-cut" cleaning method, which applies two different charge thresholds: the "picture" and "boundary" thresholds (Daum et al. 1997), the former employing a higher charge value than the latter. In the tail-cut method, a pixel passes the cleaning if either (1) its charge exceeds the picture threshold (referred as core pixel), or (2) its charge is above the boundary threshold and adjacent to a pixel exceeding the picture threshold (boundary pixel). An additional condition requires that a minimum number of core pixels are needed adjacent to the trigger pixel.

Including the temporal information in the cleaning procedure is particularly important at low energies because it provides an independent cut in addition to the one on the charge. Such an independent cut makes noise discrimination more efficient than using only charge information since background-dominated pixels do not show temporal coincidence among them. As a result, the cleaning charge thresholds can be reduced while keeping an acceptable noise level, allowing to

^{*}After pulses are spurious signals that follow genuine pulses. They are produced when an ion is accelerated back to the photocatode of the PMT (Akchurin and Kim 2007). After-pulse charge can range from 1 p.e. to several tens of p.e. and can be mistaken for true pulses.

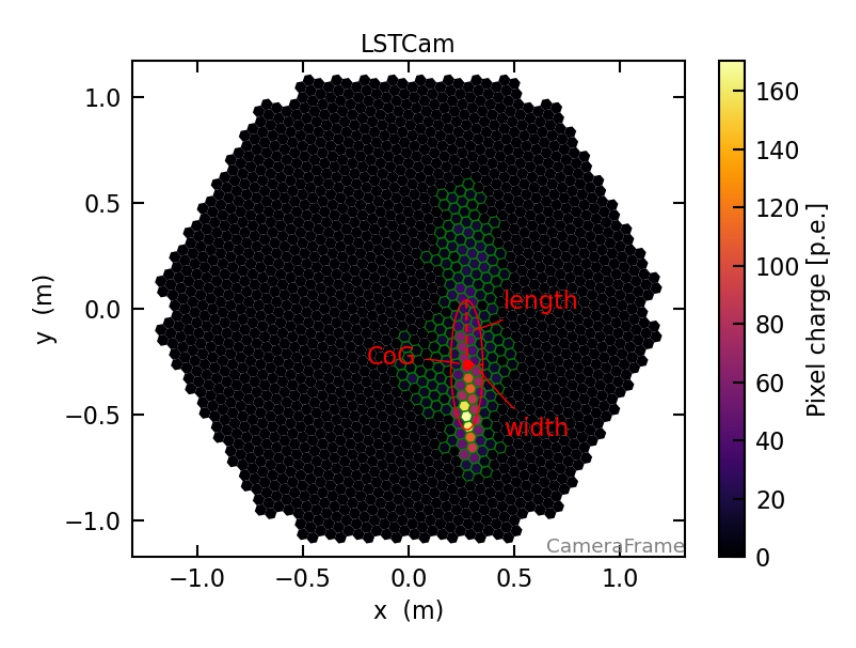


Figure 4.3: Pixel charge distribution in the LST camera frame with the first and second image moments superimposed in red. The image moments are obtained using charges from green-highlighted pixels that survive the LST image cleaning (see Sect. 4.3.3).

reduce the energy threshold. More sophisticated cleaning algorithms exist, e.g., Lessard et al. (2002) and Bond et al. (2003).

Once the images are cleaned, the surviving pixels are parametrised using the charge distribution camera image moments[†] and additional features (see Fig. 4.3; Hillas 1985; Abe et al. 2023b). The image moments include the *intensity*[‡], the centre of gravity (CoG)[§], and the *length* and *width*, which correspond to the zero, first, and second moments, respectively. *Intensity* is the total charge in the surviving pixels, the CoG is the weighted average barycenter position, and *length* and *width* are the standard deviation of the eigenvalues of the major and minor principal components of the image, respectively. The *length* parametrises the major axis of the bundled comet-like shape, while the *width* describes the EAS development along the transversal axis. The image moments can be represented as an ellipse, whose centre is the CoG and its semi-major and semi-minor axes are the *length* and *width*, respectively (see Fig. 4.3). Additional parameters such as the angle between the major principal component and the camera x-axis (ψ), the *skewness*, *kurtosis*, and *time gradient*, among others, can also be used to further parametrise the images.

In single-telescope observations, EAS reconstruction suffers from geometric degeneracy (Akerlof et al. 1991). Instead, stereoscopic observation of the same event can reconstruct the EAS development in three dimensions. A geometric reconstruction provides an initial estimation of the shower direction (viz. primary particle direction), the *impact parameter*, and the maximum EAS height (H_{max} , see Sect. 3.2.1).

[†]The parameters describing the moments up to second order and the orientation of the Cherenkov light image are known as Hillas parameters.

[‡]Also known as size.

[§]Also known as *centroid* or event position. Furthermore, the distance between the CoG and the centre of the camera is referred as *distance*.

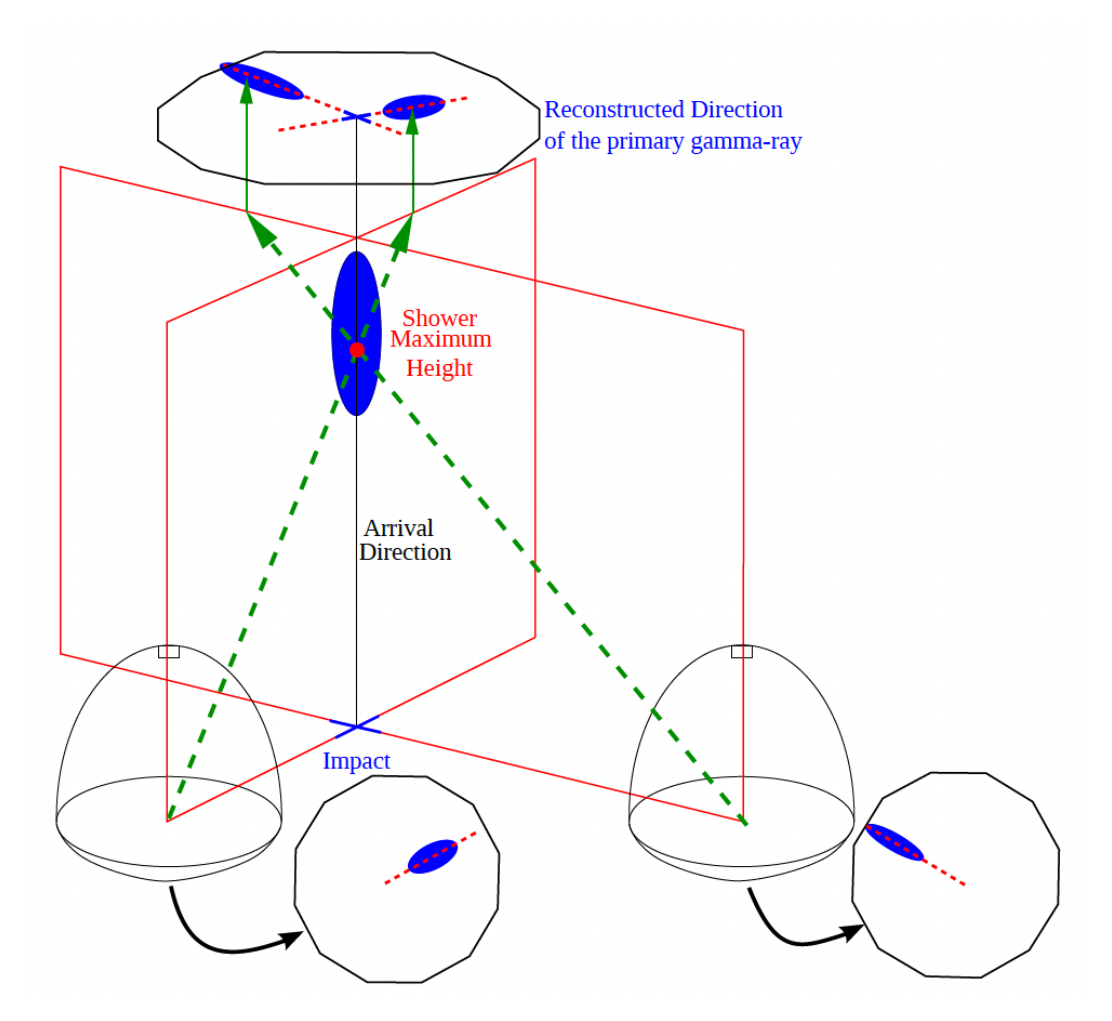


Figure 4.4: Geometric reconstruction of the EAS parameters using two telescopes. Credit: Berti (2018).

This improved parametrisation boosts both the background suppression and the accuracy of the event reconstruction (Daum et al. 1997; Maier and Knapp 2007). For example, the latter parameter is important for gamma ray/CR discrimination because (1) CRs have a larger radiation length than gamma rays and subelectromagnetic showers are produced at lower altitudes because the secondary particles have to decay, (2) muons at high impact parameters can mimic gamma rays, but the recorded light comes only from low altitudes ($H_{\rm max} \sim 2\,{\rm km}$). Figure 4.4 shows the stereoscopic reconstruction of an EAS from the Cherenkov images of two IACTs.

4.1.3 Event reconstruction

The IACT technique reconstructs the primary particle properties from the recorded images, accounting for the EAS development, the Cherenkov emission and propagation, as well as additional instrumental effects (see Sect. 3.2.3). All these effects can only be expressed analytically under simple assumptions and approximations

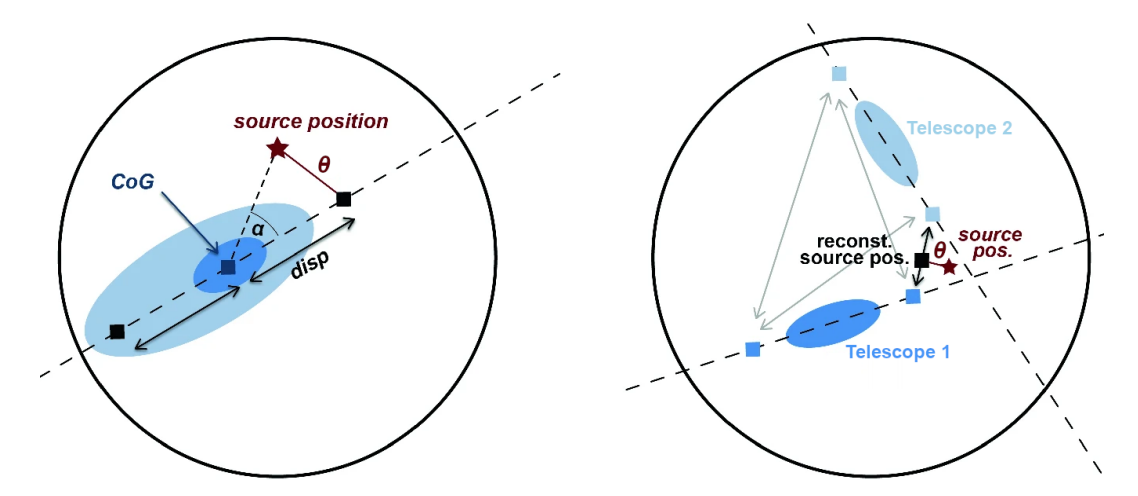


Figure 4.5: Schematic view of the *disp* method for a single telescope (left) and in a stereoscopic mode (right). The latter view describes the approach in Aleksić et al. (2016b). Image adapted from Carreto Fidalgo (2019).

(e.g. Bernlöhr et al. 2013; Aharonian et al. 2008). Consequently, Monte Carlo (MC) simulations are often employed to accurately account for them.

Machine learning techniques, trained with MC simulations, are widely used to reconstruct the properties of the primary event (reconstructed energy, direction and particle type). This reconstruction step is commonly performed using algorithms like random forest (RF) or boosted decision trees. The training datasets typically consist of MC-simulated gamma-ray and background events (typically protons), or observational background data (OFF data, e.g. Berti 2018; Abe et al. 2023b). In addition to decision tree-based methods, various other approaches can be used for parameter-based estimators including machine learning neural networks, MC-filled look-up tables, and more (Bock et al. 2004; Murach et al. 2015; D'Amico 2022).

While image parameters provide relevant information for reconstructing the primary particle properties, multiple parameters are used in parameter-based reconstruction methods, as they can contribute with complementary information. The main reconstructed particle properties include:

- Energy reconstruction. Regression algorithms or lookup tables are commonly used to estimate the reconstructed energy of the primary particle (e.g. Aleksić et al. 2012; Krawczynski et al. 2006). Both the *impact parameter* and *intensity* are relevant features for this task. Due to the wide range of energies involved, the logarithm of the *intensity* is considered. The reconstructed energy can also serve as an input parameter for reconstructing other properties (Abe et al. 2023b).
- **Direction reconstruction**. The *disp* method is widely employed to estimate the arrival direction of the primary particle. The *disp* parameter is defined as the angular separation between the CoG and the reconstructed direction (see left panel of Fig. 4.5). The *length/width* is a relevant parameter for this task, as *disp* is proportional to the ellipticity of the image (see Sect. 4.1.2; Lessard et al. 2001). In single telescope observations, the reconstructed arrival direction is assumed to lie along the semi-major axis of the image ellipse (Lessard et al. 2001), while in stereoscopic observations, the direction is reconstructed by combining the

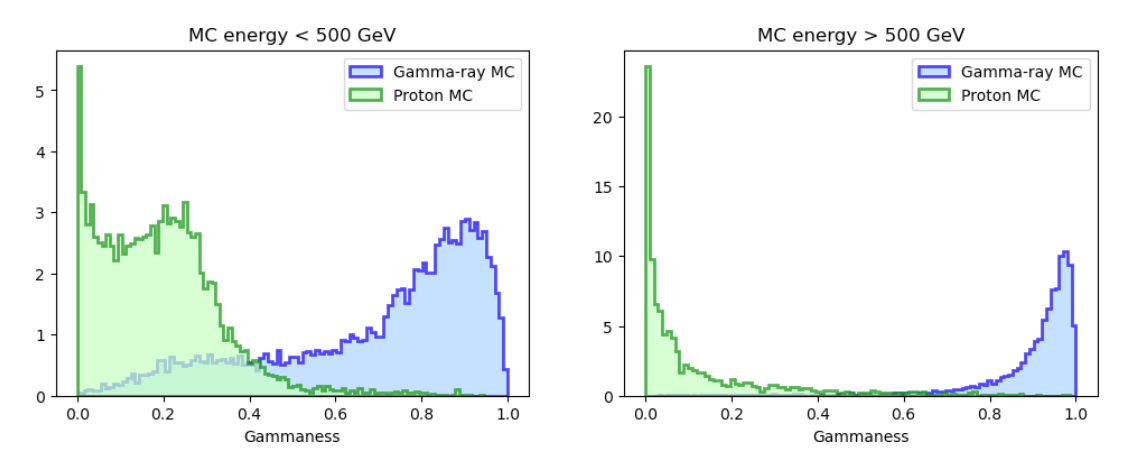


Figure 4.6: Gammaness distribution from MC gamma rays and protons. Left and right plots show the distributions for events with energies below and above 500 GeV. Credit: Mas-Aguilar (2025).

disp estimates from the multiple images, which are obtained either using machine learning or geometric methods (see right panel of Fig. 4.5; Aleksić et al. 2016b; Maier and Holder 2017; Hofmann et al. 1999). The parameter θ is used to describe the angular separation between the source position and the reconstructed position of the event (see Fig. 4.5).

• Particle classification. For bright Cherenkov images, simple cuts on image parameters can effectively distinguish gamma-ray events from the background (box cut; e.g. Lessard et al. 2001). However, for low-energy events with small, dim images, classification becomes more complicated. In such cases, classification algorithms are required (Aleksić et al. 2016b; Krause et al. 2017; Abe et al. 2023b; Ohm et al. 2009). A common discriminating variable is the gammaness (or its complement, hadroness), which indicates how likely an event is to be a gamma ray (or a hadron), with values ranging from 0 (unlikely) to 1 (highly likely). At high energies, gamma rays and CRs can be easily separated, with their gammaness distributions peaking at opposite sides of the gammaness parameter space. At low energies, however, the distributions overlap, making discrimination more difficult (see Fig. 4.6). Parameters such as the width and H_{max} provide relevant information for gamma-ray/hadron separation.

4.1.4 Event selection

A subset of surviving events is selected through event selection cuts to select gamma-ray candidates. The most important selection criteria involve the *gammaness* score, as well as the angular separation for a point-like analysis. However, additional parameter cuts can be applied to exclude poorly reconstructed events or events close to the telescope energy threshold. For instance, events near the energy threshold are contaminated by CRs and muons, whose images are too small to be accurately parametrised, leading to a large background (see Sect. 3.2.1).

The *gammaness* and angular separation cuts can be applied as a single threshold value across the entire energy range (hereafter *global cuts*), or as energy-dependent cuts. The latter are derived using an MC test sample. The method aims to retain a

fixed faction of gamma-ray events in each energy bin. For each bin, the parameter value (*gammaness* cut or angular separation cut) that satisfies this condition is considered. As a result, these cuts maintain a certain percentage of simulated gamma rays across the energy range. The cuts with this technique are known as energy-dependent *efficiency cuts*.

The specific values for the *gammaness* and angular separation cuts depend on the purpose of the analysis. For datasets with low event counts (such as high energies or short timescales), loose cuts [¶] are typically preferred to increase statistics. Conversely, at low energies or in the analysis of extended sources, tight cuts ^{||} may work better, as they provide an improved signal-to-background ratio (S/B) and reduce the systematic uncertainties in the background. However, loose cuts usually are less prone to systematics that arise from differences between MC and observational data, making them preferable for spectral analyses where minimising systematic biases is critical. The cut values can be optimised using both MC simulations or observational data by maximising the signal detection (see Sect. 4.1.6.1) or the sensitivity (see Sect. 4.1.6.3). Nevertheless, careful treatment is essential because the results are sensitive to the energy range, energy binning and spectrum.

4.1.5 Instrument response functions

The measured quantities of the recorded event must be related to the physical quantities of the incident photon to derive absolute energies and fluxes. Therefore, a parametrisation of the telescope response is required. The mathematical description that connects the reconstructed and absolute quantities is known as the instrument response functions (IRFs). The IRFs are derived from MC simulations designed to reproduce the observing conditions. These simulations undergo the same analysis steps and selection cuts as the observational data to ensure consistency. IACT IRFs are factorised into three main factors**: the effective (collection) area, the energy dispersion, and the point spread function.

• Effective area (Aeff) measures how effective the collection area of the detector is for a given absolute photon energy (true energy; E_{true}) and offset angle. It is defined as

$$A_{\rm eff} = A_{\rm sim} \frac{N_{\rm after\,cuts}}{N_{\rm total}},\tag{4.1}$$

where N_{total} and $N_{\text{after cuts}}$ are the total number of simulated events before and after applying the event selection cuts, respectively (see Sect. 4.1.4). The factor A_{sim} is the simulated area, which takes the form $A_{\text{sim}} = \pi I_{\text{max}}^2$, where I_{max} is the maximum *impact parameter* of the simulated gamma rays. Left panel of Fig. 4.7 shows Aeff at a fixed offset angle of 0.4°.

[¶]Loose cuts refer to event selection cuts that tend to prioritise completeness over purity of candidate gamma-ray events.

II In contrast to the loose cuts, the tight cuts tend to prioritise the purity over completeness of candidate gamma-ray events.

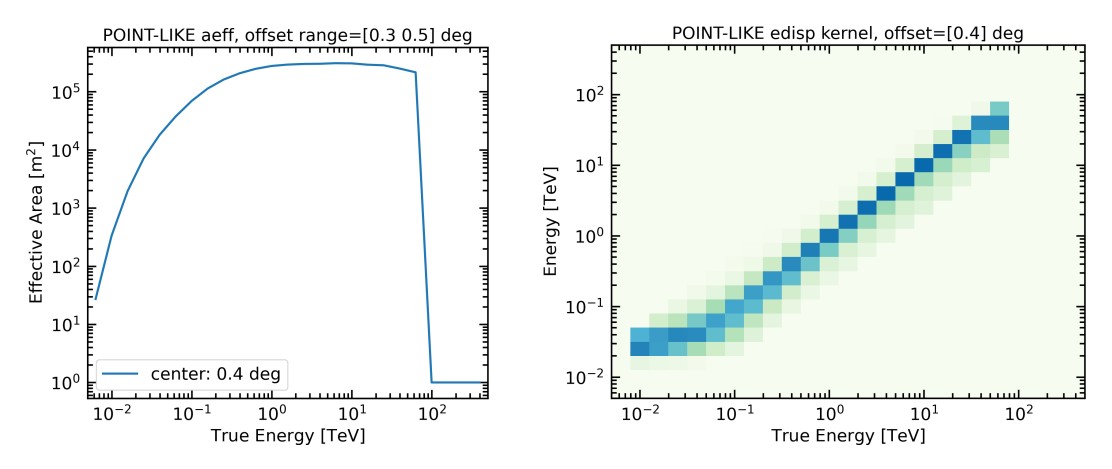


Figure 4.7: Aeff (left) and edisp matrix (right) at an offset angle of 0.4° . The IRFs correspond to MC simulation at ZA = 25° after applying energy-dependent cuts in *gammaness* and θ of 90% and 70%, respectively (Abe et al. 2024c).

- Energy dispersion (edisp) measures the energy resolution and bias. It gives the probability to reconstruct a photon with energy *E* when its true energy is *E*_{true} for a given offset angle. Due to the typical 15% energy resolution of IACTs (see Sect. 3.2.3), the reconstructed energy of gamma rays is spread across their absolute energy and worsens at the lowest energies. Right panel of Fig. 4.7 shows the edisp matrix at a fixed offset angle of 0.4°.
- **Point spread function (PSF)** quantifies the deviation of reconstructed arrival directions from a point-like source when the absolute energy of the photon is E_{true} . Typical values are in the range of 0.01° – 0.1° .

For tailored MC simulations, the exact values of the IRFs will depend on multiple circumstances such as the observing conditions (telescope pointing, NSB, ...), or the telescope performance (mirror reflectivity, PMT, ...), among others. Additionally, their values will depend on the cut in the event selection step. For example, as the ZA of the telescope increases, the effective area at low energies will reduce, whereas it will increase at high energies (see Sect. 4.1.2; Abe et al. 2023b).

In the framework of CTAO, the IRFs are computed with the python software package pyirf^{††} (Dominik et al. 2023).

4.1.6 High-level analysis

Gamma-ray-candidate events and the IRFs are used to obtain the scientific products. Depending on the purpose of the study and the characteristics of the region that is being observed, different types of analyses can be performed, e.g. the study of the spectral distribution of the gamma-ray signal, the source morphology, and the temporal variations in the recorded data. This section focuses on the analysis of point-like sources using aperture photometry. This type of analysis is also called 1-D analysis since this approach only considers the energy dimension. In contrast, analyses that use spatial information are called 3-D analyses, as they consider energy and spatial coordinates.

tthtps://github.com/cta-observatory/pyirf

VHE data analysis requires careful statistical treatment because of the inference analysis needed to derive the properties of the gamma-ray source and the large background that affects the data. Poisson statistics are typically used in IACT data. Likelihood-ratio tests are commonly used to test the null hypothesis to draw inferences from the experiment, i.e., the observation. Similarly, the normalised likelihood function is maximised for parameter estimation and model fitting. The reader is referred to Cowan (1998), Sprott (2000), Burnham and Anderson (2002), and Kenett et al. (2022) for detailed reviews of statistical inference and data analysis.

When multiple observations are considered, two type of fitting methods can be used in binned data. The stacked and joint fitting. The former gathers all the binned events into a single cube and a single log-likelihood function is used in the maximum likelihood estimation. We refer to "cube" as the resulting entity that contains data binned into bins or boundaries in a n-dimensional data cube. For example, an energy-only analysis is formed by a 1-D energy cube, a time-only analysis contains a 1D time cube, or a morphology-only study uses a 2-D cube. Combination of them can form higher-dimensional cubes such as an image-energy-time cube of four dimensions. In contrast, the joint fitting samples the different observations into different cubes, each contributing with a term in the log-likelihood function. The total log-likelihood function is obtained through the product of each observation likelihood function. Similarly, a joint fitting is considered when the data from multiple instruments are fitted simultaneously (e.g. Nigro et al. 2019).

The open-source software package Gammapy has been developed for high-level gamma-ray data analysis. Gammapy is the official software for the analysis of CTAO data and contains the scientific tools for IACT data analysis (Donath et al. 2023). This section describes typical scientific products in IACT analysis in the framework of Gammapy.

4.1.6.1 Signal detection

For a point-like source, the angular distribution of the θ parameter peaks towards the source position (see Fig. 4.5), while the background contribution from hadrons remains constant. To search for a signal, it is common to display the θ^2 distribution centred on the source position and compare it with the θ^2 distribution of a region empty of gamma-ray sources with a similar telescope acceptance.

Usually, IACTs operate in *wobble* mode: the telescope is pointed at a given offset from the source and observations are performed around the offset ring centred on the source (see Fig. 4.8; Fomin et al. 1994). The offset between the telescope pointing and the source allows to estimate the background using the opposite region in the camera. The reflected region at 180° from the telescope pointing to the source axis is used since the acceptance of the telescope should remain almost identical (Berge et al. 2007). Additionally, more regions can be used for background estimation in the offset ring, e.g., utilising symmetric regions at rotation angles $\pm 90^{\circ}$ with respect to the source. Alternatively, other pointing strategies exist such as ON/OFF or drift scan^{‡‡} observations (Weekes 1973; Weekes et al. 1989).

In the aperture photometry approach, the region where the signal is estimated is called the signal (ON) region, while regions for background estimation are

[#]The telescope is not pointing at a fixed RA/DEC position.

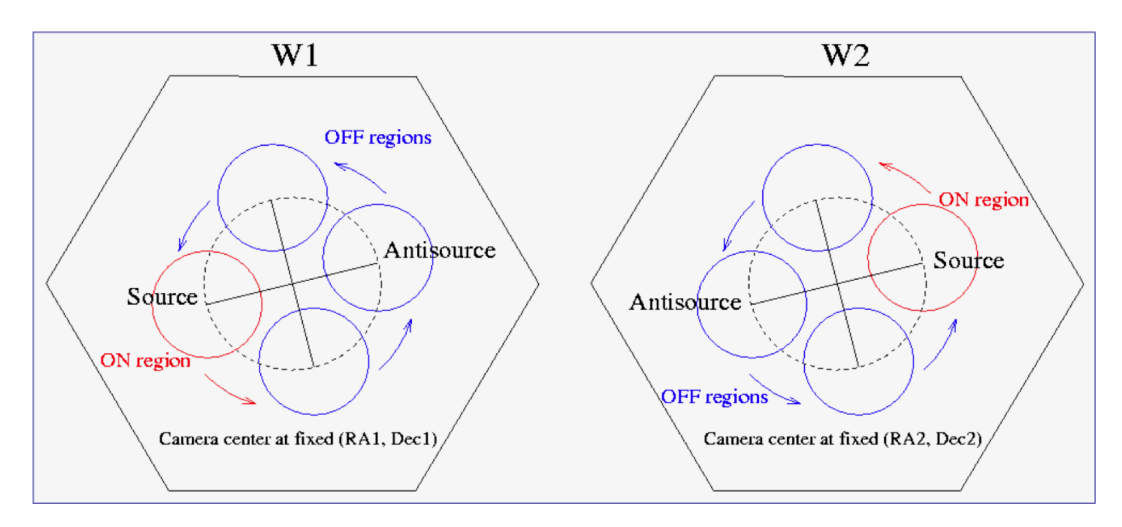


Figure 4.8: Schematic view of the wobble mode with the ON and OFF regions highlighted in red and blue, respectively. Credit: Moralejo Olaizola (2000).

called OFF regions. Their size is optimised based on the source and telescope performance. Inside these regions, the number of counts is summed up to compute the significance of detection using equation 17 of Li and Ma (1983).

4.1.6.2 Spectral energy distribution and light curve

The event list with reconstructed energy has to be unfolded from the telescope distortion to obtain absolute quantities. Two methods are typically employed: unfolding and forward folding. In this Thesis, the forward folding is the only method used. It assumes a prior spectral model to convolve with the IRFs and obtain the predicted counts for that model. Then, the observed and predicted counts are fitted (Piron et al. 2001). The reader is referred, e.g., to Anykeyev et al. (1991) and Albert et al. (2007) for further information about the unfolding approach.

The spectral energy distribution (SED) is obtained by multiplying the differential energy spectrum by E^2 . In a 1-D binned analysis, the events are binned into multiple energy bins to fit the model. The best-fit model is obtained through the Poisson maximum likelihood fitting of the data range. The SED points are computed by refitting the global best-fit model in each energy bin with a corrective factor (Donath et al. 2023). On the other hand, the light curve is obtained by integrating the differential energy spectrum in a certain energy range in a given time window. The same procedure for the flux computation as that used in the SEDs is followed to compute the light curve.

4.1.6.3 Sensitivity

The performance of the analysis can be quantified using the term *sensitivity*, which is defined as the minimum gamma-ray flux (differential or integrated) required to detect a source at 5σ significance (equation 17 in Li and Ma 1983 is commonly used at VHE gamma rays). Usually, the differential flux sensitivity is reported to describe the spectral analysis performance. Depending on the energy range, additional restrictions can be considered, such as a minimum of 10 gamma rays per energy bin or a S/B of at least 1/20 (e.g. Aleksić et al. 2016b). This definition only

applies to point-like sources and it is commonly calculated in a five-bins per decade logarithmic energy binning. In IACT data, the sensitivity is usually computed for 50 h of observation. Figure 3.8 shows the differential sensitivity for different VHE experiments. For short timescale emission studies, however, the sensitivity can be computed for observation times shorter than 50 h, or it can be expressed as a function of the observation time (see, e.g. Figs. 3.9 and 5.9).

4.2 DATA LEVELS IN CTAO

A hierarchy of data levels is established in the framework of CTAO to standardise the data products in each step of the analysis chain explained in Sect. 4.1. These levels range from the raw data to the scientific data products. They are ordered as follows (Contreras et al. 2015):

- Raw level 0 (R0). Data consisting of uncalibrated waveforms produced by the readout boards. This level is not saved to disc but automatically sent for processing.
- Raw level 1 (R1). Waveform data pre-calibrated by the data acquisition system and transformed into a common format. This level will not be recorded to disc.
- Data Level 0 (DL0). This is the first data preserved for long-term storage. It contains the R1 files reduced and divided into different data streams.
- Data Level 1 (DL1): This data level is divided into two sublevels.
 - First Data level 1 (DL1a): Single charge and timestamp (signal arrival time) per pixel. These data are the camera images.
 - Second Data level 1 (DL1b): Geometrical parametrisation of the camera images.
- Data level 2 (DL2): Parametrisation of the shower with particle type classification and estimation of its energy and direction.
- Data level 3 (DL3): Event list of selected events and IRFs. CTAO will deliver these data to the community.
- Data level 4 (DL4) and Data level 5 (DL5): Multidimensional binning of the event list and scientific data products, respectively.

4.3 LST-1 DATA ANALYSIS

This Thesis mainly uses LST-1 data. Cta-lstchain^{§§} (López-Coto et al. 2022) is the dedicated software analysis pipeline for the low-level analysis of LST-1 data. Cta-lstchain is based on ctapipe, the low-level processing pipeline software of CTAO (Linhoff et al. 2023). To make the LST-1 raw data compatible with ctapipe,

^{\$\$}https://github.com/cta-observatory/cta-lstchain

the package ctapipe_io_lst ¶¶ is currently used. The analysis of LST-1 data is detailed in this section, following the workflow outlined for analysing IACT data (see Sect. 4.1).

4.3.1 Calibration

In response to an event trigger, the readout system of LST, based on DRS4 (see Sect. 3.2.3.3), reads out a window of 40 measures sampled at a rate of about 1 GHz*** with a resolution of 12 bits per sample. A waveform for the HG and LG channels is recorded (see Sect. 3.2.3.3). These waveforms require a series of software corrections to suppress electric noise induced by the readout of DRS4, calibrations to express the signal in physical units (absolute calibration), i.e., p.e. and absolute time, and equalise the pixel response to the median camera response (relative calibration). Details on the LST calibration can be found in Cassol et al. (2025).

4.3.1.1 DRS4 calibration

The DRS4 chip produces an electric noise that affects the baseline of the signal readout and its sampling time.

Waveform corrections^{†††}. Three different software corrections are applied to obtain a uniform waveform baseline between all capacitors of the DRS4:

- Baseline correction. The baseline of each capacitor in each channel of the DRS4 is different due to small physical differences. As a result, the standard deviation of the mean baseline between capacitors is much larger than the baseline standard deviation of individual capacitors. This effect is corrected using a dedicated pedestal run in which the average baseline per capacitor is computed. Then, the signal amplitude in each capacitor is corrected using the corresponding offset (Sitarek et al. 2013).
- **DeltaT correction**. Following the individual baseline correction, a second baseline calibration is necessary since the baseline value is also affected by the last time the capacitors were read. In particular, the baseline value increases if the same capacitor is used in short successions (Nozaki et al. 2020). This extra noise is subtracted by considering the time interval between the last readout and the current time.
- **Spike subtraction**. Finally, due to the DRS4 chip design, predictable spikes appear for specific capacitors that need to be identified and subtracted (see bottom right panel of Fig. 4.9; Kobayashi et al. 2021).

The final baseline noise level is a few ADC counts (Kobayashi et al. 2021). Then, the individual capacitor baselines are aligned to 400 ADC counts to subtract it in posterior calibrations. The left panel of Fig. 4.9 shows the dispersion of the baselines before and after applying the successive waveform corrections.

 $[\]P\P$ https://github.com/cta-observatory/ctapipe_io_lst

^{***}Therefore, one waveform sample is \simeq 1 ns. The total window is about 40 ns.

^{****}Known as DRS4 waveform corrections.

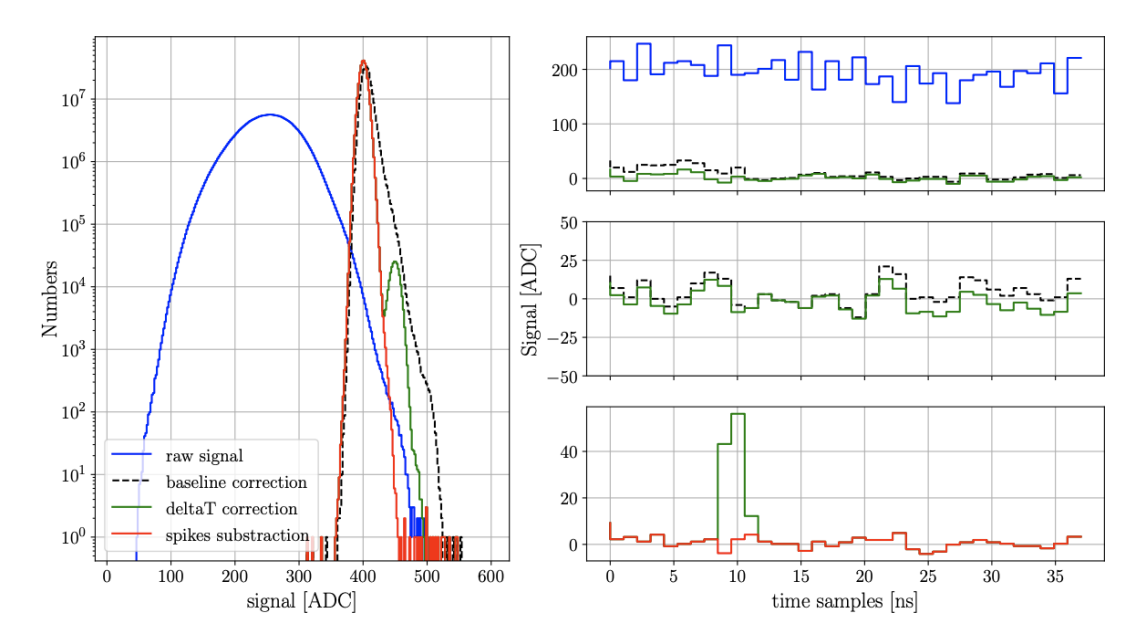


Figure 4.9: Left: Electronic noise level before and after each step of the baseline corrections. Left: Corrections applied on a waveform. Top and middle panels show the correction to the time dependence noise, while the bottom panel shows the correction to spikes. Credit: Gliwny (2024).

DRS4 pulse time correction^{‡‡‡}. The DRS4 chip has slightly uneven sampling. The sample position in the waveform at which a short-lived pulse of light is recorded can change by 1 ns up to 4 ns depending on the position of the read-out window in the DRS4 capacitor ring (Sitarek et al. 2013). The arrival time for each capacitor is calibrated using laser-calibration events (see Sect. 4.3.1.2) following the method described in Sitarek et al. (2013) through a Fourier series fitting to correct the arrival time. For pulses of 5 p.e., the typical resolution is 0.95 ns (Kobayashi et al. 2021).

4.3.1.2 *Pixel calibration (absolute and relative calibration)*

The absolute and relative calibrations are obtained per pixel per channel and estimated using multiple dedicated calibration events, which consist of so-called pedestal and flat-field (FF) events. The former are events triggered without signals, while FF events are time-coincident pulses across the camera of diffuse light from a laser ($\lambda = 355$ nm; Palatiello et al. 2019; Kobayashi et al. 2021), whose intensity can be adjusted to uniformly illuminate the camera up to 10^4 p.e. per pixel to scan the whole dynamic range. In standard conditions, the signal of an FF event corresponds to 80 p.e. per pixel.

• Absolute charge calibration. The conversion of a pulse from ADC units to its equivalent in p.e. units is addressed through the excess noise factor (F-Factor; e.g. Mirzoyan 1997). In particular, LST-1 includes a quadratic noise term to account for the non-uniform DRS4 sampling and laser fluctuations (Kobayashi et al. 2021). The obtained conversion factor (the reciprocal of the gain) is scaled

^{‡‡‡}Known as DRS4 timing or sampling (Fourier) correction. This correction is performed per event and per pixel.

by a global scaling factor to account for the different integration windows used for FF and cosmic^{§§§} events (see Sect. 4.3.2).

• Relative charge and time calibration. A homogeneous and constant flatfield response all over the camera is highly desired. However, the PMTs in the camera slightly differ among them. On the one hand, the PMTs may have different quantum efficiency curves, e.g., due to ageing or by design, responding differently to a uniform light. The charge response is homogenised through high voltage (HV) flat-fielding, i.e., the pixel HVs are adjusted based on the relative gain between the camera mean gain and individual pixel gain using the PMT gain dependency with HV. On the other hand, slight variations in the arrival time of a pulse can occur due to several factors. In addition to the uneven time sampling of DRS4 (see Sect. 4.3.1.1), these variations can be caused by small differences in the electronic paths, the lengths of the optical fibres, and different HV settings (Sitarek et al. 2013). Time equalisation is achieved through programmable delays (Saito et al. 2021). Subsequently, calibration coefficients are estimated to quantify how much the response of each pixel deviates from the average and apply these corrective coefficients to achieve the desired inter-pixel charge calibration and inter-pixel time flat-fielding.

4.3.1.3 *Cat A and Cat B calibrations*

Two different calibration protocols have been developed so far in LST-1: the real-time and offline calibrations, Category (Cat) A and B, respectively.

- Cat A calibrations are estimated using calibration events taken in dedicated observations. The calibration coefficients obtained in these observations represent the baseline calibration values.
- Cat B calibrations are estimated using calibration events taken during the data taking (interleaved events). They are used to correct the Cat A calibration coefficients during the data taking due to changes in the camera response with time. In particular, the gain and time correction are adjusted in each pixel using thousands of interleaved events. For example, changes in the camera response can arise from HV variations by stars and periods with many unusable pixels due to sudden changes in the camera illumination, among other factors.

These calibration categories align with the data products defined within CTAO, which comprises three different data products, from data produced with less precision and higher systematic for fast alert communication to the highest-quality data based on refined calibrations and more elaborated analysis techniques.

4.3.2 *Charge integration*

Different algorithms can be used to integrate the waveforms. LST-1 uses the LocalPeakWindowSum, FixedWindowSum, and GlobalPeakWindowSum algorithms of

^{§§§}The term "cosmic events" is used hereafter to refer to gamma rays and CRs that produce EASs whose Cherenkov emissions are recorded as Cherenkov images.

Algorithm name	Window width	Window shift	Peak index
${\sf LocalPeakWindowSum}\ ({\sf cosmic\ events})^{(a)}$	8	4	-
LocalPeakWindowSum (FF events)	12	5	-
FixedWindowSum (pedestal events)	12	6	18
GlobalPeakWindowSum (muon events)	8	4	-

Table 4.1: Charge integration settings used in LST-1 for each event type.

Notes. For each algorithm and event type, the window width and window shift are provided. The peak index is specified if manually set. $^{(a)}$ Note that the window range with respect to the maximum of the waveform (s_{max}) takes the form $[s_{\text{max}} - 4, s_{\text{max}} + 3]$, instead of the range stated in Abe et al. (2023b) of $[s_{\text{max}} - 3, s_{\text{max}} + 4]$.

ctapipe. All these algorithms sum up the signal in a given window of the waveform. This window is defined from a reference position in the waveform, the peak index. Then, the window is parametrised using the start position of the window with respect to peak index (window shift) and its size (window width). As waveforms are a discrete array of values (samples), the values of window shift and window width are integers associated to the number of waveform samples considered (see Table 4.1).

The waveforms of cosmic events are integrated using the LocalPeakWindowSum, which sums the signal over a window whose reference position is determined by the sample with the maximum amplitude (peak) in the waveform of the triggered pixel. Similarly, the same algorithm is considered for FF events, but with different window settings. In contrast, the charge of pedestal events are integrated with FixedWindowSum. This algorithm integrates the signal in a fixed window. In this case, the reference position is specified by the user manually using the peak index parameter. Finally, muon events use the GlobalPeakWindowSum algorithm, which sums the signal over a window with respect to the peak position from the average waveform of all pixels in the camera.

The parameter values of the charge integration algorithms for a standard analysis of LST-1 data are summarised in Table 4.1. The application of the algorithms for a cosmic, FF, and pedestal event is demonstrated in Fig. 4.10.

4.3.3 *Image cleaning*

The standard image cleaning in LST-1 considers the tail-cut method, utilising an increased picture threshold condition based on the pixel noise level through the "pedestal cleaning". Additionally, a time-coincident condition and dynamic cleaning are used:

• Tail-cut method with pedestal cleaning. The noise of a pixel is quantified using its pedestal charge bias $\langle Q_{\rm ped} \rangle$ and charge standard deviation $\sigma_{\rm Qped}$. High NSB conditions will induce large $\sigma_{\rm Qped}$ (and $\langle Q_{\rm ped} \rangle$ for some charge integration algorithms). The pedestal cleaning accounts for the pedestal noise

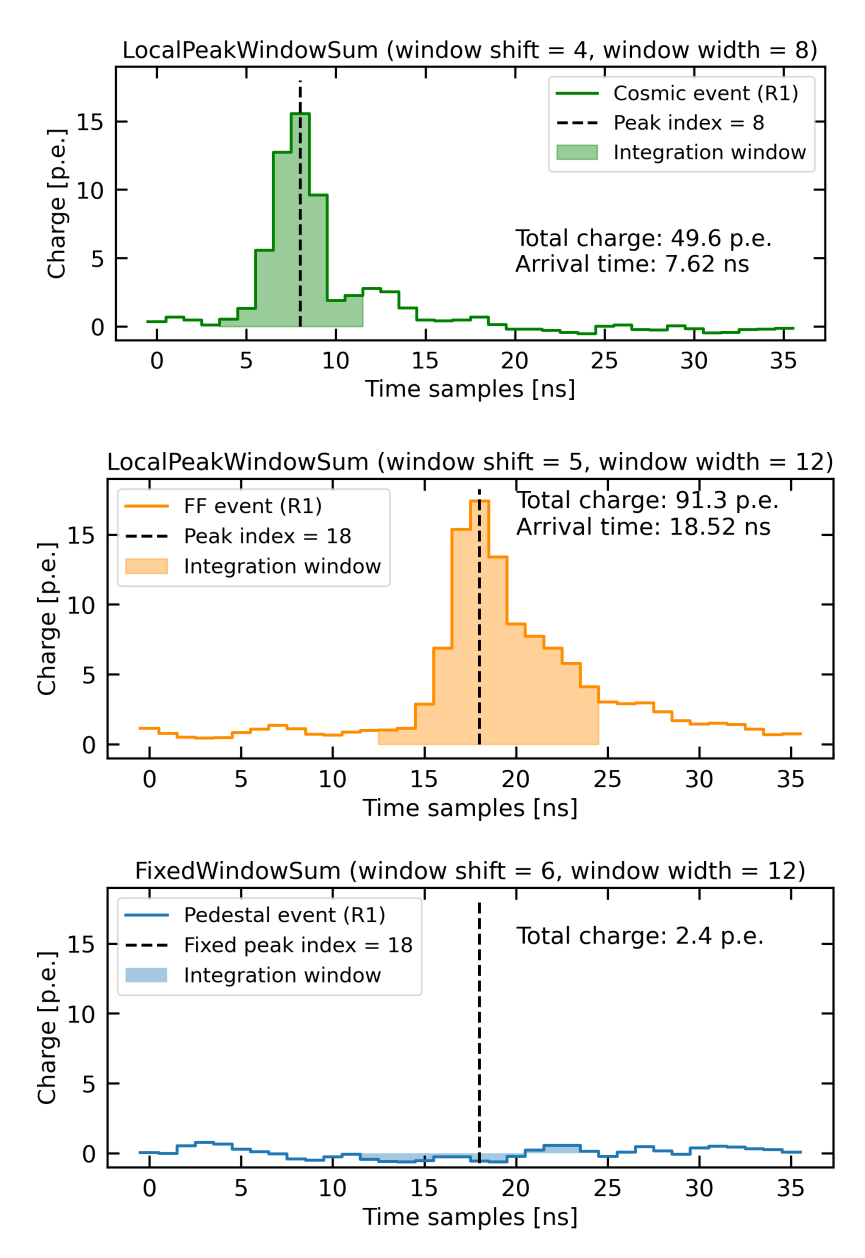


Figure 4.10: Charge as a function of the waveform (time) sample for a cosmic (top), FF (middle), and pedestal (bottom) event. The integration window and the reference peak of the charge integration algorithm employed for each event are shown. Additionally, the total charge and estimated arrival time are computed without considering the pixel-wise, event-wise time shift nor the global scaling factor applied in the F-factor method (see Sect. 4.3.1).

in the pixels by dynamically adjusting the picture threshold of individual pixels to a certain threshold with which the charge of most of the pedestal events in that pixel are not above the threshold. As a result, the increased picture threshold condition permits applying a higher cleaning at noisy pixels (e.g. around stars). In standard conditions, the tail-cut cleaning uses default picture and boundary charge threshold values of 8 p.e. and 4 p.e., respectively, and a minimum of two neighbour picture pixels (see method description in Sect. 4.1.2). The increased picture threshold condition through pedestal

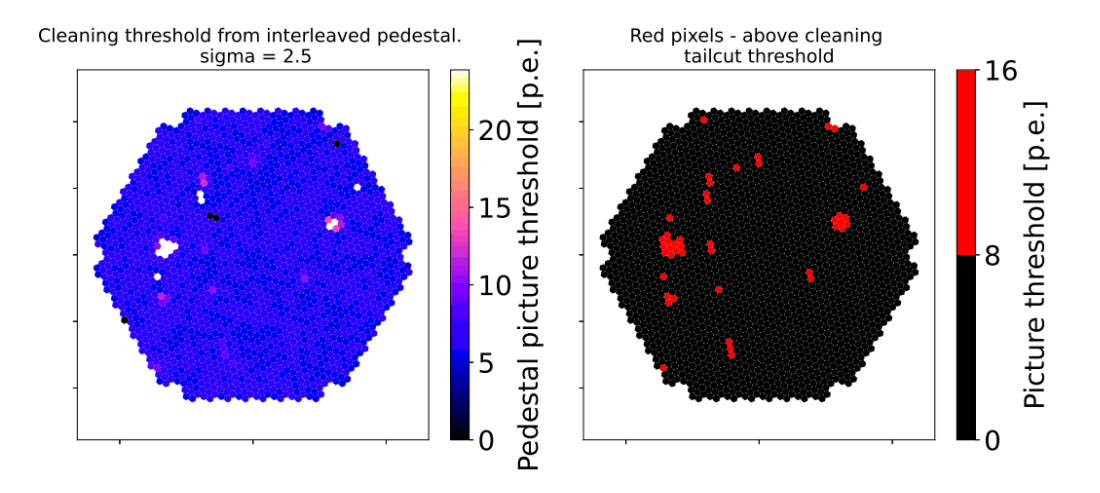


Figure 4.11: Left: Picture threshold values using the pedestal cleaning from interleaved pedestals during an observation of the Crab Nebula. Right: Pixels that fulfill the increased picture threshold condition are highlighted in red. Many pixels are highlighted because the Crab Nebula is located in a crowded region with many stars. Credit: Gliwny (2024).

cleaning is considered if a pixel satisfies $\langle Q_{\rm ped} \rangle + 2.5\sigma_{\rm Qped} > 8\,$ p.e. Then, the picture threshold is dynamically increased to $\langle Q_{\rm ped} \rangle + 2.5\sigma_{\rm Qped}$ (see Fig. 4.11). Note, however, that the baseline charge thresholds must be adjusted to avoid having a large fraction of images with increased picture threshold, as this will cause problems of response inhomogeneities in the camera and, therefore, higher discrepancy with MC simulations.

- **Time coincident**. Pixels surviving the tail-cut cleaning must have their arrival time within a 2ns window with respect to the arrival time of at least one neighbour pixel.
- **Dynamic cleaning**. Finally, pixels with charges above 3% of the average charge value from the three brightest pixels in the image are selected as signal pixels. This step allows the removal of fake image islands in bright events due to misaligned mirrors that can spoil the image parametrisation and reduce the MC-observational data agreement.

4.3.4 Event reconstruction

The properties of the primary particle are reconstructed with RFs. RFs are a collection of decision trees whose initial and node parameters for splitting are randomised with a randomised sampling procedure (Breiman 2001). The result from multiple trees is averaged for regression tasks, while the most common result is considered for classification tasks. Such a forest of decision trees helps to reduce over-fitting and averages out errors from single trees. RF algorithms have demonstrated to improve the analysis performance with respect to traditional methods such as direct selection based on the image parameters (Albert et al. 2008b).

Two independent analysis methods are available in cta-lstchain, known as source-independent and source-dependent analysis (differing in the DL1 to DL2

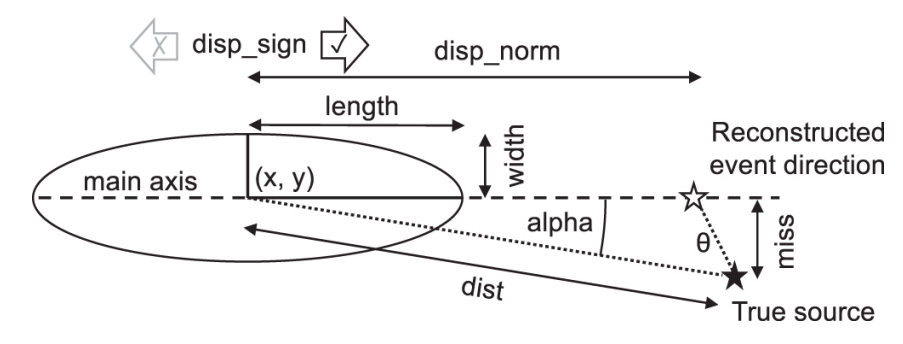


Figure 4.12: Image parameters and reconstructed parameters for the source-dependent and source-independent analyses. Credit: Abe et al. (2023b).

step). The former does not consider any prior knowledge of the gamma-ray source position and uses the *disp* method to reconstruct the direction of the primary particle. In contrast, the source-dependent analysis uses as a prior the position of a point-like source to reconstruct the events. In this analysis, the parameter known as α , the angle between the ellipse major axis and the line joining the CoG and the source position (see Fig. 4.5), is calculated and used in the event selection step and subsequently in the signal detection. Note that the properties of each event are reconstructed assuming it comes from the source position and predefined OFF positions. In contrast, θ is used in the source-independent analysis (see Sect. 4.1.3).

The reconstructed energy and particle classification are done with one RF each, whose input parameters depend on whether the source-independent or source-dependent analysis approach is used (Abe et al. 2023b). Parameters relative to the source position are used in the source-dependent analysis as features of the energy and particle classification RFs. For instance, the distance between the CoG of the image and the assumed source position (known as *dist*) and the time gradient from the source are effective parameters that correlate with the *impact parameter*. This parametrisation boosts the reconstruction of EASs for monoscopic observations at the lowest energies, where the telescope performance using the *disp* method degrades due to the small number of triggered pixels (Aliu et al. 2009).

The incident direction estimation in the source-independent analysis requires two RFs because the reconstruction of the shower direction retains some degeneracy in the *disp* method, as only one image of the shower is reconstructed given that LST-1 operates in stand-alone mode. Therefore, two possible solutions arise at equidistant distances from the image CoG on each side of the major axis of the ellipse. One RF estimates the module of the *disp* parameter, while another RF classifies the sign (see Fig. 4.12).

4.3.5 MC simulations

MC gamma rays and protons are used to train the RFs. The EAS development of the MC particles is performed with the dedicated software package CORSIKA, while the telescope response to the Cherenkov signal is reproduced with the software package sim_telarray (Heck et al. 1998; Bernlöhr 2008). These packages aim to make the simulated and observational data as similar as possible. However, some differences may arise between them due to diverse circumstances, such as degradation of the

atmospheric conditions (e.g. dust) or the telescope performance (e.g. misaligned or dirty mirrors), or changing NSB conditions, among others. The diffuse NSB is initially accounted for in the simulations, with a value set to the NSB conditions of a dark sky-field (corresponding to an average rate of 193 MHz p.e. per pixel; Abe et al. 2023b). The NSB level can be increased to the specific observing conditions at the waveform level or after the image cleaning.

The current MC production scheme in LST-1 is that both MC gamma rays and protons are simulated at predefined telescope-pointing directions, known as nodes, across the celestial sphere. The training pointing directions form a declination line, i.e. the declination of the training nodes is the same. On the other hand, the testing nodes are distributed across the celestial sphere producing a grid in the $\cos(ZA)$ – $\sin\delta$ plane, where $\delta = B_{\perp}/B_{max}$. The testing nodes are arranged in this parameter space to consider the effect of air mass traversed by the Cherenkov light and the impact of the geomagnetic field on the EAS development (see Sect. 3.2.1). Figure 4.13 shows the distribution of MC testing and training nodes.

The MC simulations are processed by applying the same cuts as the observational data during the data reduction steps. However, the increased pedestal condition in the image cleaning is not considered because no interleaved FF or pedestal events are simulated.

4.4 MAGIC+LST DATA ANALYSIS

The LST-1 facility is situated at a distance of approximately $\sim 100\,\mathrm{m}$ from MAGIC, a proximity that enables the simultaneous detection of Cherenkov light by both instruments. LST-1 and MAGIC work independently, but an offline software-trigger analysis allows the identification and reconstruction of common events with both facilities. This offline analysis provides better sensitivity than considering the two facilities independently (Abe et al. 2023c).

The software package used for the joint analysis of MAGIC and LST-1 is magic-cta-pipe [III]. Furthermore, the ctapipe_io_magic package is used to convert MAGIC custom files into a common format, as the MAGIC Collaboration is an independent experiment from CTAO and the data level and file formats are different than the ones described in Sect. 4.2, yet the general data analysis flow holds.

The offline software-trigger analysis consists of searching coincident events between MAGIC and LST-1 within a coincidence window of 0.6 µs. This search is done after applying the image cleaning on the image of each telescope and removing dim events with *intensities* below 50 p.e. (Abe et al. 2023c). MAGIC calibrates the waveform and produces camera images using the algorithms described in (Aleksić et al. 2016b; Sitarek et al. 2013; Albert et al. 2008a). Moreover, the image cleaning method known as sum image cleaning is applied in MAGIC (Aleksić et al. 2011). On the other hand, the same procedure as described in Sect. 4.3 is considered for LST-1 up to DL1.

Once the events are associated forming different telescope combinations (e.g. M1+M2, M1+LST-1, M2+LST-1, and M1+M2+LST-1), the EASs can be reconstructed

 $[\]P\P\P$ https://github.com/cta-observatory/magic-cta-pipe

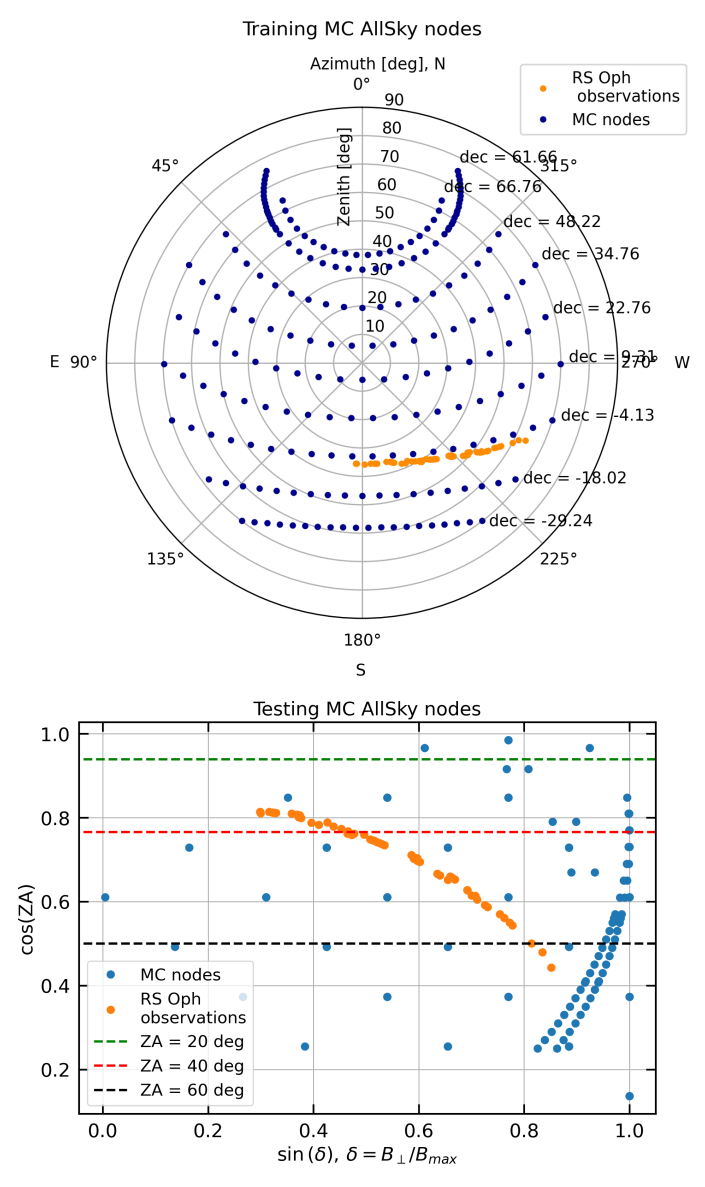


Figure 4.13: Top: Distribution of training MC nodes in horizontal coordinates. The MC nodes form the so-called declination lines. Bottom: Distribution of testing MC nodes in the $\cos(ZA)$ - $\sin\delta$ plane. The traces on the right correspond to dedicated MC simulations not following the grid pattern.

combining the images of the different telescopes. RF algorithms are used to estimate the primary particle properties. As the EAS can be reconstructed in three dimensions, the *impact parameter* and H_{max} are used as input parameters of the RFs, among others.

Note that MAGIC only records events to disc that are triggered by both telescopes. Therefore, the offline event trigger between MAGIC and LST-1 is limited by the MAGIC trigger rate. However, events may be associated with one MAGIC telescope and LST-1 if the event image of the other MAGIC telescope does not survive the cleaning and parameter cut. On the contrary, a hardware MAGIC and LST-1 trigger is being implemented that would increase the trigger rate (CTA-LST Project et al. 2024). The Hardware Stereo Trigger (HaST) is capable of processing relatively faint

events triggered by any pair of the three telescopes. In particular, it can record events detected with M1+LST-1 and M2+LST-1 pairs, which are events not handled by the software trigger. The result is an improvement of about 20% over the MAGIC+LST-1 software coincident trigger and about 30% over the MAGIC-stereo trigger.

5

Overview

NOVAE

This chapter outlines the study of nova eruptions in the gamma-ray band developed for this Thesis. Firstly, the detection of RS Ophiuchi (RS Oph) with LST-1 and the modelling of its HE/VHE gamma-ray emission are presented. Secondly, we discuss the perspective of novae detections with the array of four LSTs and the full CTAO. The results on RS Oph obtained using LST-1 observations, together with the perspective with the four LSTs have been published in Astronomy and Astrophysics (Abe et al. 2025a), while the predictions on novae detections with CTAO have been accepted for publication to the Monthly Notices of the Royal Astronomical Society (Abe et al. 2025b).

5.1 INTRODUCTION

A nova eruption is a thermonuclear runaway explosion on the surface of a white dwarf star in a binary system involving a white dwarf accreting matter, often through an accretion disc, usually from a late-type star (Gallagher and Starrfield 1978). Novae are detected across the electromagnetic spectrum as transient events exhibiting a huge and sudden increase of the source brightness. Though novae have been studied both observationally and theoretically for many decades, a comprehensive understanding of nova physics is still lacking (Iben 1982; Yaron et al. 2005; Bode and Evans 2012; Kato et al. 2014; Chomiuk et al. 2021).

Particle acceleration in novae was predicted before the launch of the *Fermi Gamma-ray Space Telescope* (see Tatischeff and Hernanz 2007). Shortly after, GeV emission from the eruption of the binary system V407 Cygni, composed of a white dwarf and an evolved red giant companion, was first detected (Abdo et al. 2010)*. The red giant in these systems produces dense circumbinary material, likely concentrated in the orbital plane. Relativistic particles accelerated via DSA in expanding shocks are thought to interact with the dense circumbinary material, generating HE gamma rays (Abdo et al. 2010; Hernanz and Tatischeff 2012; Martin and Dubus 2013).

Subsequently, novae with main sequence donor stars were also detected (known as classical novae; Ackermann et al. 2014). Multiple nova detections at HE gamma rays from several binary systems and, in particular, the classical ones, likely indicate that particle acceleration is an intrinsic phenomenon in nova systems (Morris et al. 2016). The detection of classical novae, which do not exhibit a dense circumbinary material, suggests that internal shocks between several outflows can act as an efficient mechanism to accelerate particles in novae (Metzger et al. 2014; Martin et al. 2018; Chomiuk et al. 2021).

By the time this Thesis is written, 20 novae[†] have been detected in the HE energy band with a rate of about one eruption detection per year. The majority of these

^{*}Gomez-Gomar et al. (1998) (and references therein) predicted gamma-ray emission from novae but of nuclear origin, in the keV–MeV domain.

[†]According to https://asd.gsfc.nasa.gov/Koji.Mukai/novae/latnovae.html.

events do not occur embedded in a dense environment. Additionally, all detected novae have been bright in the visible band ($\leq 10 \,\mathrm{mag}$), and the vast majority are nearby sources with distances within 5 kpc (Franckowiak et al. 2018).

Since the addition of novae as a new source class that emits in the HE gamma-ray sky (Ackermann et al. 2014), novae have generated interest in the VHE gamma-ray domain for their potential to accelerate particles to TeV energies efficiently (e.g., Metzger et al. 2016). Novae also provide an excellent opportunity to study particle acceleration on fast shock-evolution timescales. They are also relatively numerous within the Milky Way, making them accessible targets for HE astrophysics (with a Galactic nova rate estimated from different studies between 26–50 yr⁻¹; Zuckerman et al. 2023; Kawash et al. 2022; Rector et al. 2022; De et al. 2021; Shafter 2017). Nevertheless, nova observations did not succeed in a detection at VHE gamma rays (Aliu et al. 2012; Ahnen et al. 2015; Albert et al. 2022) until the 2021 eruption of RS Ophiuchi (RS Oph; H. E. S. S. Collaboration et al. 2022; Acciari et al. 2022).

When novae erupt, the detected HE emission presents a similar curved spectral shape regardless of the companion star type (Ackermann et al. 2014). However, the HE luminosity and duration differ and vary depending on the systems (e.g. Ackermann et al. 2014; Cheung et al. 2016; Sokolovsky et al. 2023). Early studies with a limited sample of classical novae suggested an inverse relation between the HE gamma-ray luminosity and its duration (Cheung et al. 2016). However, with a larger sample, this relation may no longer hold (Albert et al. 2022). Nevertheless, novae seem to emit for a longer time at HE gamma rays when the optical decline from optical maximum is shallower (Albert et al. 2022). Deep gamma-ray observations with multi-wavelength (MWL) data are required to determine whether the physical differences between the two nova types also reflect a different HE–VHE gamma-ray emission.

Below we present a study of the nova RS Oph in gamma rays as well as the perspectives for novae detection with the LST array and the full CTAO. We introduce the source RS Oph in Sect. 5.2. Section 5.3 describes the observations and the analyses of LST-1 and contemporaneous *Fermi*-LAT data. In Sect. 5.4 we discuss the model used to characterise the gamma-ray emission of RS Oph. In Sect. 5.5 the results from the LST-1 data analysis and the modelling using the *Fermi*-LAT, LST-1, MAGIC, and H.E.S.S. spectral information are presented. The model fitting procedure and robustness tests are described in Sect. 5.6. In Sect. 5.7 we discuss the results. Future expectations for nova detections with the array of LSTs and the full CTAO are addressed in Sect. 5.8. Concluding remarks are provided in Sect. 5.9.

5.2 RS OPH

The source RS Oph is a well-known binary system that experiences recurrent nova explosions that range from 8.6 up to 26.6 years (see Schaefer 2010 for a review). These explosions result from the high mass-accretion rate onto the massive white dwarf driven by the giant companion star. The accretion process in RS Oph is unclear, but the donor star may overfill its Roche lobe (Somero et al. 2017; Schaefer 2009; Booth et al. 2016). RS Oph is characterised as an embedded nova because its eruptions occur immersed in the dense wind of the post-main-sequence companion star (M0 III; Anupama and Mikołajewska 1999).

During the 2021 nova event of RS Oph, the H.E.S.S. and the MAGIC telescope facilities detected RS Oph (H. E. S. S. Collaboration et al. 2022; Acciari et al. 2022). RS Oph is the first nova that was detected at VHE gamma rays and the first confirmation of particle acceleration up to TeV energies in embedded novae. However, the exact acceleration and radiation mechanisms remain unclear, although the favoured explanation for the VHE gamma-ray emission is the hadronic scenario (Martin et al. 2018; Acciari et al. 2022; H. E. S. S. Collaboration et al. 2022; Zheng et al. 2022; Diesing et al. 2023; Sarkar et al. 2023).

LST-1 observed RS Oph during the nova phase. RS Oph is the first transient source detected with LST-1 during its commissioning phase. In this work, we report the spectral analysis and modelling of RS Oph using LST-1 and Fermi-LAT observations and exploiting published gamma-ray data obtained with the H.E.S.S. and MAGIC telescopes.

5.3 OBSERVATIONS AND DATA ANALYSIS

In this section, we describe the observation campaign conducted on RS Oph with LST-1 and the analysis procedures we used in this work (see Sect. 5.3.1). We also analyse *Fermi*-LAT data that were obtained contemporaneously with the LST-1 observations (see Sect. 5.3.2).

5.3.1 *LST-1*

LST-1 started follow-up observations of RS Oph based on its detection with *Fermi*-LAT (Cheung et al. 2021) at HE gamma rays and its bright emission in optical wavelengths. The first LST-1 observation was recorded on 9 August 2021 (MJD 59435.90), about one day after the optical trigger. LST-1 observed RS Oph for several days between 9 August and 2 September 2021 (MJD 59459.91). In this work, we analyse LST-1 data in good atmospheric[‡] and dark or low-moonlight observing conditions[§] during the observation campaign (see Table 5.1).

The LST-1 observations were performed in *wobble* mode with an offset of 0.4° (see Sect. 4.1.6.1). The LST-1 data were reduced from raw signal waveforms to a list of gamma-like events following the LST-1 standard source-independent analysis approach (see Sect. 4.3). The classification and regression methods rely on RF algorithms trained on MC gammas and protons, simulated following a declination track of -4.13° in the sky plane, close to the RS Oph declination (see Sect. 4.3.5)¶. The IRFs for each LST-1 observation were produced by interpolating the IRFs calculated at each sky direction of the test MC data to the average telescope pointing direction of each observation. The open-software package Gammapy (Donath et al. 2023; Acero et al. 2022) was used to obtain the scientific products from the gamma-like events, which were assigned based on event selection cuts. To assess the signal, the same event selection cuts in the whole energy range were used for the *gammaness*

[‡]Atmospheric transmission at 9 km above 80%.

[§]Observations with the Moon below the horizon or maximum diffuse NSB level below 2.3 photoelectrons.

[¶]The impact of using a slightly different declination value for the MC simulations and RS Oph is negligible.

Start day	Start date	$t-t_0$	Effective time after data selection	ZA range
	[MJD]	[d]	[h]	[°]–[°]
09 Aug. 2021	59435.90*	0.97	1.43	35–41
10 Aug. 2021	59436.90*	1.97	2.68	35–57
12 Aug. 2021	59438.90*	3.97	2.24	36–53
29 Aug. 2021	59455.94	21.01	0.97	46–55
30 Aug. 2021	59456.90	21.97	1.52	40-56
01 Sep. 2021	59458.98	24.05	0.32	57–64
02 Sep. 2021	59459.91	24.98	1.27	42–54

Table 5.1: Observation campaign of RS Oph with LST-1.

Notes. For each observation day, we list the day of the evening before data taking, the starting date in MJD, the starting time offset with respect to the optical trigger ($t_0 = \text{MJD}\,59434.93$; Geary 2021), the effective observation time after the data selection, and the ZA range of the observations. We mark the dates for which daily spectral analyses were performed with an asterisk.

and θ parameters. Conversely, the event selection cuts applied to the gamma-like events used to compute the SEDs and light curve are energy-dependent efficiency cuts at 70% (see Sect. 4.1.4).

We performed a spectral analysis using control sky regions (OFF regions) located around the telescope pointing at the same offset as RS Oph. OFF regions at angular offsets of 90°, 180° and 270° were used, where 0° is towards the telescope pointing and the position of RS Oph (see Sect. 4.1.6.1). OFF regions were used to subtract the background. The energy threshold of the analysis, computed as the peak position of the energy distribution of the simulated gamma-ray events from a source with a power-law spectral index equal to -4, is $E \sim 30\,\text{GeV}$.

We computed the integral fluxes on a daily basis for observations immediately after the eruption ($t - t_0 < 4\,d$, where $t_0 = \text{MJD}\,59434.93$; Geary 2021) using the spectral shape from the best-fit model for each day. Moreover, we computed integral fluxes by taking several observation days together (hereafter called joint flux; see observation days in Table 5.1), employing the best-fit spectral model in the corresponding time period. We calculated upper limits (ULs) at the 95% confidence level without considering the systematic uncertainty of the telescope energy scale. The error uncertainties correspond to 1σ statistical errors.

5.3.2 Fermi-LAT

The first detection of RS Oph at gamma rays was reported with *Fermi*-LAT (see Sect. 3.1.1), coincident with its optical discovery (Cheung et al. 2021). The temporal trend in the HE band is similar to the trend in the optical band: a flat peak emission around \sim 1 d after the eruption, preceded by a smooth power-law increase and a subsequent power-law decay (slopes between wavelengths consistent within errors).

However, the gamma-ray onset was delayed by $\sim 0.35\,\mathrm{d}$ with respect to the time of the eruption and could have reached the peak at later times than in the optical with a delay of about $0.5\,\mathrm{d}$ (Cheung et al. 2022). The HE gamma-ray emission presents significant spectral curvature, which hardens as the eruption evolves in time. The preferred origin for the HE emission is hadronic, as the model effectively explains the observed emission. No leptonic model was tested in Cheung et al. (2022).

We performed a dedicated *Fermi*-LAT analysis to obtain contemporaneous gamma-ray spectra with the LST-1 observations of RS Oph. To analyse the *Fermi*-LAT data, we considered reconstructed events between 50 MeV and 300 GeV with evclass=128 and evtype=3. Only events with good time intervals (DATA_QUAL>0 && LAT_CONFIG==1) coming below a ZA of 90° were selected.

A binned analysis within a region of interest of 20° around RS Oph was used to model the projected area of interest. We considered in the model all sources in the LAT 10-year source catalogue (4FGL-DR2) together with the Galactic diffuse and the standard isotropic background from Pass 8. All the spectral parameters of all sources within 4° to RS Oph were let free to vary above 50 MeV. No spectral differences were observed when we fixed the spectral parameters of 4FGL J1745.4—0753, the closest source to RS Oph, to its catalogue value. We adopted the latest IRFs (P8R3_SOURCE_V3) in the analysis. The data processing and analysis were performed using Fermitools v2.0.8 and Fermipy v1.0.1 (Fermi Science Support Development Team 2019; Wood et al. 2017).

We extracted the RS Oph daily SED for the days on which LST-1 observed RS Oph. A log-parabola spectral shape was used to model the HE gamma-ray emission (Acciari et al. 2022). The ULs were computed at the 95% confidence level for energy bins with test statistic (TS) values below 4, with uncertainties corresponding to 1σ statistical errors. Additionally, when a significant flux was between two ULs, it was set to UL 11 .

5.4 MODELLING

Proton-proton interactions are thought to be the emission mechanism responsible for the gamma-ray emission in RS Oph (Acciari et al. 2022; H. E. S. S. Collaboration et al. 2022; Cheung et al. 2022). However, a leptonic contribution to the observed emission cannot be discarded (Sarkar et al. 2023).

We considered the same modelling as the one used in Acciari et al. (2022) to model the gamma-ray emission from RS Oph. We considered hadronic and leptonic scenarios. We parametrised the particle spectrum as an exponential cutoff power-law (ECPL) model, while a broken power-law (BPL) model was also considered for the electron spectrum. The same nova parameter values for RS Oph (e.g. distance, ejecta velocity, photosphere radius, and temperature) as those used in Acciari et al. (2022) were assumed in this work because the data are simultaneous (see Table 5.2).

The model maps the ejecta close to a thin layer for the energetic particles. The processes involved in the gamma-ray production for the hadronic scenario are the decay of neutral and charged pions (see Sect. 2.2.4), whereas the IC process alone is considered for the leptonic scenario (see Sect. 2.2.2). Bremsstrahlung emission is

¹¹This restrictive cut was considered to ensure that the *Fermi*-LAT significant differential fluxes were as robust as possible for the model fitting.

Parameter	Values	on observ	ation day
	Day 1	Day 2	Day 4
Distance [kpc]	2.45	2.45	2.45
Photosphere radius $[R_{\odot}]$	200	200	200

10780

1 4500

1

0.1

9490

4500

1

0.1

7680

4500

1

0.1

Photosphere temperature [K]

Time after nova explosion [d]

Expansion velocity [km s⁻¹] Mass of nova ejecta [$10^{-6} M_{\odot}$]

Confinement factor

Table 5.2: Nova parameters used to model the RS Oph gamma-ray SED.

Notes. For each observation day, we list the distance, the photosphere radius, the photosphere temperature, the time after the nova explosion, the expansion velocity, the mass of nova ejecta, and the confinement factor (the relative thickness of the shell of the expelled material). The values were extracted from supplementary Table 10 of Acciari et al. (2022).

negligible because the total column density is lower than the radiation length of hydrogen (see Sect. 2.2.3; Acciari et al. 2022). The seed of photons that dominate during the eruption comes from the photosphere, whose temperature evolves in time (see Table 5.2). Gamma-gamma absorption is considered in the model (see Sect. 2.3.1). However, it is only relevant for the first day after the eruption (Acciari et al. 2022).

The SED data points at gamma rays from Fermi-LAT, LST-1, MAGIC, and H.E.S.S. were used in the model fitting. As we combine data from multiple instruments, we adapted the model fitting to account for systematic uncertainties in the energy scale of the spectra obtained by the IACT facilities. A systematic uncertainty in the energy scale between $\pm 15\%$ was considered as a nuisance parameter for each experiment on each day during the fitting process. The absolute 15% maximum value was assumed based on the reported energy-scale uncertainty from MAGIC and H.E.S.S. (Aleksić et al. 2016b; H. E. S. S. Collaboration et al. 2022). Similar systematic uncertainties are expected for LST-1 (see Fig. 11 in Abe et al. 2023c). Normally, energy-scale systematics are the dominant effect in IACTs (see Sect. 3.2.3). This is especially relevant for soft sources such as RS Oph. However, other types of systematics may contribute, such as uncertainties in the background normalisation, especially at lower energies for a single telescope (Abe et al. 2023b). Including systematic uncertainties in the model fitting reduces the number of degrees of freedom in the fitting process because a displacement of the SED points of the IACTs is allowed with respect to the original points. ULs are not included in the model-fitting minimisation.

The small distance between the LST-1 and MAGIC telescopes means that the measurements with both instruments are not fully independent. Namely, the same gamma-ray shower can be registered by both. The correlation is expected to be energy-dependent and is difficult to evaluate precisely. However, because the trigger

Table 5.3: Best-fit power-law spectral	parameter values and	d statistical detectior	n significances
(Sig.) using LST-1 data.			

Obs. day	Γ	ϕ_0 [10 ⁻¹⁰ TeV ⁻¹ cm ⁻² s ⁻¹]	Sig. [σ]
Day 1	-4.2 ± 0.3	3.3 ± 1.3	3.2
Day 2	-3.65 ± 0.13	5.9 ± 1.0	2.8
Day 4	-3.50 ± 0.15	5.9 ± 1.1	5.5
Day 1, 2 and 4	-3.73 ± 0.10	5.2 ± 0.7	6.6

Notes. Γ is the spectral index, and ϕ_0 is the amplitude at a reference energy of 130 GeV. The statistical detection significance (using equation 17; Li and Ma 1983) is computed for the full energy range.

rates of both instruments are very different and the source flux was low (i.e. large effect of the random background on the resulting spectra), we expect the correlation to be low and therefore treated the two experiments as independent.

5.5 RESULTS

We report the results of the LST-1 data analysis in Sect. 5.5.1 and compare them with the MAGIC and H.E.S.S. findings. Additionally, the results of the model parameter fitting using *Fermi*-LAT, LST-1, MAGIC, and H.E.S.S. data are presented in Sect. 5.5.2, where we also compare the outcomes of the different models.

5.5.1 LST-1 results

RS Oph was detected with LST-1 with a statistical significance of 6.6σ for the three days of LST-1 observations within the first four days from the nova eruption ($t-t_0\sim 1\,\mathrm{d}$, 2 d, and 4 d; see Table 5.1). The daily statistical significance of the detection is shown in Table 5.3. The source was not detected (1.6σ) using the observations conducted three weeks after the nova onset ($t-t_0>21\,\mathrm{d}$). We evaluated the signal detection in these two periods separately due to the 12-day temporal gap during which no observations passed the data-selection criteria.

For the purpose of aggregating data from different instruments, we defined observation days as the integer sequence of day intervals centred on t_0 . The ith observation-day interval spans over MJD $t_0 + i \pm 12\,\text{h}$. The RS Oph daily SEDs at VHE gamma-ray energies with LST-1, including the best-fit spectral models, for the first three observations with LST-1 data on days 1, 2, and 4 after the explosion are shown as blue squares in Fig. 5.1.

A power-law spectral model was adopted to fit the LST-1 data of RS Oph. The spectral index measured with LST-1 is soft for all days and seems to harden as the eruption evolves in time from observation day 1 to observation days 2–4 (see Table 5.3). However, a spectral profile with a constant index set to the weighted

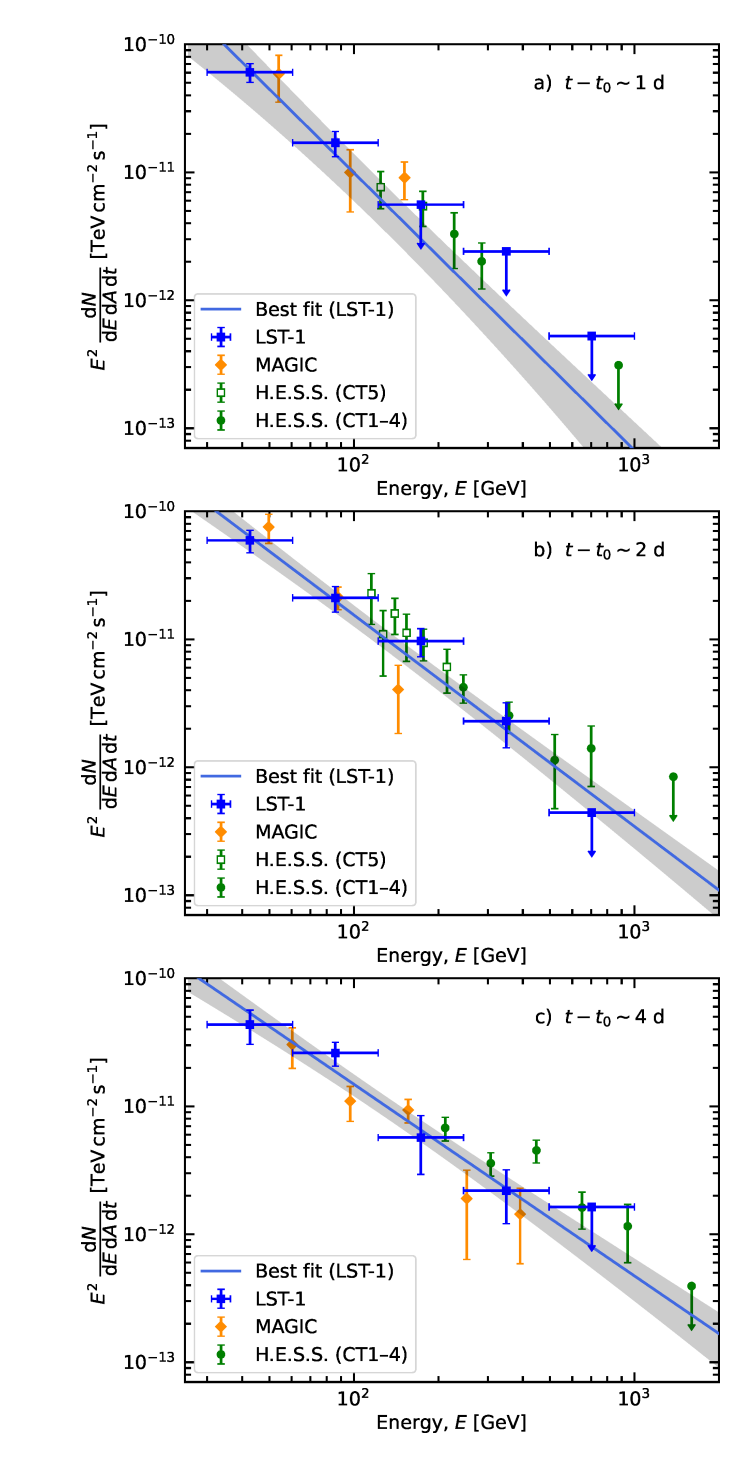


Figure 5.1: RS Oph daily SEDs at VHE gamma rays with LST-1 (blue squares), MAGIC (orange diamonds; Acciari et al. 2022), and H.E.S.S. (green empty squares and filled circles for the telescopes CT5 and CT1–4, respectively; H. E. S. S. Collaboration et al. 2022) during the same day interval. From top to bottom, panels a, b, and c correspond to observation-day intervals $t-t_0\sim 1\,\mathrm{d}$, 2 d, and 4 d, respectively. The best-fit model for LST-1 is displayed as a blue line together with the grey spectral error band.

average of the first four observation days cannot be rejected (p-value = 0.11; a

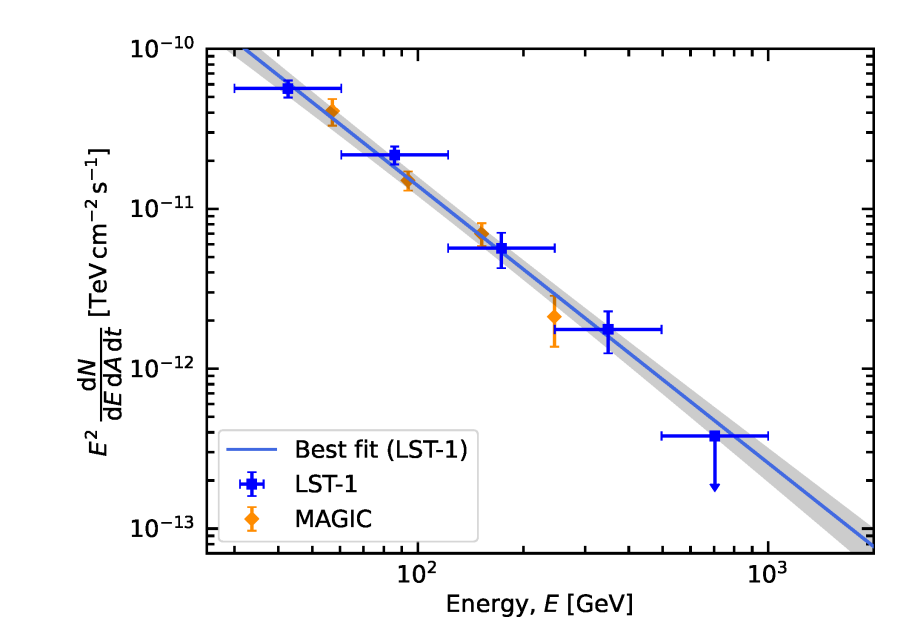


Figure 5.2: SED at VHE gamma rays obtained with LST-1 (blue squares) and MAGIC (orange diamonds; Acciari et al. 2022) using all observations between observation-day intervals $t-t_0\sim[1,4]$ d (see Table 5.1 for LST-1). The best-fit model for LST-1 is displayed as a blue line together with a grey spectral error band.

significance level** of $\alpha = 0.05$ is set to test the null hypothesis). The situation is similar for a constant-amplitude model (p-value = 0.22).

In Fig. 5.1 we compare the SEDs obtained with LST-1, MAGIC, and H.E.S.S. during the same observation-day intervals (Acciari et al. 2022; H. E. S. S. Collaboration et al. 2022). In general, it is sufficient to only consider statistical errors to obtain compatible results between LST-1 and H.E.S.S./MAGIC, while LST-1 spectra can probe lower energies than the other two IACTs. In addition to the daily SEDs shown in Fig. 5.1, the joint spectrum for the same observation days ($t-t_0\sim 1\,\mathrm{d}$, 2 d, and 4 d) with LST-1 is shown in Fig. 5.2. The joint LST-1 SED is compatible with that of MAGIC during the same time period. We note, however, that the MAGIC joint flux includes the observations on 11 August ($t-t_0\sim 3\,\mathrm{d}$), when LST-1 did not observe RS Oph.

We show in Fig. 5.3 the light curve above $100\,\text{GeV}$ for LST-1 and MAGIC (Acciari et al. 2022), including the daily and joint integral fluxes for both instruments. No significant emission is detected with LST-1 above $100\,\text{GeV}$ during the first day of data-taking (UL with TS=2.2). The source flux TS is instead above the UL criterion in the following days, yielding compatible flux values within statistical uncertainties among them. We obtain less constraining spectral parameter values and a non-significant integral flux for the first observation day than for the second and fourth day because the observation time was shorter and the intrinsic emission was likely softer. The LST-1 daily light curve differs slightly from that of MAGIC when we only consider statistical uncertainties, which suggests the presence of systematics that are not accounted for in the integral flux computation. When the data are joined, however, the joint VHE flux between observation-day intervals 1

 $^{^{**}}$ The maximum acceptable probability of committing a type I (false positive) error assigned in the test statistic.

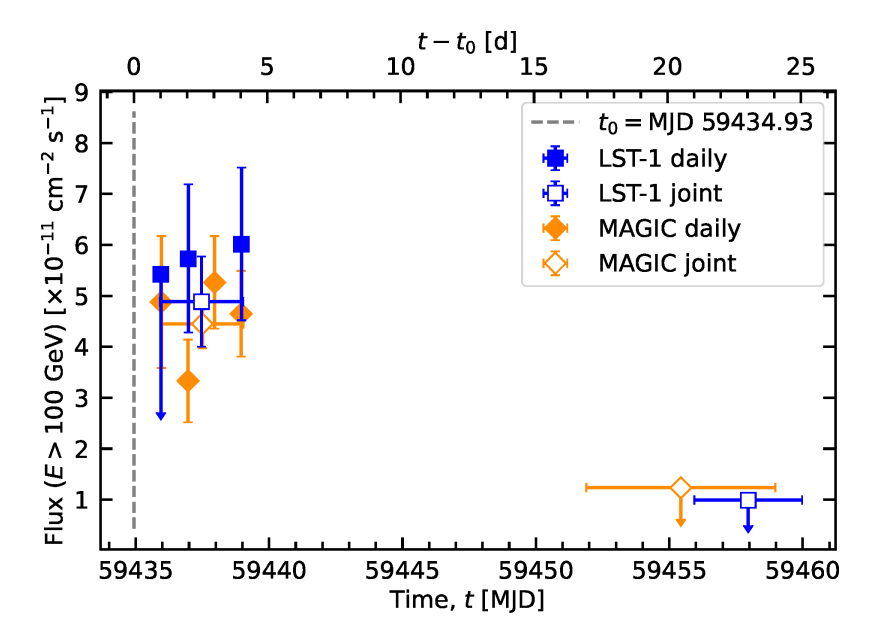


Figure 5.3: Daily integral fluxes at $E > 100\,\text{GeV}$ for LST-1 (filled blue squares) and MAGIC (filled orange diamonds; Acciari et al. 2022) as a function of MJD (bottom axis) and time after the eruption onset (top axis), which is represented as the dashed line. We also show the joint LST-1 (empty blue squares) and the joint MAGIC (empty orange diamonds) integral fluxes during observation-day intervals 1 and 4, and more than 21 days after the eruption.

and 4 with LST-1 is compatible within statistical uncertainties with the MAGIC joint integral flux for the same time window. For observations taken after $t - t_0 > 21$ d, when the source was not detected with LST-1, we computed a joint integral flux UL above 100 GeV of 10^{-11} cm⁻² s⁻¹, which was obtained by fixing the power-law spectral index to $\Gamma = -3.5$ (the spectral index of observation day 4). The result is comparable in flux level with the MAGIC findings.

5.5.2 Modelling results using Fermi-LAT and IACT data

We show in Fig. 5.4 the daily SEDs with *Fermi*-LAT together with the VHE IACT data shown in Fig. 5.1. The gamma-ray spectra span from 50 MeV up to about 1 TeV. The SED points at HE connects smoothly with that of VHE gamma rays, showing signs of curvature.

The emission model was fitted using spectral information from LST-1 and *Fermi*-LAT data (this work) together with published MAGIC and H.E.S.S. spectral information for each coincident observation-day interval with LST-1. The simplest physically motivated particle energy profile, an ECPL model, without systematic energy-scale uncertainties in the fitting process (see Sect. 5.4), was considered for the hadronic and leptonic models. The ECPL model is not able to provide a good fit to the data for the leptonic model, yielding reduced χ^2 ($\chi^2_{\rm red}$) values for each day of about 3 (p-values $\sim 10^{-5}$). The poor fit can be explained by the spectral curvature present across the HE and VHE range (as already mentioned by Acciari et al. 2022).

To reproduce the curvature of the gamma-ray spectrum for the leptonic model, we used a BPL shape to describe the energy distribution of electrons (see Acciari et al.

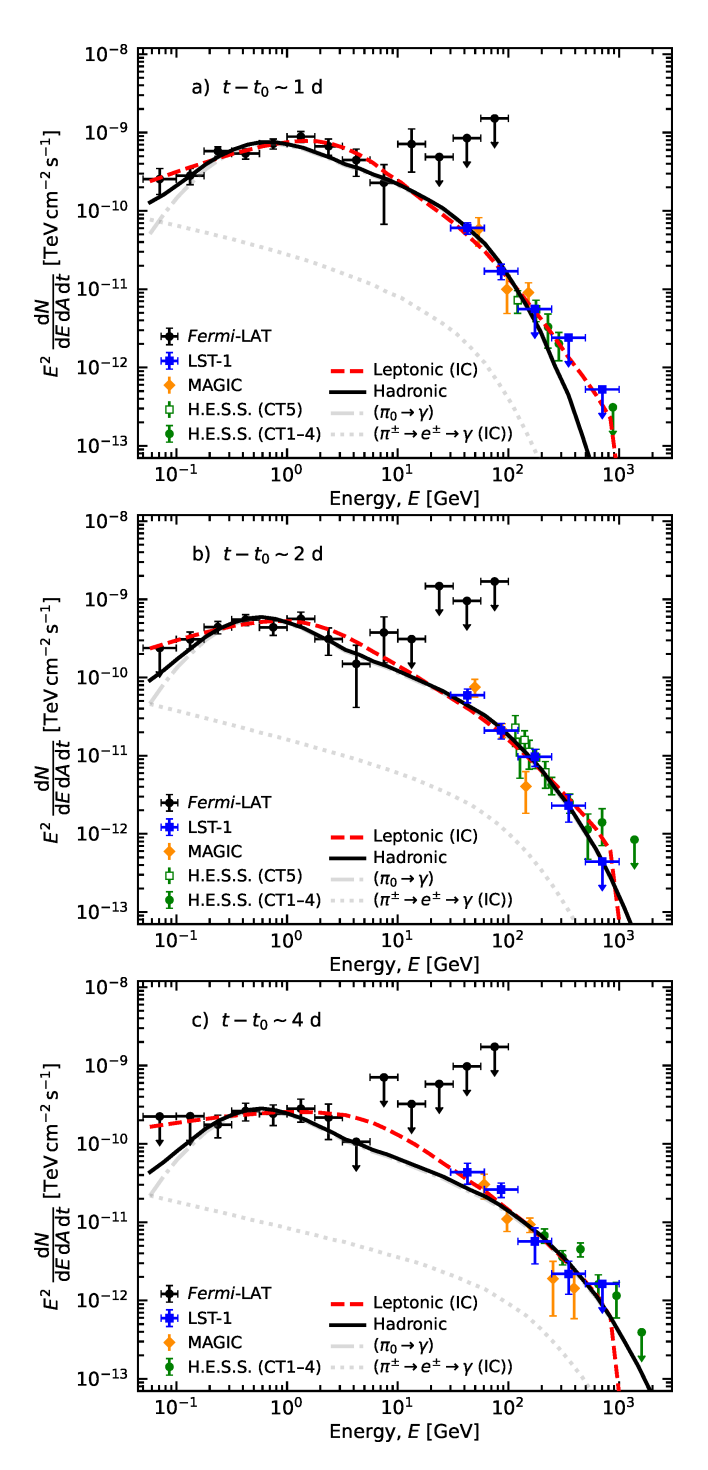


Figure 5.4: RS Oph daily SEDs from HE to VHE gamma rays using *Fermi*-LAT (black circles), LST-1 (blue squares), MAGIC (orange diamonds; Acciari et al. 2022), and H.E.S.S. (green empty squares and filled circles for the telescopes CT5 and CT1–4, respectively; H. E. S. S. Collaboration et al. 2022). From top to bottom, panels a, b and c correspond to observation-day intervals $t-t_0\sim 1\,\mathrm{d}$, 2d, and 4d, respectively. The best-fit leptonic and hadronic models are displayed as dashed red and solid black curves, respectively. For the hadronic model, the corresponding contributions from neutral and charged-pion decays are shown in grey.

Table 5.4: Model-fit results without and with systematic uncertainties using the leptonic and hadronic modelling for observation days $t - t_0 \sim 1\,\mathrm{d}$, 2 d, and 4 d.

Parameter	Best-fit va	lue on observ	ation day
	Day 1	Day 2	Day 4
Leptoni	c BPL model v	without syster	matics
Slope 1, $\Gamma_{e,1}$	$0.0^{+0.8}_{-0.6}$	$-1.3^{+1.5}_{-0.5}$	$-1.4_{-0.7}^{+0.6}$
Slope 2, $\Gamma_{e,2}$	$-3.79^{+0.17}_{-0.18}$	$-3.57^{+0.11}_{-0.15}$	$-3.52^{+0.05}_{-0.06}$
$E_{b,e}$ [GeV]	14^{+3}_{-3}	17^{+8}_{-4}	22^{+9}_{-6}
$\chi^2/N_{\rm d.o.f}$	12.9/15	24.9/21	24.9/15
$\chi^2_{\rm red}$	0.86	1.19	1.66
AIC_c	23.7	34.9	35.8
Hadronio	ECPL model	without syste	ematics
Slope, Γ_p	$-2.25^{+0.13}_{-0.13}$	$-2.49^{+0.07}_{-0.07}$	$-2.48^{+0.08}_{-0.08}$
$E_{c,p}$ [TeV]	$0.26^{+0.08}_{-0.08}$	$1.0_{-0.3}^{+0.3}$	$1.6_{-0.6}^{+0.6}$
$\chi^2/N_{\rm d.o.f}$	21.5/16	24.9/22	26.5/16
$\chi^2_{\rm red}$	1.34	1.13	1.66
AIC_c	29.1	32.0	34.1
Leptoi	nic BPL mode	l with system	atics
Slope 1, $\Gamma_{e,1}$	$0.4^{+1.9}_{-1.9}$	$-1.6^{+0.8}_{-0.3}$	$-1.4_{-0.7}^{+0.8}$
Slope 2, $\Gamma_{e,2}$	$-3.70^{+0.17}_{-0.17}$	$-3.6^{+0.2}_{-0.2}$	$-3.75^{+0.13}_{-0.11}$
$E_{\rm b,e}$ [GeV]	13^{+3}_{-3}	20^{+9}_{-8}	30^{+11}_{-10}
$\chi^2/N_{\rm d.o.f}$	12.9/12	22.8/18	16.8/12
$\chi^2_{ m red}$	1.08	1.27	1.40
AIC_c	37.1	43.4	41.0
Hadror	nic ECPL mod	el with systen	natics
Slope, Γ _p	$-2.22^{+0.06}_{-0.10}$	$-2.51^{+0.05}_{-0.05}$	$-2.40^{+0.15}_{-0.15}$
$E_{c,p}$ [TeV]	$0.23^{+0.06}_{-0.04}$	$0.9^{+0.2}_{-0.2}$	$1.0^{+0.6}_{-0.6}$
$\chi^2/N_{\rm d.o.f}$	21.1/13	20.4/19	19.9/13
$\chi^2_{\rm red}$	1.62	1.07	1.53
AICc	40.1	37.1	38.9

Notes. For the leptonic modelling, $\Gamma_{\rm e,1}$ and $\Gamma_{\rm e,2}$ are the best-fit slopes below and above the best-fit energy break ($E_{\rm b,e}$), respectively, of the electron energy distribution. For the hadronic case, $\Gamma_{\rm p}$ is the best-fit slope and $E_{\rm c,p}$ is the best-fit cutoff energy of the proton energy distribution. We provide the $\chi^2_{\rm red}$ fit statistics ($\chi^2_{\rm red} = \chi^2/N_{\rm d.o.f}$) and the daily AIC_c values (see text for details). The sum of the AIC_c values for all days for the leptonic model without and with systematics is 94.4 and 121.5, respectively, while for the hadronic model without and with systematics, it is 95.2 and 116.1, respectively. The error values correspond to the quadratic sum of 1σ fit and sampling errors (see Sect. 5.6). The units of $E_{\rm c,p}$ and $E_{\rm b,e}$ are in TeV and GeV, respectively.

2022). The fluxes of the best BPL leptonic models are shown as red curves on the daily SEDs in Fig. 5.4, while the corresponding fit results are displayed in Table 5.4. The leptonic model with a BPL spectral shape can describe well the curvature of

the spectrum with *Fermi*-LAT and IACT data. As the SED evolves with time from observation day 1 to 4, the best-fit parameters of the leptonic model evolve as well: the slope below the energy break softens while the energy break shifts towards higher energies, and the slope above the energy break hardens with time. Overall, the electron spectrum reaches higher energies with time. Note, however, that the uncertainties of the best-fit parameters of the leptonic model shown in Table 5.4 are large because the fitting process is rather dependent on the input parameter values (more information on the robustness of the fitting can be found in Sect. 5.6). The spectral parameter results are compatible within uncertainties with the best-fit leptonic model in Acciari et al. (2022).

For the hadronic spectral fit, the best ECPL model is shown as black curves on the daily SEDs in Fig. 5.4, while the corresponding fit results are displayed in Table 5.4. The spectral index softens as the eruption evolves, while the proton spectrum cutoff energy increases with time: from (0.26 ± 0.08) TeV on day 1 to (1.6 ± 0.6) TeV on day 4. A constant cutoff energy during the first three LST-1 observation days is rejected with a p-value $= 6 \times 10^{-3}$. The temporal evolution of the proton shape is similar but not compatible within the uncertainties to the one observed with Fermi-LAT and MAGIC alone (Acciari et al. 2022). The hadronic fit of all gamma-ray data presents softer proton spectra and higher cutoff energies than Fermi-LAT and MAGIC alone.

The Akaike information criterion (AIC) estimator (Akaike 1974) was used to compare different non-nested models. We summed the AIC values corrected for the second-order small-sample bias adjustment (AIC_c; Hurvich and Tsai 1989) of all observation days for the hadronic and leptonic models (\sum AIC_{c,p} and \sum AIC_{c,e}, respectively) and computed the difference of the higher to the lowest one (\sum AIC_{c,min}) to compare them (\triangle AIC_c). There is no preference between the hadronic over the leptonic model: \triangle AIC_c = 0.8, which corresponds to a relative likelihood (Akaike 1981) of 0.7, where \sum AIC_{c,min} = \sum AIC_{c,e}. The slight loss of information, that is, \triangle AIC_c > 0, experienced by using the hadronic over the leptonic model comes from the low χ^2 value for the leptonic model on observation day 1. However, on this day, the best-fit leptonic model presents the strongest spectral slope break ($\Gamma_{e,1} - \Gamma_{e,2} = 3.8^{+1.0}_{-0.8}$, where $\Gamma_{e,1}$ and $\Gamma_{e,2}$ are the slope below and above the energy break, respectively). The no-preference of the hadronic model based on the fit statistics disagrees with the results shown in Acciari et al. (2022).

We note that the $\chi^2_{\rm red}$ for all models deviates from one (see Table 5.4). Remarkable spectral discrepancies at hundreds of GeV are noticeable between the MAGIC and H.E.S.S. differential fluxes, the latter presenting a harder gamma-ray emission than MAGIC (e.g. see Fig. 5.1). The mismatch between MAGIC and H.E.S.S. results likely contributes to the worsening the goodness of the fit of the models. Thus, to account for the LST-1, MAGIC, and H.E.S.S. discrepancies due to possible energy-scale uncertainties in the IACT data analyses, the hadronic and leptonic models were refitted including systematic energy-scale uncertainties as nuisance parameters in the fitting process (see Sect. 5.6). The best-fit results are shown in Table 5.4. The hadronic and leptonic results with and without systematic are compatible and exhibit the same temporal trends of the particle spectra.

We summed the AIC_c values of all the observation days and compared the models with and without systematics. The leptonic and hadronic model fits without

systematics are both favoured over considering them ($\Delta AIC_c = 27.1$ and $\Delta AIC_c = 20.9$, with a relative likelihood of 1×10^{-6} and 3×10^{-5} for the leptonic and hadronic models, respectively). Therefore, we discarded the fit results accounting for energy-scale systematics during the model fitting and consider hereafter the leptonic and hadronic model without systematics to describe the relativistic particle energy distribution in RS Oph.

More complicated models can be considered to explain the RS Oph gamma-ray emission. A population of both electrons and protons was used in a lepto-hadronic model in Acciari et al. (2022), even though it was not preferred due to a poor fit and the fact that the derived value of the proton-to-electron luminosity ratio (Lp/Le) would be larger by an order of magnitude with respect to the results retrieved for the classical nova V339 Del (Acciari et al. 2022). We note, however, that the Lp/Le in V339 Del might not apply to RS Oph because classical novae could have a different HE particle distribution than embedded novae, since particle acceleration mechanisms and shock formation regions might differ.

The modelling of the RS Oph gamma-ray emission using two populations of relativistic particles, electrons and protons, was also studied following Acciari et al. (2022). The particle energy distribution was assumed to follow an ECPL model, for which the cutoff energies of protons and leptons were connected by the acceleration and cooling times balance (Acciari et al. 2022). Since including systematic energy-scale uncertainties as nuisance parameters was not preferred for the leptonic and hadronic models, they were excluded in the lepto-hadronic model fitting process to reduce the complexity of the fitting. The best-fit model emission is shown on the daily SEDs in Fig. 5.5 and the fit results are shown in Table 5.5. The same procedure as in Sect. 5.6 was followed to provide the uncertainties on the parameter values.

The emission of the best-fit lepto-hadronic model on observation days 1 and 4 is dominated by proton-proton interactions in both HE and VHE bands with the spectral index and cutoff energies of the proton energy distribution consistent with the values obtained with the hadronic model (see Sect. 5.5.2). On the contrary, the emission at HE gamma rays on observation day 2 originates from IC losses, while the VHE component comes from proton-proton interactions. However, the best-fit model exceeds the emission constrained by the UL in the 50–100 MeV energy bin, which is important to constrain the curvature of the spectrum. For all days, the Lp/Le remains high, with its lowest value, 64^{+20}_{-7} %, obtained on $t-t_0\sim 2$ d (see Table 5.5). We note that the best-fit model is highly dependent on the input parameters. The leptonic component can contribute to the HE emission for some solutions on $t-t_0\sim 1$ d, but with worse fit statistics than the best-fit model with the hadronic component dominating the HE band. For these solutions, the corresponding VHE emission of the model, which is associated with the hadronic component, exceeds the SED ULs provided with the IACTs.

When comparing the AIC_c values of the lepto-hadronic model with the leptonic and hadronic models, the lepto-hadronic model is less preferred over them (relative likelihood of 0.014 and 0.02, respectively). Given the no preference of the lepto-hadronic model over the hadronic/leptonic model and the dominance of proton-proton interactions in the best-fit model for $t-t_0\sim 1\,\mathrm{d}$ and 4 d, we conclude that the lepto-hadronic model is less plausible, based on gamma-ray data alone, to explain the gamma-ray spectrum.

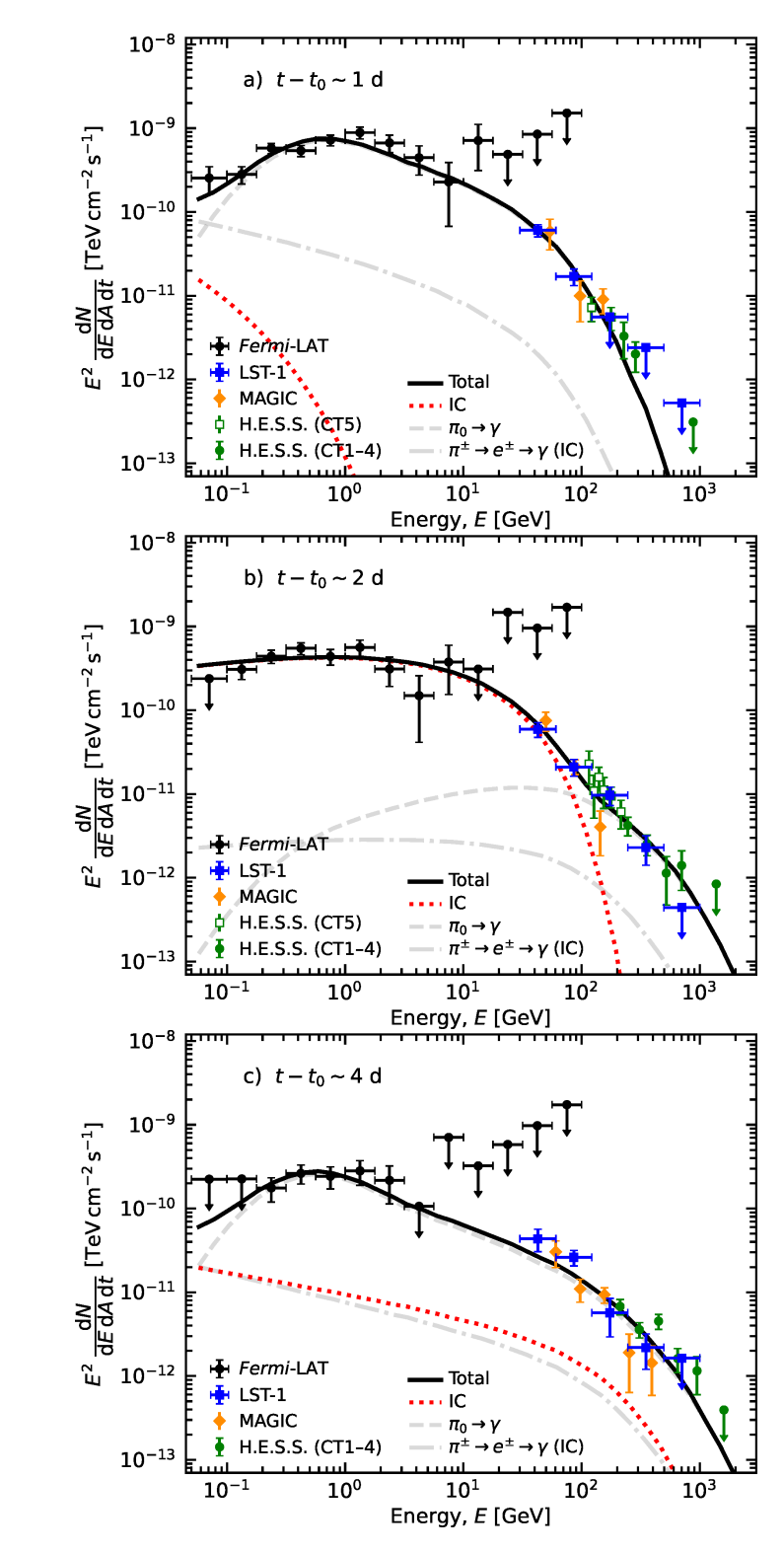


Figure 5.5: Same SEDs as Fig. 5.4 but for the best-fit lepto-hadronic model, whose total contribution is displayed as a black curve. The corresponding contributions from neutral and charged-pion decays are shown in grey and the leptonic contribution in red.

For a better interpretation of the relative likelihoods with respect to the best model according to the AIC, these were normalised to the set of positive weights

Table 5.5: Model-fit results of the	epto-hadronic modelling for observation days $t-t_0\sim 1\mathrm{d}$,
2 d and 4 d.	

Parameter	Best-fit v	alue on obser	vation day	
	Day 1	Day 2	Day 4	
Lepo-hadronic model				
Slope, Γ	$-2.25^{+0.17}_{-0.17}$	$-1.4^{+0.2}_{-0.6}$	$-2.49^{+0.05}_{-0.06}$	
$E_{c,e}$ [GeV]	$1.1_{-0.6}^{+0.6}$	26^{+6}_{-5}	290^{+90}_{-80}	
$E_{c,p}$ [TeV]	$0.26^{+0.14}_{-0.14}$	$1.1_{-0.2}^{+0.3}$	$1.8_{-0.5}^{+0.5}$	
L_p/L_e [%]	940^{+2480}_{-660}	64^{+20}_{-7}	270^{+1500}_{-270}	
$\chi^2/N_{\rm d.o.f}$	21.2/14	23.1/21	26.9/15	
$\chi^2_{ m red}$	1.51	1.10	1.79	
AIC _c	32.1	33.1	37.8	

Notes. Γ is the best-fit slope for the electron and proton energy distributions. The best-fit cutoff energy of protons and electrons is $E_{c,p}$ and $E_{c,e}$, respectively. We note that the cutoff energies of protons and electrons are in TeV and GeV, respectively. Both spectral energy distributions are related using the proton-to-electron luminosity ratio, L_p/L_e . We provide the $\chi^2_{\rm red}$ fit statistics ($\chi^2_{\rm red} = \chi^2/N_{\rm d.o.f}$) and the daily AIC_c values. The sum of the AIC_c values for all days for the lepto-hadronic model is 102.9.

Table 5.6: Information criteria measures for the models used in this work.

Model	ΔAIC_c	Relative likelihood	Akaike weight
Leptonic BPL w/o systematics	0.0	1	0.58
Hadronic ECPL w/o systematics	0.83	0.66	0.38
Leptonic BPL w/ systematics	27.04	1.35×10^{-6}	7.75×10^{-7}
Hadronic ECPL w/ systematics	21.65	2×10^{-5}	1.14×10^{-5}
Lepto-hadronic ECPL	8.5	0.014	8.52×10^{-3}

Notes. The ΔAIC_c and the relative likelihood values are shown for the leptonic BPL without (w/o) and with (w/) systematics, hadronic ECPL w/o and w/ systematics and the leptonadronic ECPL models after summing all days. The ΔAIC_c and the relative likelihood values are computed with respect to the model with $\sum AIC_{c,min}$. Also, the Akaike weights (see text) are shown.

that sum up to 1, called Akaike weights. The information criteria measures for the different models are presented in Table 5.6.

Table 5.7: Set of input reference parameter	r values assumed for the hadronic and leptonic
model for each observation day.	

Parameter	Referenc	e value oı	n observation day
	Day 1	Day 2	Day 4
Slope, Γ_p	-2.2	-2.2	-2.2
$E_{c,p}$ [TeV]	[0.2, 3]	[0.2, 3]	[0.2, 3]
Slope 1, $\Gamma_{e,1}$	-0.5	-0.6	-1.5
Slope 2, $\Gamma_{\rm e,2}$	-3.75	-3.5	-4.0
$E_{\rm b,e}$ [GeV]	15	10	35
LST-1 syst.	0.0	0.0	0.0
MAGIC syst.	0.0	0.0	0.0
H.E.S.S. syst.	0.0	0.0	0.0

5.6 ROBUSTNESS TESTS OF THE MODEL FITTING

To assess the stability of the fitting process for the hadronic and the leptonic models, the fitting was initialised modifying the initial parameter values of the particle energy distribution around a set of reference values (the input systematic IACT energy-scale values were set to zero for all executions). The reference initial parameters were fixed at the parameter results obtained by Acciari et al. (2022) and H. E. S. S. Collaboration et al. (2022). Since the cutoff energy of the proton energy distribution reported by the MAGIC and H.E.S.S. Collaborations were not the same, the input cutoff energy in the fitting was established within the energy range reported by both IACT facilities. In contrast, the assumed reference input values of the electron energy distribution were set to the best-fit results from MAGIC (see Table 5.7).

A sequence of five evenly spaced values per parameter (six for the proton cutoff energy to cover the wide input parameter range) was used to define the input parameter space. Each free parameter of the particle distribution was allowed to vary within $\pm 50\%$ of its corresponding reference value. The reference input parameter values in Table 5.7 were included in the grid. All possible combinations of the particle energy distribution parameters were considered in the fitting of the models.

The vast majority of the leptonic and hadronic model fitting executions without considering systematics converge (93% and 92%, respectively). The leptonic fitting presents more scatter of the fit results than the hadronic one likely due to the larger number of free parameters than the assumed proton spectrum shape. On the contrary, the hadronic model does not present significant variations in the output parameter values for the different input values in the parameter space. The fit results are compatible within errors for the different executions. The spread of the best-fit particle spectrum parameters at the interquartile range (IQR) for the leptonic and hadronic models without allowing for nuisance parameters describing systematics are shown in Table 5.8. One can see that the slope below the energy break of the

electron energy distribution ($\Gamma_{e,1}$) presents the most significant variations. The stability of the fitting process for the leptonic model is not as robust as the fitting of the hadronic one. Therefore, the leptonic model using a BPL model cannot constrain the parameters of the electron energy distribution as precisely as the hadronic model with an ECPL.

Most of the best-fit parameter values assemble forming unimodal distributions for the leptonic and hadronic models. The inclusion of LST-1 into the dataset reduces the dispersion of the distribution of the best-fit parameters. Nevertheless, two local minima are visible in the output parameter distributions for the leptonic fitting of observation day 1 ($t - t_0 \sim 1$ d), hence a bimodal distribution (see Fig. 5.6, where the two distributions are shown in blue and black). $\Gamma_{e,1}$ presents a local minimum peaking at negative values close to zero, while the second minimum is centred at positive values. A bump towards the positive local minimum values is also noticeable for observation day 2 ($t - t_0 \sim 2 \, \mathrm{d}$). The two local minima are smoothly connected in the χ^2 space. The local minimum close to zero peaks at a χ^2 value of $\chi^2 = 12.1$, while the other minimum is centred at $\chi^2 = 11.7$. The two local minima are possible solutions for fitting the curvature of the HE spectrum. Similarly, a bimodal distribution is also obtained if we execute the fitting of the model published by Acciari et al. (2022) together with the Fermi-LAT and MAGIC data as input spectral information, yet the fitting in Acciari et al. (2022) restricted the fitting range to $\Gamma_{\rm e,1} < -0.5$.

Although the solutions with a hard electron spectrum are difficult to explain through the classical non-relativistic DSA mechanism (see Sect. 2.1), we extended the parameter space of the model fitting to include such solutions to study the stability of the model and provide reliable uncertainties. We report the results excluding the best-fit models with $\Gamma_{e,1} > 2$ (black distribution in Fig. 5.6), which is the intersection value we obtain after fitting two normal distributions to the distribution of the best-fit $\Gamma_{e,1}$ results for observation day 1 with different input parameter values (see Fig. 5.6).

Restricting the results to $\Gamma_{e,1}$ < 2 does not significantly impact the results of the leptonic model presented in this work for several reasons. Firstly, the bestfit slope above the energy break would not present a notable change because it is constrained by the IACT data, while a slight decrease of the energy break value would result if allowing the excluded range of $\Gamma_{e,1}$. The minor differences in these parameters would be compatible within uncertainties to the reported value in Table 5.4. Secondly, the physical interpretation of the excluded solutions is the same as the ones considered in the valid range (see Sect. 5.7). Thirdly, the improvement in the fit statistics if including such solutions is marginal. Therefore, no preference between the leptonic and hadronic models could be drawn with the AIC estimator when including these solutions. In contrast, if the fitting range of the electron spectral slope below the energy break would have been restricted to values $\Gamma_{\rm e,1} < -0.5$, as in Acciari et al. (2022), the goodness of fit of the leptonic model would have been worse than most of the output models obtained in this work (see Fig. 5.6). This is attributed to the leptonic model inability to account for the positive gamma-ray emission slope below 1 GeV and posterior decay at higher energies clearly visible on observation day 1. Consequently, constraining the fitting range would have favoured the hadronic model. However, such change does not affect

Model	Parameter	Median	Median (IQR) on observation day	ion day
	'	Day 1	Day 2	Day 4
Leptonic BPL model without systematics	Slope 1, $\Gamma_{e,1}$	1.2 (3.5)	-0.2 (3.6)	-1.3 (0.9)
	Slope 2, $\Gamma_{e,2}$	-3.75 (0.08)	-3.4 (0.2)	-3.57 (0.07)
	$E_{b,e}$ [GeV]	12 (4)	11 (10)	24 (11)
Hadronic ECPL model without systematics	Slope, $\Gamma_{ m p}$	-2.252 (0.003)	-2.4934 (0.0014)	-2.476 (0.002)
	$E_{ m c,p}$ [TeV]	0.259 (0.002)	0.969 (0.008)	1.64 (0.02)
Leptonic BPL model with systematics	Slope 1, $\Gamma_{e,1}$	0.5 (1.8)	-1.4 (1.4)	-1.5 (0.8)
	Slope 2, $\Gamma_{e,2}$	-3.76 (0.15)	-3.6 (0.3)	-3.71 (0.13)
	$E_{b,e}$ [GeV]	13 (3)	18 (14)	29 (14)
	LST-1 syst.	-2 (8)	-7 (9)	-1 (8)
	MAGIC syst.	1 (9)	1 (10)	9 (8)
	H.E.S.S. syst.	4 (10)	-8 (11)	-12 (4)
Hadronic ECPL model with systematics	Slope, $\Gamma_{\rm p}$ $E_{\rm c.p}$ [TeV] LST-1 syst. MAGIC syst.	-2.18 (0.12) 0.22 (0.08) 4 (5) 0 (6) -1 (8)	-2.45 (0.07) 0.7 (0.2) -4 (9) 7 (7) -7 (8)	-2.40 (0.05) 1.0 (0.2) -3 (10) 10 (7) -10 (5)

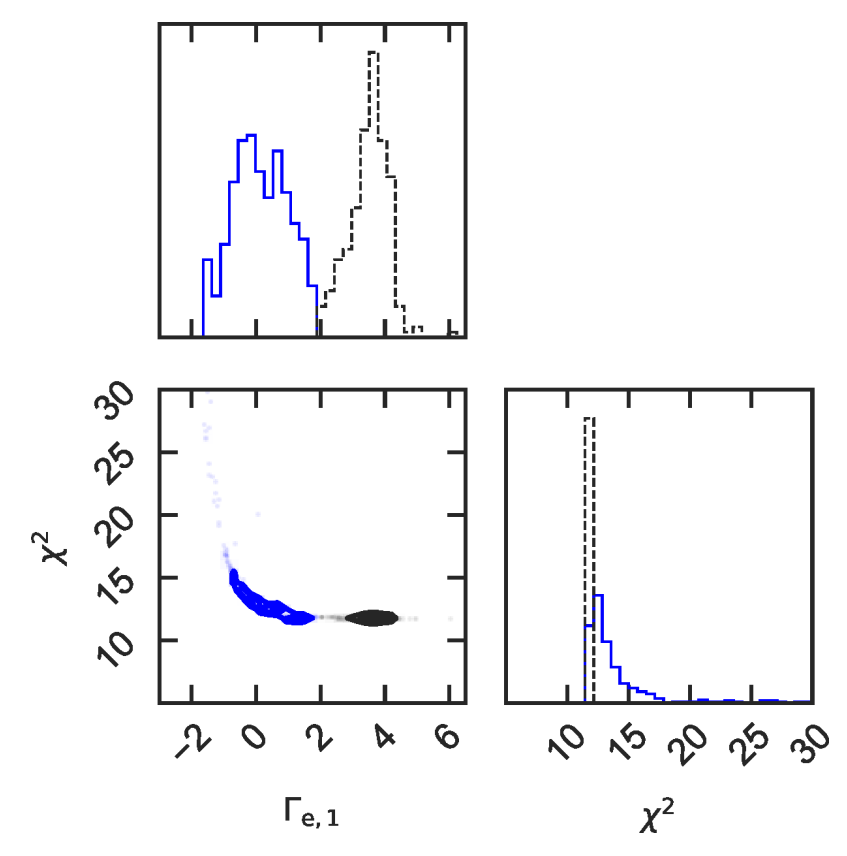


Figure 5.6: Corner plot of the best-fit $\Gamma_{e,1}$ for observation day 1 and the associated χ^2 fit value for different input values in the parameter space. The best-fit models used to provide the leptonic results without systematics in Table 5.4 are shown as solid blue lines, while the ones excluded are shown as dashed black lines (see text for details).

the fit results for observation days 2 and 4 because the emission with *Fermi*-LAT is dimmer and the curvature at HE gamma rays is less pronounced (p-value = 0.09 and 0.83 under the assumption of a flat HE emission for observation days 2 and 4, respectively). As a result, the best-fit leptonic model does not require a strong spectral slope break as in observation day 1 to provide a good fit. Both the leptonic and the hadronic models achieve comparable goodness of fit. In this regard, it is worth noting that a nova eruption with a brighter gamma-ray emission than RS Oph, e.g., T CrB, should help to constrain the population of relativistic particles responsible for the gamma-ray emission (see Sect. 5.8).

The model fit results in Table 5.4 correspond to the best-fit execution result that lies closest to the median of both the AIC distribution and the distributions of the particle spectrum parameters obtained through input value variations. If the energy-scale systematic distributions are considered, they are used as well. We report the uncertainties of the best-fit model parameters results as the quadratic sum of the parameter uncertainty of the fitting and the IQR of the output parameters for the different input value executions (see Tables 5.4 and 5.5).

Despite the scattered fit results for $\Gamma_{e,1}$, the slope above the energy break ($\Gamma_{e,2}$) is well constrained for all days thanks to the IACT spectral information at VHE gamma rays. The use of the LST-1 spectral information is relevant to constrain the

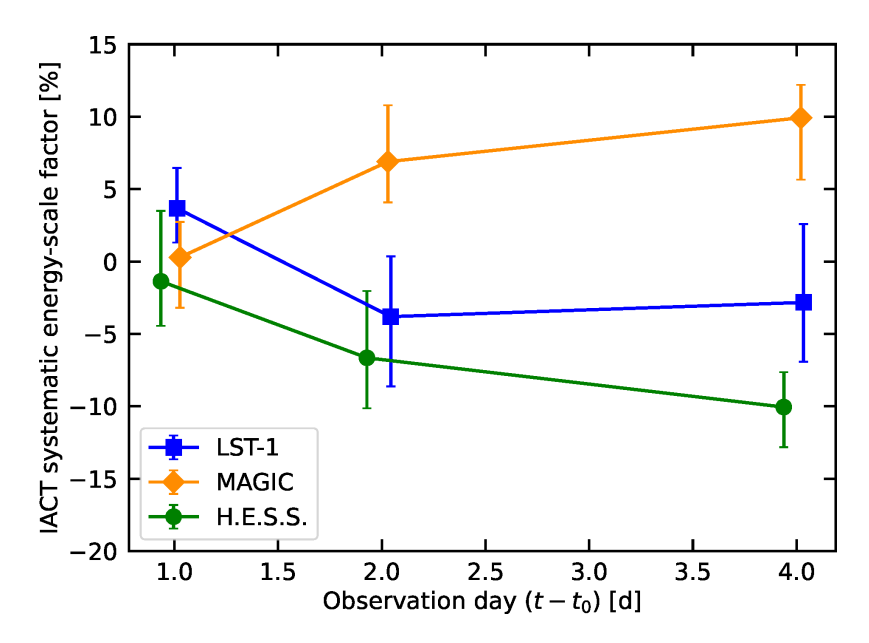


Figure 5.7: Derived systematic energy scaling factors for LST-1 (blue squares), MAGIC (orange diamonds) and H.E.S.S. (green circles) for the different observation-day intervals ($t-t_0\sim 1\,\mathrm{d}$, 2 d and 4 d). The IACT systematic energy-scale value corresponds to the median value of the IACT distribution obtained with the hadronic model when varying the input parameters. Error bars correspond to the IQR.

parameter space of solutions, which is narrower with the LST-1 data because of the smaller energy gap between *Fermi*-LAT and the IACTs data if the LST-1 SED points are considered.

When allowing for energy-scale systematics as nuisance parameters in the model fitting, the percentage of executions that converge drops to 79% and 81% for the leptonic and hadronic models, respectively, with respect to the modelling without energy-scale systematics. The output parameter distribution statistics for the modelling with systematics are shown in Table 5.8. One can notice that the parameter distribution IQRs are wider when systematics are considered than when they are not. The broader distributions are expected due to the degeneracy of adding extra parameters in the model fitting to allow shifts with respect to the original SED points. Moreover, IQR values are higher for the leptonic model than the hadronic model (expected due to the worse stability of the leptonic model than the hadronic one). The local minimum peaking at positive $\Gamma_{\rm e,1}$ values present in the leptonic modelling without systematics vanishes when systematics are considered (see Sect. 5.6). However, a long tail towards positive values remains.

The distributions of the best-fit IACTs energy-scale values for different input parameters form unimodal distributions. The spread of the distributions encompasses all the allowed values ($\pm 15\%$) for most of the cases. Interestingly, the sign and the time evolution of the peak of the derived systematic energy-scale factors for MAGIC and H.E.S.S. agree with the mismatch between the spectrum from MAGIC and H.E.S.S., and the fact that the VHE gamma-ray emission increases with time, making the difference more noticeable. Figure 5.7 shows the best-fit IACT systematic energy scaling factors obtained with the hadronic model for the different observation days. During observation days 1, 2 and 4, the best-daily-fit

systematic energy-scale values remain below 5% for LST-1, while the sequence of MAGIC and H.E.S.S. energy scaling factors start with a low-systematic value for observation day 1 and monotonically increase with time reaching an absolute systematic energy-scale value of about 10%. MAGIC systematic values remain positive for all the observation days, while H.E.S.S. ones are negative (see Fig. 5.7). As expected, no correlation between the best-fit IACT systematic uncertainties is observed.

The addition of systematic uncertainties in the energy scale causes the differential fluxes of the IACTs to shift accordingly in the SED, both in the x- and y-axis, with respect to the original ones when the systematic energy scaling factor is different from zero. The daily SEDs adopting the best-fit systematic energy-scale factors in the IACT SED data points are shown in Fig. 5.8. One can see that the differential fluxes at VHE gamma rays are concentrated in a band with less spread than the one displayed in Fig. 5.4 without systematic uncertainties taken into account. We note that the best-fit values of the IACT systematics in Fig. 5.8 are not the same as the centre values of the IACT systematics in Fig. 5.7 because the latter shows the median value and the IQR as error bars, while the former is the closest execution result with respect to both the median AIC and particle parameter distributions.

Although the hadronic model with systematics can account for the gamma-ray emission, due to rather large statistical uncertainties on the SED data points, taking into account systematic uncertainties as extra fitting parameters (three in this case) does not impact the fit statistics enough to obtain a better fit, given the reduction of degrees of freedom. Yet, systematics are foreseen to affect the SED data points. Moreover, it is worth noting that the same systematic energy-scale factor is assumed for the H.E.S.S. spectral information obtained with the array of four telescopes (CT1–4; stereo analysis) and the fifth telescope (CT5; monoscopic analysis) despite not following the exact same analysis. However, the fine agreement between both supports our simplification to reduce the number of parameters in the model fitting.

5.7 discussion

The results reported in Sect. 5.5 show that RS Oph was detected with LST-1 during several coincident days with *Fermi-*LAT, MAGIC, and H.E.S.S. In this section, we discuss the overall spectral and modelling fit results.

The data from *Fermi*-LAT, LST-1, MAGIC, and H.E.S.S. allowed us to study the emission from ~50 MeV up to TeV energies. This is the largest HE-VHE dataset compiled to date for RS Oph, for which a total exposure time of 6.35 h, 7.7 h, and 9.2 h (6.0 h) is considered for LST-1, MAGIC, and H.E.S.S. CT1–4 (CT5), respectively. While H.E.S.S. constrains the gamma-ray spectrum at about 1 TeV given its better sensitivity at these energies than that of MAGIC and LST-1, LST-1 bridges the HE and VHE gamma-ray emission and reduces the lower energy bound of the SED of IACTs to ~30 GeV. This value is lower by a factor ~2 than the MAGIC energy threshold (Acciari et al. 2022). However, the sensitivity of LST-1 is worse by a factor of ~1.5 than that of MAGIC above 100 GeV because of the advantages of the stereoscopic reconstruction mode in MAGIC (Abe et al. 2023b).

The model fitting with the Fermi-LAT, LST-1, MAGIC, and H.E.S.S. spectral information describes the spectrum of RS Oph during the first days after the

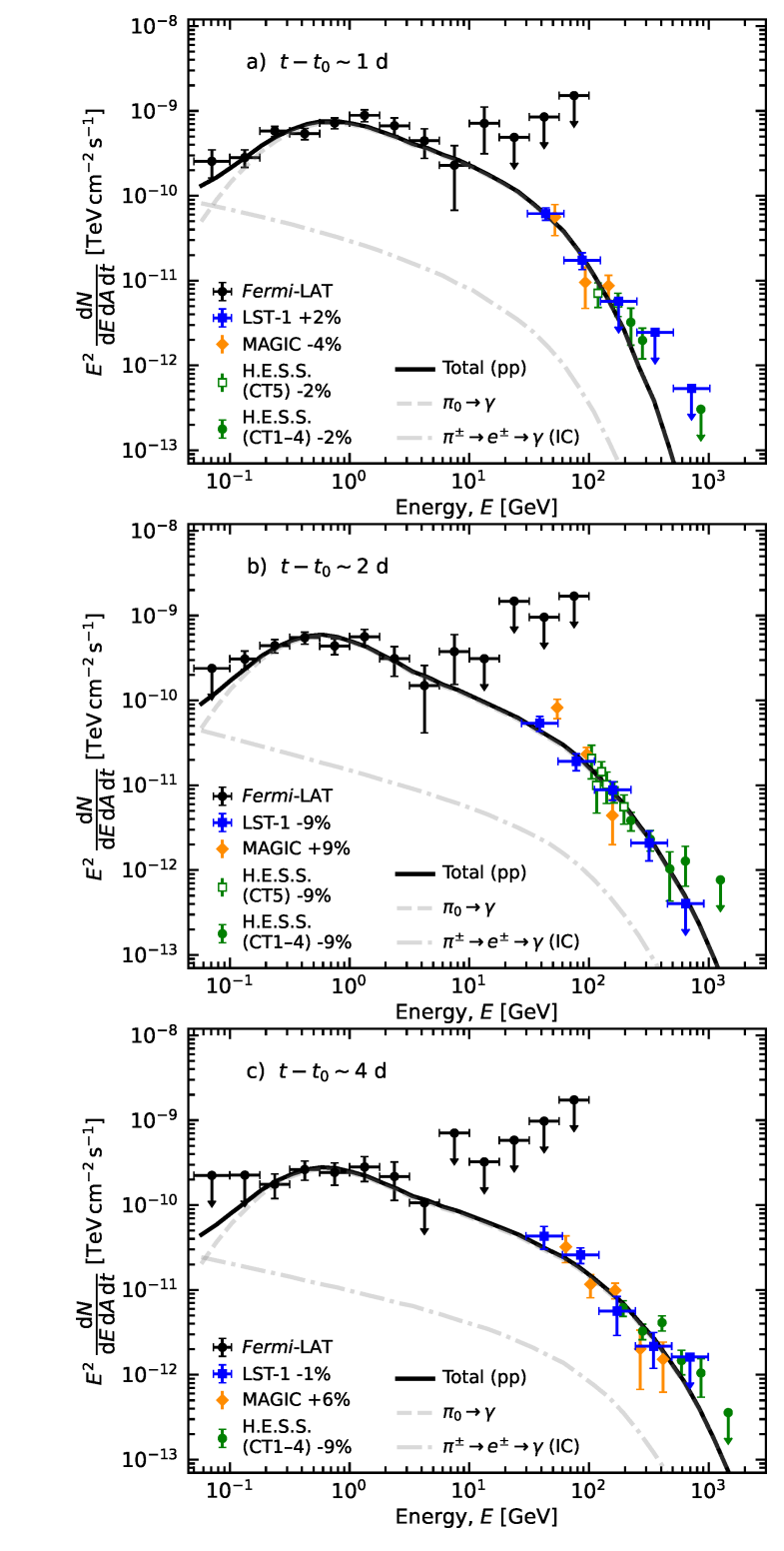


Figure 5.8: Same SEDs as Fig. 5.4 but with the IACT SED points scaled to account for the systematic energy scaling factors obtained for the best-fit hadronic model with systematics. The systematic value for each IACT is shown in the legend. In addition, the best-fit hadronic model considering energy-scale systematics is displayed as a black curve. The corresponding contributions from neutral and charged-pion decays are shown in grey.

eruption onset using a one-zone single-shock model. Although the hadronic model is slightly preferred statistically over the leptonic model by a combined *Fermi*-LAT and single IACT data fitting (Acciari et al. 2022), there is no clear preference, based on the fit statistics, between the hadronic and leptonic model using the spectral information from all instruments together.

The simplest ECPL model for the leptonic model cannot adequately describe the curvature of the gamma-ray spectral shape. We also considered the BPL energy distribution shape in the leptonic model to account for this curvature. This BPL model accounts for the presence of two distinct populations of relativistic electrons. Therefore, the curvature of the spectrum, which a single population of electrons has difficulties to reproduce through IC cooling, is caused in this case by the two populations of relativistic electrons. The leptonic scenario with a BPL model presents several difficulties with respect to the ECPL hadronic model, however. Firstly, our leptonic modelling presents multiple local minima that influence the fitting procedure through the relatively large number of free model parameters. The distribution of the best-fit slope values below the energy break ($\Gamma_{e,1}$) for observation day 1 is bimodal with two peaks, which complicates the estimation of the confidence interval of this parameter and the χ^2 statistics (see Sect. 5.6 for details). Secondly, the best-fit electron distributions have a difficult physical interpretation: they are characterised by a very different spectral slope below and above the energy break, as pointed out by Acciari et al. (2022). In particular, the slope break is more pronounced for $t - t_0 \sim 1$ d, when the emission at HE gamma-rays is bright and the curvature of the spectrum is significantly visible. A flat HE emission is rejected with a p-value of 7×10^{-5} using the Fermi-LAT SED points presented in this work. A very hard (positive or flat) $\Gamma_{e,1}$ index of the electron energy distribution suggests that the fit on the first day tries to imitate the injection of electrons with a high minimum energy (\sim 14 GeV). The injection of monoenergetic HE particles like these in novae was investigated (in the case of protons) by Bednarek and Śmiałkowski (2022). We note however that the spectrum below the break on observation day 4 is compatible within uncertainties with the classical -2 slope obtained in DSA for strong shocks (see Sect. 2.1; Drury 1983). There is no straightforward explanation for the need to inject a steep ~ -3.5 spectrum above the break, nor for the fact that the break energy is comparable (within uncertainties) to the injection energy from the first day of the nova. This picture of the required evolution of the electron energy distribution might be affected by partially cooled-down electrons that were injected at earlier phases. However, as showed by Acciari et al. (2022), the GeV electrons in RS Oph cool down on sub-day timescales. We therefore conclude that while it is possible to describe the gamma-ray observations of RS Oph with a leptonic model, the required injection electron energy distribution is not the one expected from DSA. This disfavours such a model, and we consider the hadronic scenario to be the most suitable mechanism for explaining the gamma-ray emission.

In the hadronic scenario, the average total power in protons across the first observation days ($t - t_0 \sim 1\,\text{d}$, 2 d and 4 d) is $4.3 \times 10^{43}\,\text{erg}$. For a kinetic energy of $2.0 \times 10^{44}\,\text{erg}$ (Acciari et al. 2022), this indicates that the conversion efficiency of the shock energy to proton energies is about 20%. This value is in line with the conversion efficiency estimated by Acciari et al. (2022) and above the lower limit estimated by H. E. S. S. Collaboration et al. (2022).

Systematic uncertainties in the energy scale were introduced in the model fitting to account for systematic errors in the IACT spectral results and reduce their impact on the estimated particle spectrum. However, the model with systematics is less favourable than the model without them, as the addition of three additional free parameters does not significantly improve the goodness of fit. Even though this does not imply that the dataset is free from systematic uncertainties, we chose to discard the model results that accounted for systematics as nuisance parameters. The consistent particle spectra between the hadronic models, both with and without systematics, suggest that the energy-scale uncertainties in the IACT data do not substantially affect the fit results. The primary limitations appear to originate from the small sample size and large flux uncertainties. Additionally, the limited information available from the public data points of MAGIC and H.E.S.S. complicates the application of more refined models that account for ULs, which could provide additional information. While alternative methods might address the systematics between IACTs, these are beyond the scope of this study. Although we discarded the results with systematics, it is worth noting that the sign and time evolution of the best-fit MAGIC and H.E.S.S. systematic energy scaling factors agree with the mismatch between the spectrum from MAGIC and H.E.S.S. and the fact that the gamma-ray emission at VHEs increases with time. This highlights the difference between the H.E.S.S. and MAGIC spectral fit results further (see Sect. 5.6).

We consider the best-fit proton spectrum and the subsequent gamma-ray emission from the hadronic modelling without systematics as the reference spectrum for RS Oph. The best-fit proton spectra indicate that protons increase the maximum energy that can reach, up to TeV energies, in agreement with the estimated maximum proton energy and the temporal evolution in the same time period in Cheung et al. (2022), Acciari et al. (2022), and H. E. S. S. Collaboration et al. (2022) via DSA. The evolution of the proton spectrum with time is interpreted as the finite acceleration time required for the protons in the expanding shock to accelerate from hundreds of GeV to TeV energies.

Other approaches were used to reproduce the spectral and temporal features observed in the RS Oph eruption: a multi-population particle scenario of electrons and protons (Acciari et al. 2022; Sarkar et al. 2023), or a multi-shock scenario approach (Diesing et al. 2023). In the former approach, the non-thermal radio detection at early times supports the presence of relativistic electrons that rise early during the eruption for both classical and embedded novae (e.g., Chomiuk et al. 2014; Finzell et al. 2018; Weston et al. 2016; O'Brien et al. 2006; Molina et al. 2024). In particular, non-thermal radio emission has been detected coincident with HE gamma rays in embedded novae (Linford et al. 2017; de Ruiter et al. 2023; Nyamai et al. 2023). For instance, synchrotron emission (see Sect. 2.2.1) was detected coincident in time with the gamma-ray emission in RS Oph (de Ruiter et al. 2023) and the gamma-ray nova candidate V1535 Sco (Linford et al. 2017; Franckowiak et al. 2018). However, the gamma-ray contribution from IC losses at early times is unclear. A detailed multi-frequency follow-up monitoring is required to obtain a precise spectrum to constrain the physics that cause the broad non-thermal emission. When the lepto-hadronic model in Acciari et al. (2022) was fitted with all available gamma-ray data, the HE component was described by IC, but with a hard spectral

index, and it was disfavoured with respect to the leptonic and the hadronic models by the fit statistics. This might imply that there are further components within the very early gamma-ray emission from recurrent nova. Constraining these possible additional components goes beyond the scope of this study, however, and requires early MWL observations of nova.

On the other hand, connected to the multi-shock scenario, the non-spherical ejecta observed in RS Oph and expected in embedded novae driven by the secondary star (Munari et al. 2022; Booth et al. 2016; Orlando et al. 2017; Islam et al. 2024), the multiple velocity components in the 2021 RS Oph nova (Diesing et al. 2023), and a possible localised shock-acceleration event (Cheung et al. 2022) support the idea of a system with multiple shocks that evolve during the eruption. However, a single hadronic population model with spherical symmetry can reproduce the observed spectrum and temporal evolution at HE and VHE gamma-ray energies with acceptable accuracy (see Table 5.4). Furthermore, the temporal evolution of the proton energy distribution seems reasonably explained by the finite acceleration time for particles to reach TeV energies. To shed light on this matter, the observation of future bright novae with detectors with better sensitivities and deeper monitoring campaigns could help to distinguish between the acceleration mechanisms and the contribution of non-thermal emission from a multiple particle population scenario (single or multiple shocks in a hadronic or lepton-hadronic scenario).

5.8 STUDYING NOVAE WITH LSTS AND CTAO

In this section, we study the prospects of detecting further novae using LST-1, the upcoming LST array of CTAO-N, and the full CTAO. A parametric study based on phenomenological parameters involved in the emission of gamma rays in nova eruptions is performed to estimate the capability to constrain these parameters with CTAO observations. We also consider dedicated numerical simulations of RS Oph to assess the expected detectability with CTAO.

5.8.1 *Perspectives with the LST array*

The source RS Oph belongs to a specific nova class in which a binary system with a giant donor companion star undergoes recurrent eruptions. This class contains a few members: T CrB, V3890 Sgr, V745 Sco, and RS Oph (Bode and Evans 2012). T CrB is the closest system to Earth from this class (~ 0.9 kpc; Gaia Collaboration et al. 2023), followed by RS Oph. T CrB is expected to erupt again in the mid-2020s (Schaefer 2023; Schaefer et al. 2023; Luna et al. 2020). If we assume that T CrB will manifest the same spectral profile as RS Oph, T CrB will likely present a brighter flux than RS Oph by a factor of ~7, making T CrB one of the brightest novae at gamma rays up to date. In Fig. 5.9, the best-fit SED models of seven embedded (V407 Cyg, T CrB, and RS Oph) and classical (V906 Car, V959 Mon, V1324 Sco, and V339 Del) novae detected at HE gamma rays are displayed together with the tentative gamma-ray SED from T CrB based on the RS Oph spectral shape on day 1, with the flux amplitude scaled to account for the difference in distance between the two systems. The observed SED for the different novae is diverse, possibly due to their intrinsic nature and/or distance. Moreover, the observed SED

models were estimated considering different observation time spans depending on the duration of the gamma-ray detection^{††}. Between 17 and 27 days of data were used to produce the gamma-ray spectral models in Fig. 5.9 (except RS Oph; Aydi et al. 2020; Ackermann et al. 2014). Hence, the displayed gamma-ray spectrum cannot accurately describe the maximum flux level or any spectral variability during the nova events. In addition, the gamma-ray flux for the *Fermi-LAT* novae was extrapolated to the CTAO energy range assuming the best-fit spectral shape reported with *Fermi-LAT*, consisting of an ECPL for the first novae detected with *Fermi-LAT*. In contrast, a log-parabola model was considered for V906 Car, which resembles the RS Oph spectral shape, but has a lower flux. The expected bright gamma-ray flux of T CrB should help to constrain the parameters of the particle population that causes the gamma-ray emission in novae.

It is still an open question whether classical novae can emit VHE gamma rays or if a bright VHE gamma-ray emission requires a similar binary system configuration as in RS Oph, that is, a recurrent nova embedded in the red giant star envelope. Related to the former, the brightest classical nova detected at HE gamma rays so far is V906 Car (Aydi et al. 2020). Its best-fit SED model is displayed in Fig. 5.9 together with the detection sensitivity curves for LST-1 and the array of four LSTs of CTAO-N for an integration time of 5h and 50h. The standard definition of sensitivity at VHE gamma-rays is used (see Sect. 4.1.6.3). Note that the sensitivity curves for LST-1 correspond to the average performance at $ZA < 35^{\circ}$ (Abe et al. 2023b), while the LST array sensitivity curves are computed at $ZA = 20^{\circ \ddagger}$. Different novae will be observed with LSTs and will culminate at different ZA. Hence, some of them may not be observable at this low ZA, implying that the sensitivity at low energies that can be achieved in these observations will degrade. When we compare the sensitivity curves for one and four LSTs, the latter outperforms the former by an order of magnitude at energies below 100 GeV. This improvement is due to the larger collection area and improved background rejection by the stereotrigger method. Figure 5.9 shows that the V906 Car SED model remains below the sensitivity curve of LST-1 even for 50 hours of integrated time. Nonetheless, when the CTAO will be operational and the four LSTs dominate the sensitivity of CTAO in the low-energy range, the possibility of detecting fainter novae than RS Oph will grow. The LST array sensitivity for 50 h reaches a flux level similar to the model emission of V906 Car at tens of GeV. This observation time can be challenging to achieve in fast eruptions, but a detection with a shorter integration time may be possible for closer novae than V906 Car. Furthermore, since the nova SED models in Fig. 5.9 are time averaged (except RS Oph), the nova spectral models underestimate the emission level in the peak of the gamma-ray phase, when a detection is most probable.

We note, however, that the emission models in Fig. 5.9 highly depend on the assumption that the observed spectral shape at HE gamma rays is constrained enough and can be extrapolated to the VHE gamma-ray band. At HE gamma rays, the spectral curvature for most novae is better described by an ECPL shape with cutoff photon energies at a few GeV (e.g. Ackermann et al. 2014; Cheung et al.

⁺⁺V906 Car SED model does not satisfy this criterion because *Fermi*-LAT observations were restricted due to solar panel issues.

[#]Specifically, the IRFs at 20° in zenith and with an average azimuth.

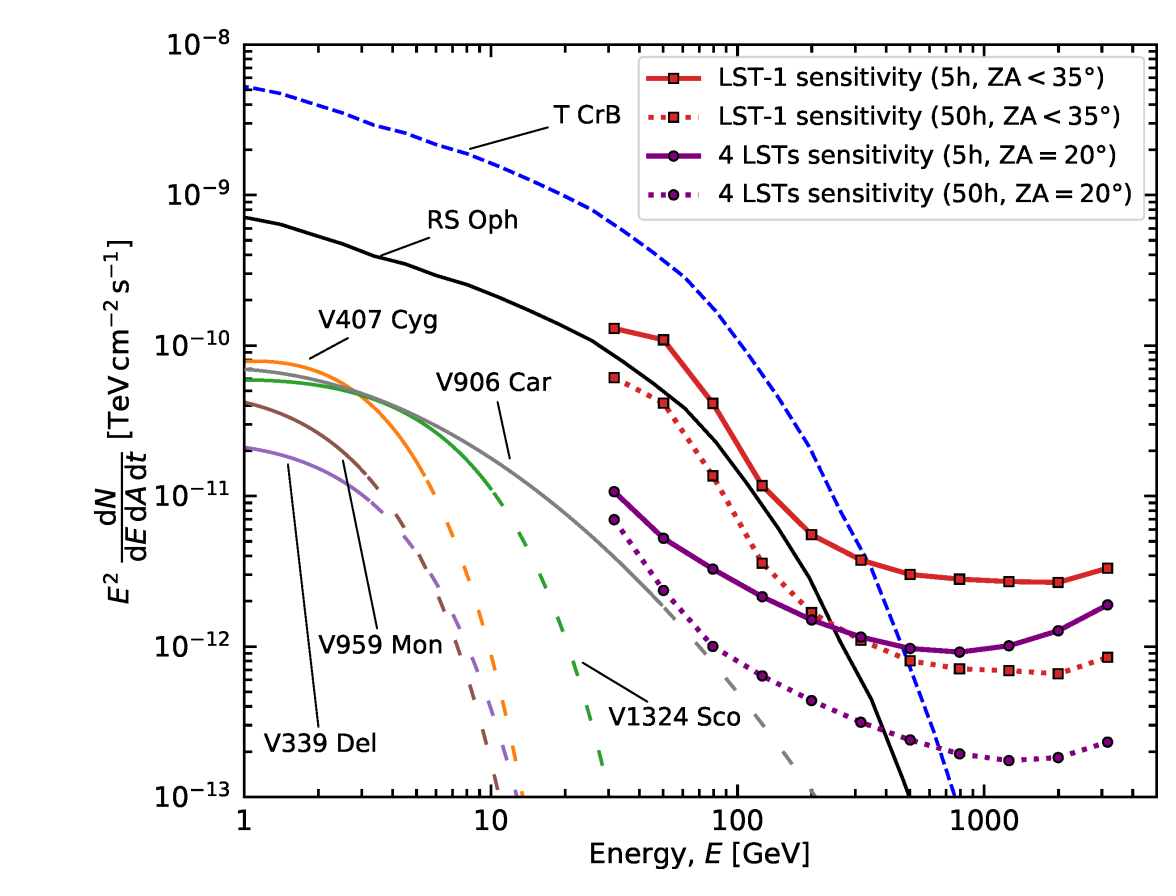


Figure 5.9: Best-fit SED models for RS Oph (black; this work, $t-t_0\sim 1\,\mathrm{d}$), V906 Car (grey; Aydi et al. 2020), the first novae detected with *Fermi*-LAT (V407 Cyg, orange; V1324 Sco, green; V959 Mon, brown; V339 Del, violet; Ackermann et al. 2014), and the expected SED from T CrB (blue). The solid region of the nova SEDs corresponds to the energy range where the model was fitted to the data, while the spaced-dashed region corresponds to the extrapolation region of the model. In addition, the sensitivity curves for LST-1 at low zenith angles (ZA < 35°; red square curves; Abe et al. 2023b) and the four LSTs of CTAO-N at ZA = 20° (purple circle curves; using the latest prod5-v0.1 IRFs in Cherenkov Telescope Array Observatory and Cherenkov Telescope Array Consortium 2021) for 5 and 50 hours of observation time are displayed as solid and dotted curves, respectively.

2016). Nevertheless, the emission of RS Oph and V906 Car, the brightest embedded and classical novae, are better explained by a log-parabola shape (Acciari et al. 2022; H. E. S. S. Collaboration et al. 2022; Aydi et al. 2020). Acciari et al. (2022) suggested that the spectral shape of RS Oph is not different from other novae, but its bright emission is the cause of the VHE gamma-ray detection. The expected TeV emission in the case of V407 Cyg and V339 Del for an RS Oph-like spectrum would be below the reported UL constraints (Acciari et al. 2022). Under this assumption, the extrapolated emission for the ECPL model for HE novae will underestimate the emission of an RS-Oph-like shape at VHE gamma rays.

Moreover, the VHE emission will depend on the properties of the system and the ejecta if the observed cutoff energy in the photon spectrum of all novae originates from the balance between acceleration and cooling processes. In this regard, Abe

et al. (2025b) explored the capabilities of CTAO to constrain the physical parameters of novae from a modelling approach, assuming that the VHE gamma rays are produced through hadronic interactions. The novae detectability and extension in time would depend on the shock velocity and the total mass contained in the ejecta. These constraints on the VHE emission, together with detailed MWL contemporaneous observations, will be relevant for constraining the physical parameters of the nova phenomena and for determining whether the physical differences in embedded and classical nova systems also reflect in their gamma-ray emission.

5.8.2 Constraining physical parameters with CTAO

We utilised a phenomenological approach to study the parameter space of gammaray emission from novae with CTAO. The emission was assumed to be produced by hadronic processes from π^0 decay (see Sect. 2.2.4; Kafexhiu et al. 2014), as indicated by the gamma-ray emission in RS Oph (see Sect. 5.7). The π^0 decay radiative model was parametrised using the target proton density (n_h) and the relativistic proton energy distribution. For the latter, we considered a particle distribution function parametrised as an ECPL. We described the parameter space under study as a 3D space, where we set the parameter space domain in the range of plausible values based on observed novae at gamma rays. A 2D grid was defined with different values for the prefactor (A) and the cutoff energy (E_{cp}) of the proton energy distribution, the former in the range between $A = [10^{28}, 10^{32}]$ protons eV⁻¹ at a pivot energy of 100 GeV and the latter in the range between $E_{cp} = [10, 1000]$ GeV. Two values for the target proton density were used for the third axis, $n_h = 10^8 \, \text{cm}^{-3}$ and $n_h = 10^{11} \,\mathrm{cm}^{-3}$, which correspond to typical shock density values in novae (Metzger et al. 2016). The distance to the gamma-ray emitter was fixed to $d = 2 \,\mathrm{kpc}$. The spectral energy distribution for each model was obtained using the software package Naima (Zabalza 2015).

The emission detectability was assessed for both arrays of CTAO using the official IRFs from prod5-v0.1 in the Alpha configuration (20deg-AverageAz for 5 h observation time). The results of the simulations for CTAO-N and CTAO-S are shown in *panels a* and *b* of Fig. 5.10, respectively. The total proton energy above 100 GeV (W_p) multiplied by $\frac{n_b}{d^2}$, hereafter the "effective proton energy reservoir", was used as a function of E_{cp} to display the ratio between the integral source flux and the CTAO sensitivity. This ratio was computed to obtain a qualitative estimation of the novae detection capabilities of CTAO for each model in the parameter space. The higher the integral flux-to-CTAO-sensitivity ratio, the more feasible the detection. Moreover, the region where we would detect each model with CTAO in at least one energy bin is lower-delimited in Fig. 5.10 by a dashed orange line to have a more precise boundary of the detection region. Therefore, the region between the dashed orange line and the white region (integral flux-to-CTAO-sensitivity close to 0) delimits the border of the parameter space where CTAO will likely begin to detect the gamma-ray emission with the assumed spectral models. Qualitatively, RS Oph would be located approximately in the top right corner of Fig. 5.10, while

^{\$\$}The prefactor is the amplitude of the model at a given reference energy. Its units in Naima are particles eV^{-1} .

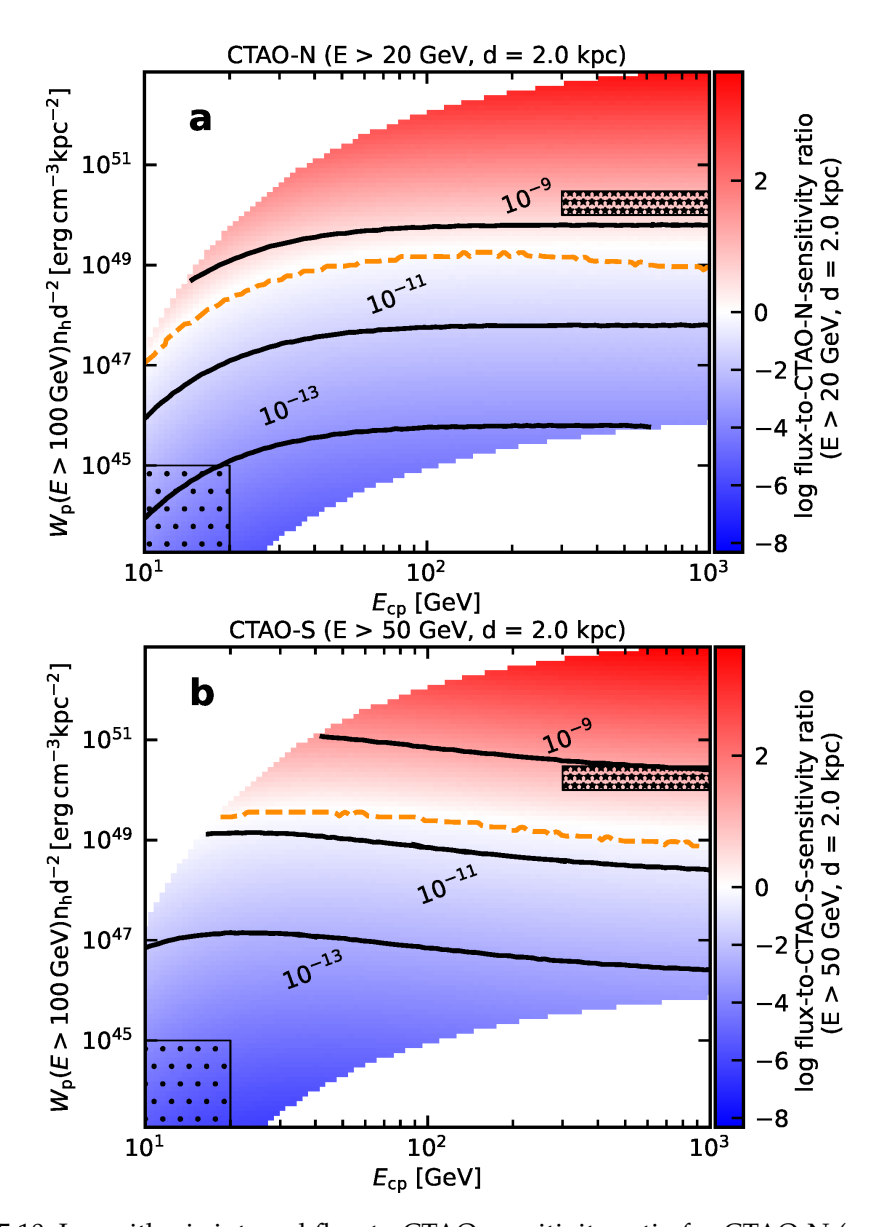


Figure 5.10: Logarithmic integral flux-to-CTAO-sensitivity ratio for CTAO-N (panel a), integrated above 20 GeV and CTAO-S (panel b), integrated above 50 GeV for different values in the defined parameter space (see text for details) of $n_{\rm h}$, cutoff energy ($E_{\rm cp}$) and prefactor (A) of the proton energy distribution function at a fixed distance of $d=2.0\,{\rm kpc}$. The sensitivity was computed for a total observation time of 5 hours. The orange dashed line indicates the domain in the parameter space with detection in at least one energy bin for different values of $n_{\rm h}$, $E_{\rm cp}$ and A. Solid black lines are curves at constant integrated flux (10^{-13} , 10^{-11} and $10^{-9}\,{\rm cm}^{-2}{\rm s}^{-1}$) above 20 GeV and 50 GeV for CTAO-N and CTAO-S panels, respectively. The regions where V959 Mon and RS Oph would be approximately located in the parameter space are marked with black dots and stars, respectively.

V959 Mon (the first classical nova discovered by *Fermi*-LAT; Ackermann et al. 2014) would be in the lower left region in these panels.

The integral gamma-ray emission and the integral flux-to-CTAO-sensitivity ratio in Fig. 5.10 increases as the effective proton energy reservoir and E_{cp} increase. Both top regions of panels a and b in Fig. 5.10 have positive values of integral flux-to-CTAO-sensitivity ratio (about 30% of the total combinations), while the bottom region have negative values (about 70% of the total combinations). When comparing the results between CTAO-N and CTAO-S, the former extends the parameter space region with positive integral flux-to-CTAO-sensitivity towards models with E_{cp} < 250 GeV. On the other hand, the latter presents a wider detection region for $E_{cp} > 250 \,\text{GeV}$ than CTAO-N. CTAO-N overperforms CTAO-S with about 10% more detections. The better performance of CTAO-N at low energies is expected because the parameter space under study was restricted to produce most of the gamma-ray emission below 1 TeV, as it is observed from current novae detected at gamma rays. Therefore, the lack of LSTs, which dominates the CTAO sensitivity at these energies (Cherenkov Telescope Array Consortium et al. 2019), in the Southern array (Alpha configuration) will reduce the parameter space of detectability with CTAO-S.

5.8.3 Simulations of RS Oph with CTAO

It is expected that RS Oph will undergo another eruption when CTAO will be in operation. Hence, we carried out numerical simulations of RS Oph to estimate its detectability with CTAO along the temporal evolution of the eruption.

We performed the numerical simulations of RS Oph with CTAO using the official IRFs from prod5-v0.1 for the CTAO northern and southern arrays. The closest IRFs set to the culmination of RS Oph in the CTAO-N and CTAO-S site were used (North-40deg-SouthAz, South-20deg-NorthAz) for 0.5 h observation time. A total of 59 daily observations of 1 hour each were simulated starting one day after the beginning of the nova eruption (batches of 100 simulations per day). We simulated this source based on the gamma-ray spectral and temporal profile reported by the MAGIC and H.E.S.S. Collaborations, respectively. The best daily-fit spectral logparabola models from Acciari et al. (2022) were considered to model the gamma-ray emission. Spectral variations were only contemplated for the simulations of the first four days, when spectral information in Acciari et al. (2022) was available during the eruption. The spectral parameter values utilised in the different log-parabola models are shown in Table 5.9. After the fourth day, the spectral profile was fixed to that of the last day with available spectral data, and the simulated gamma-ray emission was scaled to follow the power-law temporal decay reported by H.E.S.S. We set the index value of the power-law decay to 1.4.

The statistical detection significance as a function of time is shown in Fig. 5.11. The results confirm that RS Oph would be clearly detected with CTAO-N and CTAO-S for the first days, reaching a detection significance of about 60σ and 30σ in an hour with CTAO-N and CTAO-S, respectively. RS Oph is not only detectable with CTAO during the first days after the eruption, but CTAO would also daily detect RS Oph up to 20 and 15 days after the eruption with the northern and southern arrays, respectively. If we consider the combined data of 5 and 10 adjacent days with CTAO-N, the detection would be possible even up to 36–40 and 46–55

Table 5.9: Daily parameter values of the log-parabola spectral models used to simulate RS Oph. Adapted from Acciari et al. (2022).

Model day	Prefactor at 130 GeV $[10^{-10} \text{TeV}^{-1} \text{cm}^{-2} \text{s}^{-1}]$	α	β
Day 1	5.40	3.86	0.194
Day 2	4.54	3.73	0.175
Day 3	5.37	3.64	0.173
Day 4 – 59	5.00	3.44	0.147

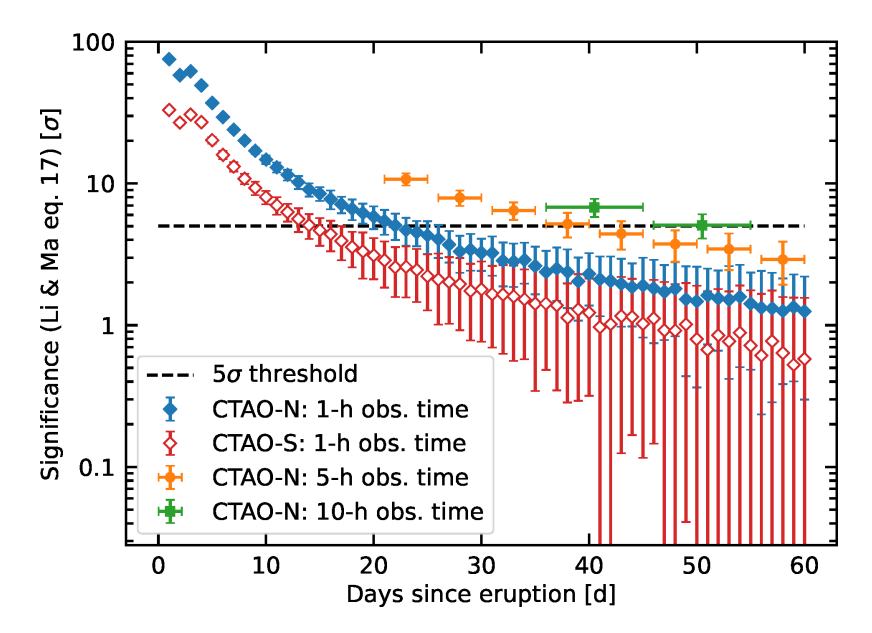


Figure 5.11: Daily statistical detection significance (equation 17 of Li and Ma 1983) from 1-hour simulated observation with CTAO-N and CTAO-S (blue filled diamonds and red empty diamonds, respectively) as a function of the number of days since the eruption of RS Oph. The 5-day (i.e. 5 h of total observation time, filled orange circles) and 10-day (i.e. 10 h of total observation time, filled green squares) combined significance for CTAO-N are computed when the daily and 5-day statistical detection significance are below a 5σ detection (dashed black line), respectively. Error bars correspond to the standard deviation of the statistical detection significance distribution for the 100 simulations per day.

days, respectively. The 5σ detection would be limited down to 23–27 and 38–47 days with CTAO-S.

The resulting SED for the first simulated observation (day 1 after the eruption) is shown in Fig. 5.12 together with the observed spectrum obtained with MAGIC for the same observation time. The results suggest that CTAO will be able to probe the gamma-ray emission for several weeks after the eruption with a precise spectral coverage at least during the first days. Using 1-h observation, CTAO would be able to characterise the curvature of the VHE gamma-ray emission of RS Oph (e.g. in the case of the simulated observation of day 1, a log-parabola spectral model is preferred over a power-law model at a 3.7σ level).

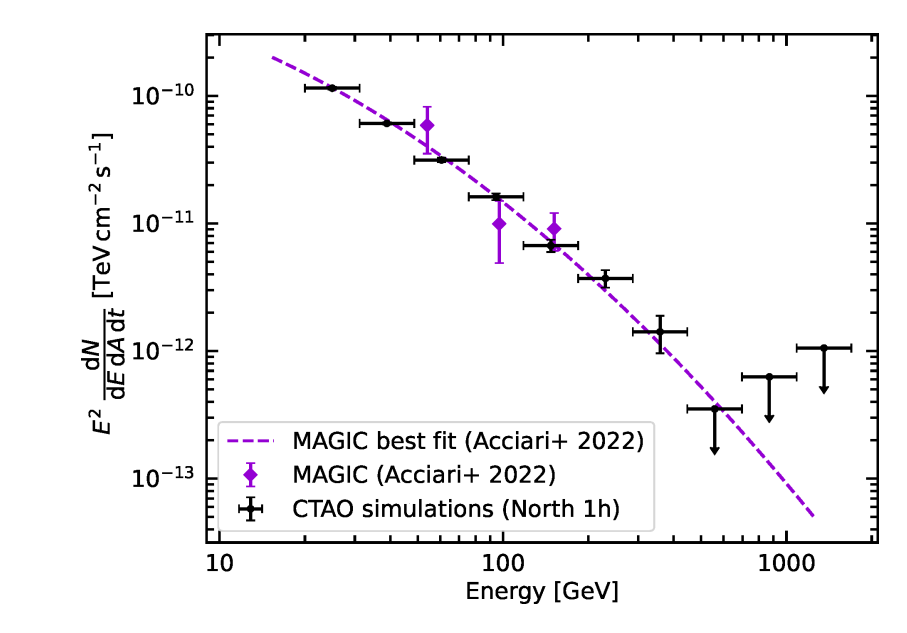


Figure 5.12: VHE gamma-ray SED of RS Oph after 1 day since the eruption. The best-fit model from Acciari et al. (2022) using MAGIC and *Fermi-LAT* for the first night of observation is used (violet dashed line) to simulate the source with CTAO. The CTAO-N flux points for a 1-h observation time are shown as black points. The MAGIC flux points (computed using 1-h observation time of data after cuts) from Acciari et al. (2022) are also displayed (violet points).

5.9 CONCLUSIONS

The source RS Oph is the first nova that was detected at VHE gamma rays and the first transient source that was detected with the first LST of the future CTAO. During the first observation days after the eruption ($t - t_0 \sim 1\,\mathrm{d}$, 2 d, and 4 d), RS Oph was statistically detected at 6.6σ with LST-1 and was characterised by a soft power-law emission at energies $E = [0.03, 1]\,\mathrm{TeV}$. LST-1 spectral results are consistent with the emission reported with MAGIC and H.E.S.S. in coincident observation-day intervals with LST-1. We did not detect RS Oph with LST-1 after 21 days after the eruption onset.

We obtained the particle energy spectrum during the LST-1 observations immediately after the eruption onset by using the most complete gamma-ray spectrum to date, including *Fermi*-LAT, LST-1, H.E.S.S., and MAGIC spectral information. The simpler spectral shape of the hadronic model supports the hadronic over the leptonic scenario to explain the RS Oph gamma-ray emission, although the relative likelihood of the two models is comparable. The proton energy spectrum evolves with time, increasing the maximum energy of the accelerated protons from hundreds of GeV up to TeV energies between observation-day intervals 1 and 4 after the eruption. The results were validated with a set of robustness tests.

In the following years, other novae can be expected to be detectable by IACTs. The next eruption of T CrB is foreseen to occur in mid-2020a and likely become a bright nova at gamma-ray energies. An event like this is expected to give outstanding constraints in the evolution of gamma-ray emission during the eruption phase and on the maximum energy attainable by the accelerated particles in embedded novae. In the near future, the better sensitivity of the LST array with respect to

current facilities at low energies will allow us to probe fainter gamma-ray fluxes. A better sensitivity may enable the detection of classical novae, a nova type yet to be detected at VHE gamma rays.

Once the full CTAO array is operational, CTAO is expected to give strong constraints only to a sub-space of the whole parameter space under study. About 30% of the area of the parameter space covered in Fig. 5.10 could be likely detected with CTAO, particularly in the case that the relativistic protons have a high value of prefactor and cutoff energy. Assuming that the target proton number density is the number density of the main ejection of matter in the eruption, the results suggest that for denser ejecta, the detection region with CTAO will cover a relatively wider range of parameter values of the relativistic proton energy distribution. CTAO-N should outperform CTAO-S for novae with $E_{\rm cp} < 250\,{\rm GeV}$, while for $E_{\rm cp} > 250\,{\rm GeV}$, CTAO-S should perform better than CTAO-N as expected given the different instrument set ups composing the two observatories.

If one assumes that the next RS Oph eruption follows the same behaviour as the 2021 eruption, a plausible assumption based on the similarities observed at radio, optical and X-ray for the first weeks between 2006 and 2021 eruptions (Munari et al. 2022; Acciari et al. 2022; Page et al. 2022), CTAO observations can provide a deep coverage of the gamma-ray emission with unprecedented detail, allowing to probe the maximum energy of the accelerated particles and the nova physical conditions across different eruption stages.

6

CORE-COLLAPSE SUPERNOVAE

Overview

This chapter contains the results of the analysis of data taken on two core-collapse supernovae (CCSNe) observed with LST-1, SN 2023ixf and SN 2024bch. The work related to SN 2023ixf corresponds to a paper in preparation, while the study of SN 2024bch with LST-1 has been submitted for publication to Astronomy and Astrophysics.

6.1 INTRODUCTION

A core-collapse SN (CCSN) event marks the explosive end of the evolution of a massive star ($M \ge 8 M_{\odot}$; Woosley et al. 2002; Smartt 2009). CCSNe are some of the most energetic events in the Universe (total released energy $\sim 10^{53}$ erg; Heger et al. 2003). The SN explosion occurs when the collapse of the star is stopped by the formation of a proto-neutron star. This event creates a shock wave (core bounce) that propagates through the infalling outer part of the core material. The shock wave is further energized with neutrino capture and magnetic fields and powers the ejection of the outer layers of the star. The result of this explosive phenomenon is a bright MWL transient event (Bethe 1990; Woosley and Bloom 2006; Gal-Yam 2017; Jerkstrand et al. 2025).

SNe with hydrogen-rich spectra are classified as Type II SN and represent the most common SN type (Shivvers et al. 2017). In contrast, SN lacking hydrogen lines are classified as Type I, which can be produced from core-collapse or thermonuclear explosions (Type Ia SNe). CCSNe without silicon absorption lines are divided into Type Ib and Ic, which either lack hydrogen lines or hydrogen and helium features in their spectra, respectively. The spectral differences among Type II, Ib and Ic SNe are attributed to the loss of the external layers of the progenitor star. Type Ib SNe have lost most of their hydrogen-rich envelope, whereas Type Ic SNe have additionally lost most of their helium-rich layers. This envelope removal is interpreted as the result of stellar-wind mass losses or binary interaction (Woosley et al. 1993; Podsiadlowski 1992). If the hydrogen layers of the progenitor star are not fully stripped, early-time hydrogen lines can be detected that subsequently disappear. This in-between group of SNe is classified as Type IIb.

The progenitor stars of Type II are typically associated with red supergiants with masses between $\sim 8-18\,M_\odot$ at zero-age main sequence (Smartt et al. 2009). These stars are characterised by wind velocities of $10-30\,\mathrm{km\,s^{-1}}$ and mass-loss rates of about $10^{-6}\,M_\odot\,\mathrm{yr^{-1}}$ (van Loon et al. 2005; Mauron and Josselin 2011). Additionally, unstable massive stars known as luminous blue variables may produce giant eruptions and explode as SNe (Smith 2017; Weis and Bomans 2020). Enhanced mass-loss rate ($\dot{M} \sim [10^{-5}, 10^{-3}]\,M_\odot\,\mathrm{yr^{-1}}$) expanding at a few hundred km yr⁻¹ is observed in these unstable stars that may additionally undergo giant eruptions with further mass-loss rate that can even mimic SN explosions (Humphreys and Davidson 1994; Smith 2017). Wolf-Rayet (WR) stars may additionally be progenitors

of a fraction of the hydrogen-poor SNe (Filippenko 1997). However, their population may not produce most of these hydrogen-poor SNe (Eldridge et al. 2013; Lyman et al. 2016). WR stars undergo large mass-loss rates of $\dot{M} \approx [10^{-6}, 10^{-4}] \, M_{\odot} \, \mathrm{yr}^{-1}$ with winds of thousands of km yr⁻¹ (Nugis and Lamers 2000; Niedzielski and Skorzynski 2002).

The mass-loss history of the progenitor star is tightly bound to its end and is key for determining its SN type (Smith 2014; Renzo et al. 2017; Modjaz et al. 2019). In general, the more massive the star, the higher the rate of mass loss through powerful winds (Humphreys and Davidson 1994; Nugis and Lamers 2000). In addition, binary interaction and eruptive events can further enhance the mass-loss rate (Podsiadlowski 1992; Fuller 2017; Ofek et al. 2013a). The expelled material remains in the progenitor star circumstellar medium (CSM). If the mass loss rate is abundant close in time to the SN explosion (from days to hundreds of years), spectral features related to the ejecta-CSM interaction arise (e.g. Strotjohann et al. 2021; Pastorello et al. 2007; Smith et al. 2008). SNe displaying ejecta-CSM interaction signatures are classified with an "n", e.g., Type IIn SN, as they exhibit narrow emission lines with broad wings over a blue continuum (Schlegel 1990; Chugai 2001). Such lines are believed to arise from the photo-ionisation of the un-shocked CSM and its interaction with the ejecta (Chugai 1991; Chugai and Danziger 1994). Additionally, CSM properties can be probed with X-ray and radio observations (e.g. Ofek et al. 2013b; Chevalier 1998; Berger et al. 2023). Notably, ejecta-CSM features have been observed in all CCSN spectral-based groups, i.e., Type IIn, Ibn, and Icn SN (see review in Fuller 2017). Most Type IIn SNe are associated with luminous blue variable progenitors (e.g. Gal-Yam and Leonard 2009).

Early-time spectroscopic observations (known as "flash" or rapid spectroscopic observations) revealed that SNe commonly present narrow lines associated with the flash ionisation of the CSM material after the shock breakout (Khazov et al. 2016; Waxman and Katz 2017; Bostroem et al. 2024; Bruch et al. 2023; Hinds et al. 2025). These narrow lines are called "flash ionisation" lines and give information on the mass-loss rate in the last stages of the progenitor star before the explosion and the mass, composition and extension of the near surrounding CSM (Svirski et al. 2012; Gal-Yam et al. 2014; Yaron et al. 2017). Typically, flash ionisation lines disappear within days after the explosion ($t \leq 10\,\mathrm{d}$; Khazov et al. 2016). Persistent narrow emission lines from ejecta-CSM interaction are characteristic of Type I/IIn SNe (e.g. Stathakis and Sadler 1991; Tartaglia et al. 2020).

The light curves of CCSNe are diverse because of the intrinsic differences in evolution and mass loss history among progenitor stars, CSM properties, and explosion parameters (e.g. Modjaz et al. 2019). Depending on the observed optical light curve decay rate, Type II SN can be further classified into Type II-L and II-P SNe. The former SNe present a fast *linear* decay after the luminosity peak, while Type II-P SNe have a distinct *plateau* phase (Barbon et al. 1979). These differences are linked to the recombination of the hydrogen envelope (Woosley et al. 1987). Since the amount of hydrogen is reduced, the plateau phase of Type II-P reduces until it is less pronounced or absent, which is the case of Type II-L (e.g. Anderson et al. 2014; Gutiérrez et al. 2017).

Ejecta-CSM interactions do not appear to be a phenomenon limited to specific SNe. Instead, they seem to be widespread across a variety of progenitor masses and

all types of SNe (Fraser 2020). Interacting SN exhibit vastly diverse observational light-curve features. For instance, some SNe present a brighter luminosity peak that takes longer to reach than in non-interacting SN, a behaviour associated with a massive progenitor star and CSM. In contrast, narrow emission lines have also been detected in rather faint SNe with erratic light curves. Moreover, ejecta-CSM interaction features are present in SNe with similar declines to Type II-L- and Type II-P-like non-interacting SNe (Nyholm et al. 2020).

In recent years, it has been proposed that at least some CCSNe can be TeV–PeV particle accelerators, contributing to the bulge of CRs through particle acceleration in the collision between the SN blastwave and the dense CSM (Tatischeff 2009; Murase et al. 2011; Bell et al. 2013). In such environments, proton-proton interactions are expected to occur, and subsequent HE and VHE gamma rays can be produced (see Sect. 2.2.4; Cristofari et al. 2022; Brose et al. 2022). Models suggest that SNe surrounded by an enhanced CSM are the best candidates for efficient proton acceleration and subsequent VHE gamma-ray emission. For instance, luminous blue variable and red supergiant (RSG) progenitor stars present high mass-loss rate and wind densities, which create favourable conditions for particle acceleration and subsequent non-thermal emission.

When the CCSN occurs embedded in the CSM, it generates a fast-moving forward shock that propagates outward and interacts with the nearby CSM and a reverse shock that interacts with the ejecta. Since the density of the CSM decreases with distance, we expect the highest gamma-ray luminosities to be reached shortly after the eruption (Tatischeff 2009; Brose et al. 2022). However, strong VHE gamma-ray attenuation can occur over the first few days due to the interaction of the putative gamma rays and the low-energy photons from the SN photosphere (see Sect. 2.3.1; Cristofari et al. 2022).

By the time this Thesis is written, no firm detection of HE or VHE gamma-ray emission from SNe has been achieved (see review by Carosi and López-Oramas 2024). At HE gamma rays, several source candidates have been claimed to be associated with SNe, including the Type II-P SN 2004dj (Xi et al. 2020), the superluminous hydrogen-poor SN 2017egm (Li et al. 2024), the peculiar luminous Type II iPTF14hls (Yuan et al. 2018) and the SN candidates AT2018iwp and AT2019bvr (Prokhorov et al. 2021). However, these HE source candidates present low statistical significance and large localisation uncertainties. At VHE gamma rays, observations on dedicated SNe have been performed with IACTs without yielding a significant detection. These studies include the observations of the Type Ia SN 2014J with MAGIC (Ahnen et al. 2017b), the monitoring of several CCSNe with H.E.S.S. (H. E. S. S. Collaboration et al. 2019), and the observation campaign on the superluminous SN 2015bn and SN 2017egm with VERITAS (Acharyya et al. 2023).

This chapter is organised as follows. Sections 6.2 and 6.3 describe the observations, data analysis, and results on SN 2023ixf and SN 2024bch, respectively. We discuss the obtained results in Sect. 6.4, and we provide our conclusions in Sect. 6.5.

6.2 sn 2023ixf

The Type II SN 2023ixf was discovered in the Galaxy M101 (6.85 ± 0.15 Mpc; Riess et al. 2022) on 19 May 2023 at 17:27:15 UTC (MJD 60083.72; Itagaki 2023). The

explosion time is estimated to have occurred on 18 May 2023 at 18:00 UTC, about one day before the discovery (MJD 60082.75, hereafter T_0 ; Hosseinzadeh et al. 2023). The optical emission increased in the days following the discovery, reaching the peak magnitude about ≈ 5 days after the explosion. Afterwards, the emission decay remained shallow in a plateau decaying phase for almost three months. Subsequently, the ejecta became transparent, entering the so-called nebular phase following a fast linear decay.

The progenitor has been identified to be an RSG star with an estimated mass of $8\text{--}20\,\mathrm{M}_\odot$ (e.g. Pledger and Shara 2023; Kilpatrick et al. 2023; Kozyreva et al. 2025). Flash spectroscopic observations within a few days after discovery revealed narrow emission lines consistent with a confined, asymmetric and inhomogeneous CSM (Bostroem et al. 2024; Jacobson-Galán et al. 2023; Smith et al. 2023).

The pre-existent, dense CSM within which the ejecta interacted has also been characterised at other wavelengths. In the infrared (IR) band, the progenitor star showed a mid-IR excess before the explosion, which is most likely explained by a dusty CSM. Furthermore, significant pre-explosion IR variability has been discovered (Kilpatrick et al. 2023).

At X-rays, SN 2023ixf was first detected by the *Nuclear Spectroscopic Telescope Array* (*NuSTAR*) on 22 and 29 May 2023 (MJD 60086.74 and 60093.37, $\sim T_0 + 4$ d and $\sim T_0 + 11$ d, respectively; Grefenstette et al. 2023), the *X-ray Multi-mirror Mission-Newton* (*XMM-Newton*) on 27 May 2023 (T0 + 9; Nayana et al. 2024) and the *Chandra X-ray Observatory* on 31 May 2023 (MJD 60095.65, $\sim T_0 + 13$ d; Chandra et al. 2023). These early detections of hard X-ray emission are produced by material heated in the interaction between the forward shock and the confined CSM. Finally, the early non detections at radio until about one month after the explosion, on 17 June 2023 (MJD 60112.04) by the Karl G. Jansky Very Large Array (VLA) (Matthews et al. 2023), have been explained by the initial high-column densities ahead of the heated material (Chandra et al. 2023).

No significant HE gamma-ray emission was detected with *Fermi*-LAT on SN 2023ixf within a month after T_0 . The derived ULs constrain the CR acceleration on this source at early times, estimated to be \leq 1% (Martí-Devesa et al. 2024). Complementary VHE gamma-ray data are required to constrain the gamma-ray spectrum at the highest energies and, subsequently, the maximum energy of the CRs accelerated during the event. SN 2023ixf is the closest and one of the brightest CCSNe visible in the Northern hemisphere since MAGIC and LST-1 are operational. Consequently, this close and bright event provides a unique opportunity to observe this kind of events and study the possibilities of CCSNe to be VHE gamma-ray emitters. In this work, we aim to constrain the VHE emission from SN 2023ixf.

In this section, we present the observations of SN 2023ixf in the deepest campaign ever performed at VHE gamma rays on a CCSN covering both the rise and plateau phases. Section 6.2.1 summarises the observational campaign performed with MAGIC and LST-1 IACT facilities. In Sect. 6.2.3, we describe the model used to divide the data. The analysis procedure is described in Sect. 6.2.2, while results are shown in Sect. 6.2.4.

6.2.1 Observations

We triggered joint MAGIC and LST-1 early-time observations via target of opportunity (ToO) on SN 2023ixf to search for early VHE gamma-ray emission. Observations started on 20 May 2023 at 21:30 UTC ($T_0 + 2.15 \, d$), only one day after the discovery, and extended until 22 June 2023 ($T_0 + 35.18 \, d$).

Both IACT facilities performed observations under the same observation scheme in *wobble* mode: a sequence of four recursive telescope pointings around SN 2023ixf position with an offset from the source of 0.4° (see Sect. 4.1.6.1). The observation time on every telescope pointing was about 20 min. With this strategy and under simultaneous observations, we can perform a three-telescope stereoscopic analysis, MAGIC+LST-1 (see Sect. 4.4).

The observations were taken with the Moon below and above the horizon, hereafter designed *dark* and *moon* observations, respectively. MAGIC collected almost 60 h of data between dark and moon conditions, whereas LST-1 gathered about 47 h of data, taken in dark or low-moon conditions. Eventually, about 42 h of data were taken simultaneously with LST-1 and MAGIC. We analyse simultaneous observations with MAGIC and LST-1, which provide better performance than considering the two facilities separately (see Sect. 4.4; Abe et al. 2023c). We summarise the joint observation campaign in Table 6.1, where the effective observation time is shown for each night.

The rapid classification of SN 2023ixf as a Type II SN, its close distance, luminous peak, and signs of ejecta-CSM interactions triggered extensive observations during the different phases of the SN explosion within the first month after the explosion. The first five observation days were taken during the rising phase of the light curve and the luminosity peak. Subsequent observations in June occurred during the shallow decay in the plateau phase. The final dataset is 25.6 hours of dark or low-moonlight observing conditions after data quality selection (see Table 6.1).

6.2.2 Analysis

We performed an offline software search of coincident events triggering the three telescopes by matching the event timestamps. Once identified, the events are reconstructed with the dedicated pipeline magic-cta-pipe v0.3.1 (more details in Sect. 4.4 and in Abe et al. 2023c).

After the timestamp matching algorithm, the stereoscopic parameters are calculated and used for the direction and energy reconstruction, as well as in the gamma-hadron separation through RF algorithms (see Sect. 4.1.3). Dim, poorly-parametrised events (intensity < 50 p.e. and width > 0) are excluded for the stereoscopic reconstruction. The parametrised images of the three telescopes are weighted to obtain a single parametrisation per event using the image intensity (Abe et al. 2023c).

The dedicated MAGIC+LST-1 MC simulations are initially produced with an NSB corresponding to a dark-sky patch (see Sect. 4.3.5). In order to improve the matching of observational data and MC simulations, the NSB of the MC simulations is increased through additional Poissonian noise after summing up the charge in

Start day	Start date	Time since T_0	Observation time after data selection	ZA range
	[MJD]	[d]	[h]	[°]–[°]
20 May 2023	60084.90	2.15	5.66	25–61
21 May 2023	60085.98	3.23	1.31	26–31
22 May 2023	60086.93	4.18	1.52	25–40
23 May 2023	60088.02	5.27	2.39	29–47
27 May 2023	60092.10	9.35	0.55	45–48
12 Jun. 2023	60107.91	25.16	2.64	25–37
15 Jun. 2023	60110.94	28.19	2.46	27–43
18 Jun. 2023	60113.91	31.16	0.53	25–26
19 Jun. 2023	60114.91	32.16	2.71	26-42
20 Jun. 2023	60115.91	33.16	2.12	26-43
21 Jun. 2023	60116.91	34.16	2.62	26-43
22 Jun. 2023	60117.93	35.18	1.10	27–35

Table 6.1: Observation campaign of SN 2023ixf with MAGIC and LST-1.

Notes. For each MAGIC+LST-1 joint observation day, we list the day of the evening before data taking, the starting date in MJD, the starting time offset with respect to the explosion time ($T_0 = MJD 60082.75$; Hosseinzadeh et al. 2023), the MAGIC+LST-1 observations time after the data selection, and the ZA range of the observations.

each pixel of the camera. Six different values of the Poisson variances are considered to tune the MC simulations, ranging from 0.5 p.e. to 3 p.e. in steps of 0.5 p.e.

The observational data are divided based on the NSB conditions during their data taking and binned according to the Poisson variances simulated in the MC reprocessing. The properties of the primary particle are reconstructed using the corresponding RFs.

We selected events surviving the image cleaning in LST-1 and at least one MAGIC telescope (see Sect. 4.4). In particular, we apply energy-dependent 90% efficiency cuts on the *gammaness* parameter. The IRFs are computed using the nearest MC simulations to each run.

We perform a spectral analysis using aperture photometry with the open-software package Gammapy (Donath et al. 2023; Acero et al. 2022). Three equidistant OFF regions located around the telescope pointing at the same offset and size as the ON region (centred on SN 2023ixf) are used to estimate and subtract the background. We consider a radius of 0.2° to perform the spectral analysis, regardless of the event reconstructed energy.

6.2.3 Model-based data division

The intense SN photosphere is expected to attenuate the VHE gamma-ray emission via photon-photon pair production (see Sect. 2.3.1). This effect is particularly relevant at early times when the photosphere is bright and the fast shock produced

by the SN explosion is expanding in the CSM (e.g. Tatischeff 2009; Marcowith et al. 2014; Cristofari et al. 2022; Brose et al. 2022). As a result, early times interpretation of VHE gamma-ray observations from SNe should consider careful treatment of gamma-gamma attenuation.

To accurately estimate the pair-creation opacities at early times, a time-dependent, anisotropic modelling is required because of two main reasons. Firstly, both the SN shock and photosphere are expanding. The physical properties of the latter, such as photon density and temperature, evolve with time. Secondly, the relative position between the shock and the photosphere affects the number of photons reaching the shock, which, in turn, determines the probability of photon-photon pair creation (Cristofari et al. 2020).

To assess the division of the LST-1 data, we used the time-dependent anisotropic model in Cristofari et al. (2022) tailored to SN 2023ixf physical parameters. Based on the predicted attenuation of the VHE gamma-ray emission, we divide the MAGIC+LST-1 dataset into two subsamples.

The first sub-sample (hereafter sample A) corresponds to the early observation before and around the peak luminosity. During these observations, the early VHE emission is expected to be significantly attenuated at $E > 100\,\text{GeV}$. However, given the inverse relation of emission with time (Tatischeff 2009), the emission at $E < 100\,\text{GeV}$, where the gamma-gamma attenuation is less severe than at higher energies, is expected to reach the maximum. Sample A encompasses observations taken during May 2023 ($T_0 < 10\,\text{d}$; see Table 6.1). These observations occurred in the phase of enhanced CSM density (Jacobson-Galán et al. 2023).

The second subsample (hereafter sample B) contains the rest of the observations conducted after $T_0 + 24 \,\mathrm{d}$ in June 2023 (see Table 6.1). In sample B, the gammagamma absorption is expected to be less severe and without large changes with time compared to earlier phases of the explosion. The VHE gamma-ray emission is predicted to reach the maximum observed emission level.

6.2.4 Results

No significant VHE gamma-ray emission is detected from SN 2023ixf during the joint observations of MAGIC+LST-1, in either samples A or B (see Sect. 6.2.3). We assume a power-law spectral model to constrain the VHE gamma-ray emission. The spectral index (Γ) is fixed to $\Gamma=-2$ during the fitting process. We calculate ULs at the 95% confidence level. The SEDs for samples A and B are shown in Fig. 6.1. We derive comparable ULs between the two samples, at the level of $\sim 10^{-12}\,\mathrm{erg}\,\mathrm{cm}^{-2}\,\mathrm{s}^{-1}$ at the lowest energies of hundreds of GeV. At higher energies, we constrain the emission at a level of few $\times 10^{-13}\,\mathrm{erg}\,\mathrm{cm}^{-2}\,\mathrm{s}^{-1}$.

The integral flux is derived using the same spectral model assumption as the SED computation. Figure 6.2 shows the light curve above 200 GeV for the two samples during non-coincident days. The emission is constrained for both samples at the level of few $\times 10^{-13}$ cm⁻² s⁻¹.

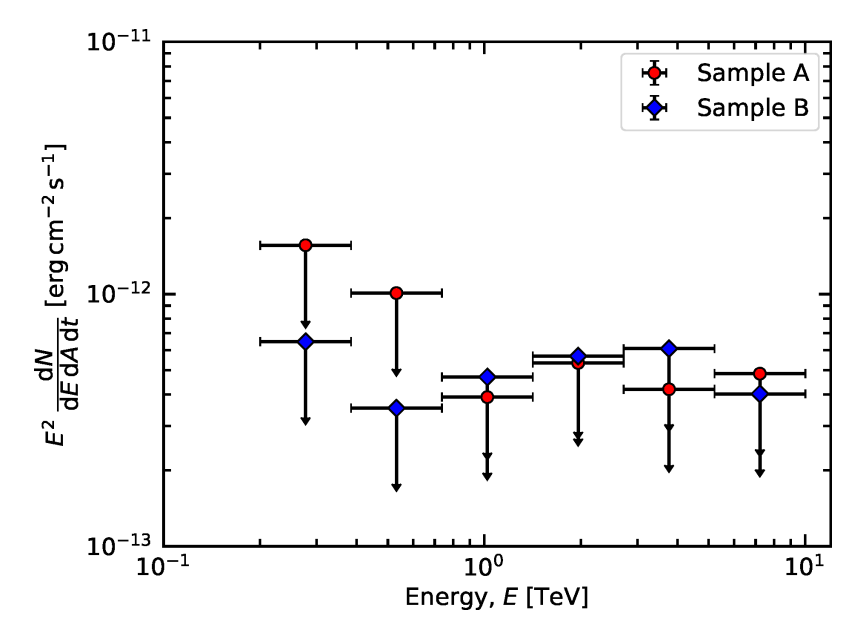


Figure 6.1: SED of SN 2023ixf in VHE gamma rays obtained with MAGIC and LST-1 during the raising and peak luminosity in red (Sample A) and the plateau phase in blue (Sample B).

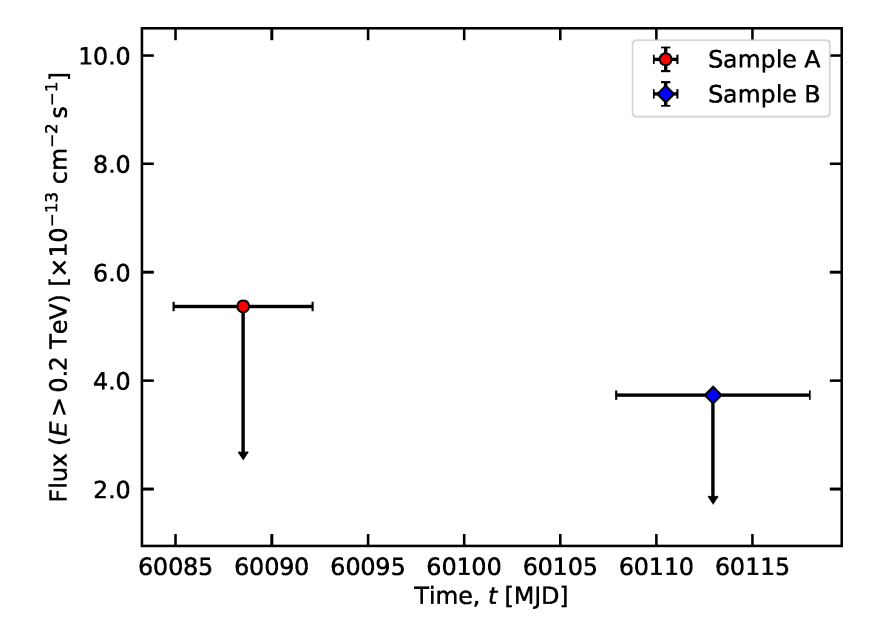


Figure 6.2: Integral fluxes of SN 2023ixf obtained with MAGIC and LST-1 for samples A and B in red and blue, respectively. We note that the observations in the two samples are performed on non-coincident days (see Table 6.1).

6.3 sn 2024bch

SN 2024bch was discovered on 29 January 2024 at 06:02:50 UTC in the galaxy NGC 3206 (at a distance $d \sim 20\,\mathrm{Mpc}$; Tully et al. 2016), at coordinates RA/Dec (J2000): 155.4592°, 56.9267° (Wiggins 2024). It was initially classified as a Type IIn SN based on its spectral similarity to SN 1998S at 3.5 days post-explosion (Balcon 2024). Subsequent optical observations resulted in a revised classification of SN 2024bch as a Type II SN with CSM interaction (Tartaglia et al. 2024; Andrews et al. 2025).

Start day	Start date	Time since T_0	Observation time after data selection	ZA range
	[MJD]	[d]	[h]	[°]–[°]
13 Feb. 2024	60354.03	15.76	3.5	28–34
14 Feb. 2024	60355.06	16.79	2.7	28-34
15 Feb. 2024	60356.06	17.79	3.8	28-35
16 Feb. 2024	60357.11	18.84	2.2	28–35
18 Feb. 2024	60359.20	20.93	0.8	38-43
06 Mar. 2024	60376.02	37.75	1.5	28–30

Table 6.2: Observation campaign of SN 2024bch with LST-1.

Notes. For each observation day, we list the day of the evening before data taking, the starting date in MJD, the starting time offset with respect to the discovery ($T_0 = \text{MJD} 60338.25196759 \text{ Wiggins } 2024$), the observations time after the data selection, and the ZA range of the observations.

In this section, we present VHE gamma-ray follow-up observations of SN 2024bch conducted with LST-1. We describe the observations and data analysis in Sects. 6.3.1 and 6.3.2, respectively. Results are presented in Sect. 6.3.3.

6.3.1 Observations

ToO observations of SN 2024bch with LST-1 were initiated on 13 February 2024 (MJD 60353), approximately two weeks after its discovery. The follow-up was intentionally delayed to avoid the early phase when significant gamma-gamma attenuation is expected (see Sect. 6.2.3). Observations were conducted over six nights between February and March 2024, accumulating a total exposure time of 14.6 h within a ZA range of 28°–43° (see Table 6.2). Data were acquired in *wobble* mode with an offset of 0.4° (see Sect. 4.1.6.1), under good atmospheric conditions and during dark to low moonlight periods.

6.3.2 Data analysis

The low-level data analysis follows the standard, source-independent analysis described in Sect. 4.3, utilising the cta-lstchain software package (López-Coto et al. 2024). MC simulations, generated at a fixed declination of +61.66° (4.73° from the position of SN 2024bch) are employed to reconstruct the properties of the primary particles (see Sects. 4.3.4 and 4.3.5). Energy-dependent efficiency cuts at 70% for *gammaness* and θ are applied to obtain the gamma-ray-like events. Furthermore, faint events with *intensities* below 50 p.e. are excluded to minimise contamination from events close to the energy threshold (see Sect. 4.1.4).

We performed an aperture photometry spectral analysis using the open-software package Gammapy (Donath et al. 2023; Acero et al. 2024). Background estimation is performed using a single OFF region, defined as the reflected region with respect

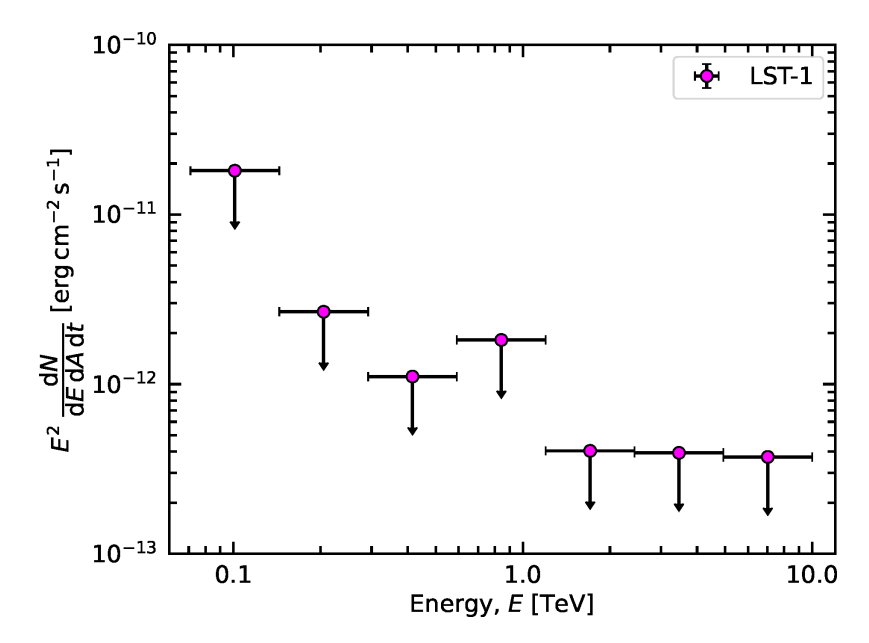


Figure 6.3: SED obtained using all the LST-1 observations of SN 2024bch.

to the ON region centred on the position of SN 2024bch (see Sect. 4.1.6.1). Only one OFF region was used in this case because of pointing instabilities during the observations.

6.3.3 Results

No significant VHE gamma-ray excess was detected on any of the observed nights or in the full dataset. To constrain the gamma-ray emission from SN 2024bch, we compute the SED in the range between 75 GeV and 10 TeV stacking all the observations (see Sect. 4.1.6). A power-law spectral model with a fixed spectral index to $\Gamma=-2$ is assumed. We calculate ULs at the 95% confidence level. The SED is shown in Fig. 6.3. We can constrain the observed emission from 10^{-11} erg cm $^{-2}$ s $^{-1}$ at 100 GeV down to few $\times 10^{-13}$ – 10^{-12} erg cm $^{-2}$ s $^{-1}$ above 1 TeV.

We computed night-wise integral flux ULs between 100 GeV and 10 TeV considering the best-fit spectral model on each night. The light curve is shown in Fig. 6.4. Additionally, we constrain the integral flux using the full dataset. This result is also shown in Fig. 6.4. The daily light curve constrains the emission at few $\times 10^{-12}\,\mathrm{cm^{-2}\,s^{-1}}$, while the integral flux UL for the full dataset is at the level of about $10^{-12}\,\mathrm{cm^{-2}\,s^{-1}}$. We note, however, that the time span of the stacked integral flux between 13 February and 6 March 2024 is poorly covered after 18 February because the presence of the Moon prevented observations with a low energy threshold. Furthermore, we note that the integral flux ULs are sensitive to the assumed spectral index. In particular, if one assumes that the spectral index is $\Gamma=-2.5$, the flux ULs increase by a factor of \sim 2.

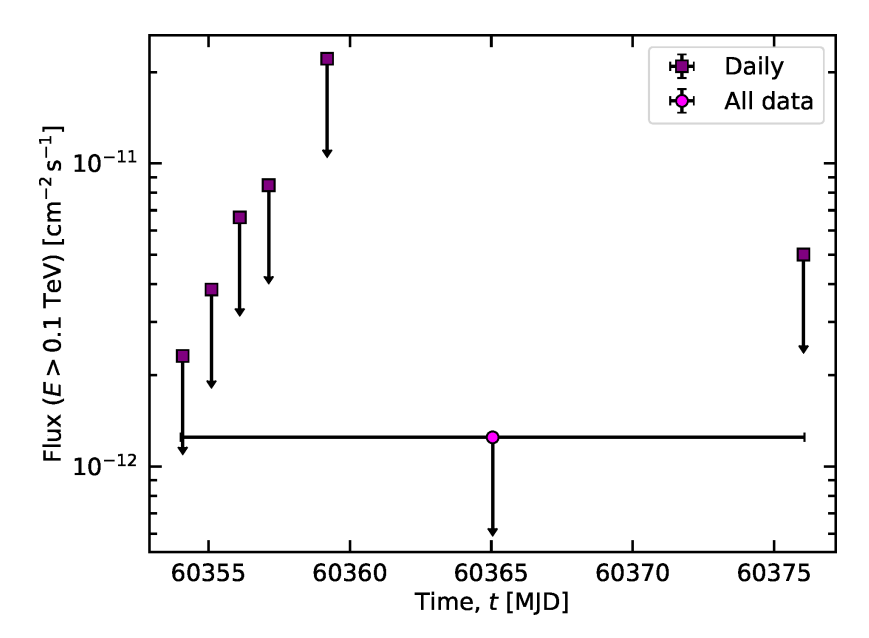


Figure 6.4: Light curve of SN 2024bch computed between 100 GeV and 10 TeV. We compare the night-wise light curve (purple) with the integrated flux UL, obtained by stacking all results together (fuchsia).

6.4 DISCUSSION

The flux ULs derived for SN 2023ixf and SN 2024bch constrain the VHE gamma-ray emission above 200 GeV and 100 GeV, respectively. The corresponding integral flux ULs at these energies are at the level of few $\times 10^{-13}$ cm⁻² s⁻¹ for SN 2023ixf and few $\times 10^{-12}$ cm⁻² s⁻¹ for SN 2024bch. These values correspond to about 0.2% and 1% of the Crab Nebula flux, respectively. The lower energy threshold of LST-1 and higher sensitivity of MAGIC+LST-1 observations enable probing the emission of CCSNe down to energies where the gamma-gamma absorption is not as severe as in the TeV band. No previous IACT observations of SNe were carried out with such a low energy threshold (Ahnen et al. 2017b; H. E. S. S. Collaboration et al. 2019; Acharyya et al. 2023). Additionally, IACT observations at tens to hundreds of GeV provide competitive, sensitive observations to short-timescale emission compared to the *Fermi*-LAT sensitivity at these energies with similar exposures (see Sect. 3.2.3.2; Funk et al. 2013).

Gamma-ray observations can also constrain the physical properties of the CSM. Under the assumption that the gamma rays arise from proton-proton interactions with the wind of the progenitor star, the mass-loss rate over the wind velocity $(\dot{M}/v_{\rm w})$ can be constrained (e.g. Dwarkadas 2013; H. E. S. S. Collaboration et al. 2019). In a steady-wind scenario (Chevalier 1982), the density profile as a function of the radius R takes the form

$$\rho_{\rm w} = \frac{\dot{M}}{4\pi v_{\rm w}} R^{-s} \,, \tag{6.1}$$

where s=2 and $\dot{M}/v_{\rm w}$ is assumed to be constant. Dwarkadas (2013) derived the relation between the emitted gamma-ray flux above a certain energy $F_{\gamma}(>E)$ and $\dot{M}/v_{\rm w}$. This theoretical model assumes that a fraction ξ of the total kinetic energy of the shock is used to accelerate CRs. The differential energy gain that CR acquire

during acceleration is $d\epsilon_{\rm CR}=2\pi\xi R_{\rm sh}\rho_{\rm sh}v_{\rm sh}^3dt$, where $R_{\rm sh}$, $\rho_{\rm sh}$, and $v_{\rm sh}$ are the shock radius, density, and velocity, respectively. Proton-proton interactions occur when the accelerated protons interact with target material from the swept-up material by the shock (see Sect. 2.2.4). For a steady-wind scenario, the differential swept-up material is described as $dM_{\rm sw}=4\pi\rho_{\rm w}r^2dr$. The contact discontinuity* between the ejecta, with density profile $\rho_{\rm ej}\propto v^{-n}$, and a stationary medium, with density $\rho_{\rm w}$, expands as $R_{\rm CD}=mC_1t^m$, where m=(n-3)/(n-s) (Chevalier 1982). The forward shock radius can be related to $R_{\rm CD}$ as $R_{\rm sh}=\kappa R_{\rm CD}$, where κ is fixed in the case of a self-similar solution (Chevalier 1982). Under the above-mentioned framework and considering the fact that the emitting volume is confined to a fraction β of the total volume (the shocked region has a volume $V=4\pi\beta R_{\rm sh}^3/3$), the gamma-ray flux from proton-proton interaction takes the form (Drury et al. 1994; Dwarkadas 2013):

$$F_{\gamma}(>E,t) = \frac{3q_{\gamma}\xi(\kappa C_1)m^3}{32\pi^2(3m-2)\beta\mu m_{\rm p}d^2} \left(\frac{\dot{M}}{v_{\rm w}}\right)^2 t^{m-2},\tag{6.2}$$

where q_{γ} is the gamma-ray emissivity normalised to the CR energy density (Drury et al. 1994), μ is the mean molecular weight, $m_{\rm p}$ is the proton mass, d is the distance to the SN, and t is the offset time of the observations with respect to the explosion event. Equation 6.2 can be expressed as a function of the shock velocity $v_{\rm sh} = R_{\rm sh}/t = \kappa m C_1 t^{m-1}$ as (H. E. S. S. Collaboration et al. 2019):

$$F_{\gamma}(>E,t) = \frac{3q_{\gamma}\xi v_{\rm sh}m^2}{32\pi^2(3m-2)\beta\mu m_{\rm p}d^2} \left(\frac{\dot{M}}{v_{\rm w}}\right)^2 t^{-1}.$$
 (6.3)

For a wind density profile (s=2) and typical values of n, which range between 7–12, m ranges between 0.8–0.9 (H. E. S. S. Collaboration et al. 2019). To derive the $\dot{M}/v_{\rm w}$ ULs of SN 2023ixf and SN 2024bch from VHE observations with MAGIC+LST-1 and LST-1, respectively, we consider for both SNe a canonical 10% proton-acceleration efficiency, $\mu=1.4$, and $\beta=0.5$ (Dwarkadas 2013; H. E. S. S. Collaboration et al. 2019). On the other hand, q_{γ} can be estimated based on numerical calculations accounting for the spectral index and the energy threshold used to compute the integral flux (Drury et al. 1994). Table 6.3 shows the constraints on $\dot{M}/v_{\rm w}$ accounting for the distance and shock velocity inferred for each SN. We use the flux ULs computed with several non-coincident observation days. The offset time associated with the flux UL used in Eq. 6.3 and Table 6.3 is calculated based on the exposure-weighted average of the mid-time for each observations. The derived $\dot{M}/v_{\rm w}$ ULs without considering gamma-ray attenuation are of the order of $10^{-5}~M_{\odot}~\rm yr^{-1}~km^{-1}~\rm s$ (see Table 6.3).

As previously discussed, VHE gamma rays have the disadvantage of being affected by photon-photon pair creation, which attenuates the emitted flux (see Sect. 2.3.1). As a result, the derived $\dot{M}/v_{\rm w}$ estimates with VHE gamma-ray data will be too restrictive if the gamma-gamma attenuation is not accounted for, especially at early times. Therefore, to correct the gamma-ray flux ULs due to photon-photon pair creation, the integral flux has to be multiplied by $e^{\tau_{\gamma\gamma}}$ (see Sect. 2.3). That is, the right-hand side of Eq. 6.3 must be multiplied by this quantity. During the few

^{*}Region that separates the shocked ejecta and shocked ambient gas.

[†]But see Chandra et al. (2024).

Dataset	Exposure-weighted average time after explosion	$\dot{M}/v_{ m w}$	
	[d]	$[\times 10^{-6} M_{\odot} \mathrm{yr}^{-1} \mathrm{km}^{-1} \mathrm{s}]$	
Sample A (SN 2023ixf)	3.66	6	
Sample B (SN 2023ixf)	30.95	17	
All data (SN 2024bch)	20.49	20	

Table 6.3: ULs on $\dot{M}/v_{\rm w}$ without considering gamma-ray attenuation.

Notes. The exposure-weighted average time after the explosion and the UL on $\dot{M}/v_{\rm w}$ are provided for the datasets of SN 2023ixf (samples A and B) and SN 2024bch (all data). For SN 2023ixf, we used $q_{\gamma}(E>200\,{\rm GeV},\alpha=4.1)=6\times10^{-17}\,{\rm erg^{-1}\,cm^3\,s^{-1}}$ (H-atom) $^{-1}$ (Drury et al. 1994), $v_{\rm sh}=9$, 000 km s $^{-1}$ (Jacobson-Galán et al. 2023) † , and $d=6.85\,{\rm Mpc}$ (Riess et al. 2022). For SN 2024bch, we used $q_{\gamma}(E>100\,{\rm GeV},\alpha=4.1)=1.2\times10^{-16}\,{\rm erg^{-1}\,cm^3\,s^{-1}}$ (H-atom) $^{-1}$ (Drury et al. 1994), $v_{\rm sh}=7$, 000 km s $^{-1}$ (Tartaglia et al. 2024), and $d=20\,{\rm Mpc}$ (Tully et al. 2016). We note that the values of $v_{\rm sh}$ are approximate estimates, intended to be consistent within an order of magnitude to the real value.

days after the explosion, the value of $\tau_{\gamma\gamma}$ is of the order of tens to few units at VHE gamma rays. The opacity should decrease to a value of about a few or one after a few tens of days, while it should further diminish to a value of one or a fraction after month timescales. In contrast, other wavebands such as radio, optical or X-ray can also constrain the CSM physical parameters without the complications introduced by photon-photon pair creation. In these bands, close CCSNe are often observationally detected as bright sources. Furthermore, in special cases, CCSNe can even be spatially resolved at radio wavelengths for nearby explosions (e.g. Marcaide et al. 1995a,b; Bietenholz et al. 2003; Krauss et al. 2012). Consequently, CSM constraints can be inferred in general more precisely at other bands than gamma rays (e.g. Teja et al. 2023; Grefenstette et al. 2023; Chandra et al. 2024; Berger et al. 2023).

SN 2023ixf was notably followed up at multiple wavelengths. The estimated M value for SN 2023ixf depends on the time of observations. Early-time (2 days post-explosion) observations from narrow-line studies estimate \dot{M} at an order of magnitude of $10^{-2} M_{\odot} \text{ yr}^{-1}$ (e.g. Jacobson-Galán et al. 2023; Bostroem et al. 2024; Zimmerman et al. 2024). The non-detection of radio emission at early times due to absorption is also consistent with this enhanced mass-loss rate (Berger et al. 2023; Iwata et al. 2025). X-ray observations at few to tens of days after the explosion place a mass-loss rate at about $10^{-4} M_{\odot} \text{ yr}^{-1}$ that decreases following a wind-like profile (Grefenstette et al. 2023; Panjkov et al. 2024; Chandra et al. 2024). Note that this estimate of \dot{M} at X-rays is in tension with millimetre-band observations at that time (Berger et al. 2023). The radio data exclude the range between few 10^{-6} – $10^{-2} M_{\odot} \,\mathrm{yr}^{-1}$, in agreement with the derived value of $10^{-6} \,M_{\odot} \,\mathrm{yr}^{-1}$ from optical spectra to model comparison at later times (Jacobson-Galán et al. 2023; Berger et al. 2023). However, this discrepancy can be eased if the CSM is confined and non-homogeneous in regions above the shock-breakout (e.g. Berger et al. 2023). The transition in the CSM structure is estimated to take place between $T_0 + [3.5, 4.5]$ d, at a radius of few $\times 10^{14}$ cm. The \dot{M} value derived from VHE gamma-ray observations in sample A (see Sect. 6.2.3), adopting a wind velocity of $100\,{\rm km\,s^{-1}}$, can be easily accommodated within the estimates of $\dot{M}\sim 10^{-6}$ – $10^{-4}\,M_{\odot}\,{\rm yr^{-1}}$ given the large attenuation that gamma rays experience within the first days. On the other hand, the \dot{M} UL computed from sample B is comparable to the \dot{M} estimates at other wavelengths without considering gamma-ray attenuation.

In contrast to the case of SN 2023ixf, the electromagnetic observations of SN 2024bch have been solely reported in the optical band. Andrews et al. (2025) obtained an estimated mass-loss rate between 10^{-3} – $10^{-2}\,M_\odot$ yr $^{-1}$ from model comparison with the early spectra. Although this enhanced mass-loss rate may be limited to weeks or years before the explosion, the presence of CSM signatures at later times points to an extended CSM with distinct structured regions that may in addition be asymmetric. Ejecta-CSM interactions were observed at 60 days after the explosion. We note, however, that despite the signature of ejecta-CSM interaction at about 60 days, the origin of the narrow lines due to ejecta-CSM interactions is still debated (Andrews et al. 2025; Tartaglia et al. 2024). If the CSM interaction origin of the early-time narrow lines is true, its contribution is low, and it is not required to explain the luminosity of the explosion. The \dot{M} value derived with all the LST-1 observations of SN 2024bch, assuming a wind velocity of 100 km s $^{-1}$, is about $10^{-3}\,M_\odot\,\mathrm{yr}^{-1}$ without considering gamma-ray attenuation. The UL should increase at most by three orders of magnitude if the attenuation is considered.

SN 2023ixf and SN 2024bch are CCSNe that exhibit signatures of ejecta-CSM interaction. However, the high-ionisation lines completely disappeared within few days after the explosion, indicating a dense and confined CSM (Jacobson-Galán et al. 2023; Smith et al. 2023; Andrews et al. 2025). A significant fraction of SNe may show similar signs of confined interaction shortly after the explosion (Khazov et al. 2016; Bruch et al. 2023; Hinds et al. 2025). Although SN 2023ixf and SN 2024bch present a dense asymmetric CSM, the CSM of SN 2024bch may be more extended than in SN 2023ixf, but displays a lower level of ejecta-CSM interactions than SN 2023ixf, whose bright peak luminosity may be explained with additional power from the ejecta-CSM interaction. Models such as those in Cristofari et al. (2022) and Brose et al. (2022) assume a steady wind scenario without accounting for this enhanced confined CSM. Moreover, a shallower decay slope than the steady-wind scenario profile of s = -2 can explain the observation of some interacting SNe (e.g. Moriya 2023; Nayana et al. 2024). As a result, the proton-proton interaction efficiency and gamma-ray emissivity would be enhanced in shocks sweeping up the CSM. At early times, however, photon-photon pair creation is important (potentially attenuating the VHE gamma-ray flux by several orders of magnitude; Cristofari et al. 2022; Brose et al. 2022). Therefore, even if the gamma-ray emission is enhanced due to a dense compact CSM, this emission may remain undetectable. Once the confined CSM is surpassed, the proton-proton efficiency and gamma-ray emissivity will diminish due to the density drop. The observation of close SNe with ejecta-CSM interaction signatures, as in the case of SN 2023ixf and SN 2024bch, is crucial for probing gamma-ray emission in CCSNe. On the contrary, Type Ia SNe are expected to have lower CSM than CCSNe. Consequently, they are expected to have less efficient proton-proton interactions and gamma-ray emission (Smith 2014).

As emphasised throughout this chapter, precise modelling of the photon-photon pair creation is essential for estimating the intrinsic gamma-ray emission at early times and inferring the physical properties of SNe. However, this task is complex (see Sect. 6.2.3). The gamma-gamma opacities are highly sensitive to the model parameter values, which can drastically alter the derived opacities by orders of magnitude. Furthermore, small variations of the parameter values can significantly alter the gamma-ray attenuation relevance with time at energies between tens to hundreds of GeV, which is a critical energy range for IACTs such as MAGIC and LSTs. Therefore, precise MWL data are required to constrain the parameters related to the opacities, such as the photosphere and the hydrodynamical evolution. Photonphoton pair creation requires a minimum energy to create an electron-positron pair and additionally depends on the number density of the surrounding photon field. The attenuation is expected to be the highest at early times when the photosphere reaches the highest luminosity and temperature. As the explosion evolves with time, these quantities decrease. The energy range affected by gamma-gamma paircreation will shrink at low energies, as low-energy gamma rays will start being unattenuated because the minimum energy for a pair creation process will not be reached. The observation at tens to hundreds of GeV is critical for the early detection of SNe.

A stringent constraint on the particle acceleration efficiency of <1% in SN 2023ixf was derived based on its non-detection with *Fermi*-LAT within a month after the explosion (Martí-Devesa et al. 2024). Although this value is lower than the canonical 10% particle acceleration efficiency value, this constraint can be eased if an inhomogeneous environment is considered or the time window when the shock is not collisionless is excluded (Martí-Devesa et al. 2024; Kimura and Moriya 2024). Gamma-ray observations can provide valuable information about the physical parameters related to non-thermal particle acceleration. These observations complement MWL SN studies. Even when only upper limits are derived, they can still offer important constraints on particle acceleration and non-thermal emission. For example, the temporal evolution of the particle acceleration efficiency may be constrained if MWL data can characterise the rest of the physical properties of the system.

Interestingly, the configuration of the CSM in CCSNe can, to some extent, be compared to the CSM that is found in symbiotic recurrent nova such as RS Oph[‡] (see Sect. 5.2). In these systems, the nova occurs embedded in the red giant wind with additional over-densities concentrated in the orbital plane through binary interaction. A non-spherical ejecta may develop, additionally leading to complex spatial remnants (see Sect. 5.7; Bode and Evans 2012). Similarly, SN 2023ixf and SN 2024bch show signs of an asymmetric-confined CSM. While shocks that form in novae are generally slower than SNe, they partially overlap between them. Moreover, the nova photosphere will also partially attenuate the gamma rays, but with less efficient photon-photon pair creation due to the fainter photon energy field and characteristic temperature of the nova photosphere than the hotter SN photosphere. These similarities suggest that novae and SNe are, to some extent, phenomenologically connected. Therefore, novae can be used as valuable systems

[‡]In contrast, the low CSM of classical novae could be related to the low-density environment of Type Ia SNe compared with CCSNe.

for testing particle acceleration and improving the understanding of supersonic shocks, offering insights into similar processes occurring in both types of systems while we await a close and bright SN.

6.5 CONCLUSIONS

SN 2023ixf and SN 2024bch are two close Type II SNe that exhibit early-time signatures of ejecta-CSM interaction. In particular, SN 2023ixf is the closest CCSN detected in the last 10 years with a bright peak luminosity. Dedicated ToO observations were conducted with MAGIC+LST-1 on SN 2023ixf and only with LST-1 on SN 2024bch within the first 40 days after the explosion. SN 2023ixf observations began as early as one day after the discovery, while SN 2024bch was observed after ten days to minimise the gamma-ray attenuation on the observed flux at early times. Although no significant VHE gamma-ray emission is detected for either SNe, we constrain their emission to few $\times 10^{-13}$ cm⁻² s⁻¹ and 10^{-12} cm⁻² s⁻¹ above 200 GeV and 100 GeV, for SN 2023ixf and SN 2024bch, respectively. The obtained flux ULs for SN 2023ixf represent the deepest ULs at low-energy VHE gamma rays across different phases of the SN explosion. The differential and integral flux ULs derived can serve as valuable information to constrain theoretical models if proper gamma-gamma attenuation is accounted for.

7

GAMMA-RAY BURSTS

Overview

This chapter contains the work on the data analysis and physical interpretation of the observations with LST-1 of GRB 221009A, the brightest gamma-ray burst (GRB) since their first observation in the late sixties. In particular, this GRB is dubbed as the "brightest-of-all-time" (BOAT) burst. This chapter includes also the first moon-adapted analysis of LST-1. A dedicated paper has been submitted for publication to The Astrophysical Journal Letters.

7.1 INTRODUCTION

GRBs are brief, intense pulses of gamma rays peaking in the MeV band, detected at an average rate of \sim 1 per day, randomly distributed in the sky (Meegan et al. 1992). The initial, prompt phase of their emission exhibits irregular variability and typically lasts seconds to minutes (Fishman et al. 1994). This is followed by the afterglow phase, where emission across the electromagnetic spectrum decays more gradually, over timescales of hours up to months (van Paradijs et al. 2000). Based on the duration and spectra of the prompt emission, they are classified as either shortor long-duration GRBs (Kouveliotou et al. 1993). Long GRBs are known to typically originate from the core collapse of some massive stars (Woosley and Bloom 2006), while short GRBs are widely thought to be triggered by the coalescence of binary compact objects (Berger 2014; Margutti and Chornock 2021). For either GRB class, the event is believed to generate collimated jets of plasma with ultrarelativistic bulk velocities, within which the prompt emission is produced and observed as a GRB when the jet is oriented close to our line of sight (Rees and Mészáros 1994). The afterglow emission from the radio band up to the GeV band is robustly interpreted as synchrotron radiation by electrons accelerated in a blast wave, triggered by the interaction of the jet with the ambient medium (Mészáros and Rees 1997; Sari et al. 1998; Piran and Nakar 2010). IC radiation by the same electrons can induce afterglows at even higher photon energies (Fan and Piran 2008). For reviews on GRBs, see, e.g., Mészáros (2002), Piran (2004), Gehrels and Mészáros (2012), and Kumar and Zhang (2015).

Gamma-ray emission at VHEs from GRBs had been long expected (Mészáros et al. 1994; Zhang and Mészáros 2001; Inoue et al. 2013; Kakuwa et al. 2012; Nava 2018), but was not observationally verified until recently with the detection of VHE gamma-ray emission of four different GRBs with the MAGIC and H.E.S.S. telescope facilities from GRB 190114C (MAGIC Collaboration et al. 2019b), GRB 180720B (Abdalla et al. 2019), GRB 190829A (H. E. S. S. Collaboration et al. 2021), and GRB 201216C (Abe et al. 2023a). These detections confirmed that at least some long GRBs emit VHE gamma rays during the afterglow phase (Nava 2021; Miceli and Nava 2022; Noda and Parsons 2022). For short GRBs, a $\sim 3\sigma$ hint was reported by MAGIC for GRB 160821B (Acciari et al. 2021).

Below we present the results for GRB 221009A obtained during the follow-up campaign with LST-1. This includes the earliest observations of GRB 221009A by an IACT in a period not covered by other VHE facilities. We contextualise these results, compare them with theoretical models of VHE afterglow emission from structured jets, and address the physical implications. This section is organised as follows. Sections 7.2 and 7.3 describe GRB 221009A and the observing conditions under which the data were obtained, respectively. The details on the data analysis are given in Sect. 7.4. The results are presented in Sect. 7.5, and we compare the obtained data with theoretical models and discuss physical implications in Sect. 7.6. Finally, we provide our conclusions in Sect. 7.7.

7.2 GRB 221009A

On 9 October 2022 at 13:16:59.99 UTC, hereafter T_0 , the Gamma-ray Burst Monitor (GBM) on board the Fermi Gamma-ray Space Telescope detected an extremely bright burst at 0.01-1 MeV lasting hundreds of seconds (Lesage et al. 2022, 2023)*. The Swift-Burst Alert Telescope (BAT) reported the detection of a very bright transient at 15–150 keV at 14:10:17 UTC at the coordinates RA/Dec (J2000): 288.2643°, 19.7712° (Dichiara et al. 2022; Williams et al. 2023), triggering follow-up observations by other instruments. From the detections by Fermi-GBM and Swift-BAT coincident in time and localisation, the source was recognised as an extremely bright, long GRB, labelled GRB 221009A (Kennea et al. 2022). Other satellites such as AGILE-GRID (Tavani et al. 2023), Insight-Hard X-ray Modulation Telescope (Insight-HXMT) (Tan et al. 2022), and Gravitational wave high-energy Electromagnetic Counterpart Allsky Monitor-C (GECAM-C) (Liu et al. 2022) also detected the event. From optical spectroscopic follow-up observations, the redshift of the source was determined to be z = 0.1505 (Castro-Tirado et al. 2022). In HE gamma rays, Fermi-LAT reported extremely bright emission (Bissaldi et al. 2022), the bulk of which started \sim 200 seconds after the GBM trigger pulse, and manifested rapid variability in flux and spectra for \sim 200 seconds afterwards (Axelsson et al. 2024). Due to the brightness of the event, Fermi-LAT suffered from a strong pile-up at early times. During the prompt phase that lasted for more than 600 s, a photon of 99.3 GeV was detected at $T_0 + 240$ s, while a photon of 400 GeV was detected at $T_0 + \sim 9$ h in the afterglow phase. These are the highest-energy photons seen by Fermi-LAT from a GRB during each phase (Pillera et al. 2022; Axelsson et al. 2024). LHAASO was observing the region of the sky that included GRB 221009A during the prompt and afterglow phases and reported the detection of VHE gamma rays from the GRB by the WCDA detector between 200 GeV to 7 TeV at more than 250σ (Huang et al. 2022; LHAASO Collaboration et al. 2023). LHAASO also reported the detection of the GRB with the KM2A detector from $\simeq 3 \text{ TeV}$ to $\simeq 13 \text{ TeV}$ during the period T_0 + [230,900] s (LHAASO Collaboration 2023). The HAWC gamma-ray observatory reported observations starting at $T_0 + \sim 8$ h, providing a preliminary differential flux UL at 1 TeV (Ayala and HAWC Collaboration 2022). Rapid follow-up observations of GRB 221009A by IACTs were prevented by the brightness of the full Moon on

^{*}A bright, line-like emission feature of unknown origin with temporal evolution in both energy (from \sim 12 MeV to \sim 6 MeV) and luminosity (from \sim 10⁵⁰ erg/s to $2 \cdot 10^{49}$ erg/s) was identified in the *Fermi-GBM* data (Ravasio et al. 2024).

9 October 2022. H.E.S.S. observations started at $T_0 + 53 \,\mathrm{h}$ and ULs were reported between 650 GeV and 10 TeV (Aharonian et al. 2023).

Follow-up observations were also conducted at all wavelengths spanning the radio, optical, and X-ray bands, resulting in the most extensive MWL coverage of a long GRB to date (Laskar et al. 2023; Williams et al. 2023; Kann et al. 2023; O'Connor et al. 2023; Rhodes et al. 2024; Giarratana et al. 2024). This led to some unique inferences regarding the underlying physical processes. Firstly, the temporal and spectral properties of the VHE gamma-ray and X-ray emission seen up to a few 1,000 seconds showed that they likely originate from an afterglow due to a narrow jet with an opening angle of ~0.6° (LHAASO Collaboration et al. 2023; An et al. 2023). On the other hand, the temporal behaviour of the radio to X-ray emission at later times cannot be explained by such a narrow jet and requires a separate emission region. This is most plausibly identified with a wider, outer jet surrounding the narrower, inner jet (Gill and Granot 2023; Sato et al. 2023b; Ren et al. 2024; Zheng et al. 2024; Zhang et al. 2025). Such structured jets, for which basic jet parameters like the kinetic energy and bulk velocity depend on the angle from the jet axis (Mészáros et al. 1998; Rossi et al. 2002; Zhang and Mészáros 2002), are naturally expected in realistic models of jet formation and propagation in GRBs (Morsony et al. 2007; Mizuta and Ioka 2013; Gottlieb et al. 2021). Notwithstanding some indications in previous GRBs (Sharan Salafia and Ghirlanda 2022; Sato et al. 2023a), GRB 221009A represents the first long GRB with strong evidence for a structured jet. It offers a unique opportunity to probe the physics of jet formation and propagation in long GRBs, which is still not well understood (Kumar and Zhang 2015). However, afterglow models accounting for such structured jets are more complicated compared to standard, simpler afterglow models, and effectively constraining them requires comprehensive MWL observations. In particular, more VHE gamma-ray data at late times are highly desirable, in addition to the ULs obtained by H.E.S.S. and HAWC.

LST-1 started observing GRB 221009A at 1.33 days after the burst and continued for more than 20 days. It constitutes the largest GRB campaign conducted by LST-1 to date, with deep coverage of the late afterglow phase. The analysis of the first two days of data required meticulous treatment of the NSB, as the observations were acquired under moonlight conditions.

7.3 OBSERVATIONS

LST-1 (see Sect. 3.2.3.3) is optimised to operate under *astronomical* darkness and absence of the Moon (hereafter *dark*). If PMTs are exposed to bright environments, they experience accelerated ageing and a significant gain reduction. Therefore, around full moon periods, observations are halted due to the high NSB from the Moon (see Sect. 3.2.3). However, observations in low moonlight conditions are feasible. These observations, hereafter referred as *moonlight* observations, increase the duty cycle of IACTs by \sim 30% with respect to the \sim 1,500 h/yr of data in *dark* conditions (Ahnen et al. 2017a; Archambault et al. 2017; Ohm and Wagner 2023). Increasing the duty cycle is relevant for all source types, but it is particularly critical for fast-evolving transient sources. Yet, they come at the cost of degraded telescope performance and higher systematic uncertainties on the estimated spectrum, as

Start day	Start date	$T-T_0$	Time after	ZA range
			data selection	
	[MJD]	[d]	[h]	[°]–[°]
10 Oct. 2022	59862.88*	1.33	1.75	31–54
12 Oct. 2022	59864.89*	3.33	1.42	34–52
15 Oct. 2022	59867.85	6.30	0.80	25–52
16 Oct. 2022	59868.88	7.32	2.35	34–65
17 Oct. 2022	59869.85	8.30	2.41	28-60
23 Oct. 2022	59875.86	14.30	2.01	34-61
25 Oct. 2022	59877.89	16.33	1.18	45-59
26 Oct. 2022	59878.87	17.32	1.42	42–58

Table 7.1: Observations of GRB 221009A with LST-1 in October 2022.

Notes. For each observation day, we list the day of the evening before data taking, the starting date, the starting time offset with respect to the burst trigger (T_0 ; Lesage et al. 2022), the observation time after the data selection, and the ZA range of the observations. The data taking under bright moonlight conditions are marked with an asterisk.

the IACT data analysis is sensitive to NSB conditions (see Sect. 4.1). Moonlight observations can be conducted with reduced HV to reduce the operational gain of PMTs and observe across all the NSB levels encountered when the Moon is above the horizon.

The night after the detection of GRB 221009A, on 9 October 2022, no operations of LST-1 were possible due to the presence of the full moon. However, due to the exceptional nature of this event, observations were resumed with reduced HV on 10 October 2022 ($T_0 + 1.33 \, \text{d}$) and continued on 12 October 2022 ($T_0 + 3.33 \, \text{d}$), with camera problems preventing observations on 11 October 2022 (see Table 7.1). A total of 3.17 h of data were acquired under bright moonlight conditions. The observation campaign continued until the end of November 2022, extending for two moon periods. In this work, we focus on the observations in *moonlight* and *dark* conditions of October 2022. A total of 10.17 h of good-quality observations were obtained in dark conditions in October 2022. This is summarised in Table 7.1.

LST-1 observations were performed in *wobble* mode (see Sect. 4.1.6.1). During the observation campaign, four telescope pointing directions were considered, each at 0.4° offset from the reported position of *Swift*-BAT (Dichiara et al. 2022). The telescope pointings were equally spaced around the GRB 221009A position, starting in the positive direction along the right ascension axis with respect to the source. The observation time at each wobble position was 20 min.

7.4 DATA ANALYSIS

The analysis of the presented data is divided according to the specific observing conditions during their acquisition. We consider a moonlight-adapted analysis (see Sect. 7.4.2) to process the first two observation nights (see Table 7.1), and standard dark analysis to process the rest of the data (see Sect. 7.4.1). Both analyses are performed with the dedicated software analysis pipeline cta-lstchain (see Sect. 4.3; López-Coto et al. 2023). The two independent analysis chains in cta-lstchain, i.e., the source-independent and the source-dependent analysis, are used in this work (see Sect. 4.3.4). The former, being the standard analysis scheme for CTAO (see Sect. 3.2.3.2), is selected as the reference analysis discussed in Sects. 7.4.1 and 7.4.2, while the latter is used as a cross-check to verify the consistency and robustness of the results. Details on the source-dependent analysis are presented in Sect. 7.4.3.

7.4.1 Analysis of observations in dark conditions

The LST-1 performance under dark conditions has been studied in Abe et al. (2023b) and described in Sect. 4.3. A similar analysis is used for the GRB 221009A observations in dark conditions (see Table 7.1). This approach considers a single calibration per observation obtained from calibration events (FF and pedestal events) taken in a dedicated observation run on the same night (Cat A calibrations; see Sect. 4.3.1). The signals in the waveforms are integrated with the LocalPeakWindowSum algorithm of ctapipe (see Sect. 4.3.2). Subsequently, the image cleaning applied is the tail-cut method, utilising an increased picture threshold condition based on the pixel noise level. Additionally, a time-coincident condition and dynamic cleaning are used (see Sect. 4.3.3).

The energy, incident direction, and *gammaness* of the events are estimated through RF algorithms, which are trained with MC gamma rays and protons (see Sect. 4.3.5). We need to adjust the NSB on the MC simulations to the specific NSB level in the FoV of GRB 221009A. Due to the proximity of GRB 221009A to the galactic plane ($b \sim 4.3^{\circ}$), the NSB level is similar to a galactic source like the Crab Nebula. The extra NSB for the analysis of GRB 221009A is accounted for through the addition of random Poissonian noise on the camera images before the image cleaning stage.

The selection criteria for gamma-like events are optimised using data from the Crab Nebula, which were collected under conditions similar to those of the GRB 221009A observations. We discard dim events with *intensity* below 50 p.e. Global cuts in the *gammaness* parameter and θ parameter are used to assess the statistical significance of the detection. Energy-dependent, efficiency-based cuts on the *gammaness* and θ parameters are used for the spectral analysis. Three sets of *gammaness* cuts (50%, 70%, and 90%) are tested, while the efficiency cut on the θ parameter is kept at 70% (see Sect. 4.1.4). The Crab Nebula spectra obtained with these cuts are consistent with those in the literature. Among the three sets of cuts, the *gammaness* efficiency cut at 90% provides the most stable results throughout the energy range studied, and is selected for the analysis of GRB 221009A observations.

The energy threshold of the analysis is defined as the peak energy position of the MC gamma-ray rates, weighted to the assumed spectral index of the source, after the event selection. Assuming an observed spectral index of $\Gamma = -3$ for GRB 221009A (LHAASO Collaboration et al. 2023), the energy threshold for the dark data is from \sim 20 GeV to \sim 200 GeV at 25°, and 65° zenith angles, respectively.

We perform a spectral analysis using the science analysis tools in the software package Gammapy (Donath et al. 2023; Acero et al. 2022). The joint likelihood fitting

method is used, in which three control regions (OFF) are employed to estimate the background (see Sect. 4.1.6). These OFF positions are defined from the three reflected positions with respect to GRB 221009A and the telescope pointing direction at equidistant rotation angles (see Sect. 4.1.6.1). Only events above the energy threshold are used during the fitting process.

7.4.2 Analysis of observations in moonlight conditions

The sensitive PMTs that are used to detect the faint Cherenkov light in LST-1 are affected by high NSB conditions. The scatter of the moonlight in the atmosphere increases the anode current in the PMTs of the whole camera. Observations taken under moonlight conditions become noisy due to spurious NSB triggers, which produce larger noise fluctuations and more after-pulse signals in the waveforms as the NSB increases. As a consequence, the pulse timing and signal reconstruction are affected, worsening the precision in the event reconstruction and gamma/hadron separation for moonlight data with respect to observations taken in dark conditions. A dedicated data analysis is needed to ensure the best telescope performance under the atypical observing conditions and different trigger and camera settings (e.g. reduced HV) that affect the moonlight observations of GRB 221009A with LST-1. The following modifications to the standard analysis chain (see Sect. 7.4.1) are made to adapt it to the moonlight conditions:

- The camera calibrations are adjusted to account for fast changes in the observing conditions: interleaved calibration events during the data taking are acquired to perform a continuous correction of the initial calibration parameters (Cat B calibrations; see Sect. 4.3.1).
- In addition, we consider the algorithm NeighborPeakWindowSum of ctapipe to integrate the pulse of the waveform. NeighborPeakWindowSum sums the signal over a window centred around the peak position, which is determined from the averaged waveform of the triggered pixel and its adjacent pixels. In particular, we considered a window width of 7 waveform samples, starting 3 samples before the estimated peak position (see Sect. 4.3.2).
- Concerning image cleaning, we employ the tail-cut method with the time-coincident condition and dynamic cleaning. The image cleaning levels are increased by a factor ∼2.5 compared with the values applied to the dark data. These values are determined by limiting the fraction of images from interleaved pedestal events that pass the image cleaning to less than 4%.

These adaptations are considered after evaluating multiple charge-integration and image-cleaning algorithm combinations. For example, we test different window shifts and sizes to integrate the signals (see Sect. 4.3.2), ranging between 8 (4) and 6 (2) samples in size (shift). We also study if the pulse shape of the signal between the observations in nominal and reduced HV significantly changed. However, differences of a few per cent are found among them. Therefore, no serious effects on the analysis are expected from changes in the pulse shape. Moreover, as the integration window is modified with respect to the standard one (see Sect. 4.3.2),

the global scaling factor applied to the calibrations is modified accordingly (see Sect. 4.3.1).

During the GRB observations in moonlight conditions, the NSB level increased during the data taking following the Moon rising. The NSB level between two consecutive 20 min observations is high enough to require a per-observation analysis, where the NSB on the MC simulations and image cleaning levels are consequently adjusted. The MC events are simulated with noisier waveforms to match the level of observed NSB in the data. Subsequently, we fine-tune the match between MC and observational data on a per-observation basis at the camera image level by adding random Poissonian noise.

We select gamma-like events and produce the final analysis products following the same procedure as for the analysis in dark conditions. For the moon-adapted analysis, the event selection cuts are optimised with Crab Nebula observations in similar NSB conditions to GRB 221009A with reduced HV. A cut in *intensity* below 200 p.e. is applied to remove dim events. For the spectral analysis, we use energy-dependent, efficiency-based cuts of 50% and 70% for the *gammaness* and θ parameters, respectively. In this case, the tightest *gammaness* cut from the tested set is selected because the alternative cuts (70% and 90% in *gammaness*), while also yielding results consistent with the Crab Nebula spectrum reported in the literature, are more sensitive to variations in the lower energy bound of the fitting range.

The tighter image cleaning with increasing NSB and different telescope pointing directions as a function of ZA affects the energy threshold of the analyses. In particular, for 10 October, the energy threshold, assuming an observed spectral index of $\Gamma=-3$, increases from $\sim\!100\,\text{GeV}$ to $300\,\text{GeV}$ from the first to the last observation.

7.4.3 Source-dependent analysis

The same configurations as the source-independent analysis are adapted for the MC production for both the moon and dark datasets. Specifically, the same techniques are used to match the NSB level of the simulation with that of the moonlight observations, and the same algorithms are used to optimise the charge extraction and the image cleaning performance of LST-1 (see Sect. 7.4.2). Parameters unique to the source-dependent analysis are introduced for the RF generation (see Sect. 4.3.4). Differences in the analysis settings arise after the event reconstruction of each Cherenkov shower image. For the spectral analysis, the efficiency of energy-dependent gammaness cut is 50% and 80% for moonlight and dark datasets, respectively. The efficiency of energy-dependent α parameter cut is 70% for both the moon and dark dataset.

7.5 RESULTS

The reconstructed squared angular distributions of gamma-like events centred on the GRB 221009A coordinates and the average background regions for the first day of observation ($T_0 + 1.33$ d) are shown in Fig. 7.1. We obtain an excess at 4.1σ statistical significance (using equation 17 of Li and Ma 1983). For the second day of observations at $T_0 + 3.33$ d, the statistical significance is 0.8σ . As no signal was

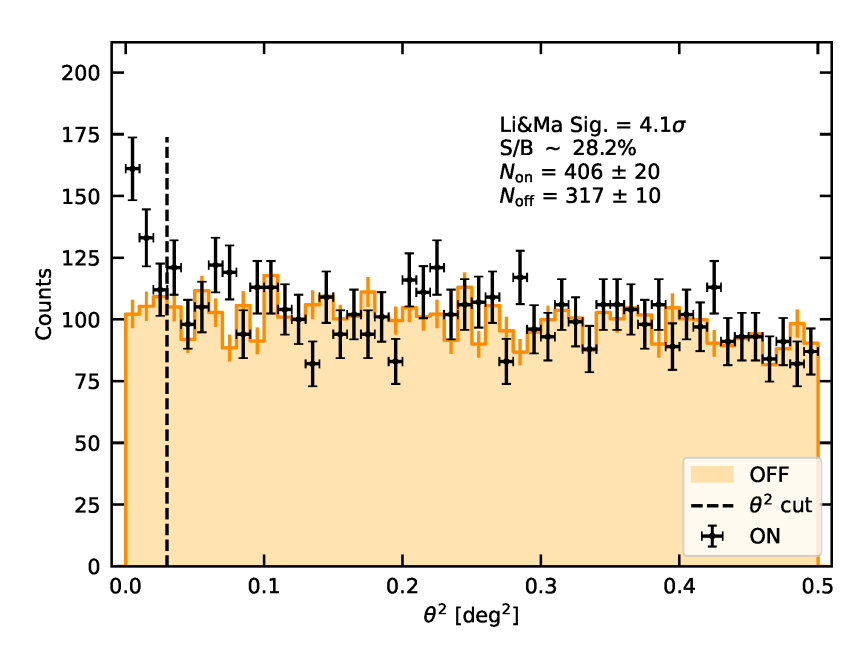


Figure 7.1: θ^2 plot using observations recorded at $T_0 + 1.33$ d. The θ^2 distributions centred at the GRB 221009A position (ON) and the mean background estimation from the three reflected regions (OFF) are displayed as black points and dark orange error bars, respectively. The vertical dashed line indicates the angular size used to compute the detection statistical significance (Li&Ma Sig.) and S/B. The vertical error bars correspond to 1σ statistical errors.

observed at $T_0 + 3.33$ d, guided by the power-law temporal decay observed at other wavelengths, we stack all the dark time data, which allows us to obtain better constraints on the SED of GRB 221009A. No significant excess is observed using all the dark observations together (-0.4σ using data within $T_0 + [6.30, 17.32]$ d). Results using the source-dependent analysis chain are consistent with that reported above for the source-independent analysis: at $T_0 + 1.33$ d, the excess reaches a statistical significance of 4.6σ , while the significance is compatible with the background for the datasets at later times. The angular distributions of gamma-ray events for the first night are shown in Fig. 7.2. Instead of θ angle for the standard analysis, the α angle is used here to calculate the excess counts.

A power-law model is assumed to describe the putative intrinsic signal of GRB 221009A to perform the spectral analysis. The expected attenuation due to the EBL is accounted for using the Domínguez et al. (2011) model for redshift z=0.1505 (see Sect. 2.3.1). We note that for such values of z, the choice of the EBL model is not critical. Given the limited significance of the excess, the intrinsic spectral index (Γ) is fixed to $\Gamma=-2$ during the fitting process and the computation of the SED and light curve. This index is similar to that seen by LHAASO at much earlier epochs (LHAASO Collaboration et al. 2023). We also checked the case of assuming $\Gamma=-3$, and obtain comparable results. The range of Γ we consider covers the value of $\Gamma\sim-2.5$ determined by Fermi-LAT at energies and times that overlap with the LST-1 observations (Axelsson et al. 2024). ULs are computed at a 95% confidence level when the TS is below 4, otherwise points with error bars are placed. Error uncertainties correspond to 1σ statistical errors.

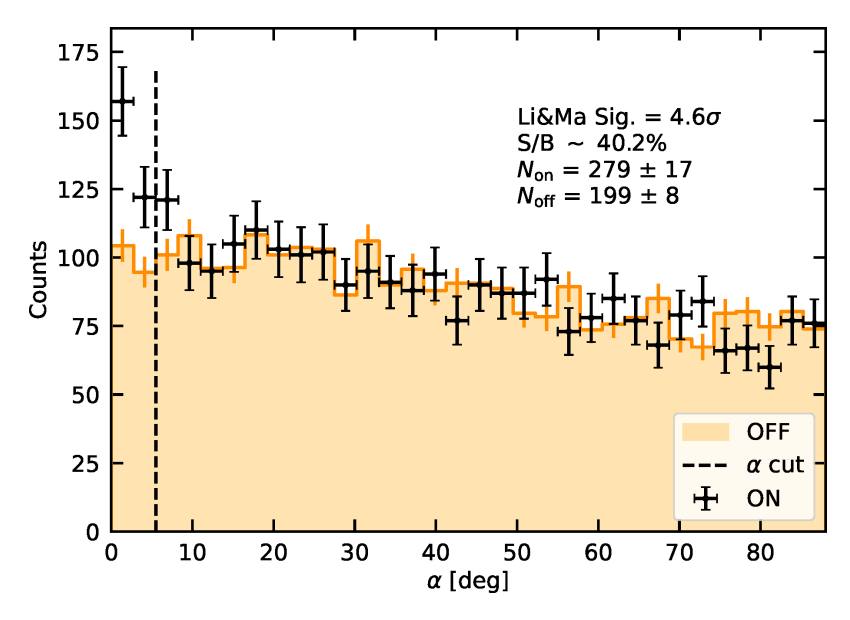


Figure 7.2: Same as Fig. 7.1, but displaying the α distributions at $T_0 + 1.33$ d after analysis cuts. The vertical dashed line indicates the α cut value, below which the detection statistical significance (Li&Ma Sig.) is computed. The vertical error bars correspond to 1σ statistical errors.

Figure 7.3 shows the SEDs for the three periods using the moonlight ($T_0 + 1.33$ d and $T_0 + 3.33$ d) and dark ($T_0 + [6.30, 17.32]$ d) observations. The lower energy bound is 200 GeV and 50 GeV for the moonlight and dark analyses, respectively. We can constrain the EBL-corrected SED points to be below a few $10^{-11}\,\mathrm{erg}\,\mathrm{cm}^{-2}\,\mathrm{s}^{-1}$ at E < 1 TeV, with the most constraining ULs at several hundreds of GeV. For the first observation day, we obtain a SED point with a local TS = 6.9 in the energy bin between 0.38 TeV and 0.74 TeV. We obtain compatible SED results with the source-dependent analysis, for which a significant SED point (TS = 9.0) is also obtained in the same energy bin for the observations at $T_0 + 1.33 \,\mathrm{d}$, while ULs constrain the emission at a similar differential flux level. The comparison between the SEDs from the source-independent and source-dependent analysis are shown in Fig. 7.4. We note that the SED for the source-dependent analysis at $T_0 + 1.33$ d is shifted towards higher flux values/ULs, compared to the source-independent SED across the studied energy range. On the contrary, this shift is not visible for $T_0 + 3.33$ d and $T_0 + [6.30, 17.32]$ d data (see Fig. 7.4). The presence of this shift only at $T_0 + 1.33$ d may be caused by accentuated systematic uncertainties due to the high NSB conditions affecting these observations. Yet, overall, no significant difference is observed between the two analysis for any of the periods.

The effect of varying the background normalisation by $\pm 0.5\%$ is shown in Fig. 7.3 to evaluate possible systematic errors in the background estimation. A $\pm 0.5\%$ relative difference in events between the control OFF regions and the mean OFF events are observed for the dark observations at the lowest energies ($E < 200\,\text{GeV}$), where the number of events is large, $\mathcal{O}(10^5-10^6)$. The modification of the background normalisation by $\pm 0.5\%$ corresponds to a $\sim 60\%$ relative difference in the estimated SED ULs at the lowest energies for $T_0 + [6.30, 17.32]$ d. As pointed out in Abe et al. (2023b), the monoscopic configuration of LST-1 leads to modest background suppression power close to the threshold of the telescope. On the contrary, the tighter

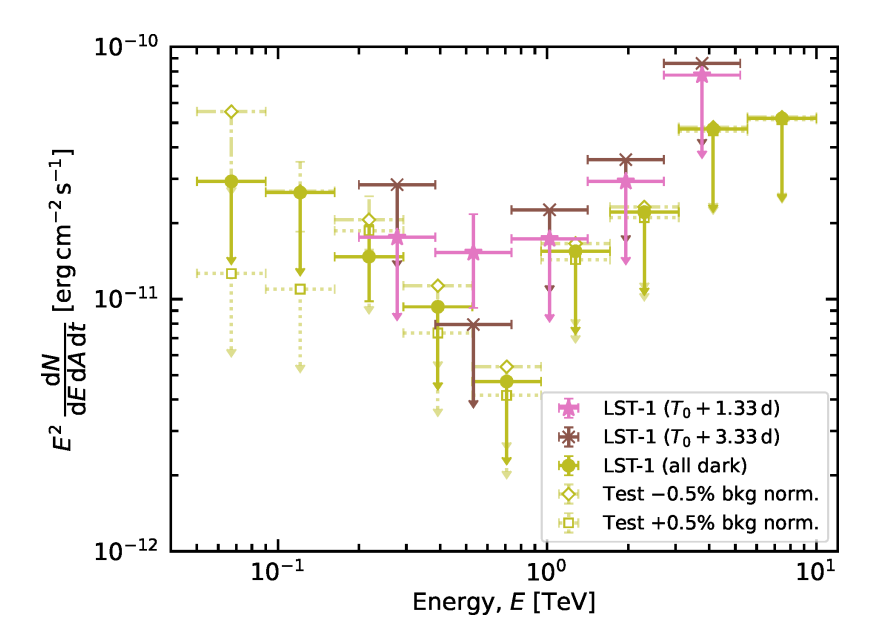


Figure 7.3: Intrinsic SED of GRB 221009A corrected for EBL attenuation on 10 October 2022 $(T_0+1.33\,\mathrm{d};\,\mathrm{pink})$, 12 October 2022 $(T_0+3.33\,\mathrm{d};\,\mathrm{brown})$ and between 15 and 27 October 2022 (all dark, $T_0+[6.30,17.32]\,\mathrm{d};\,\mathrm{olive})$, respectively. For the latter SED, the diamond and square olive empty markers show the effect of increasing and reducing by 0.5% the normalisation of the background, respectively.

cuts and higher energy fit range used for the moonlight observations reduce the number of events to $\mathcal{O}(10^3)$, making the systematic uncertainty associated with the background normalisation not relevant for this dataset. Applying the background normalisation test on the estimated SEDs at $T_0 + 1.33$ d and $T_0 + 3.33$ d results in small changes (less than 3%).

The integral energy flux is computed keeping the intrinsic spectral index of the power-law model fixed to $\Gamma=-2$, the same value assumed in the SED computation. The energy flux with LST-1 is computed between 0.3 TeV to 5 TeV for a clear comparison with data from other VHE gamma-ray experiments. Note that the computed energy flux depends on the choice of the intrinsic spectral index since the higher energies are more affected by EBL attenuation. If $\Gamma=-3$ is adopted, the energy flux is reduced by about a factor of 2. Additionally, the integration interval at high energies is loosely constrained compared with the lowest energies, which gathers most of the observed excess.

The energy flux is estimated in four different time periods, two for the moonlight observations ($T_0 + 1.33 \,\mathrm{d}$ and $T_0 + 3.33 \,\mathrm{d}$) and two for the dark observations. The first subset of the dark dataset gathers the data recorded during intervals closer to the burst trigger ($T_0 + [6.30, 8.30] \,\mathrm{d}$), while the second collects those at later intervals ($T_0 + [14.30, 17.32] \,\mathrm{d}$). This is motivated by the wide time window of the dark observations, and the lack of good-quality data for several days in a row (see Table 7.1). These results are shown in Fig. 7.5, starting at about $10^5 \,\mathrm{s}$ after the burst trigger.

At $T_0 + 1.33$ d, both the energy flux and UL point obtained with LST-1 are shown given the putative signal on this observation day (TS = 4.6 in the energy range of 0.3–5 TeV). The ULs at E = [0.3, 5] TeV constrain the EBL-corrected energy flux

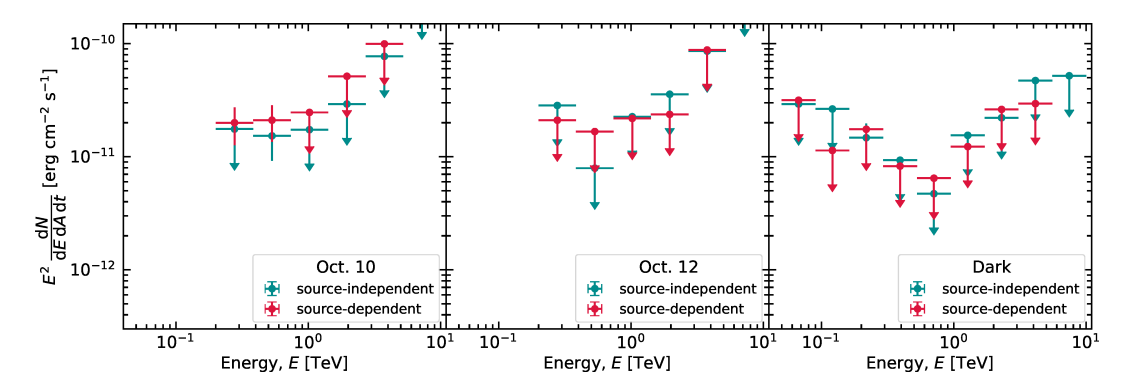


Figure 7.4: Comparison of SEDs between source-independent (blue) and source-dependent (red) approaches using the datasets on 10 October 2022 ($T_0 + 1.33$ d; left), 12 October 2022 ($T_0 + 3.33$ d; middle) and between 15 and 27 October 2022 (all dark, $T_0 + [6.30, 17.32]$ d; right).

at the level of a few $10^{-11}\,\mathrm{erg}\,\mathrm{cm}^{-2}\,\mathrm{s}^{-1}$. The light curve derived with the source-dependent analysis is consistent with that in Fig. 7.5 and can be compared with the source-dependent light curve in Fig. 7.6. However, at $T_0+1.33\,\mathrm{d}$, the energy flux between 0.3 TeV to 5 TeV (TS=14.3) for the source-dependent analysis is about two times higher than the energy flux for the source-independent analysis. They are separated by 1.5σ when considering the error bars of the data points. This suggests that systematic errors are the responsible source of error for this mismatch and are comparable to the statistical ones.

The energy flux of GRB 221009A measured by different instruments is also shown in Fig. 7.5. The light curve spans over 20 days with the reference time at $T_0 + 226 \,\mathrm{s}$, the VHE afterglow onset (T^* ; LHAASO Collaboration et al. 2023). Right after the burst trigger, LHAASO unveils the onset of the afterglow emission at VHE gamma rays (0.3–5 TeV) during the first hour after the burst. Coincident with LHAASO, Fermi-LAT and AGILE-GRID detect GRB 221009A in the HE band (Axelsson et al. 2024; Tavani et al. 2023). In particular, an extended emission up to few 10^5 s is detected with Fermi-LAT (0.1–100 GeV), coincident in time with part of the LST-1 observations. In Fig. 7.5 we include only the light curve obtained with AGILE-GRID in the HE gamma-ray band within 1 ks after T_0 for reference. The corresponding Fermi-LAT light curve is excluded from this time interval to avoid overcrowding the figure. After several hours, a preliminary differential flux UL at 1 TeV (Ayala and HAWC Collaboration 2022) is reported with HAWC that is shown in Fig. 7.5 as a UL in energy flux (0.3–5 TeV) corrected for EBL attenuation with the Domínguez et al. (2011) model and assuming an intrinsic spectral index of $\Gamma = -2$. HAWC bridges the early observations by LHAASO at VHE gamma rays with the first observations performed by an IACT from LST-1 at $T_0 + 1.33$ d. Monitoring by IACTs continued during the following days, leading to several ULs with H.E.S.S. and LST-1. The original H.E.S.S. energy fluxes, in the range E = [0.65, 10] TeV, are recomputed to the 0.3–5 TeV energy range using the spectral index value assumed in Aharonian et al. (2023). The recomputed energy-flux ULs constrain the emission at a similar level to LST-1 ULs. These gamma-ray observations are summarised in the light curve in Fig. 7.5, where we also plot the Swift-XRT energy flux (0.3–10 keV) for reference.

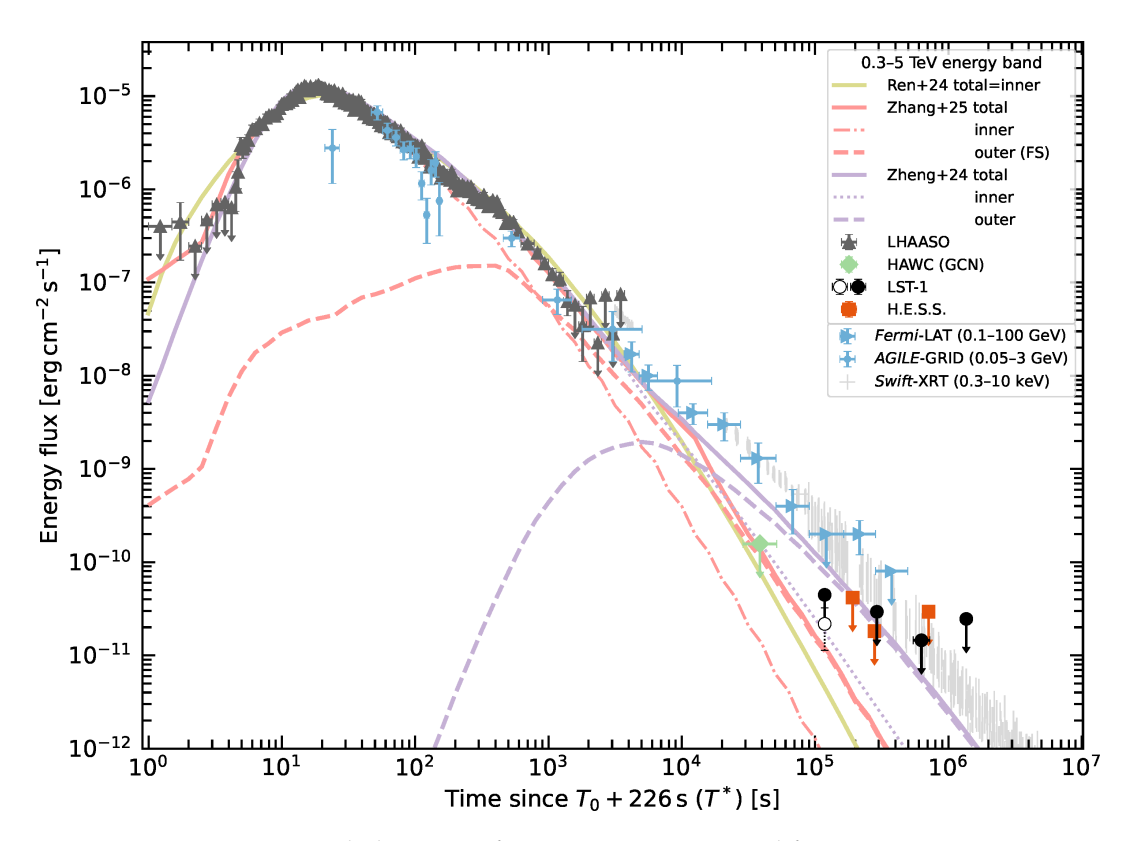


Figure 7.5: MWL intrinsic light curve of GRB 221009A corrected for EBL attenuation versus time since the burst trigger (*T*₀) shifted by +226s (see text). The energy fluxes for the energy range 0.3–5 TeV with LHAASO (dark grey vertical triangles; LHAASO Collaboration 2023), HAWC (green diamond; adapted from Ayala and HAWC Collaboration 2022, see text), LST-1 (black filled and empty circles for ULs and the energy flux point, respectively; this work) and H.E.S.S. (orange squares; adapted from Aharonian et al. 2023, see text) are compared with the best-fit emission models from Ren et al. (2024), Zhang et al. (2025), and Zheng et al. (2024) in pale gold, red and purple, respectively. For the latter two models, the contributions from the inner and outer jet regions are also shown separately. In addition, the light curve at HE gamma rays with *AGILE*-GRID (light blue dots; Tavani et al. 2023) and *Fermi*-LAT (light blue horizontal triangles; Extended Table 3 of Axelsson et al. 2024) are displayed with the energy fluxes at X-rays with *Swift*-XRT (light grey; Williams et al. 2023).

In summary, a positive deviation in excess counts from a background-only hypothesis is obtained at 4.1σ in the region of GRB 221009A with LST-1 at T_0 + 1.33 d. Afterwards, we measure no significant excess in non-coincident days between T_0 + [3.33, 17.32] d. The SEDs with LST-1 probe the afterglow emission at the lowest energies of the VHE band, an energy range not previously studied with good sensitivity for GRB 221009A. In particular, the best differential sensitivity with LST-1 is obtained at few hundreds of GeV (Abe et al. 2023b), where the effect of EBL attenuation is small. The energy fluxes obtained with LST-1 provide deep constraints at a few $10^{-11}\,\mathrm{erg}\,\mathrm{cm}^{-2}\,\mathrm{s}^{-1}$ between 0.3–5 TeV after T_0 + 1.33 d. The LST-1 observations on 10 October 2022 are the closest to T_0 obtained by an IACT, filling the gap between the HAWC UL (approximately one day before) and H.E.S.S. observations (approximately one day after).

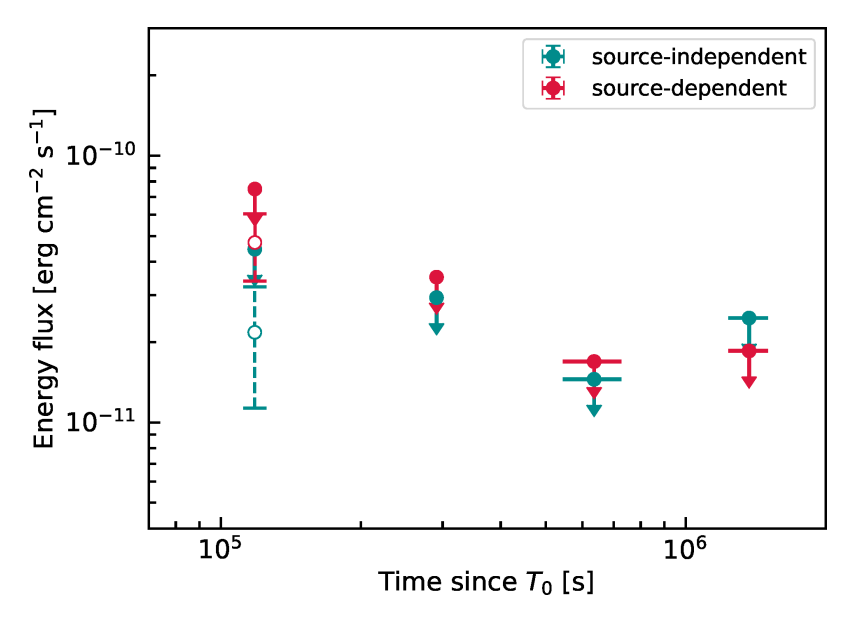


Figure 7.6: Comparison of intrinsic light curves (0.3–5 TeV) between source-independent (blue) and source-dependent (red) approaches. As in Fig. 7.5, both the energy flux and ULs at $T_0 + 1.33$ d, are shown to illustrate the putative signal. Note that data points after $T_0 + 10^6$ s cover different time ranges due to the different data selection criteria between the analyses.

7.6 DISCUSSION

The results obtained from observations of GRB 221009A with LST-1 described above are compared with selected theoretical models for the MWL emission of this burst, and the physical implications are addressed below.

The VHE light curves of GRB 221009A observed by LHAASO in different energy bands are consistent with broken power laws, implying that most of the emission originates from the afterglow. A key finding is the achromatic break in the light curve at $\sim T^* + 670 \,\mathrm{s}$. This is most plausibly interpreted as a jet break. The term "break" refers to the change in the slope of the decay in the light curve and it is caused by a geometric effect of the jet. In particular, it appears by the decrease in emissivity when the opening angle of the relativistically beamed radiation from the decelerating blast wave becomes wider than that of the emitting jet plasma (Sari et al. 1999; Rhoads 1999)[†]. The jet break time constrains the halfopening angle of the jet to be $\sim 0.6^{\circ}$, much narrower than that inferred for most previously known GRBs (LHAASO Collaboration et al. 2023). Coverage at other wavelengths contemporaneous with the LHAASO observations is sparse, but Xrays were measured at some early epochs by Insight-HXMT and GECAM-C with light curves similar to LHAASO, showing that the emission can originate from the same narrow jet (An et al. 2023). If this narrow jet was the only emitting region, light curves at all other wavelengths after the break time are expected to be relatively steep, similar to that at VHE gamma rays seen by LHAASO. However, the observed HE gamma-ray, X-ray, and optical light curves at $T \gtrsim T^* + 1000 \,\mathrm{s}$ reveal decay slopes that are considerably shallower, strongly indicating that an

[†]For alternative interpretations, see Khangulyan et al. (2024) and Foffano et al. (2024)

emission region separate from the narrow jet is necessary. The most likely such region is a wider, outer jet surrounding the narrower, inner jet. In general, physical properties of the jet such as the kinetic energy E_{kin} and bulk Lorentz factor $\Gamma_{b,0}$ can be distributed as nontrivial functions of angle θ from the jet axis. GRB afterglow models assuming such jet configurations as initial conditions are referred to as "structured jet" models (Mészáros et al. 1998; Sharan Salafia and Ghirlanda 2022), as opposed to the standard, simpler assumption employed in most earlier studies of "top-hat" jets, where E_{kin} and $\Gamma_{b,0}$ are distributed uniformly up to a certain angle. Structured jets are physically more realistic, as such configurations can arise when the jet forms (Zhang et al. 2024), and are also robustly expected when the jet propagates through the progenitor star and interacts with stellar material (Morsony et al. 2007; Mizuta and Ioka 2013; Gottlieb et al. 2021). The afterglow of GRB 170817A, associated with a neutron star merger detected in GWs, provided the first clear evidence for a structured jet in a GRB, albeit for an atypical, short GRB (Mooley et al. 2018). For long GRBs, some previous studies suggested that the available data can be modelled better by structured jet models than simpler models (Sharan Salafia and Ghirlanda 2022; Sato et al. 2023a), but the conclusions were not definitive. GRB 221009A provides the strongest case to date that a structured jet is indispensable to explain the MWL afterglow of a long GRB (Gill and Granot 2023; Sato et al. 2023b; O'Connor et al. 2023; Ren et al. 2024; Zheng et al. 2024; Zhang et al. 2025).

The MWL afterglow of GRB 221009A offers unique prospects for probing the jet structure in a long GRB that may be difficult to achieve otherwise. However, as the functional forms for $E_{\rm kin}(\theta)$ or $\Gamma_{\rm b,0}(\theta)$ are not known a priori, structured jet afterglow models necessarily entail a large number of parameters, often more than 20, compared to simpler afterglow models usually characterised by 8 parameters. Even for the extensive MWL data obtained for GRB 221009A, this poses a challenge.

This is illustrated by comparing three structured jet afterglow models in the literature that describe reasonably well the published MWL data of GRB 221009A: Ren et al. (2024), Zheng et al. (2024), and Zhang et al. (2025). All three models assume the density profile of the circumburst medium $n_{\text{CBM}}(R)$ to be constant with radius R in the inner parts and declines as R^{-2} in the outer parts. Also common to all three are an inner jet component that is uniform but narrow, as required to account for the observed data before a few ks after T^* . At these epochs, the emission is attributed mainly to the forward shock of this inner jet, with X-rays and VHE gamma rays dominated by synchrotron and SSC emission, respectively, and HE gamma rays bridging these two components (see Sects. 2.2.1 and 2.2.2). The models also have outer jet components with assumed functional forms for $E_{\text{kin}}(\theta)$ and $\Gamma_{\text{b,0}}(\theta)$ that are somewhat different between the models, though not to a significant extent. Synchrotron emission from the forward shock of this outer jet is primarily responsible for the optical to X-ray emission starting from a few ks after T^* . For each model, the authors determined the best-fit values for the parameter set.

Figure 7.5 compares the light curves at 0.3–5 TeV for the available data including our LST-1 results with the models presented in Ren et al. (2024), Zheng et al. (2024), and Zhang et al. (2025). As a reference point for the power radiated in VHE gamma rays, we also show only the data for the X-ray and HE light curves. Corresponding

model curves, as well as optical and radio data vs models, are shown in the papers above. Interestingly, although all models provide broadly acceptable fits to the published dataset including LHAASO, the VHE predictions for the models diverge at late times, differing by more than an order of magnitude in energy flux between them after $\sim T^* + 1\,\mathrm{d}$. Thus, in conjunction with the published MWL data, our LST-1 results provide valuable additional constraints on these structured jet models.

Firstly, conservatively considering our data at $T_0 + 1.33$ d to be a UL, we disfavour the model by Zheng et al. (2024) whose VHE gamma-ray flux around this time due to SSC from the outer jet is the highest among the three, and which was marginally consistent with the H.E.S.S. ULs. Given the numerous model parameters, it is possible that a different set of parameters can still allow a suitable fit of all data; nevertheless, our UL disfavours at least the parameter space discussed as fiducial by Zheng et al. (2024). On the other hand, the VHE gamma-ray emission in the models by Ren et al. (2024) and Zhang et al. (2025) are below our UL.

Next, considering our 4.1σ excess as actual gamma rays from GRB 221009A, the VHE gamma-ray flux is quite consistent with the Zhang et al. (2025) model. While the VHE gamma-ray flux in the Ren et al. (2024) model falls somewhat short of our data, it may not be incompatible, as other parameter values than the fiducial ones might solve this discrepancy. It is notable that although the VHE gamma-ray flux at $\sim T^* + 1$ d in these two models are similar, their origins are quite different. For Ren et al. (2024), the VHE gamma-ray emission at $\sim T^* + 1$ d is a continuation of what is seen by LHAASO, with the SSC emission from the inner jet dominating at all times. Contrastingly, for Zhang et al. (2025), the SSC emission from the outer jet takes over as the dominant component starting from a few ks after T^* , as was also the case for Zheng et al. (2024). Distinguishing between Ren et al. (2024) and Zhang et al. (2025) is not possible with the current data, and requires more spectral and temporal coverage.

Despite the apparent similarities in the model assumptions, comparison of the best-fit parameter values actually reveals significant differences among the three models. For example, the values of $n_{\text{CBM}}(R=0)$ differ between the models by up to 4 orders of magnitude, and there are correspondingly large differences in the parameters related to the magnetic field ϵ_{B} and electron acceleration efficiency ϵ_{e} . Thus, even with the extensive MWL data obtained for GRB 221009A, realistic structured jet models still appear to be under-constrained, and significant degeneracies in the parameters remain.

We present in Fig. 7.7 a brief graphic comparison of the parameters in the structured jet afterglow models of Ren et al. (2024), Zheng et al. (2024), and Zhang et al. (2025). The aim is to simply illustrate the sizeable disparities in the best-fit parameters between the models, rather than a detailed discussion of the physical implications or the quality of fits to the observed data, which is beyond our scope.

Figure 7.7 compares $E_{\rm kin}(\theta)$ (initial kinetic energy vs angle from jet axis), $\Gamma_{\rm b,0}(\theta)$ (initial bulk Lorentz factor vs angle from jet axis), $n_{\rm CBM}(R)$ (circumburst medium density vs radius), and the microphysical parameters $\epsilon_{\rm B,0}$ (fraction of post-shock energy in magnetic field), $\epsilon_{\rm e,0}$ (fraction of post-shock energy in accelerated electrons), and $\xi_{\rm e,0}$ (fraction in number of accelerated electrons) for the inner jet, and analogous parameters $\epsilon_{\rm B,1}$, $\epsilon_{\rm e,1}$ and $\xi_{\rm e,1}$ for the outer jet. Only Ren et al. (2024) provide errors

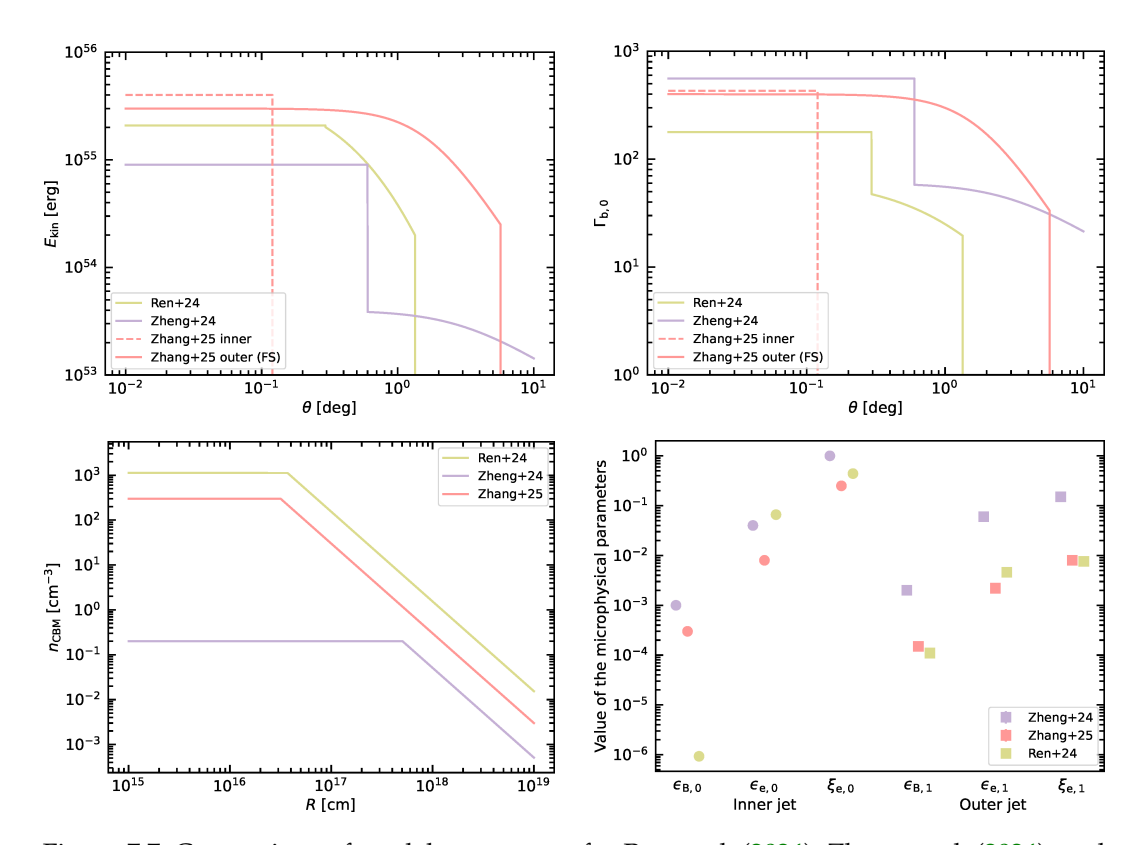


Figure 7.7: Comparison of model parameters for Ren et al. (2024), Zheng et al. (2024), and Zhang et al. (2025). Top left: $E_{\rm kin}(\theta)$, initial kinetic energy vs angle from jet axis. Top right: $\Gamma_{\rm b,0}(\theta)$, initial bulk Lorentz factor vs angle from jet axis. Bottom left: $n_{\rm CBM}(R)$, circumburst medium density vs radius. Bottom right: $\varepsilon_{\rm B,0}$, fraction of post-shock energy in magnetic field, $\varepsilon_{\rm e,0}$, fraction of post-shock energy in accelerated electrons, and $\xi_{\rm e,0}$, fraction in number of accelerated electrons for the inner jet; $\varepsilon_{\rm B,1}$, $\varepsilon_{\rm e,1}$, and $\xi_{\rm e,1}$, analogous quantities for the outer jet.

for the parameters from a Markov Chain MC analysis, and these are not shown for consistency in the comparison.

Particularly large differences between the models can be seen for $\epsilon_{\rm B,0}$, $n_{\rm CBM}$ at small R, and $E_{\rm kin}(\theta)$ and $\Gamma_{\rm b,0}(\theta)$ at large θ . This indicates that for constraining such structured jet afterglow models with large number of parameters, the available MWL data is insufficient, and requires more extensive spectral and temporal coverage including VHE observations. In this context, GRB are among the primary targets for follow-up observations with CTAO (Inoue et al. 2019), which is expected to shed light on key aspects of GRB physics due to its improved sensitivity. In particular, the low energy threshold that LSTs offer to CTAO allows probing the lowest gamma-ray energies that are less affected by EBL attenuation (see Sects. 2.3, 3.2.3.2 and 3.2.3.3).

Quantitatively evaluating the impact of our data for constraining the model parameters and the physics of structured jets is beyond the scope of this work. Below we outline qualitatively how this may be approached with future, high-sensitivity observations of GRBs with IACTs covering the earliest to latest possible timescales. For a given epoch ("snapshot"), a sufficiently well measured broadband spectrum of the afterglow, particularly spectral breaks that reflect electron injection and cooling, and the SSC to synchrotron flux ratio, mainly constrain the

microphysical parameters such as the electron injection index p, $\epsilon_{\rm B}$, and $\epsilon_{\rm e}$ (see Chapt. 2). The VHE gamma-ray band is crucial as the emission is likely distinct from electron synchrotron radiation, with different dependences on the parameters (Piran and Nakar 2010; Inoue et al. 2013; Nava 2018). In practice, this may not be straightforward as components each from the inner and outer jets can overlap, but at least it can be done for the component dominating at that epoch. Obtaining a series of such snapshots throughout the afterglow evolution then constrains mainly the dynamical parameters $E_{\rm kin}(\theta)$ and $\Gamma_{\rm b,0}(\theta)$, and $n_{\rm CBM}(R)$, leading us to valuable new information on the physics of GRB jet formation and propagation. There are also potential multi-messenger implications for CRs and neutrinos as discussed in Zhang et al. (2025), whose model appears most consistent with our data. They attribute the emission exceeding 10 TeV seen at $\sim T_0 + [500, 800]$ s (LHAASO Collaboration 2023) primarily to synchrotron radiation by UHE protons accelerated at the reverse shock, a hypothesis that could have been tested if sufficiently early follow-up by IACTs was possible.

7.7 CONCLUSIONS

GRB 221009A, the "brightest-of-all-time" GRB and first long GRB with strong evidence for a structured jet, was observed by LST-1. The high NSB in the hours following the GRB alert due to the full Moon prevented rapid follow-up by IACTs. LST-1 was the first IACT to start observing at $T_0 + 1.33$ d, covering epochs that were missed by other VHE facilities. Here we addressed for the first time the challenge of analysing LST-1 data of a GRB in moonlight conditions, presenting a scheme adapted to handle the high NSB conditions at the analysis level. We obtain an excess signal at a statistical significance of 4.1σ for that night, constraining the intrinsic emission from GRB 221009A at the level of few 10^{-11} erg cm⁻² s⁻¹ at E = 0.3-5 TeV. ULs are derived at $T_0 + 3.33$ d, still under moonlight conditions, and during later times, from $T_0 + 6.30 \,\mathrm{d}$ to $T_0 + 17.32 \,\mathrm{d}$ without the Moon. These analyses were cross-checked with an independent method and compatible results were obtained. Our data was compared to different realistic models of afterglows from structured jets that adequately describe published MWL data for GRB 221009A, but imply significant differences in the VHE gamma-ray emission after approximately one day. Depending on the model, this can be dominated by SSC from either the narrow inner jet or the wider outer jet, and the flux can vary by more than an order of magnitude. Although all models were consistent with the LHAASO data and H.E.S.S. ULs, those that implied VHE gamma-ray flux at one day significantly exceeding 10^{-11} erg cm⁻² s⁻¹ are disfavoured by our results. If the observed excess corresponds to a gamma-ray signal from GRB 221009A, the VHE gamma-ray flux is consistent with a subset of the models, although we cannot distinguish between an inner and outer jet origin. Future, sensitive IACT observations of GRBs, such as CTAO, over a broad range of timescales, together with comprehensive MWL data, should help to clarify the nature of structured jets and provide new insight into the physics of jets in long GRBs.

8

This Thesis was developed during a decisive period in ground-based VHE astrophysics. A transition is occurring from private, experiment-based IACT facilities, such as MAGIC, to the establishment of an open IACT observatory, CTAO. The studies reported here focus on the scientific exploitation of LST-1 during its commissioning phase. The LST-1 has been designed to provide unique capabilities to detect gamma-ray sources at energies from tens to hundreds of GeV. This Thesis accounts for the study of several type of transient systems based on observations conducted with LST-1, validating its performance to follow up fast-evolving gamma-ray sources.

GENERAL CONCLUSIONS

We have been involved in the entire process leading to the results reported in this Thesis: from the scientific justification of the observation proposals, to the evaluation of follow-up observations, the data acquisition, the reduction and analysis of these data, as well as the interpretation and publication of the obtained results. Particular emphasis was placed on testing and optimising the data analysis pipeline. We contributed to the development of a number of software packages and scientific tools required for the analysis of LST-1 data.

During the development of this Thesis, multiple transient or variable sources were observed with LST-1, including neutrino alerts, GW events, GRBs, AGN flares, gamma-ray and X-ray binaries, stellar flares, novae, supernovae, soft gamma repeaters, and colliding-wind binaries. Despite contributing to some extent to the acquisition and/or data analysis of these transient events, the main focus of the Thesis was on the study of novae, supernovae and GRBs:

- Novae. LST-1, together with the MAGIC and H.E.S.S. telescopes, have set a new milestone at VHE gamma rays with the detection of the eruption of RS Oph in 2021, the first nova detected at this energy range. Characterised with a very soft spectrum, the obtained results with LST-1 allow us to study RS Oph at tens of GeV, the lowest energies unveiled with IACTs. We use contemporaneous *Fermi*-LAT, MAGIC, and H.E.S.S. data with LST-1 to advance the physical understanding of this new VHE source type. A hadronic scenario provides a satisfactory explanation for the gamma-ray emission observed in RS Oph. Additional work has been developed to assess the possibility of detecting more novae with the LST array and when the CTAO is operational.
- Core-collapse supernovae. CCSNe remain undetected at VHE gamma rays.
 The potential of CCSNe to accelerate particles to TeV/PeV energies and the
 subsequent emission of gamma rays in relatively short timescales after the
 explosion make the LSTs well suited for the observation of CCSNe. We report
 the LST-1 observations of two close CCSNe, SN 2023ixf and SN 2024bcn,
 providing important constraints on their emission within the first months
 after the explosion.

• Gamma-ray bursts. The detection of VHE gamma-ray emission from long GRBs in 2019 provided a new window for the study of this type of transient events, which are nevertheless still poorly understood. LST-1 participated in the observations of GRB 221009A, the brightest GRB to date. We find a gamma-ray excess with a statistical significance of 4.1σ during the observations taken 1.33 days after the burst, followed by background-compatible results for the later days. We are able with these data to provide relevant constraints on its emission in a stage of the explosion for which no previous sensitive VHE observations were available.

All these achievements demonstrate the capabilities of LST-1 to follow up rapidly-evolving gamma-ray events and to advance and explore the physics leading to this transient emission. The three remaining LSTs of CTAO-N are being constructed by the time this Thesis is written. The stereoscopic observations with the four LSTs in the upcoming years will open a new window from tens to hundreds of GeV to faint and fast-evolving sources. The LSTs will be crucial for advancing the physical understanding and providing new insights into the poorly-known physics of gamma-ray transient sources. Hopefully, we may detect the first VHE electromagnetic counterpart of GWs, the first VHE detection of short GRBs and CCSNe, or a detailed characterisation of the processes leading to long GRBs and novae.



TEMPORAL RESOLUTION ESTIMATOR FOR TRANSIENT SOURCES

Studying fast variable emission is crucial for comprehending the acceleration process of gamma-ray sources and testing the validity of fundamental laws. We developed an algorithm, Temporal Resolution Estimator for Transient Sources (TRETS)* (Aguasca-Cabot et al. 2022, 2023), which aims to retrieve the shortest temporal resolution to obtain significant fluxes while considering a given threshold for the source detection significance level. This algorithm produces a variable light curve without a human-based time-bin definition that can bias the results.

We implemented an iterative process that increases the number of events used to compute the statistical significance of detecting a source over the background. Once the statistical significance surpasses a certain threshold (Y_1) , the flux is estimated assuming a given spectral model, e.g., the best-fit spectral shape of the entire dataset. An additional condition requires that the flux points statistical significance reaches a given threshold (Y_2) . These details can be specified by the user, among other features. The algorithm is developed for IACT data analysis. In particular, it uses gamma-like events whose primary particles are reconstructed. For more information about the data processing and the analysis methods used to reach this data level, we refer the reader to Chapt. 4. TRETS is developed in the framework of Gammapy (Donath et al. 2023). A detailed flowchart of the algorithm is shown in Fig. A.1.

The current version of the algorithm can only be used in aperture photometry analysis (see Sect. 4.1.6). As the algorithm aims to obtain the shortest time resolution, few counts are considered in the detection significance evaluation. As a result, we implemented both the frequentist and Bayesian approaches. The former uses equation 17 in Li and Ma (1983), while an equivalent equation for the Bayesian inference can be found in Gillessen and Harney (2005).

TRETS can be executed either from an event-wise list of gamma-ray-like events (DL3) or after binning them in different energy bins (DL4; see Sect. 4.2). This possibility provides the user with a flexible starting point to apply the algorithm, adds modularity to the tool, and avoids unnecessary re-analysis of archival data already processed. Moreover, this feature is particularly relevant for simplifying the numerical simulations.

TRETS can combine events from adjacent observations to overcome the typical non-continuous observation mode in IACTs. A maximum time window can be set to limit the time offset between the timestamp of the last event in the previous observation and the timestamp of the first event in the subsequent observation.

Two methods can be used to increase the number of events in each iteration: either a fixed number of events or a fixed time window. Figure A.1 considers the latter approach. Selecting either option depends on the specific scientific case and

^{*}https://github.com/aaguasca/TRETS

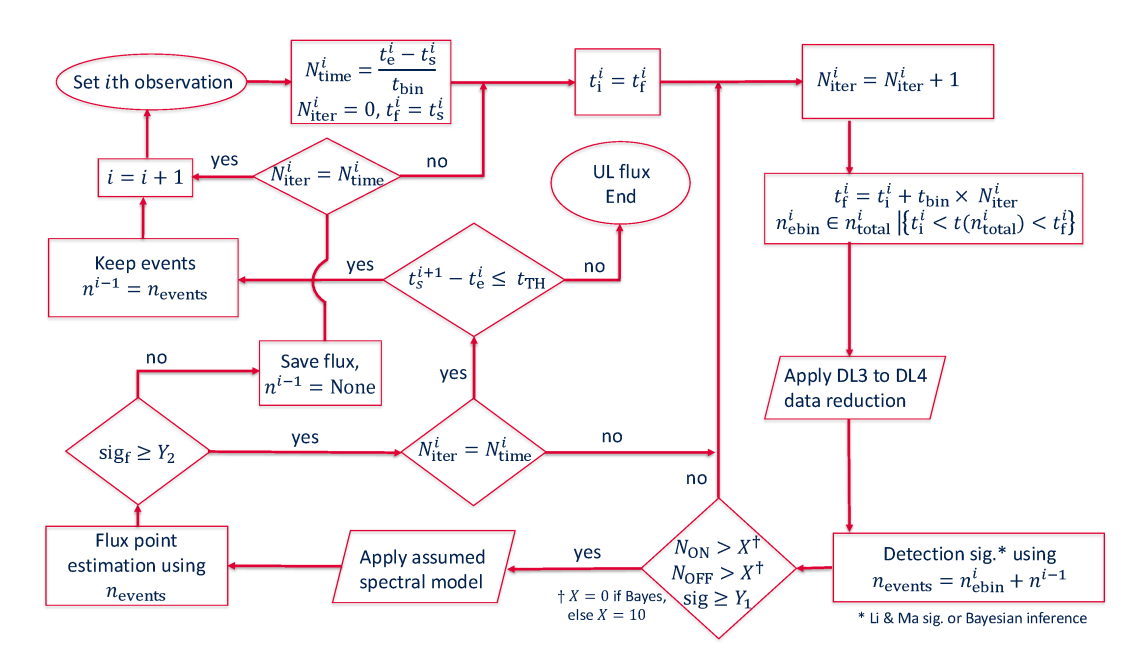


Figure A.1: Flowchart of the TRETS algorithm. n refers to the collection of events, t represents time, N indicates counters, and quantities with superscript i are associated with the ith observation. In particular, $t_{\rm s}^i$ and $t_{\rm e}^i$ are the time of the first and last event. $n_{\rm total}^i$ lists the total number of events. $N_{\rm ON}$ and $N_{\rm OFF}$ are the number of events from $n_{\rm events}$ located in the ON and OFF regions and are used to compute the significance (sig). Y_1 and Y_2 are the statistical significance thresholds set for the detection and the flux point, whose statistical significance value is ${\rm sig}_f$. $t_{\rm TH}$ is the maximum threshold time for combining the events between two observations, and $t_{\rm bin}$ is the time bin set by the user.

the computational cost. For example, a fixed time window may be recommended for data analysed with loose cuts due to the large number of events.

We applied the algorithm to both observational data and numerical simulations of transient gamma-ray sources to demonstrate the capabilities of TRETS. Section A.1 discusses the application of TRETS to numerical simulations of a transient source such as RS Oph, while Sect. A.2 presents the results for observational data obtained with LST-1 on BL Lacertae during a bright flare. Conclusions and future work are addressed in Sect. A.3.

A.1 APPLICATION TO NUMERICAL SIMULATIONS

The number of gamma-ray events from the source and background are simulated using Gammapy, which only allows simulations of gamma-ray events in a binned map in spatial and energy coordinates without the temporal information of the events. Therefore, the events within a simulated observation cannot be split sequentially based on the event timestamp. Therefore, TRETS performs the iterative process of adding events for the statistical significance computation on an observation-wise basis, i.e., each step adds the total number of events in each simulated observation. As a result, the shortest temporal resolution is limited to the livetime of the simulation itself (see example of RS Oph below).

Gammapy uses Poissonian distributions to describe the gamma-ray events simulated for signal and background. The expected number of events during a fixed simulation livetime is determined by the source model and the background model. We note that the forward-folding method is used to convert the source and background model into measured events by the experiment. Since the aperture photometry analysis is employed, only the Aeff and edisp are required (see Sect. 4.1.6.2).

We performed numerical simulations of RS Oph (see Sect. 5.2), making use of the IRFs for CTAO-N from prod5-v0.1 in the Alpha configuration (Cherenkov Telescope Array Observatory and Cherenkov Telescope Array Consortium 2021). We considered the same simulation prescription to model the spectral and temporal evolution of RS Oph, as done in Sect. 5.8.3. The livetime of the simulated observations was fixed to one minute. As a result, the numerical simulations consist of 60 observations of one-minute exposure per day for 60 days.

Figure A.2 shows the light curve obtained with TRETS (see settings in Table. A.1). At early times, when the source is bright, the algorithm divides the data into multiple flux points with short time bins. In contrast, as time goes by and the flux decreases following the power-law temporal decay, the time bins of the integral fluxes increase. The shortest and longest time intervals span observation exposures of 1 min to 15 h[†], respectively. We also show in Fig. A.2 the light curve obtained by combining the numerical simulations of five consecutive observation days, i.e., using a total of 5 h of observation time. Both light curves follow the same power-law temporal decay trend.

The unprecedented (possibly) sub-minute temporal resolution that may be achievable at early times in the RS Oph nova explosion will allow us to characterise the gamma-ray emission on these systems at timescales never explored. Using the TRETS algorithm to optimise time bins for statistically significant detections or well-sampled spectra could potentially uncover new physical insights from these systems. Firstly, a fine temporal sampling of the flux with sufficient photon statistics at a statistically significant level could reveal intra-night variability. The temporal resolution down to 1 min can probe the emission region on timescales never explored before, which may reveal enhanced emission that arises from particle acceleration in multiple time-evolving shocks in the ejecta (formed from internal shocks between multiple ejections of material or external shocks between ejecta and the inhomogeneous circumbinary medium). Secondly, the characterisation of the spectral emission at different times can improve our derivation of the radiating particle population energy spectrum to test the DSA models involved in the supersonic shocks of novae and the temporal evolution of the gamma-gamma pair creation with the low-energy photons from the photosphere.

A.2 APPLICATION TO OBSERVATIONAL DATA

BL Lacertae (BL Lac) is a jetted active galactic nucleus at z = 0.069. It was first detected at VHE gamma rays in 1998 (Neshpor et al. 2001) and detected by LST-1 on 11 July 2021 during an enhanced activity at gamma rays (Cortina and CTA LST Collaboration 2021). BL Lac is known to undergo short (a few minutes duration)

 $^{^{\}dagger}$ The time bin in Fig. A.2 has a width of \sim 15 days because 1 h of observation time is simulated per day.

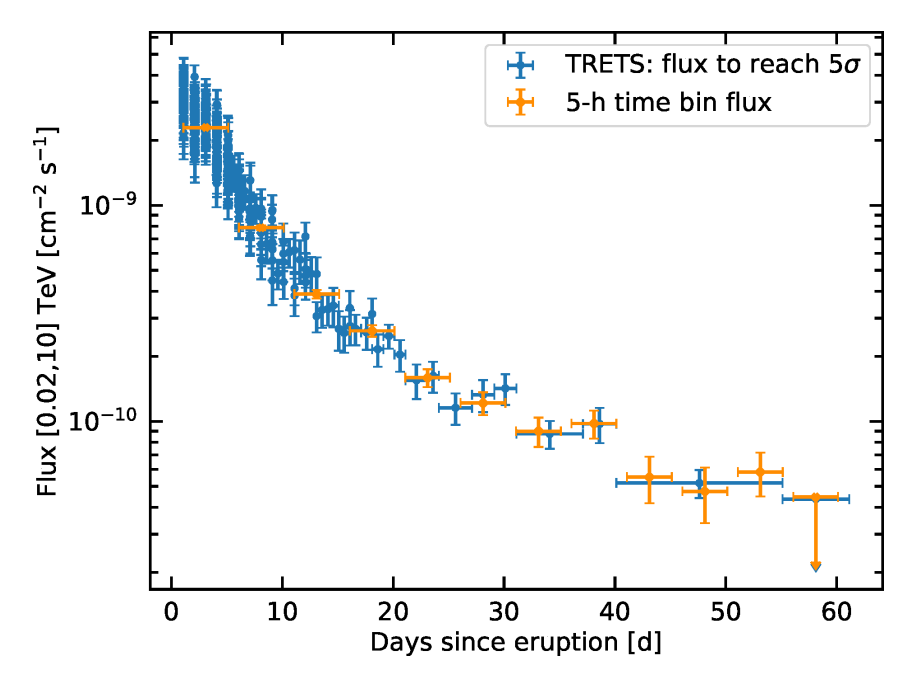


Figure A.2: Comparison between the light curve of numerical simulations of RS Oph produced with TRETS (blue) and a fixed time window of 5 h observation time (i.e. combining 5 days of 1 h observation time; orange). The vertical error bars correspond to 1σ statistical errors, and ULs are computed at the 95% confidence level.

Table A.1: TRETS parameters for the numerical simulations of RS Oph.

Parameter	$Y_1 [\sigma]$	<i>Υ</i> ₂ [σ]	t _{TH} [d]	t _{bin}	Spectral model
Value	5	2	15	livetime of each simulation (1 min)	log parabola

Notes. Y_1 and Y_2 are the statistical significance thresholds set for the detection and the flux point, t_{TH} is the maximum threshold time for combining the events between two observations, t_{bin} is the time bin set by the user, and "Spectral model" is the model used to compute the integral flux (see Fig. A.1). The log-parabola spectral model uses the best-fit parameter values obtained with MAGIC using all the observations within the first four days after the eruption (Acciari et al. 2022).

variable gamma-ray flares (MAGIC Collaboration et al. 2019a). In 9 August 2021, BL Lac also displayed a flare activity observed with LST-1 (Nozaki et al. 2023). The emission during that day reached a flux of about 3–4 times that of the Crab Nebula at 100 GeV, displaying intra-night variability (Nozaki et al. 2023).

We applied TRETS to the observations taken on BL Lac with LST-1 during its flare on 9 August 2021. The effective time of the observations spans about 2 h. Figure A.3 shows the light curve using TRETS (see settings in Table. A.2), together with the light curves produced with conventional observation-wise and 5 min fixed time binning. The light curves display variability, which is observed as two-peaked increases in flux separated by about 1 h. The TRETS light curve is distributed around the observation-wise integral fluxes and the 5 min light curve.

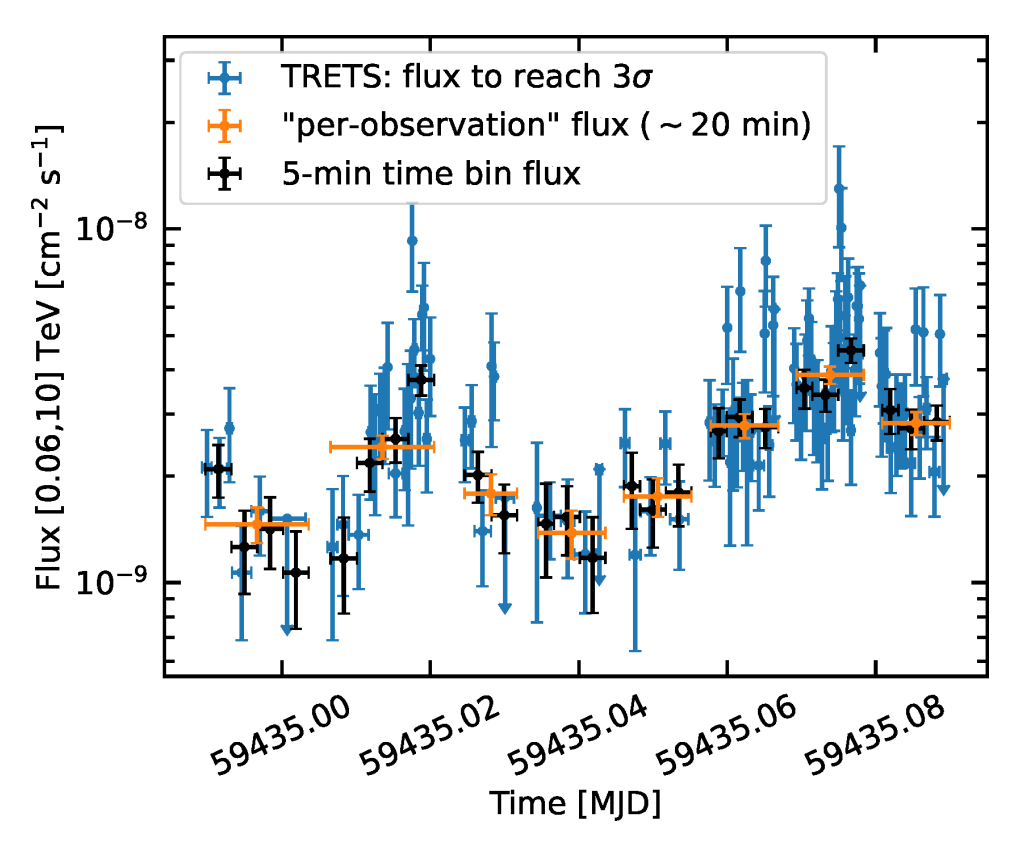


Figure A.3: BL Lac light curve on 9 Aug. 2021. The TRETS light curve (blue) is compared with the flux points computed using the duration of each observation (per-observation flux; orange) and a fixed time interval of 5 minutes (black). The vertical error bars correspond to 1σ statistical errors, and ULs are computed at the 95% confidence level.

For a proper comparison between two light curves, matching their temporal resolution is required. For this reason, we produced a weighted average light curve by grouping the integral fluxes obtained with TRETS. The weight of the *i*th TRETS flux that overlaps in time with the reference flux point is computed as

$$w_i = \frac{1}{\sigma_i^2} \times \frac{t_i^{\text{in}} - t_i^{\text{out}}}{t_i^{\text{total}}} \times \frac{1}{1 + \max(0, TS_{\text{TH}} - TS_i)}, \tag{A.1}$$

where σ_i is the 1σ statistical error of the ith integral flux, t_i^{in} and t_i^{out} are the time inside and outside the reference flux time bin, t_i^{total} is the time bin of the ith flux, TS_{th} is the threshold TS for a flux UL, and TS_i is the TS value of the flux. The second term is added to account for fluxes partially outside the time interval, while the third term is included to consider ULs. The weighted statistical errors are summed quadratically.

Figure A.4 shows the light curve obtained using flux time bins defined as the elapsed time of each observation, while Fig. A.5 displays the light curve utilising a fixed time interval of 5 minutes. These light curves are considered as a reference to produce the weighted average light curve with TRETS. Figures A.4 and A.5 compare the reference per-observation and 5-min flux light curves with the weighted average TRETS integral fluxes, respectively. The weighted average TRETS integral fluxes are

Table A.2: TRETS parameters considered for LST-1 data taken on BL Lac.

Parameter	$Y_1 [\sigma]$	$Y_2 [\sigma]$	t _{TH} [min]	t _{bin} [s]	Spectral model
Value	3	2	1	1	log parabola

Notes. Y_1 and Y_2 are the statistical significance thresholds set for the detection and the flux point, $t_{\rm TH}$ is the maximum threshold time for combining the events between two observations, $t_{\rm bin}$ is the time bin set by the user, and the spectral model used to compute the integral flux (see Fig. A.1). The log-parabola spectral model uses the best-fit parameter values obtained by fitting all the data on 9 Aug. 2021. Note that the units of $t_{\rm TH}$ are minutes.

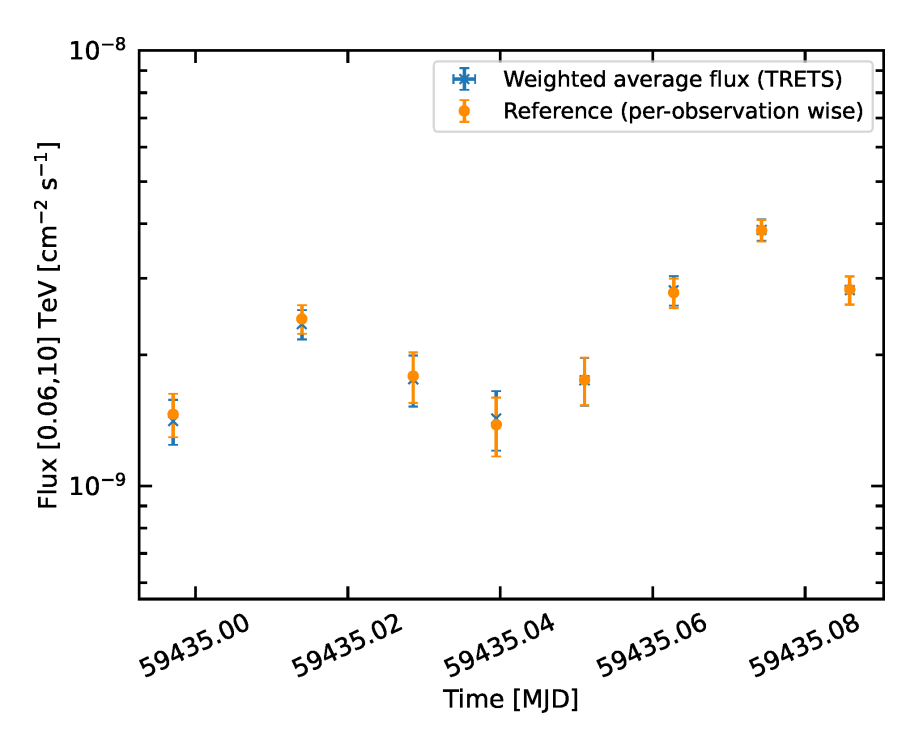


Figure A.4: Same light curve as Fig. A.3 for BL Lac. The flux points computed using the duration of each observation (orange) are compared with the weighted-average light curve from TRETS (blue).

compatible within errors to the reference light curves. The good agreement between them highlights the reliable flux points derived with TRETS.

Applying the algorithm to the BL Lac data, LST-1 has a temporal resolution shorter than 1 min, within which the source is detected at a statistical significance of at least 3σ for this BL Lac dataset (see Fig. A.6). Moreover, we investigated how the temporal resolution increases as the threshold for the statistical significance of the detection is increased. Figure A.7 shows the median statistics of the distribution of flux time intervals, viz. the distribution in Fig. A.6, for different detection statistical significance thresholds. As the threshold for a flux computation increases from 3σ to 10σ , the median of the distribution increases from less than one minute to about 9 minutes. Remarkably, about two minutes of data are required for a detection with a 5σ pre-trial detection significance. Such a well-sampled light curve can

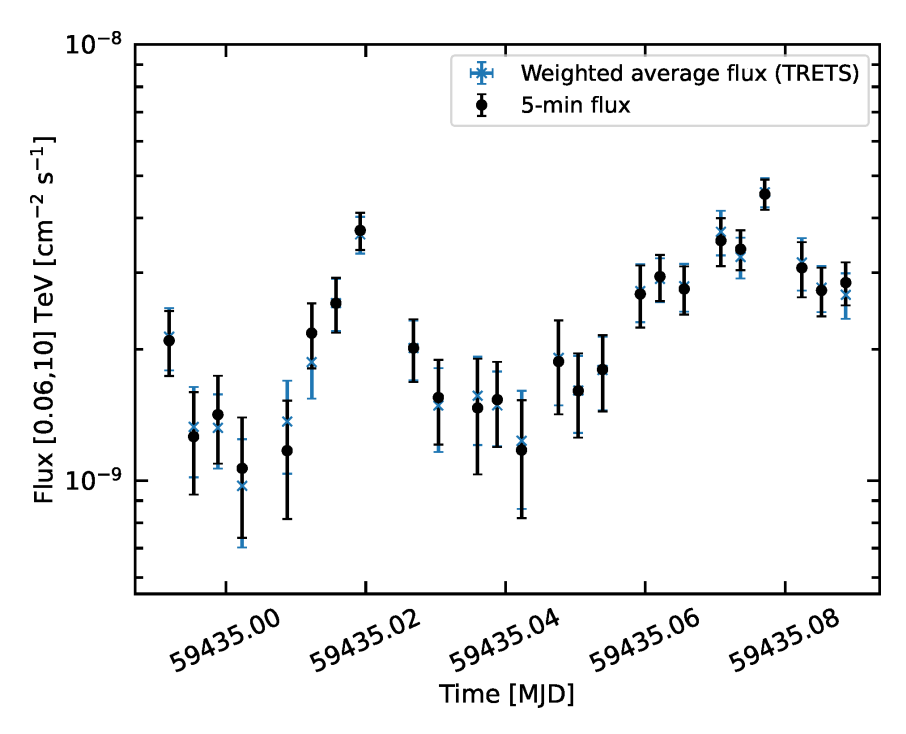


Figure A.5: Same light curve as Fig. A.3 for BL Lac. The flux points computed using a fixed 5 minute time interval (black) are compared with the weighted-average light curve from TRETS (blue).

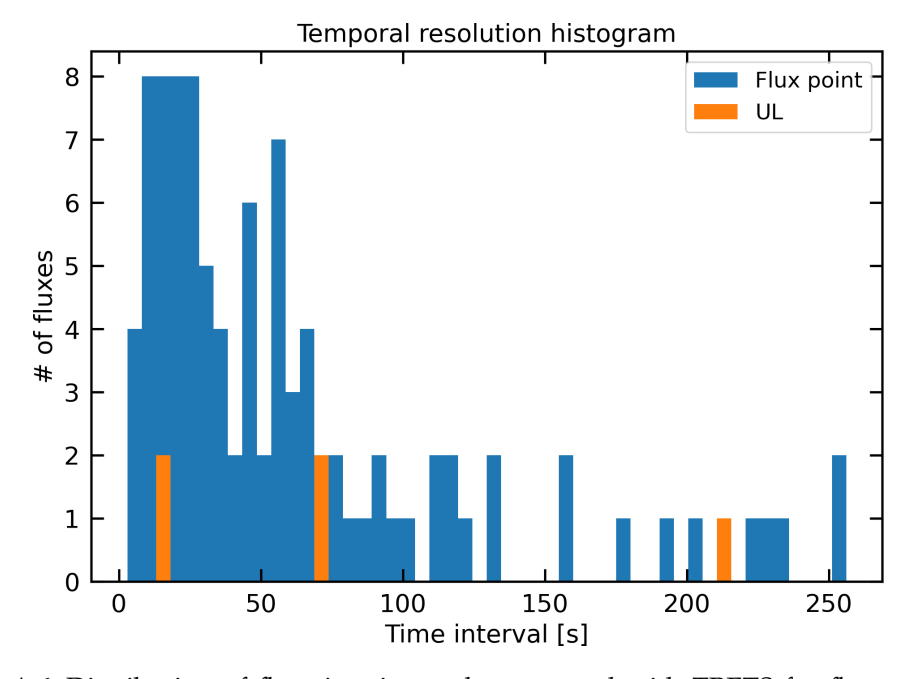


Figure A.6: Distribution of flux time intervals computed with TRETS for fluxes with a detection statistical significance of 3σ from BL Lac observations.

help to better investigate the mechanisms responsible for the short-time variability and eventually constrain the physical parameters of the emitting region. We note, however, that this temporal resolution is sensitive to the flux level of the source, the observing conditions, and the specific data analysis applied to the data.

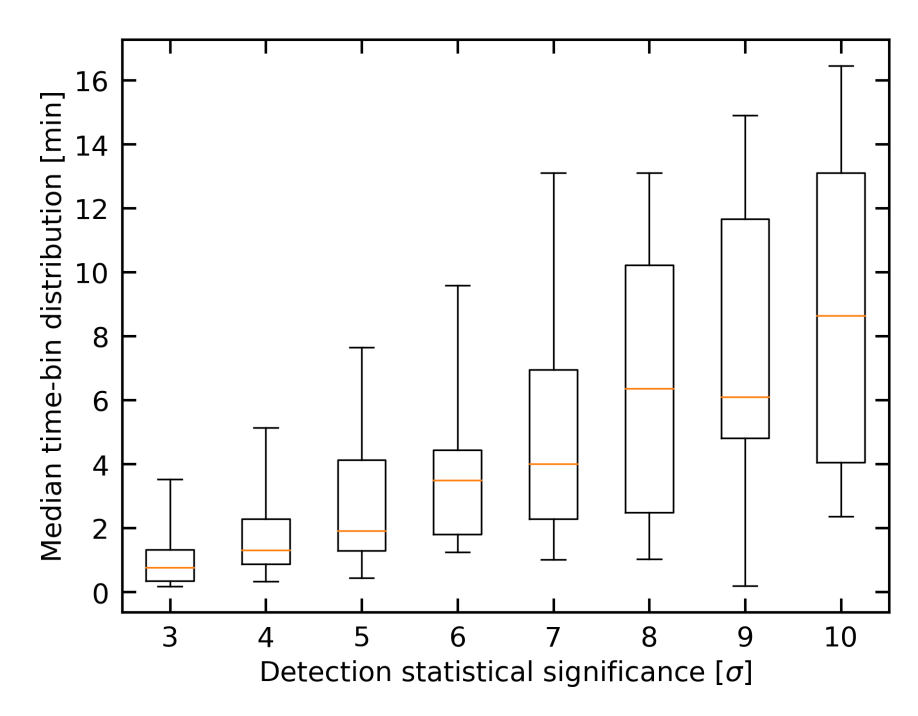


Figure A.7: Median time-bin distribution for different detection statistical significance thresholds in TRETS using BL Lac observations. The median is marked as a horizontal orange line, the boxes delimit the first and third quartile (Q1 and Q3, respectively) of the distribution, while lower (upper) error bars mark the $Q1 - 1.5 \times IQR$ (Q3 + 1.5 × IQR).

A.3 CONCLUSIONS AND FUTURE WORK

TRETS is a tool to produce a time-variable light curve. We obtain the time intervals where the statistical significance of the detection is above a given threshold. Moreover, TRETS allow us to estimate the time required for a variable source to be detected above a given statistical significance level. TRETS light curve avoids light-curve binning biases, as it assigns the time bin based on the source detection significance. There is no need for a human-based time-binning definition unrelated to the intrinsic source flux variability (e.g., "observation-by-observation", "day-by-day", "week-by-week"). This algorithm can be used in real-time or offline analysis. The algorithm applicability can be very diverse, such as light curve production, schedule optimisation, and detectability studies, among others.

We demonstrated the algorithm capabilities using numerical simulations for a transient source that exhibits a power-law decay as RS Oph. We additionally applied TRETS to the observational data of BL Lac that showed intra-night variability. The light curves obtained with TRETS are in good agreement with the light curve obtained on a fixed 5 min binning and per-observation basis.

The shortest temporal resolution achieved with TRETS can provide key observables to derive stringent constraints on the underlying gamma-ray emission processes, absorption mechanisms and the physical parameters of the emitting region to advance in our understanding of transient sources.

Further studies are required to address several aspects yet not implemented in TRETS. We list below some of them.

- A change in the observed flux can result from either an intrinsic change in
 the emitted flux or due to variations of the observing conditions during the
 data-taking, as well as due to effects related to the data analysis. A tool to
 assess the origin of the variable emission is needed. Several observables can
 be used as diagnostic tools to address these changes. For example, the rate of
 counts in control regions as a function of time can be used for this purpose.
- TRETS may poorly estimate the time at which a flare starts or finishes, or even miss a dim flare because the number of previously sampled events can dampen the significance due to the iterative nature of the algorithm. The accurate estimation of the start and end time of an enhanced emission episode would certainly help in these kind of transient studies. Several methods are under investigation and may be included in the algorithm to address these requirements.
- TRETS considers the statistical significance detection to bin the data. We note, however, that this value does not consider the number of trial factors that result from binning the entire period. The inclusion of trial factors in the calculations is work in progress.

B

OBSERVATIONS OF CLASSICAL NOVAE WITH LST-1

An observational program devoted to nova observations is active in LST. This program aims to trigger rapid follow-up observations of novae for their study at gamma rays. By the time this Thesis is written, four novae have been followed up with LST-1: nova Cas 2021 (V1405 Cas), nova Her 2021 (V1674 Her), nova RS Oph in 2021, and nova U Sco in 2022 (see Table. B.1).

In this Appendix, we describe the results of the gamma-ray data taken on V1405 Cas, V1674 Her, and U Sco, whereas the reader is referred to Chapt. 5 for the study of RS Oph. For the study of these novae, we have made use of gamma-ray data obtained with *Fermi*-LAT and LST-1. Sections B.1, B.2, and B.3 describe the eruption of V1405 Cas in 2021, V1674 Her in 2021, and U Sco in 2022, together with the observations performed with LST-1. The dedicated LST-1 and *Fermi*-LAT analyses performed for all these novae are reported in Sects. B.4 and B.5, respectively. The results of these analyses are presented in Sect. B.6, whereas a short summary of novae observations with LST-1 is provided in Sect. B.7.

B.1 v1405 cas

V1405 Cas was discovered on 18 March 2021 and classified as a classical nova at a distance of about 1.7 kpc (Maehara et al. 2021; Gaia Collaboration et al. 2023). The top panel of Fig. B.1 shows the light curve during this nova event obtained in the optical V band from the American Association of Variable Star Observers (AAVSO) database (Vollmann 2024). The optical emission of V1405 Cas post-eruption remained enhanced, compared to its quiescence state, in a *plateau phase* (V < 8 mag) that lasted for about 7 months (Munari et al. 2021b). During this period, several flaring episodes were observed, each presenting increased optical activity than the plateau emission level. The luminosity peak reached an apparent magnitude in the V band of about 5 on 10 May 2021. The optical spectra from the luminosity peak to several days post-maximum present a drastic evolution in the emission lines, transitioning from a slim profile with velocities of \sim 700 km s⁻¹ to the emergence of multiple high-velocity components (Valisa et al. 2023). Notably, *Fermi*-LAT detected a hint of a signal on the V1405 Cas direction during this period (Buson et al. 2021).

LST-1 observed V1405 Cas during the maximum flaring episode in May 2021 for four consecutive days, starting on 12 May 2021 (see Table B.1). All observations were recorded with the Moon below the horizon. However, they were partly affected by low atmospheric transmission, so the final dataset comprises only two days of data, taken on 12 and 13 May 2021, with a total of 1.76 hours of good quality data. These dates are marked in the top panel of Fig. B.1.

Variable Name	Eruption discovery (t_0)	$t_{\rm start} - t_0$	Obs. time	ZA range	HE Detection
	UTC	[d]	[h]	[°]–[°]	
V1405 Cas	2021-03-18 10:10:34	55.74	1.76	53–59	hint $(4\sigma)^{(a)}$
V1674 Her	2021-06-12 04:34:02	1.79	4.38	12-43	$yes^{(b)}$
RS Oph	2021-08-08 22:19:12	0.97	10.94	35-64	$yes^{(c)}$
U Sco	2022-06-06 17:17:14	0.19	2.82	47–69	no

Table B.1: Observation summary for the novae observed with LST-1.

Notes. For each novae observed with LST-1, we list the date of the eruption (t_0), the starting time offset with respect to t_0 , the observation time after the data selection, the ZA range of the observations, and if the eruption was detected at HE gamma-ray emission. ^(a)Buson et al. (2021), ^(b)Li (2021), ^(c)Cheung et al. (2022).

B.2 v1674 HER

The classical nova V1674 Her was discovered on 12 June 2021*. V1674 Her has been detected across the electromagnetic spectrum, from radio to gamma rays. In the optical, it is characterised by a rapid 1-day steep rise from quiescence to peak, which reached a magnitude 6 in the V band, followed by some of the fastest decay rates ever observed in novae (see middle panel of Fig. B.1; Woodward et al. 2021). Spectroscopic observations revealed multiple components with velocities at several thousand km s⁻¹, which are interpreted as multiple outflows at different velocities (Munari et al. 2021a; Woodward et al. 2021; Aydi et al. 2021). This broadband emission can be explained by the shocks that arose due to the collision and shock of these fast outflows (Sokolovsky et al. 2023). V1674 Her distance is poorly constrained, with proposed distances in the range of \sim 3–9 kpc depending on the estimation method (Woodward et al. 2021; Drake et al. 2021; Sokolovsky et al. 2023).

LST-1 performed follow-up observations at about 1.79 d after its discovery on 12 June 2021 (see Fig. B.1 and Table B.1). Observations were taken with the Moon below the horizon for a total time of 4.38 h. These data are mildly affected by low atmospheric transmission. We considered all the observations to search for gamma-ray signal and constrain its emission. We note, that a tailored analysis is required to account for these non-optimal observing conditions, which is work in progress.

B.3 U SCO

U Sco belongs to the reduced class of recurrent novae in the Milky Way (e.g. Bode and Evans 2012), with a recurrence time of \sim 10 years (Schaefer 2010). The source has been observed multiple times during a nova phase, with its last eruption taking place on 6 June 2022 (Moriyama 2022). The binary system consists of a massive white dwarf star and a K2 IV companion star (Mason 2011; Anupama and Dewangan 2000). The distance to this system is largely unknown, ranging between

^{*}http://www.cbat.eps.harvard.edu/unconf/followups/J18573095+1653396.html

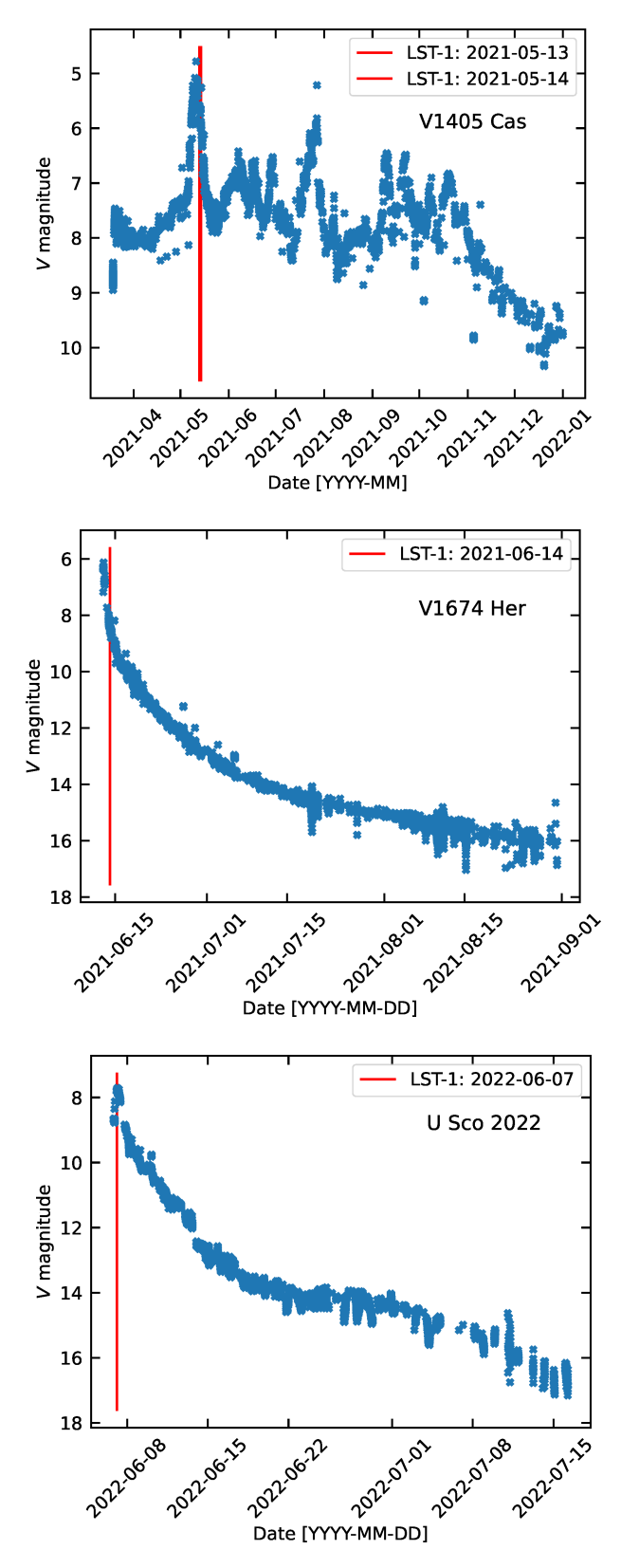


Figure B.1: From top to bottom, the optical light curve in the *V* band of nova V1405 Cas, V1674 Her, and U Sco 2022 (Vollmann 2024). Vertical red lines mark the dates in which LST-1 performed observations.

 \sim 8.5 and \sim 15 kpc (Schaefer 2010). The light curve of U Sco is characterised by a rapid decline, which takes about 1.2 days to decay by two optical magnitudes from the peak at $V \approx 8$ mag. This attribute places U Sco among the fastest-evolving nova systems together with V1674 Her. The bottom panel of Figure B.1 shows the optical light curve of U Sco in the V band (Vollmann 2024).

LST-1 observations were taken during the eruption in 2022 with a time delay of less than 0.2 days. Observations occurred with the Moon above and below the horizon and at high ZA (see Table B.1). We selected data with the Moon below the horizon. The total observation time with good-quality data is 2.82 h. The dates corresponding to this dataset are shown in Fig. B.1.

B.4 LST-1 DATA ANALYSIS

We analyse LST-1 data taken on V1674 Her, V1405 Cas and U Sco using cta-lstchain (Moralejo et al. 2025). A standard LST-1 analysis is performed from the raw data to produce the final list of gamma-ray events (see Sect 4.3). In particular, we utilise the closest MC declination line to each novae to train the RFs (see Sect. 4.3.5). The simulated NSB on the MC data is increased to match the average diffuse NSB in the FoV of each nova campaign, and the IRFs are computed by interpolating the IRFs derived from the closest MC nodes to the telescope pointing of each observation. We perform an aperture photometry analysis using 3 OFF regions, both for the signal detection (see Sect. 4.1.6.1) and the spectral analysis (see Sect. 4.1.6.2). Global cuts are used to compute the statistical significance of detection. In contrast, energy-dependent efficiency cuts at 70% for the *gammaness* and θ parameters are used for spectral and light curve studies. For both cuts, we additionally apply an event selection cut to exclude events with *intensities* below 50 p.e.

B.5 FERMI-LAT DATA ANALYSIS

We carried out a dedicated analysis of Fermi-LAT data obtained during the eruptions of V1405 Cas, V1674 Her, and U Sco to search for HE gamma-ray signal and constrain their emission during the LST-1 observations. We followed the same analysis prescription for the three analyses. We consider events between 100 MeV and 300 GeV from evclass=128 and FONT+BACK event types (evtype=3). Only events below ZA of 90° are used to avoid contamination from the Earth's limb. Furthermore, only events recorded within good time intervals are considered (DATA_QUAL>0 && LAT_CONFIG==1). We account for all sources in the LAT 14-year catalogue (4FGL-DR4) within a FoV of 25° around the source of interest. Moreover, the diffuse and Galactic components from Pass 8 are considered. Sources within 8° from the source of interest and TS above 9 are left free during the fitting process. A power-law spectral shape is assumed to describe the emission of the novae, whose initial value is set to -2.2, which is the typical best-fit spectral index found in other gamma-ray novae (e.g. Ackermann et al. 2014; Cheung et al. 2016). The position of the source is fixed to the coordinates in the optical band. A binned analysis is performed in which the source of interest is located in the centre of the FoV. Events are binned into a 15°×15° grid with a pixel size of 0.1°. Eight bins per

energy decade are considered. We utilise the IRFs from Pass 8 (P8R3_SOURCE_V3), and the analyses are performed with Fermipy v1.3.1, employing Fermitools v2.2 (Fermi Science Support Development Team 2019; Wood et al. 2017).

We compute integral fluxes in time bins of 24 h. The light curve probes the HE gamma-ray emission of the three novae within days before and after the eruption. The start and stop time of the light curve with respect to the nova discovery changes according to the prior information on the source. Additionally, we compute the SED of each novae during the LST-1 observations taking all the data between 12:00 UTC of the day preceding and 12:00 UTC of the day succeeding the night of LST-1 data taking. This procedure is considered for V1674 Her and U Sco. In contrast, the analysis is slightly modified for V1405 Cas because of the enhanced background contribution in the FoV of this nova due to its proximity to the galactic plane. For V1405 Cas, we increased the time lapse for the flux computation to 5 d, and fixed the spectral index of the spectral model of V1405 Cas to -2.2.

B.6 RESULTS

None of the sources is detected with LST-1 using a total of 1.76 h, 4.38 h, and 2.82 h of observation time taken on V1405 Cas, V1674 Her, and U Sco, respectively. In contrast, at HE gamma rays, a signal excess at a statistical significance level of TS=21 is obtained between 21–26 May 2021 on the position of V1405 Cas. Furthermore, we detect V1674 Her on 13 June 2021, the first time bin after the eruption, at TS=33. U Sco, however, is not detected in the studied period. These findings at HE gamma rays agree with the results reported in previous studies (Buson et al. 2021; Li 2021). The enhanced gamma-ray signal in V1405 Cas and V1674 Her is not coincident with the LST-1 observations.

Given the non-detection with LST-1 and *Fermi*-LAT at the time of LST-1 observations, we consider a power-law spectral model with a fixed spectral index. We assume a value of -3.5 during the computation of the SED at VHE gamma rays for all novae. Such a soft spectral index value is considered assuming that its eventual gamma-ray emission has a spectral index similar to the one detected in RS Oph during the first days after the eruption at these energies. We calculate the SED with *Fermi*-LAT and LST-1 to constrain the emission between 100 MeV and 10 TeV from these classical novae. We describe the specific results of V1405 Cas, V1674 Her, and U Sco in Sects. B.6.1, B.6.2, and B.6.3, respectively. We compute integral flux ULs if either the source *TS* is below 9, the number of predicted counts is below 4, or the flux error over the flux is above 60%.

в.6.1 V1405 Cas

The top panel of Fig. B.2 shows the light curve of V1405 Cas above 100 MeV obtained with *Fermi*-LAT. The light curve spans the time from 45 d to 75 d after the eruption, covering the rise and the decay of the maximum peak in time bins of 5 days. The position of the optical peak in the light curve is shown, as well as the position of the mid-time of the LST-1 observations. ULs are calculated for most of the time intervals at the level of a few $\times 10^{-7}$ cm⁻² s⁻¹. Only the flux in the time bin between $t_0 + [64, 69]$ d, in which a hint of signal at TS = 21 is detected, is above the UL

criterion threshold. The flux point is at the level of $2 \times 10^{-7} \, \text{cm}^{-2} \, \text{s}^{-1}$ and offset with respect to the LST-1 observations by 9.8 d at later times. This offset time is computed using the mid time of the analysed temporal bin to the closest LST-1 observation in time.

The bottom panel of Fig. B.2 shows the SED from 100 MeV to 10 TeV. *Fermi*-LAT ULs reach down to few $\times 10^{-11}\,\mathrm{erg}\,\mathrm{cm}^{-2}\,\mathrm{s}^{-1}$ at few GeV, and their values monotonically increase below and above this energy. On the other hand, LST-1 ULs decrease from few $\times 10^{-11}\,\mathrm{erg}\,\mathrm{cm}^{-2}\,\mathrm{s}^{-1}$ at few hundred of GeV to an order of magnitude lower in flux than *Fermi*-LAT at energies above $\sim 1\,\mathrm{TeV}$. We also show in this plot the gamma-ray emission of the hadronic model of RS Oph obtained by fitting *Fermi*-LAT, LST-1, MAGIC, and H.E.S.S. SED points at $t-t_0\sim 2\,\mathrm{d}$ (see Sect. 5.5.2). We can constrain the gamma-ray emission of V1405 Cas at GeV energies at the level of 10% of that of RS Oph at GeV energies. The ULs with LST-1, in contrast, are located above the emission level of RS Oph at VHE gamma rays due to its soft emission at those energies.

в.6.2 V1674 Her

The daily *Fermi*-LAT light curve of V1674 Her above 100 MeV is displayed in the top panel of Fig. B.3. HE gamma-ray emission is detected only within a day after the eruption, at the level of 1.1×10^{-6} cm⁻² s⁻¹. This significant flux point is offset with respect to the LST-1 observations by 1.07 d at earlier times (see Sect. B.6.1 for details on the computation of this time offset). Similarly, the calculated HE ULs at other periods with no detection constrain the emission at a similar flux level of $\approx 1.5 \times 10^{-6}$ cm⁻² s⁻¹.

We show on the bottom panel of Fig. B.3 the SED using Fermi-LAT and LST-1 data. ULs at HE gamma rays constrain the emission below a few $\times 10^{-10}$ erg cm $^{-2}$ s $^{-1}$, while the ULs with LST-1 are the level of $\times 10^{-12}$ erg cm $^{-2}$ s $^{-1}$ above a few hundred of GeV. These constraints allow us to rule out the emission of an RS-Oph-like spectral shape down to 50% of its flux. Note that the increase in the flux level at HE gamma rays with respect to the ULs derived for V1405 Cas in the same band is mostly attributed to the reduction of exposure by about a half (see bottom panel of Fig. B.2).

в.6.3 *U Sco*

The top panel of Fig. B.4 shows the daily integral fluxes of U Sco above 100 MeV, all of them reaching a TS below 9. The UL fluxes increase from 2×10^{-6} cm⁻² s⁻¹ at the eruption time to about 3×10^{-5} cm⁻² s⁻¹ four days later. This increase by about an order of magnitude is due to an uneven exposure of *Fermi-LAT* on the position of U Sco. LST-1 observations were taken when the exposure time started to decrease compared with the exposure days before the eruption, when the ULs are at 1.5×10^{-6} cm⁻² s⁻¹. Possibly, the non-detection with *Fermi-LAT* may be influenced by the large distance to the source, which may have decreased the putative gamma-ray flux below the detection level.

We show in the bottom panel of Fig. B.4 the gamma-ray SED of U Sco during the observations of LST-1. The derived ULs at HE gamma rays are within

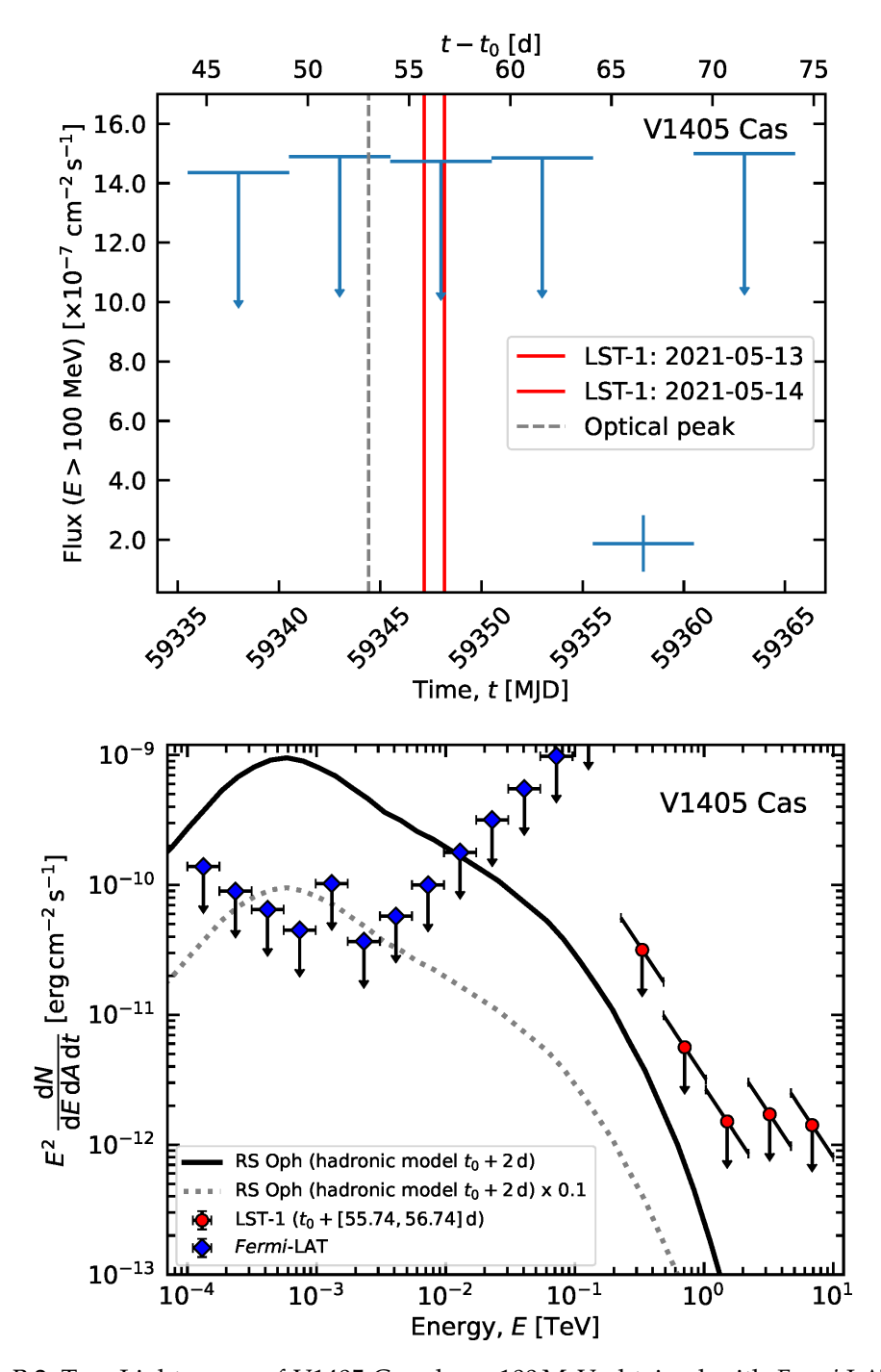


Figure B.2: Top: Light curve of V1405 Cas above 100 MeV obtained with *Fermi*-LAT. The eruption discovery time and the mid-time of the LST-1 daily observations are marked with vertical dashed grey and red lines, respectively. Bottom: SED of V1405 Cas with *Fermi*-LAT (blue diamonds) and LST-1 (red circles). The emission of the best-fit hadronic model of RS Oph at $t-t_0\sim 2\,\mathrm{d}$ is shown as a solid black curve together with its scaled down emission to 10% level (grey dotted curve). For both plots, the vertical error bars correspond to 1σ statistical errors, and ULs are computed at the 95% confidence level.

 10^{-10} – 10^{-9} erg cm⁻² s⁻¹. In contrast, the ULs computed with LST-1 data probe the emission at energies above 100 GeV at a level of 10^{-12} – 10^{-11} erg cm⁻² s⁻¹. As a

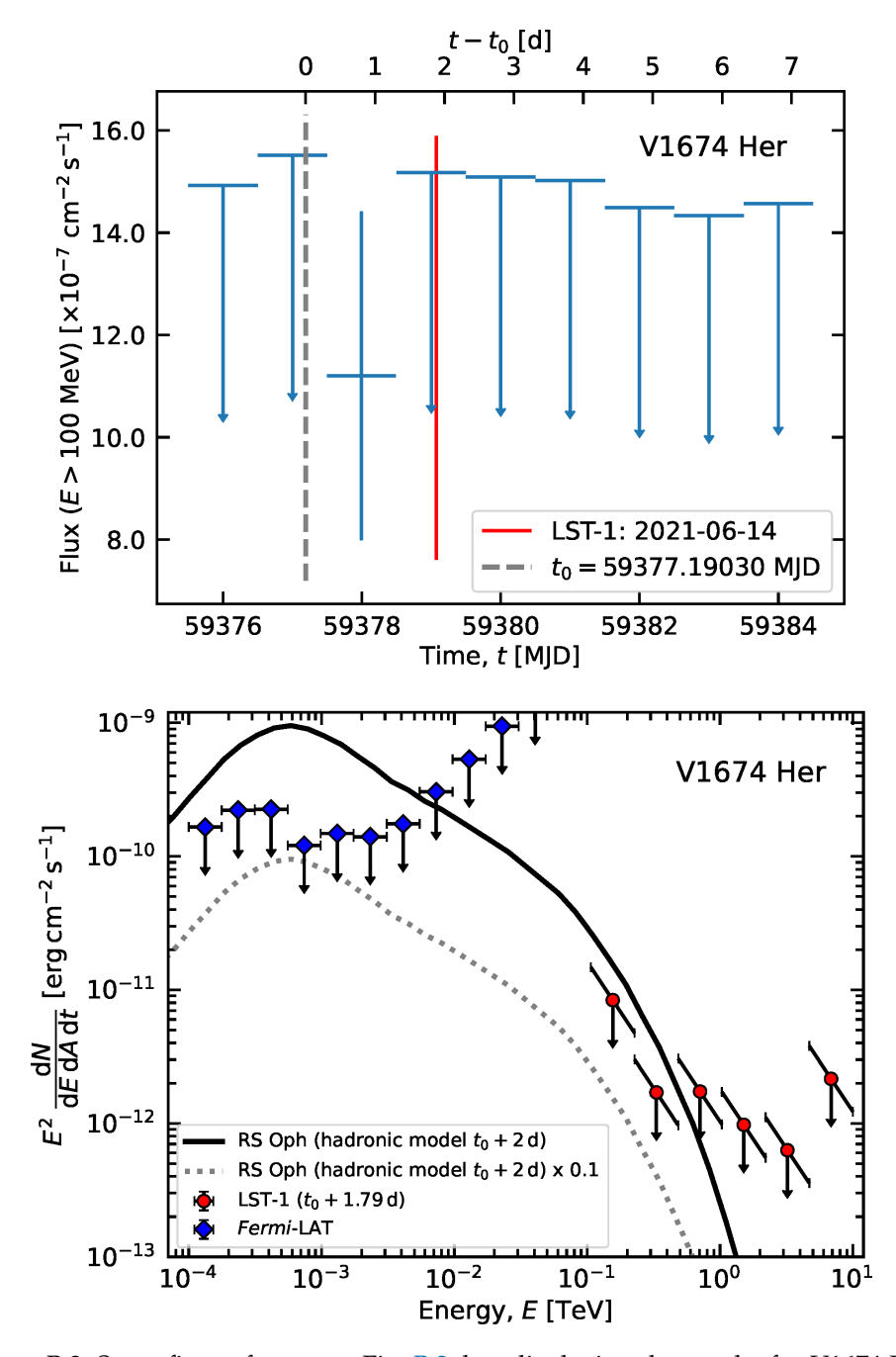


Figure B.3: Same figure format as Fig. B.2, but displaying the results for V1674 Her.

result, we can constrain the HE emission at 1 GeV at about 50% of that of RS Oph on day 2 after the eruption, while the VHE gamma-ray ULs reach the RS Oph emission level at hundreds of GeV.

B.7 SUMMARY

Nova explosions are some of the transient sources that LST-1 is actively observing. By the time this Thesis is written, four novae have been followed up with LST-1. Among them, three are classical novae (V1405 Cas, V1674 Her, and U Sco) and

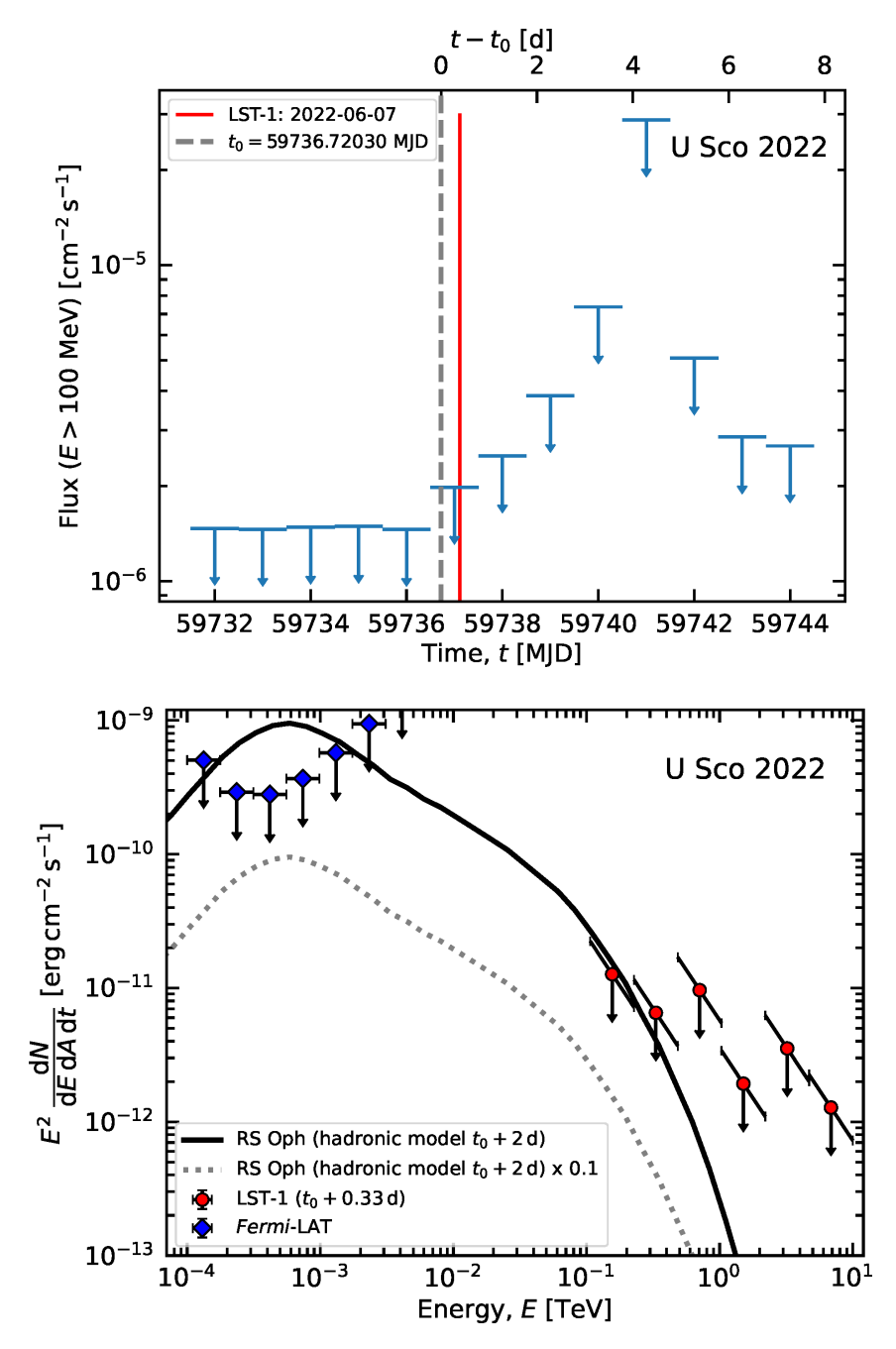


Figure B.4: Same figure format as Fig. B.2, but displaying the results for U Sco. Note that the flux values in the top plot are represented in log scale.

the symbiotic nova RS Oph, which is the only nova detected at VHE gamma rays. Additionally, two of them, U Sco and RS Oph, undergo multiple recurrent eruptions within about human timescales. The observations conducted with LST-1 on these classical novae yield a compatible signal with the background. We constrain its gamma-ray emission from 100 MeV to 10 TeV through a dedicated *Fermi*-LAT and LST-1 analysis. We contextualise the derived ULs by comparing them with the emission of the best-fit hadronic model that describes the most complete HE and VHE dataset obtained in the case of RS Oph.



CODE DEVELOPMENTS IN THE CONTEXT OF IACTS

In addition to private code development for the pieces of code needed for all the steps in the data analysis, tests, and checks of LST-1 and MAGIC+LST-1 data, we contributed to developing and debugging software for LST, MAGIC+LST-1 and CTAO, including the open-source software packages Gammapy, cta-lstchain, lstmcpipe, ctapipe, magic-cta-pipe, and ctapipe_io_magic. We list in Table C.1 issues and pull requests opened to report bugs, request new features, and address their implementations.

Table C.1: Issue and pull request numbers opened in each repository.

Repository name	Issue number	Pull request number
Gammapy	3664, 3801, 4038, 4145, 4349, 4497, 5339, 5628	3669, 3800, 4054, 4041, 4104, 4428, 4816, 5345, 5645, 5460
cta-lstchain	865, 954, 1019, 1020, 1045	867, 1119, 1120, 1170, 1210
lstmcpipe	151, 171, 290, 309	409
ctapipe	-	2608, 2613
magic-cta-pipe	212	-
ctapipe_io_magic	67	-

LIST OF ACRONYMS

a.s.l. above sea level

AAVSO American Association of Variable Star Observers

ACT atmospheric Cherenkov telescope

ADC analog-to-digital converter

Aeff Effective area

AGILE Astro-Rivelatore Gamma a Immagini Leggero

AGNs active galactic nuclei

AIC Akaike information criterion

BAT Burst Alert Telescope
BPL broken power-law

Cat Category

CCSN core-collapse SN

CGRO Compton Gamma Ray Observatory

CoG centre of gravity

COMPTEL imaging Compton telescope

COS-B Celestial Observation Satellite B

COSI Compton Spectrometer and Imager

CR cosmic ray

CSM circumstellar medium

CTAO Cherenkov Telescope Array Observatory

CTAO-N CTAO-North
CTAO-S CTAO-South
DL0 Data Level 0
DL1 Data Level 1

DL1a First Data level 1
DL1b Second Data level 1

DL2 Data level 2
DL3 Data level 3
DL4 Data level 4
DL5 Data level 5

DRS4 Domino Ring Sampler 4
DSA Diffusive shock acceleration

EAS extensive air/atmospheric shower

EBL extragalactic background light
ECPL exponential cutoff power-law

edisp Energy dispersion

EGRET Energetic Gamma Ray Experiment Telescope

FF flat-field FoV field of view

GBM Gamma-ray Burst Monitor

GECAM-C Gravitational wave high-energy Electromagnetic Counterpart

All-sky Monitor-C

GRB gamma-ray burst

GRID Gamma Ray Imaging Detector

GW gravitational wave

H.E.S.S. High Energy Stereoscopic System

HaST Hardware Stereo Trigger

HAWC High-Altitude Water Cherenkov

HE high energy ($100 \,\text{MeV} < E < 100 \,\text{GeV}$)

HG high gain
HV high voltage

IACT imaging atmospheric Cherenkov telescope

IBIS Imager on Board INTEGRAL Satellite

IC inverse Compton IQR interquartile range

Insight-HXMT Insight-Hard X-ray Modulation Telescope

INTEGRAL INTErnational Gamma-Ray Astrophysics Laboratory

IR infrared

IRF instrument response function

ISM interstellar medium

KN Klein-Nishina

LAT Large Area Telescope

LG low gain

LHAASO Large High Altitude Air Shower Observatory

Lp/Le proton-to-electron luminosity ratio

LST Large-Sized Telescope

LST-1 first LST
M1 MAGIC I
M2 MAGIC II

MAGIC Major Atmospheric Gamma-ray Imaging Cherenkov

MC Monte Carlo

MST Medium-Sized Telescope

MWL multi-wavelength

NSB night sky background

NuSTAR Nuclear Spectroscopic Telescope Array

OSO-3 Orbiting Solar Observatory 3

p.e. photoelectrons

PMT Photomultiplier tube
PSF Point spread function

R0 Raw level 0
R1 Raw level 1
RF random forest
RSG red supergiant

S/B signal-to-background ratio

SAS-2 Second Small Astronomy Satellite

SED spectral energy distribution

SN supernova

SPI SPectrometer on INTEGRAL
SSC synchrotron self-Compton
SST Small-Sized Telescope
ToO target of opportunity

TRETS Temporal Resolution Estimator for Transient Sources

TS test statistic

UHE ultra-high energy ($E > 100 \,\text{TeV}$)

UL upper limit

VERITAS Very Energetic Radiation Imaging Telescope Array System

VHE very-high energy ($100 \,\text{GeV} < E < 100 \,\text{TeV}$)

VLA Very Large Array

WCD water Cherenkov detector

WCDA water Cherenkov detector array

WR Wolf-Rayet

XMM-Newton X-ray Multi-mirror Mission-Newton

ZA zenith angle

- Abbott, B. P. et al. (2020). "Prospects for observing and localizing gravitational-wave transients with Advanced LIGO, Advanced Virgo and KAGRA." In: *Living Reviews in Relativity* 23.1, p. 3. DOI: 10.1007/s41114-020-00026-9.
- Abdalla, H. et al. (2019). "A very-high-energy component deep in the γ -ray burst afterglow." In: *Nature* 575.7783, pp. 464–467. DOI: 10.1038/s41586-019-1743-9. arXiv: 1911.08961 [astro-ph.HE].
- Abdalla, H. et al. (2021). "Evidence of 100 TeV γ -ray emission from HESS J1702-420: A new PeVatron candidate." In: A&A 653, A152. DOI: 10.1051/0004-6361/202140962. arXiv: 2106.06405 [astro-ph.HE].
- Abdo, A. A. et al. (2010). "Gamma-Ray Emission Concurrent with the Nova in the Symbiotic Binary V407 Cygni." In: *Science* 329.5993, pp. 817–821. DOI: 10.1126/science.1192537. arXiv: 1008.3912 [astro-ph.HE].
- Abdollahi, S. et al. (2022). "Incremental Fermi Large Area Telescope Fourth Source Catalog." In: *ApJS* 260.2, p. 53. DOI: 10.3847/1538-4365/ac6751. arXiv: 2201. 11184 [astro-ph.HE].
- Abe, H. et al. (2021). "Status and results of the prototype LST of CTA." In: *Proceedings of 37th International Cosmic Ray Conference PoS(ICRC2021)*. Vol. 395, p. 872. DOI: 10.22323/1.395.0872.
- Abe, H et al. (2023a). "MAGIC detection of GRB 201216C at z= 1.1." In: Monthly Notices of the Royal Astronomical Society 527.3, 5856–5867. DOI: 10.1093/mnras/stad2958. URL: http://dx.doi.org/10.1093/mnras/stad2958.
- Abe, H. et al. (2023b). "Observations of the Crab Nebula and Pulsar with the Large-sized Telescope Prototype of the Cherenkov Telescope Array." In: *The Astrophysical Journal* 956.2, p. 80. DOI: 10.3847/1538-4357/ace89d. URL: https://dx.doi.org/10.3847/1538-4357/ace89d.
- Abe, H. et al. (2023c). "Performance of the joint LST-1 and MAGIC observations evaluated with Crab Nebula data." In: A&A 680, A66. DOI: 10.1051/0004-6361/202346927. arXiv: 2310.01954 [astro-ph.IM].
- Abe, H. et al. (2024a). "Constraints on axion-like particles with the Perseus Galaxy Cluster with MAGIC." In: *Physics of the Dark Universe* 44, p. 101425. doi: 10.1016/j.dark.2024.101425. arXiv: 2401.07798 [astro-ph.HE].
- Abe, K. et al. (2023). "First Science Results from CTA LST-1 Telescope and status of LST-2-4." In: *Proceedings of 38th International Cosmic Ray Conference PoS(ICRC2023)*. Vol. 444, p. 731. DOI: 10.22323/1.444.0731.
- Abe, K. et al. (2024b). "A new method of reconstructing images of gamma-ray telescopes applied to the LST-1 of CTAO." In: A&A 691, A328. DOI: 10.1051/0004-6361/202450889. arXiv: 2410.16042 [astro-ph.HE].
- Abe, K. et al. (2024c). "GRB 221009A observations with LST-1 at VHE gamma rays." In: *Proceedings of High Energy Phenomena in Relativistic Outflows VIII*—*PoS(HEPROVIII)*. Vol. 461, p. 058. DOI: 10.22323/1.461.0058.

- Abe, K. et al. (2025a). "Detection of RS Oph with LST-1 and modelling of its HE/VHE gamma-ray emission." In: *A&A* 695, A152. DOI: 10.1051/0004-6361/202452447. arXiv: 2503.13283 [astro-ph.HE].
- Abe, K. et al. (2025b). "Galactic transient sources with the Cherenkov Telescope Array Observatory." In: *MNRAS*. DOI: 10.1093/mnras/staf655. arXiv: 2405.04469 [astro-ph.HE].
- Abe, S. et al. (2024d). "Dark matter line searches with the Cherenkov Telescope Array." In: *J. Cosmology Astropart. Phys.* 2024.7, p. 047. DOI: 10.1088/1475-7516/2024/07/047. arXiv: 2403.04857 [hep-ph].
- Abe, S. et al. (2025c). "Combined search in dwarf spheroidal galaxies for branon dark matter annihilation signatures with the MAGIC telescopes." In: *J. Cosmology Astropart. Phys.* 2025.3, p. 020. DOI: 10.1088/1475-7516/2025/03/020.
- Abeysekara, A. U. et al. (2017). "Extended gamma-ray sources around pulsars constrain the origin of the positron flux at Earth." In: *Science* 358.6365, pp. 911–914. DOI: 10.1126/science.aan4880. arXiv: 1711.06223 [astro-ph.HE].
- Abeysekara, A. U. et al. (2018). "Very-high-energy particle acceleration powered by the jets of the microquasar SS 433." In: *Nature* 562.7725, pp. 82–85. DOI: 10.1038/s41586-018-0565-5. arXiv: 1810.01892 [astro-ph.HE].
- Abeysekara, A. U. et al. (2020). "Multiple Galactic Sources with Emission Above 56 TeV Detected by HAWC." In: *Phys. Rev. Lett.* 124.2, p. 021102. DOI: 10.1103/PhysRevLett.124.021102. arXiv: 1909.08609 [astro-ph.HE].
- Abeysekara, A. U. et al. (2023). "The High-Altitude Water Cherenkov (HAWC) observatory in México: The primary detector." In: *Nuclear Instruments and Methods in Physics Research A* 1052, p. 168253. DOI: 10.1016/j.nima.2023.168253. arXiv: 2304.00730 [astro-ph.HE].
- Acciari, V. A. et al. (2022). "Proton acceleration in thermonuclear nova explosions revealed by gamma rays." In: *Nature Astronomy* 6, pp. 689–697. DOI: 10.1038/s41550-022-01640-z. arXiv: 2202.07681 [astro-ph.HE].
- Acciari, V. A. et al. (2021). "MAGIC observations of the nearby short gamma-ray burst GRB 160821B." In: *The Astrophysical Journal* 908.1, p. 90.
- Acero, F. et al. (2013). "Gamma-ray signatures of cosmic ray acceleration, propagation, and confinement in the era of CTA." In: *Astroparticle Physics* 43, pp. 276–286. DOI: 10.1016/j.astropartphys.2012.05.024. arXiv: 1209.0582 [astro-ph.HE].
- Acero, F. et al. (2022). *Gammapy: Python toolbox for gamma-ray astronomy*. Version 1.0. If you use this software, please cite it using the metadata from this file. DOI: 10.5281/zenodo.7311399. URL: https://doi.org/10.5281/zenodo.7311399.
- Acero, F. et al. (2024). Gammapy: Python toolbox for gamma-ray astronomy. Version v1.2. DOI: 10.5281/zenodo.10726484. URL: https://doi.org/10.5281/zenodo.10726484.
- Acharya, B. S. et al. (2013). "Introducing the CTA concept." In: *Astroparticle Physics* 43, pp. 3–18. DOI: 10.1016/j.astropartphys.2013.01.007.
- Acharyya, A. et al. (2019). "Monte Carlo studies for the optimisation of the Cherenkov Telescope Array layout." In: *Astroparticle Physics* 111, pp. 35–53. DOI: 10.1016/j.astropartphys.2019.04.001. arXiv: 1904.01426 [astro-ph.IM].
- Acharyya, A. et al. (2023). "VERITAS and Fermi-LAT Constraints on the Gamma-Ray Emission from Superluminous Supernovae SN2015bn and SN2017egm." In: *ApJ* 945.1, p. 30. DOI: 10.3847/1538-4357/acb7e6. arXiv: 2302.06686 [astro-ph.HE].

- Ackermann, M. et al. (2013). "Detection of the Characteristic Pion-Decay Signature in Supernova Remnants." In: *Science* 339.6121, pp. 807–811. DOI: 10.1126/science. 1231160. arXiv: 1302.3307 [astro-ph.HE].
- Ackermann, M. et al. (2014). "Fermi establishes classical novae as a distinct class of gamma-ray sources." In: *Science* 345.6196, pp. 554–558. DOI: 10.1126/science. 1253947. arXiv: 1408.0735 [astro-ph.HE].
- Aguasca-Cabot, A., P. Bordas, and M. Ribó (2023). "Temporal resolution of transient sources with LST-1: application to BL Lacertae." In: *Highlights on Spanish Astrophysics XI*. Ed. by M. Manteiga et al., p. 129.
- Aguasca-Cabot, A., P. Bordas, and M. Ribó (2022). *Temporal resolution of transient sources with LST-1: application to BL Lacertae*. DOI: 10.5281/zenodo.7042520. URL: https://doi.org/10.5281/zenodo.7042520.
- Aharonian, F. A. (2004). Very high energy cosmic gamma radiation: a crucial window on the extreme Universe. DOI: 10.1142/4657.
- Aharonian, F. A. and A. M. Atoyan (1981). "Compton Scattering of Relativistic Electrons in Compact X-Ray Sources." In: *Ap&SS* 79.2, pp. 321–336. DOI: 10.1007/BF00649428.
- Aharonian, F. A. and A. M. Atoyan (2000). "Broad-band diffuse gamma ray emission of the galactic disk." In: *A&A* 362, pp. 937–952. DOI: 10.48550/arXiv.astro-ph/0009009. arXiv: astro-ph/0009009 [astro-ph].
- Aharonian, F. A. et al. (1997a). "The potential of ground based arrays of imaging atmospheric Cherenkov telescopes. I. Determination of shower parameters." In: *Astroparticle Physics* 6.3-4, pp. 343–368. DOI: 10.1016/S0927-6505(96)00069-2.
- Aharonian, F. A. et al. (1997b). "The potential of the ground based arrays of imaging atmospheric Cherenkov telescopes. II. Gamma ray flux sensitivities." In: *Astroparticle Physics* 6.3-4, pp. 369–377. DOI: 10.1016/S0927-6505(96)00070-9.
- Aharonian, F. et al. (2006). "Observations of the Crab nebula with HESS." In: *A&A* 457.3, pp. 899–915. DOI: 10.1051/0004-6361:20065351. arXiv: astro-ph/0607333 [astro-ph].
- Aharonian, F. et al. (2008). "High energy astrophysics with ground-based gamma ray detectors." In: *Reports on Progress in Physics* 71.9, p. 096901. DOI: 10.1088/0034-4885/71/9/096901.
- Aharonian, F. et al. (2021). "Observation of the Crab Nebula with LHAASO-KM2A a performance study." In: *Chinese Physics C* 45.2, p. 025002. DOI: 10.1088/1674-1137/abd01b. arXiv: 2010.06205 [astro-ph.HE].
- Aharonian, F. et al. (2023). "H.E.S.S. Follow-up Observations of GRB 221009A." In: *ApJ* 946.1, p. L27. DOI: 10.3847/2041-8213/acc405. arXiv: 2303.10558 [astro-ph.HE].
- Ahnen, M. L. et al. (2015). "Very high-energy γ -ray observations of novae and dwarf novae with the MAGIC telescopes." In: A&A 582, A67. DOI: 10.1051/0004-6361/201526478. arXiv: 1508.04902 [astro-ph.HE].
- Ahnen, M. L. et al. (2017a). "Performance of the MAGIC telescopes under moonlight." In: *Astroparticle Physics* 94, pp. 29–41. DOI: 10.1016/j.astropartphys. 2017.08.001. arXiv: 1704.00906 [astro-ph.IM].
- Ahnen, M. L. et al. (2017b). "Very-high-energy gamma-ray observations of the Type Ia Supernova SN 2014J with the MAGIC telescopes." In: *A&A* 602, A98. DOI: 10.1051/0004-6361/201629574. arXiv: 1702.07677 [astro-ph.HE].

- Akaike, H. (1974). "A new look at the statistical model identification." In: *IEEE Transactions on Automatic Control* 19.6, pp. 716–723. DOI: 10.1109/TAC.1974.1100705.
- Akaike, H. (1981). "Likelihood of a model and information criteria." In: *Journal of Econometrics* 16.1, pp. 3–14. DOI: https://doi.org/10.1016/0304-4076(81)90071-3. URL: https://www.sciencedirect.com/science/article/pii/0304407681900713.
- Akchurin, N. and H. Kim (2007). "A study on ion initiated photomultiplier afterpulses." In: *Nuclear Instruments and Methods in Physics Research A* 574.1, pp. 121–126. DOI: 10.1016/j.nima.2007.01.093.
- Akerlof, C. W. et al. (1991). "Locating Very High Energy Gamma-Ray Sources with Arcminute Accuracy." In: *ApJ* 377, p. L97. DOI: 10.1086/186125.
- Albert, A. et al. (2020). "3HWC: The Third HAWC Catalog of Very-high-energy Gamma-Ray Sources." In: *ApJ* 905.1, p. 76. DOI: 10.3847/1538-4357/abc2d8. arXiv: 2007.08582 [astro-ph.HE].
- Albert, A. et al. (2022). " γ -Ray Emission from Classical Nova V392 Per: Measurements from Fermi and HAWC." In: *The Astrophysical Journal* 940.2, p. 141. DOI: 10.3847/1538-4357/ac966a. URL: https://dx.doi.org/10.3847/1538-4357/ac966a.
- Albert, J. et al. (2007). "Unfolding of differential energy spectra in the MAGIC experiment." In: *Nuclear Instruments and Methods in Physics Research A* 583.2-3, pp. 494–506. DOI: 10.1016/j.nima.2007.09.048. arXiv: 0707.2453 [astro-ph].
- Albert, J. et al. (2008a). "FADC signal reconstruction for the MAGIC telescope." In: *Nuclear Instruments and Methods in Physics Research A* 594.3, pp. 407–419. DOI: 10.1016/j.nima.2008.06.043. arXiv: astro-ph/0612385 [astro-ph].
- Albert, J. et al. (2008b). "Implementation of the Random Forest method for the Imaging Atmospheric Cherenkov Telescope MAGIC." In: *Nuclear Instruments and Methods in Physics Research A* 588.3, pp. 424–432. DOI: 10.1016/j.nima.2007.11.068. arXiv: 0709.3719 [astro-ph].
- Aleksić, J. et al. (2011). "Observations of the Crab Pulsar between 25 and 100 GeV with the MAGIC I Telescope." In: *ApJ* 742.1, p. 43. DOI: 10.1088/0004-637X/742/1/43. arXiv: 1108.5391 [astro-ph.HE].
- Aleksić, J. et al. (2012). "Performance of the MAGIC stereo system obtained with Crab Nebula data." In: *Astroparticle Physics* 35.7, pp. 435–448. doi: 10.1016/j.astropartphys.2011.11.007. arXiv: 1108.1477 [astro-ph.IM].
- Aleksić, J. et al. (2016a). "The major upgrade of the MAGIC telescopes, Part I: The hardware improvements and the commissioning of the system." In: *Astroparticle Physics* 72, pp. 61–75. DOI: 10.1016/j.astropartphys.2015.04.004. arXiv: 1409.6073 [astro-ph.IM].
- Aleksić, J. et al. (2016b). "The major upgrade of the MAGIC telescopes, Part II: A performance study using observations of the Crab Nebula." In: *Astroparticle Physics* 72, pp. 76–94. DOI: 10.1016/j.astropartphys.2015.02.005. arXiv: 1409.5594 [astro-ph.IM].
- Aliu, E. et al. (2009). "Improving the performance of the single-dish Cherenkov telescope MAGIC through the use of signal timing." In: *Astroparticle Physics* 30.6, pp. 293–305. DOI: 10.1016/j.astropartphys.2008.10.003. arXiv: 0810.3568 [astro-ph].

- Aliu, E. et al. (2012). "VERITAS Observations of the Nova in V407 Cygni." In: *The Astrophysical Journal* 754.1, p. 77. DOI: 10.1088/0004-637X/754/1/77. URL: https://dx.doi.org/10.1088/0004-637X/754/1/77.
- Amenomori, M. et al. (1999). "Observation of Multi-TEV Gamma Rays from the Crab Nebula using the Tibet Air Shower Array." In: *ApJ* 525.2, pp. L93–L96. DOI: 10.1086/312342. arXiv: astro-ph/9909172 [astro-ph].
- Amenomori, M. et al. (2019). "First Detection of Photons with Energy beyond 100 TeV from an Astrophysical Source." In: *Phys. Rev. Lett.* 123.5, p. 051101. DOI: 10.1103/PhysRevLett.123.051101. arXiv: 1906.05521 [astro-ph.HE].
- Amenomori, M. et al. (2021). "First Detection of sub-PeV Diffuse Gamma Rays from the Galactic Disk: Evidence for Ubiquitous Galactic Cosmic Rays beyond PeV Energies." In: *Phys. Rev. Lett.* 126.14, p. 141101. DOI: 10.1103/PhysRevLett.126.141101. arXiv: 2104.05181 [astro-ph.HE].
- An, Z.-H. et al. (2023). "Insight-HXMT and GECAM-C observations of the brightest-of-all-time GRB 221009A." In: *arXiv e-prints*, arXiv:2303.01203. DOI: 10.48550/arXiv.2303.01203. arXiv: 2303.01203 [astro-ph.HE].
- Anderson, J. P. et al. (2014). "Characterizing the V-band Light-curves of Hydrogenrich Type II Supernovae." In: *ApJ* 786.1, p. 67. DOI: 10.1088/0004-637X/786/1/67. arXiv: 1403.7091 [astro-ph.HE].
- Andrews, J. E. et al. (2025). "Asymmetries and Circumstellar Interaction in the Type II SN 2024bch." In: *ApJ* 980.1, p. 37. DOI: 10.3847/1538-4357/ada555. arXiv: 2411.02497 [astro-ph.HE].
- Antonelli, L. A. (2023). "The CTA LST South as part of the CTA+ program." In: *Proceedings of 38th International Cosmic Ray Conference PoS(ICRC2023)*. Vol. 444, p. 755. DOI: 10.22323/1.444.0755.
- Anupama, G. C. and G. C. Dewangan (2000). "The 1999 Outburst of the Recurrent Nova U Scorpii." In: *AJ* 119.3, pp. 1359–1364. DOI: 10.1086/301249.
- Anupama, G. C. and J. Mikołajewska (1999). "Recurrent novae at quiescence: systems with giant secondaries." In: *A&A* 344, pp. 177–187. arXiv: astro-ph/9812432 [astro-ph].
- Anykeyev, V. B., A. A. Spiridonov, and V. P. Zhigunov (1991). "Comparative investigation of unfolding methods." In: *Nuclear Instruments and Methods in Physics Research A* 303.2, pp. 350–369. DOI: 10.1016/0168-9002(91)90802-W.
- Archambault, S. et al. (2017). "Gamma-ray observations under bright moonlight with VERITAS." In: *Astroparticle Physics* 91, pp. 34–43. DOI: https://doi.org/10.1016/j.astropartphys.2017.03.001. URL: https://www.sciencedirect.com/science/article/pii/S0927650517300762.
- Atkins, R. et al. (2000). "Milagrito, a TeV air-shower array." In: *Nuclear Instru*ments and Methods in Physics Research A 449.3, pp. 478–499. DOI: 10.1016/S0168-9002(00)00146-7. arXiv: astro-ph/9912456 [astro-ph].
- Atwood, W. B. et al. (2009). "The Large Area Telescope on the Fermi Gamma-Ray Space Telescope Mission." In: *ApJ* 697.2, pp. 1071–1102. DOI: 10.1088/0004-637X/697/2/1071. arXiv: 0902.1089 [astro-ph.IM].
- Auger, P. et al. (1939). "Extensive Cosmic-Ray Showers." In: *Reviews of Modern Physics* 11.3-4, pp. 288–291. DOI: 10.1103/RevModPhys.11.288.
- Axelsson, M et al. (2024). "GRB 221009A: the BOAT Burst that Shines in Gamma Rays." In: *arXiv preprint arXiv:2409.04580*.

- Ayala, H. and HAWC Collaboration (2022). "GRB 221009A: Upper limits from HAWC 8 hours after trigger." In: *GRB Coordinates Network* 32683, p. 1.
- Aydi, E. et al. (2021). "Multi-wavelength follow up of the very fast Nova Herculis 2021 (TCP J18573095+1653396)." In: *The Astronomer's Telegram* 14710, p. 1.
- Aydi, E. et al. (2020). "Direct evidence for shock-powered optical emission in a nova." In: *Nature Astronomy* 4, pp. 776–780. DOI: 10.1038/s41550-020-1070-y. arXiv: 2004.05562 [astro-ph.HE].
- Balcon, C. (2024). "Transient Classification Report for 2024-01-29." In: *Transient Name Server Classification Report* 2024-284, p. 1.
- Baldini, L. (2014). "The Silicon Strip Tracker of the Fermi Large Area Telescope: the first 5 years." In: *Proceedings of 22nd International Workshop on Vertex Detectors*—*PoS(Vertex2013)*. Vol. 198, p. 039. DOI: 10.22323/1.198.0039.
- Ballet, J. et al. (2023). "Fermi Large Area Telescope Fourth Source Catalog Data Release 4 (4FGL-DR4)." In: *arXiv e-prints*, arXiv:2307.12546. DOI: 10.48550/arXiv. 2307.12546. arXiv: 2307.12546 [astro-ph.HE].
- Barbon, R., F. Ciatti, and L. Rosino (1979). "Photometric properties of type II supernovae." In: *A&A* 72, pp. 287–292.
- Bartoli, B. et al. (2011). "Long-term Monitoring of the TeV Emission from Mrk 421 with the ARGO-YBJ Experiment." In: *ApJ* 734.2, p. 110. DOI: 10.1088/0004-637X/734/2/110. arXiv: 1106.0896 [astro-ph.HE].
- Bartoli, B. et al. (2013). "TeV Gamma-Ray Survey of the Northern Sky Using the ARGO-YBJ Detector." In: *ApJ* 779.1, p. 27. DOI: 10.1088/0004-637X/779/1/27. arXiv: 1311.3376 [astro-ph.HE].
- Bartoli, B. et al. (2014). "Identification of the TeV Gamma-Ray Source ARGO J2031+4157 with the Cygnus Cocoon." In: *ApJ* 790.2, p. 152. DOI: 10.1088/0004-637X/790/2/152. arXiv: 1406.6436 [astro-ph.HE].
- Bednarek, W. (1997). "Cascade initiated by VHE γ -rays in the radiation field of a close massive companion." In: A&A 322, pp. 523–532.
- Bednarek, W. and A. Śmiałkowski (2022). "High-energy neutrinos from fast winds in novae." In: *MNRAS* 511.3, pp. 3339–3345. DOI: 10.1093/mnras/stac243. arXiv: 2201.10810 [astro-ph.HE].
- Begelman, M. C., B. Rudak, and M. Sikora (1990). "Consequences of Relativistic Proton Injection in Active Galactic Nuclei." In: *ApJ* 362, p. 38. DOI: 10.1086/169241.
- Bell, A. R. (1978). "The acceleration of cosmic rays in shock fronts I." In: *MNRAS* 182, pp. 147–156. DOI: 10.1093/mnras/182.2.147.
- Bell, A. R. et al. (2013). "Cosmic-ray acceleration and escape from supernova remnants." In: MNRAS 431.1, pp. 415–429. DOI: 10.1093/mnras/stt179. arXiv: 1301.7264 [astro-ph.HE].
- Berestetskii, V., E. Lifshitz, and L. Pitaevskii (1982). *Quantum Electrodynamics*. Vol. 4. Course of Theoretical Physics. Butterworth-Heinemann.
- Berge, D., S. Funk, and J. Hinton (2007). "Background modelling in very-high-energy γ -ray astronomy." In: A&A 466.3, pp. 1219–1229. DOI: 10.1051/0004-6361:20066674. arXiv: astro-ph/0610959 [astro-ph].
- Berger, E. (2014). "Short-Duration Gamma-Ray Bursts." In: *ARA&A* 52, pp. 43–105. DOI: 10.1146/annurev-astro-081913-035926. arXiv: 1311.2603 [astro-ph.HE].

- Berger, E. et al. (2023). "Millimeter Observations of the Type II SN 2023ixf: Constraints on the Proximate Circumstellar Medium." In: *ApJ* 951.2, p. L31. DOI: 10.3847/2041-8213/ace0c4. arXiv: 2306.09311 [astro-ph.HE].
- Bernlöhr, K. (2008). "Simulation of imaging atmospheric Cherenkov telescopes with CORSIKA and sim_telarray." In: *Astroparticle Physics* 30.3, pp. 149–158. DOI: 10.1016/j.astropartphys.2008.07.009. arXiv: 0808.2253 [astro-ph].
- Bernlöhr, K. et al. (2013). "Monte Carlo design studies for the Cherenkov Telescope Array." In: *Astroparticle Physics* 43, pp. 171–188. DOI: 10.1016/j.astropartphys. 2012.10.002. arXiv: 1210.3503 [astro-ph.IM].
- Berti, A. (2018). "Study of astrophysical transients with the MAGIC telescopes." PhD thesis. Trieste U.
- Bethe, H. A. (1990). "Supernova mechanisms." In: *Reviews of Modern Physics* 62.4, pp. 801–866. DOI: 10.1103/RevModPhys.62.801.
- Bethe, H. and W. Heitler (1934). "On the Stopping of Fast Particles and on the Creation of Positive Electrons." In: *Proceedings of the Royal Society of London Series A* 146.856, pp. 83–112. DOI: 10.1098/rspa.1934.0140.
- Bietenholz, M. F., N. Bartel, and M. P. Rupen (2003). "SN 1993J VLBI. III. The Evolution of the Radio Shell." In: *ApJ* 597.1, pp. 374–398. DOI: 10.1086/378265. arXiv: astro-ph/0307382 [astro-ph].
- Bissaldi, E. et al. (2022). "GRB 221009A or Swift J1913.1+1946: Fermi-LAT detection." In: GRB Coordinates Network 32637, p. 1.
- Bitossi, M., R. Paoletti, and D. Tescaro (2016). "Ultra-Fast Sampling and Data Acquisition Using the DRS4 Waveform Digitizer." In: *IEEE Trans. Nucl. Sci.* 63.4, pp. 2309–2316. DOI: 10.1109/TNS.2016.2578963.
- Blasi, P. (2013). "The origin of galactic cosmic rays." In: *A&A Rev.* 21, p. 70. DOI: 10.1007/s00159-013-0070-7. arXiv: 1311.7346 [astro-ph.HE].
- Blumenthal, G. R. and R. J. Gould (1970). "Bremsstrahlung, Synchrotron Radiation, and Compton Scattering of High-Energy Electrons Traversing Dilute Gases." In: *Reviews of Modern Physics* 42.2, pp. 237–271. DOI: 10.1103/RevModPhys.42.237.
- Blümer, J., R. Engel, and J. R. Hörandel (2009). "Cosmic rays from the knee to the highest energies." In: *Progress in Particle and Nuclear Physics* 63.2, pp. 293–338. DOI: 10.1016/j.ppnp.2009.05.002. arXiv: 0904.0725 [astro-ph.HE].
- Bock, R. K. et al. (2004). "Methods for multidimensional event classification: a case study using images from a Cherenkov gamma-ray telescope." In: *Nuclear Instruments and Methods in Physics Research A* 516.2-3, pp. 511–528. DOI: 10.1016/j.nima.2003.08.157.
- Bode, M. F. and A. Evans (2012). Classical Novae.
- Bolmont, J. et al. (2022). "First Combined Study on Lorentz Invariance Violation from Observations of Energy-dependent Time Delays from Multiple-type Gamma-Ray Sources. I. Motivation, Method Description, and Validation through Simulations of H.E.S.S., MAGIC, and VERITAS Data Sets." In: *ApJ* 930.1, p. 75. DOI: 10.3847/1538-4357/ac5048. arXiv: 2201.02087 [astro-ph.HE].
- Bond, I. H., A. M. Hillas, and S. M. Bradbury (2003). "An island method of image cleaning for near threshold events from atmospheric Čerenkov telescopes." In: *Astroparticle Physics* 20.3, pp. 311–321. DOI: 10.1016/S0927-6505(03)00193-2.

- Booth, R. A., S. Mohamed, and P. Podsiadlowski (2016). "Modelling the circumstellar medium in RS Ophiuchi and its link to Type Ia supernovae." In: *MNRAS* 457.1, pp. 822–835. DOI: 10.1093/mnras/stw001. arXiv: 1601.02635 [astro-ph.HE].
- Borla Tridon, D. et al. (2010). "The MAGIC-II gamma-ray stereoscopic telescope system." In: *Nuclear Instruments and Methods in Physics Research A* 623.1, pp. 437–439. DOI: 10.1016/j.nima.2010.03.028.
- Bosch-Ramon, V. and D. Khangulyan (2009). "Understanding the Very-High Emission from Microquasars." In: *International Journal of Modern Physics D* 18.3, pp. 347–387. DOI: 10.1142/S0218271809014601. arXiv: 0805.4123 [astro-ph].
- Bose, D. et al. (2022). "Ground-based gamma-ray astronomy: history and development of techniques." In: *European Physical Journal Special Topics* 231.1, pp. 3–26. DOI: 10.1140/epjs/s11734-021-00396-3. arXiv: 2201.04719 [astro-ph.IM].
- Bostroem, K. A. et al. (2024). "Circumstellar Interaction in the Ultraviolet Spectra of SN 2023ixf 14–66 Days After Explosion." In: *The Astrophysical Journal Letters* 973.2, p. L47.
- Bowden, C. C. G. et al. (1992). "The effect of the geomagnetic field on TeV gamma -ray detection." In: *Journal of Physics G Nuclear Physics* 18.2, pp. L55–L60. DOI: 10.1088/0954-3899/18/2/007.
- Breiman, L. (2001). "Random Forests." In: *Machine Learning* 45, pp. 5–32. DOI: 10.1023/A:1010933404324.
- Brose, R., I. Sushch, and J. Mackey (2022). "Core-collapse supernovae in dense environments particle acceleration and non-thermal emission." In: *MNRAS* 516.1, pp. 492–505. DOI: 10.1093/mnras/stac2234.
- Bruch, R. J. et al. (2023). "The Prevalence and Influence of Circumstellar Material around Hydrogen-rich Supernova Progenitors." In: *ApJ* 952.2, p. 119. doi: 10. 3847/1538-4357/acd8be. arXiv: 2212.03313 [astro-ph.HE].
- Burnham, K. and D. Anderson (2002). *Model Selection and Multimodel Inference: A Practical Information-Theoretic Approach*. New York: Springer-Verlag.
- Buson, S., C. C. Cheung, and P. Jean (2021). "Fermi-LAT Gamma-ray Detection of Nova V1405 Cas 2021." In: *The Astronomer's Telegram* 14658, p. 1.
- Cao, Z. et al. (2019). "The Large High Altitude Air Shower Observatory (LHAASO) Science Book (2021 Edition)." In: *arXiv e-prints*, arXiv:1905.02773. DOI: 10.48550/arXiv.1905.02773. arXiv: 1905.02773 [astro-ph.HE].
- Cao, Z. et al. (2021). "Ultrahigh-energy photons up to 1.4 petaelectronvolts from 12 γ -ray Galactic sources." In: *Nature* 594.7861, pp. 33–36. DOI: 10.1038/s41586-021-03498-z.
- Cao, Z. et al. (2024). "The First LHAASO Catalog of Gamma-Ray Sources." In: *ApJS* 271.1, p. 25. DOI: 10.3847/1538-4365/acfd29. arXiv: 2305.17030 [astro-ph.HE].
- Carosi, A. and A. López-Oramas (2024). "A Very-High-Energy Gamma-Ray View of the Transient Sky." In: *Universe* 10.4, p. 163. DOI: 10.3390/universe10040163. arXiv: 2404.17480 [astro-ph.HE].
- Carreto Fidalgo, D. (2019). "Revealing the most energetic light from pulsars and their nebulae." Búsqueda de la radiación de mayor energía procedente de púlsares y sus nebulosas. Tesis de la Universidad Complutense de Madrid, Facultad de Ciencias Físicas, leída el 20/09/2018. PhD thesis. Universidad Complutense de Madrid. URL: https://hdl.handle.net/20.500.14352/16841.
- Cassol, F. et al. (2025). "LST Camera Calibration Paper." Manuscript in preparation.

- Castro-Tirado, A. J. et al. (2022). "GRB 221009A: 10.4m GTC spectroscopic redshift confirmation." In: *GRB Coordinates Network* 32686, p. 1.
- Čerenkov, P. A. (1937). "Visible Radiation Produced by Electrons Moving in a Medium with Velocities Exceeding that of Light." In: *Physical Review* 52.4, pp. 378–379. DOI: 10.1103/PhysRev.52.378.
- Chadwick, P. (2021). "35 Years of Ground-Based Gamma-ray Astronomy." In: *Universe* 7.11, p. 432. DOI: 10.3390/universe7110432.
- Chandra, P. et al. (2023). "Chandra X-ray detection of supernova SN 2023ixf in M101." In: *The Astronomer's Telegram* 16073, p. 1.
- Chandra, P. et al. (2024). "Chandra's Insights into SN 2023ixf." In: *ApJ* 963.1, p. L4. DOI: 10.3847/2041-8213/ad275d. arXiv: 2311.04384 [astro-ph.HE].
- Cherenkov Telescope Array Consortium et al. (2019). *Science with the Cherenkov Telescope Array*. DOI: 10.1142/10986.
- Cherenkov Telescope Array Observatory and Cherenkov Telescope Array Consortium (2021). CTAO Instrument Response Functions prod5 version v0.1. Version v0.1. DOI: 10.5281/zenodo.5499840. URL: https://doi.org/10.5281/zenodo.5499840.
- Cheung, C. C., S. Ciprini, and T. J. Johnson (2021). "Fermi-LAT Gamma-ray Detection of the Recurrent Nova RS Oph." In: *The Astronomer's Telegram* 14834, p. 1.
- Cheung, C. C. et al. (2016). "Fermi-LAT Gamma-Ray Detections of Classical Novae V1369 Centauri 2013 and V5668 Sagittarii 2015." In: *ApJ* 826.2, p. 142. doi: 10. 3847/0004-637X/826/2/142. arXiv: 1605.04216 [astro-ph.HE].
- Cheung, C. C. et al. (2022). "Fermi LAT Gamma-ray Detection of the Recurrent Nova RS Ophiuchi during its 2021 Outburst." In: *ApJ* 935.1, p. 44. doi: 10.3847/1538-4357/ac7eb7. arXiv: 2207.02921 [astro-ph.HE].
- Chevalier, R. A. (1982). "The radio and X-ray emission from type II supernovae." In: *ApJ* 259, pp. 302–310. DOI: 10.1086/160167.
- Chevalier, R. A. (1998). "Synchrotron Self-Absorption in Radio Supernovae." In: *ApJ* 499.2, pp. 810–819. DOI: 10.1086/305676.
- Chitnis, V. R. and P. N. Bhat (1998). "Čerenkov photon density fluctuations in extensive air showers." In: *Astroparticle Physics* 9.1, pp. 45–63. DOI: 10.1016/S0927-6505(98)00007-3. arXiv: astro-ph/9802201 [astro-ph].
- Chomiuk, L., B. D. Metzger, and K. J. Shen (2021). "New Insights into Classical Novae." In: *ARA&A* 59, pp. 391–444. DOI: 10.1146/annurev-astro-112420-114502. arXiv: 2011.08751 [astro-ph.HE].
- Chomiuk, L. et al. (2014). "Binary orbits as the driver of γ -ray emission and mass ejection in classical novae." In: *Nature* 514.7522, pp. 339–342. DOI: 10.1038/nature13773. arXiv: 1410.3473 [astro-ph.HE].
- Chugai, N. N. (1991). "Evidence for energizing of H alpha emission in type II supernovae by ejecta-wind interaction." In: *MNRAS* 250, p. 513. DOI: 10.1093/mnras/250.3.513.
- Chugai, N. N. (2001). "Broad emission lines from the opaque electron-scattering environment of SN 1998S." In: *MNRAS* 326.4, pp. 1448–1454. DOI: 10.1111/j. 1365-2966.2001.04717.x. arXiv: astro-ph/0106234 [astro-ph].
- Chugai, N. N. and I. J. Danziger (1994). "SN 1988Z: low-mass ejecta colliding with the clumpy wind?" In: MNRAS 268, pp. 173–180. DOI: 10.1093/mnras/268.1.173.

- Commichau, S. C. et al. (2008). "Monte Carlo studies of geomagnetic field effects on the imaging air Cherenkov technique for the MAGIC telescope site." In: *Nuclear Instruments and Methods in Physics Research A* 595.3, pp. 572–586. DOI: 10.1016/j.nima.2008.07.144. arXiv: 0802.2551 [astro-ph].
- Contreras, J. L. et al. (2015). "Data model issues in the Cherenkov Telescope Array project." In: *34th International Cosmic Ray Conference (ICRC2015)*. Vol. 34. International Cosmic Ray Conference, p. 960. DOI: 10.22323/1.236.0960. arXiv: 1508.07584 [astro-ph.IM].
- Cortina, J. and M. Teshima (2015). "Status of the Cherenkov Telescope Array Large Size Telescopes." In: 34th International Cosmic Ray Conference (ICRC2015). Vol. 34. International Cosmic Ray Conference, p. 943. DOI: 10.22323/1.236.0943. arXiv: 1508.06438 [astro-ph.IM].
- Cortina, J. and CTA LST Collaboration (2021). "Detection of very-high-energy gamma-ray emission from BL Lac with the LST-1." In: *The Astronomer's Telegram* 14783, p. 1.
- Cowan, G. (1998). Statistical data analysis.
- Cristofari, P. et al. (2020). "Time-dependent high-energy gamma-ray signal from accelerated particles in core-collapse supernovae: the case of SN 1993J." In: *MNRAS* 494.2, pp. 2760–2765. DOI: 10.1093/mnras/staa984.
- Cristofari, P. et al. (2022). "The first days of Type II-P core collapse supernovae in the gamma-ray range." In: *MNRAS* 511.3, pp. 3321–3329. DOI: 10.1093/mnras/stac217.
- CTA-LST Project, T. et al. (2024). "Low energy performance boost through a hardware stereoscopic trigger between CTA LST1 and MAGIC." In: 38th International Cosmic Ray Conference, p. 700.
- D'Amico, G. (2022). "Statistical Tools for Imaging Atmospheric Cherenkov Telescopes." In: *Universe* 8.2, p. 90. DOI: 10.3390/universe8020090. arXiv: 2202.04590 [astro-ph.IM].
- Daum, A. et al. (1997). "First results on the performance of the HEGRA IACT array." In: Astroparticle Physics 8.1, pp. 1–11. DOI: https://doi.org/10.1016/S0927-6505(97)00031-5. URL: https://www.sciencedirect.com/science/article/pii/S0927650597000315.
- De Angelis, A. and M. Pimenta (2018). *Introduction to Particle and Astroparticle Physics*. DOI: 10.1007/978-3-319-78181-5.
- de Naurois, M. (2012). "Very High Energy astronomy from H.E.S.S. to CTA. Opening of a new astronomical window on the non-thermal Universe." Habilitation à diriger des recherches. Université Pierre et Marie Curie Paris VI. url: https://tel.archives-ouvertes.fr/tel-00687872.
- de Naurois, M. and D. Mazin (2015). "Ground-based detectors in very-high-energy gamma-ray astronomy." In: *Comptes Rendus Physique* 16.6-7, pp. 610–627. DOI: 10.1016/j.crhy.2015.08.011. arXiv: 1511.00463 [astro-ph.IM].
- de Ruiter, I. et al. (2023). "Low-frequency radio observations of recurrent nova RS Ophiuchi with MeerKAT and LOFAR." In: MNRAS 523.1, pp. 132–148. DOI: 10.1093/mnras/stad1418. arXiv: 2301.10552 [astro-ph.HE].
- De, K. et al. (2021). "A Population of Heavily Reddened, Optically Missed Novae from Palomar Gattini-IR: Constraints on the Galactic Nova Rate." In: *ApJ* 912.1, p. 19. DOI: 10.3847/1538-4357/abeb75. arXiv: 2101.04045 [astro-ph.HE].

- Dichiara, S. et al. (2022). "Swift J1913.1+1946 a new bright hard X-ray and optical transient." In: *GRB Coordinates Network* 32632, p. 1.
- Diesing, R. et al. (2023). "Evidence for Multiple Shocks from the γ -Ray Emission of RS Ophiuchi." In: *The Astrophysical Journal* 947.2, p. 70. DOI: 10.3847/1538-4357/acc105. URL: https://dx.doi.org/10.3847/1538-4357/acc105.
- Domínguez, A. et al. (2011). "Extragalactic background light inferred from AEGIS galaxy-SED-type fractions." In: *MNRAS* 410.4, pp. 2556–2578. DOI: 10.1111/j. 1365-2966.2010.17631.x. arXiv: 1007.1459 [astro-ph.CO].
- Dominik, R. M., M. Linhoff, and J. Sitarek (2023). "Interpolation of Instrument Response Functions for the Cherenkov Telescope Array in the Context of pyirf." In: *Proceedings, 38th International Cosmic Ray Conference*. Vol. 444. 618. Nagoya, Japan. DOI: 10.22323/1.444.0703.
- Donath, A. et al. (2023). "Gammapy: A Python package for gamma-ray astronomy." In: *A&A* 678, A157. DOI: 10.1051/0004-6361/202346488. arXiv: 2308.13584 [astro-ph.IM].
- Drake, J. J. et al. (2021). "The Remarkable Spin-down and Ultrafast Outflows of the Highly Pulsed Supersoft Source of Nova Herculis 2021." In: *ApJ* 922.2, p. L42. DOI: 10.3847/2041-8213/ac34fd. arXiv: 2110.14058 [astro-ph.HE].
- Drury, L. O., F. A. Aharonian, and H. J. Voelk (1994). "The gamma-ray visibility of supernova remnants. A test of cosmic ray origin." In: *A&A* 287, pp. 959–971. DOI: 10.48550/arXiv.astro-ph/9305037. arXiv: astro-ph/9305037 [astro-ph].
- Drury, L. O. (1983). "REVIEW ARTICLE: An introduction to the theory of diffusive shock acceleration of energetic particles in tenuous plasmas." In: *Reports on Progress in Physics* 46.8, pp. 973–1027. DOI: 10.1088/0034-4885/46/8/002.
- Dwarkadas, V. V. (2013). "Exploring the γ -ray emissivity of young supernova remnants I. Hadronic emission." In: *MNRAS* 434.4, pp. 3368–3377. DOI: 10.1093/mnras/stt1252. arXiv: 1307.4414 [astro-ph.HE].
- Eldridge, J. J. et al. (2013). "The death of massive stars II. Observational constraints on the progenitors of Type Ibc supernovae." In: *MNRAS* 436.1, pp. 774–795. DOI: 10.1093/mnras/stt1612. arXiv: 1301.1975 [astro-ph.SR].
- Errando, M. and T. Saito (2024). "How to Detect Gamma Rays from Ground: An Introduction to the Detection Concepts." In: *Handbook of X-ray and Gamma-ray Astrophysics*. Ed. by C. Bambi and A. Santangelo. Singapore: Springer Nature Singapore, pp. 2483–2519. DOI: 10.1007/978-981-19-6960-7_61. URL: https://doi.org/10.1007/978-981-19-6960-7_61.
- Fan, Y.-Z. and T. Piran (2008). "High-energy γ -ray emission from gamma-ray bursts before GLAST." In: *Frontiers of Physics in China* 3.3, pp. 306–330. DOI: 10.1007/s11467-008-0033-z. arXiv: 0805.2221 [astro-ph].
- Fermi Science Support Development Team (2019). Fermitools: Fermi Science Tools. Astrophysics Source Code Library, record ascl:1905.011.
- Ferrière, K. M. (2001). "The interstellar environment of our galaxy." In: *Reviews of Modern Physics* 73.4, pp. 1031–1066. DOI: 10.1103/RevModPhys.73.1031. arXiv: astro-ph/0106359 [astro-ph].
- Fichtel, C. E. et al. (1975). "High-energy gamma-ray results from the second Small Astronomy Satellite." In: *ApJ* 198, pp. 163–182. DOI: 10.1086/153590.
- Filippenko, A. V. (1997). "Optical Spectra of Supernovae." In: *ARA&A* 35, pp. 309–355. DOI: 10.1146/annurev.astro.35.1.309.

- Finzell, T. et al. (2018). "A Detailed Observational Analysis of V1324 Sco, the Most Gamma-Ray-luminous Classical Nova to Date." In: *ApJ* 852.2, p. 108. DOI: 10.3847/1538-4357/aaa12a. arXiv: 1701.03094 [astro-ph.SR].
- Fishman, G. J. et al. (1994). "The first BATSE gamma-ray burst catalog." In: *The Astrophysical Journal Supplement Series*, vol. 92, no. 1, p. 229-283 92, pp. 229-283.
- Foffano, L., M. Tavani, and G. Piano (2024). "Theoretical Modeling of the Exceptional GRB 221009A Afterglow." In: *ApJ* 973.2, p. L44. DOI: 10.3847/2041-8213/ad76a3. arXiv: 2409.02859 [astro-ph.HE].
- Foffano, L. et al. (2021). "Monitoring the pointing of the Large Size Telescope prototype using star reconstruction in the Cherenkov camera." In: *Proceedings of 37th International Cosmic Ray Conference PoS(ICRC2021)*. Vol. 395, p. 712. DOI: 10.22323/1.395.0712.
- Fomin, V. et al. (1994). "New methods of atmospheric Cherenkov imaging for gamma-ray astronomy. I. The false source method." In: *Astroparticle Physics* 2.2, pp. 137–150. DOI: https://doi.org/10.1016/0927-6505(94)90036-1. URL: https://www.sciencedirect.com/science/article/pii/0927650594900361.
- Franckowiak, A. et al. (2018). "Search for gamma-ray emission from Galactic novae with the Fermi -LAT." In: *A&A* 609, A120. DOI: 10.1051/0004-6361/201731516. arXiv: 1710.04736 [astro-ph.HE].
- Frank, I. M. and I. E. Tamm (1937). "Coherent visible radiation of fast electrons passing through matter." In: *Compt. Rend. Acad. Sci. URSS* 14.3. Ed. by V. L. Ginzburg, B. M. Bolotovsky, and I. M. Dremin, pp. 109–114. DOI: 10.3367/UFNr. 0093.1967100.0388.
- Fraser, M. (2020). "Supernovae and transients with circumstellar interaction." In: *Royal Society Open Science* 7.7, p. 200467. DOI: 10.1098/rsos.200467.
- Fuller, J. (2017). "Pre-supernova outbursts via wave heating in massive stars I. Red supergiants." In: MNRAS 470.2, pp. 1642–1656. DOI: 10.1093/mnras/stx1314. arXiv: 1704.08696 [astro-ph.SR].
- Funk, S., J. A. Hinton, and CTA Consortium (2013). "Comparison of Fermi-LAT and CTA in the region between 10-100 GeV." In: *Astroparticle Physics* 43, pp. 348–355. DOI: 10.1016/j.astropartphys.2012.05.018. arXiv: 1205.0832 [astro-ph.HE].
- Gaia Collaboration et al. (2023). "Gaia Data Release 3. Summary of the content and survey properties." In: *A&A* 674, A1. DOI: 10.1051/0004-6361/202243940. arXiv: 2208.00211 [astro-ph.GA].
- Gaisser, T. K. (1991). Cosmic Rays and Particle Physics.
- Gaisser, T. K. and A. M. Hillas (1977). "Reliability of the Method of Constant Intensity Cuts for Reconstructing the Average Development of Vertical Showers." In: *International Cosmic Ray Conference*. Vol. 8. International Cosmic Ray Conference, p. 353.
- Gal-Yam, A. and D. C. Leonard (2009). "A massive hypergiant star as the progenitor of the supernova SN 2005gl." In: *Nature* 458.7240, pp. 865–867. DOI: 10.1038/nature07934.
- Gal-Yam, A. (2017). "Observational and Physical Classification of Supernovae." In: *Handbook of Supernovae*. Ed. by A. W. Alsabti and P. Murdin, p. 195. DOI: 10.1007/978-3-319-21846-5_35.

- Gal-Yam, A. et al. (2014). "A Wolf-Rayet-like progenitor of SN 2013cu from spectral observations of a stellar wind." In: *Nature* 509.7501, pp. 471–474. DOI: 10.1038/nature13304. arXiv: 1406.7640 [astro-ph.HE].
- Gallagher, J. S. and S. Starrfield (1978). "Theory and observations of classical novae." In: *ARA&A* 16, pp. 171–214. doi: 10.1146/annurev.aa.16.090178.001131.
- Gaug, M. et al. (2019). "Using Muon Rings for the Calibration of the Cherenkov Telescope Array: A Systematic Review of the Method and Its Potential Accuracy." In: *ApJS* 243.1, p. 11. DOI: 10.3847/1538-4365/ab2123. arXiv: 1907.04375 [astro-ph.IM].
- Geary, K. (2021). "Outburst of RS Ophiuchi." In: VSNET-alert 26131, p. 1. URL: http://ooruri.kusastro.kyoto-u.ac.jp/mailarchive/vsnet-alert/26131.
- Gehrels, N. and P. Mészáros (2012). "Gamma-Ray Bursts." In: *Science* 337.6097, p. 932. DOI: 10.1126/science.1216793. arXiv: 1208.6522 [astro-ph.HE].
- Ghisellini, G. (2013). Radiative Processes in High Energy Astrophysics. Vol. 873. DOI: 10.1007/978-3-319-00612-3.
- Giarratana, S. et al. (2024). "The expansion of the GRB 221009A afterglow." In: *A&A* 690, A74. DOI: 10.1051/0004-6361/202348524. arXiv: 2311.05527 [astro-ph.HE].
- Gill, R. and J. Granot (2023). "GRB 221009A afterglow from a shallow angular structured jet." In: *Monthly Notices of the Royal Astronomical Society: Letters* 524.1, pp. L78–L83. DOI: 10.1093/mnrasl/slad075. eprint: https://academic.oup.com/mnrasl/article-pdf/524/1/L78/54609034/slad075.pdf. URL: https://doi.org/10.1093/mnrasl/slad075.
- Gillessen, S. and H. L. Harney (2005). "Significance in gamma-ray astronomy the Li & Ma problem in Bayesian statistics." In: *A&A* 430, pp. 355–362. DOI: 10.1051/0004-6361:20035839. arXiv: astro-ph/0411660 [astro-ph].
- Ginzburg, V. L. and S. I. Syrovatskii (1964). The Origin of Cosmic Rays.
- Gliwny, P. (2024). "Developing low-energy data analysis methods for Large-Sized Telescopes and observations of Flat-Spectrum Radio Quasars with Cherenkov telescopes." PhD thesis. University of Lodz.
- Goldwurm, A. and A. Gros (2022). "Coded Mask Instruments for Gamma-Ray Astronomy." In: *Handbook of X-ray and Gamma-ray Astrophysics*. Ed. by C. Bambi and A. Sangangelo, p. 15. DOI: 10.1007/978-981-16-4544-0_44-1.
- Gomez-Gomar, J. et al. (1998). "Gamma-ray emission from individual classical novae." In: *MNRAS* 296.4, pp. 913–920. DOI: 10.1046/j.1365-8711.1998.01421.x. arXiv: astro-ph/9711322 [astro-ph].
- Gottlieb, O., E. Nakar, and O. Bromberg (2021). "The structure of hydrodynamic γ -ray burst jets." In: *MNRAS* 500.3, pp. 3511–3526. doi: 10.1093/mnras/staa3501. arXiv: 2006.02466 [astro-ph.HE].
- Gould, R. J. and G. P. Schréder (1967a). "Opacity of the Universe to High-Energy Photons." In: *Physical Review* 155.5, pp. 1408–1411. DOI: 10.1103/PhysRev.155.1408.
- Gould, R. J. and G. P. Schréder (1967b). "Pair Production in Photon-Photon Collisions." In: *Physical Review* 155.5, pp. 1404–1407. DOI: 10.1103/PhysRev.155.1404.
- Grefenstette, B. W. et al. (2023). "Early Hard X-Rays from the Nearby Core-collapse Supernova SN 2023ixf." In: *ApJ* 952.1, p. L3. DOI: 10.3847/2041-8213/acdf4e. arXiv: 2306.04827 [astro-ph.HE].

- Gueta, O. (2021). "The Cherenkov Telescope Array: layout, design and performance." In: *Proceedings of 37th International Cosmic Ray Conference PoS(ICRC2021)*. Vol. 395, p. 885. DOI: 10.22323/1.395.0885.
- Gutiérrez, C. P. et al. (2017). "Type II Supernova Spectral Diversity. II. Spectroscopic and Photometric Correlations." In: *ApJ* 850.1, p. 90. doi: 10.3847/1538-4357/aa8f42. arXiv: 1709.02799 [astro-ph.HE].
- H. E. S. S. Collaboration et al. (2019). "Upper limits on very-high-energy gamma-ray emission from core-collapse supernovae observed with H.E.S.S." In: *A&A* 626, A57. DOI: 10.1051/0004-6361/201935242. arXiv: 1904.10526 [astro-ph.HE].
- H. E. S. S. Collaboration et al. (2021). "Revealing x-ray and gamma ray temporal and spectral similarities in the GRB 190829A afterglow." In: *Science* 372.6546, pp. 1081–1085. DOI: 10.1126/science.abe8560. arXiv: 2106.02510 [astro-ph.HE].
- H. E. S. S. Collaboration et al. (2022). "Time-resolved hadronic particle acceleration in the recurrent nova RS Ophiuchi." In: *Science* 376.6588, pp. 77–80. DOI: 10.1126/science.abn0567. arXiv: 2202.08201 [astro-ph.HE].
- Hartman, R. C. et al. (1999). "The Third EGRET Catalog of High-Energy Gamma-Ray Sources." In: *ApJS* 123.1, pp. 79–202. DOI: 10.1086/313231.
- Heck, D. et al. (1998). *CORSIKA: a Monte Carlo code to simulate extensive air showers*. Heger, A. et al. (2003). "How Massive Single Stars End Their Life." In: *ApJ* 591.1, pp. 288–300. DOI: 10.1086/375341. arXiv: astro-ph/0212469 [astro-ph].
- Heitler, W. (1954). Quantum theory of radiation.
- Hermsen, W. et al. (1977). "New high energy gamma-ray sources observed by COS B." In: *Nature* 269, pp. 494–495. DOI: 10.1038/269494a0.
- Hernanz, M. and V. Tatischeff (2012). "High Energy Emission of Symbiotic Recurrent Novae: RS Oph and V407 Cyg." In: *Baltic Astronomy* 21, pp. 62–67. DOI: 10.1515/astro-2017-0359. arXiv: 1111.4129 [astro-ph.HE].
- Hillas, A. M. (1982a). "Angular and energy distributions of charged particles in electron-photon cascades in air." In: *Journal of Physics G Nuclear Physics* 8.10, pp. 1461–1473. DOI: 10.1088/0305-4616/8/10/016.
- Hillas, A. M. (1982b). "The sensitivity of Cerenkov radiation pulses to the longitudinal development of cosmic-ray showers." In: *Journal of Physics G Nuclear Physics* 8.10, pp. 1475–1492. DOI: 10.1088/0305-4616/8/10/017.
- Hillas, A. M. (1984). "The Origin of Ultra-High-Energy Cosmic Rays." In: *ARA&A* 22, pp. 425–444. DOI: 10.1146/annurev.aa.22.090184.002233.
- Hillas, A. M. (1985). "Cerenkov Light Images of EAS Produced by Primary Gamma Rays and by Nuclei." In: 19th International Cosmic Ray Conference (ICRC19), Volume 3. Ed. by F. C. Jones. Vol. 3. International Cosmic Ray Conference, p. 445.
- Hinds, K.-R. et al. (2025). "Inferring CSM Properties of Type II SNe Using a Magnitude-Limited ZTF Sample." In: *arXiv e-prints*, arXiv:2503.19969. DOI: 10.48550/arXiv.2503.19969. arXiv: 2503.19969 [astro-ph.HE].
- Hofmann, W. (2006). "Performance Limits for Cherenkov Instruments." In: *arXiv e-prints*, astro-ph/0603076. DOI: 10.48550/arXiv.astro-ph/0603076. arXiv: astro-ph/0603076 [astro-ph].
- Hofmann, W. et al. (1999). "Comparison of techniques to reconstruct VHE gammaray showers from multiple stereoscopic Cherenkov images." In: *Astroparticle Physics* 12.3, pp. 135–143. DOI: 10.1016/S0927-6505(99)00084-5. arXiv: astro-ph/9904234 [astro-ph].

- Holder, J. et al. (2006). "The first VERITAS telescope." In: *Astroparticle Physics* 25.6, pp. 391–401. DOI: 10.1016/j.astropartphys.2006.04.002. arXiv: astro-ph/0604119 [astro-ph].
- Hosseinzadeh, G. et al. (2023). "Shock Cooling and Possible Precursor Emission in the Early Light Curve of the Type II SN 2023ixf." In: *ApJ* 953.1, p. L16. DOI: 10.3847/2041-8213/ace4c4. arXiv: 2306.06097 [astro-ph.HE].
- Huang, Y. et al. (2022). "LHAASO observed GRB 221009A with more than 5000 VHE photons up to around 18 TeV." In: *GRB Coordinates Network* 32677, p. 1.
- Humphreys, R. M. and K. Davidson (1994). "The Luminous Blue Variables: Astrophysical Geysers." In: *PASP* 106, p. 1025. DOI: 10.1086/133478.
- Hurvich, C. M. and C.-L. Tsai (1989). "Regression and time series model selection in small samples." In: *Biometrika* 76.2, pp. 297–307.
- Iben I., J. (1982). "Hot accreting white dwarfs in the quasi-static approximation." In: *ApJ* 259, pp. 244–266. DOI: 10.1086/160164.
- Inoue, S. et al. (2019). "KSP: Transients." In: *Science with the Cherenkov Telescope Array*. Ed. by B. S. Acharya et al., pp. 163–198. DOI: 10.1142/9789813270091_0009.
- Inoue, S. et al. (2013). "Gamma-ray burst science in the era of the Cherenkov Telescope Array." In: *Astroparticle Physics* 43, pp. 252–275. DOI: 10.1016/j.astropartphys.2013.01.004. arXiv: 1301.3014 [astro-ph.HE].
- Islam, N., K. Mukai, and J. L. Sokoloski (2024). "X-Rays from RS Ophiuchi's 2021 Eruption: Shocks In and Out of Ionization Equilibrium." In: *ApJ* 960.2, p. 125. doi: 10.3847/1538-4357/ad1041. arXiv: 2311.17156 [astro-ph.HE].
- Itagaki, K. (2023). "Transient Discovery Report for 2023-05-19." In: *Transient Name Server Discovery Report* 2023-1158, p. 1.
- Iwata, Y. et al. (2025). "Radio Follow-up Observations of SN 2023ixf by Japanese and Korean Very Long Baseline Interferometers." In: *ApJ* 978.2, p. 138. DOI: 10.3847/1538-4357/ad9a62. arXiv: 2411.07542 [astro-ph.HE].
- Jacobson-Galán, W. et al. (2023). "SN 2023ixf in Messier 101: photo-ionization of dense, close-in circumstellar material in a nearby type II supernova." In: *The Astrophysical journal letters* 954.2, p. L42.
- Jerkstrand, A., D. Milisavljevic, and B. Müller (2025). "Core-collapse supernovae." In: arXiv e-prints, arXiv:2503.01321. DOI: 10.48550/arXiv.2503.01321. arXiv: 2503.01321 [astro-ph.HE].
- Jones, F. C. (1968). "Calculated Spectrum of Inverse-Compton-Scattered Photons." In: *Physical Review* 167.5, pp. 1159–1169. DOI: 10.1103/PhysRev.167.1159.
- Jones, F. C. and D. C. Ellison (1991). "The plasma physics of shock acceleration." In: *Space Sci. Rev.* 58.1, pp. 259–346. DOI: 10.1007/BF01206003.
- Kafexhiu, E. et al. (2014). "Parametrization of gamma-ray production cross sections for p p interactions in a broad proton energy range from the kinematic threshold to PeV energies." In: *Phys. Rev. D* 90.12, p. 123014. DOI: 10.1103/PhysRevD.90.123014. arXiv: 1406.7369 [astro-ph.HE].
- Kakuwa, J. et al. (2012). "Prospects for detecting gamma-ray bursts at very high energies with the Cherenkov Telescope Array: GRB detection rate with CTA." In: Monthly Notices of the Royal Astronomical Society 425.1, 514–526. DOI: 10.1111/j.1365-2966.2012.21490.x. URL: http://dx.doi.org/10.1111/j.1365-2966.2012.21490.x.

- Kann, D. A. et al. (2023). "GRANDMA and HXMT Observations of GRB 221009A: The Standard Luminosity Afterglow of a Hyperluminous Gamma-Ray Burst-In Gedenken an David Alexander Kann." In: *ApJ* 948.2, p. L12. doi: 10.3847/2041-8213/acc8d0. arXiv: 2302.06225 [astro-ph.HE].
- Kato, M. et al. (2014). "Shortest Recurrence Periods of Novae." In: *ApJ* 793.2, p. 136. DOI: 10.1088/0004-637X/793/2/136. arXiv: 1404.0582 [astro-ph.SR].
- Kawash, A. et al. (2022). "The Galactic Nova Rate: Estimates from the ASAS-SN and Gaia Surveys." In: *ApJ* 937.2, p. 64. DOI: 10.3847/1538-4357/ac8d5e. arXiv: 2206.14132 [astro-ph.SR].
- Kelner, S. R., F. A. Aharonian, and V. V. Bugayov (2006). "Energy spectra of gamma rays, electrons, and neutrinos produced at proton-proton interactions in the very high energy regime." In: *Phys. Rev. D* 74.3, p. 034018. DOI: 10.1103/PhysRevD.74.034018. arXiv: astro-ph/0606058 [astro-ph].
- Kenett, R., S. Zacks, and P. Gedeck (2022). *Modern Statistics: A Computer-Based Approach with Python*. DOI: 10.1007/978-3-031-07566-7.
- Kennea, J. A., M. Williams, and Swift Team (2022). "GRB 221009A: Swift detected transient may be GRB." In: *GRB Coordinates Network* 32635, p. 1.
- Khangulyan, D., F. A. Aharonian, and S. R. Kelner (2014). "Simple Analytical Approximations for Treatment of Inverse Compton Scattering of Relativistic Electrons in the Blackbody Radiation Field." In: *ApJ* 783.2, p. 100. doi: 10.1088/0004-637X/783/2/100. arXiv: 1310.7971 [astro-ph.HE].
- Khangulyan, D. et al. (2007). "TeV light curve of PSR B1259-63/SS2883." In: *MNRAS* 380.1, pp. 320–330. DOI: 10.1111/j.1365-2966.2007.12075.x. arXiv: astro-ph/0605663 [astro-ph].
- Khangulyan, D., F. Aharonian, and A. M. Taylor (2024). "Naked Forward Shock Seen in the TeV Afterglow Data of GRB 221009A." In: *ApJ* 966.1, p. 31. DOI: 10.3847/1538-4357/ad3550. arXiv: 2309.00673 [astro-ph.HE].
- Khazov, D. et al. (2016). "Flash Spectroscopy: Emission Lines from the Ionized Circumstellar Material around <10-day-old Type II Supernovae." In: *ApJ* 818.1, p. 3. DOI: 10.3847/0004-637X/818/1/3. arXiv: 1512.00846 [astro-ph.HE].
- Kierans, C., T. Takahashi, and G. Kanbach (2022). "Compton Telescopes for Gamma-Ray Astrophysics." In: *Handbook of X-ray and Gamma-ray Astrophysics*. Ed. by C. Bambi and A. Sangangelo, p. 18. DOI: 10.1007/978-981-16-4544-0_46-1.
- Kilpatrick, C. D. et al. (2023). "SN 2023ixf in Messier 101: A Variable Red Supergiant as the Progenitor Candidate to a Type II Supernova." In: *ApJ* 952.1, p. L23. DOI: 10.3847/2041-8213/ace4ca. arXiv: 2306.04722 [astro-ph.SR].
- Kimura, S. S. and T. J. Moriya (2024). "High-energy gamma-ray and neutrino emissions from interacting supernovae based on radiation hydrodynamic simulations: a case of SN 2023ixf." In: *arXiv e-prints*, arXiv:2409.18935. DOI: 10.48550/arXiv. 2409.18935. arXiv: 2409.18935 [astro-ph.HE].
- Kirk, J. G. et al., eds. (1994). *Plasma Astrophysics*. DOI: 10.1007/3-540-31627-2.
- Kniffen, D. A. et al. (1974). "Gamma radiation from the Crab Nebula above 35 MeV." In: *Nature* 251.5474, pp. 397–399. DOI: 10.1038/251397a0.
- Knoll, G. F. (2000). Radiation detection and measurement.
- Kobayashi, Y. et al. (2021). "Camera Calibration of the CTA-LST prototype." In: *Proceedings of 37th International Cosmic Ray Conference PoS(ICRC2021)*. Vol. 395, p. 720. DOI: 10.22323/1.395.0720.

- Kouveliotou, C. et al. (1993). "Identification of Two Classes of Gamma-Ray Bursts." In: *ApJ* 413, p. L101. DOI: 10.1086/186969.
- Kozyreva, A. et al. (2025). "SN 2023ixf: An average-energy explosion with circumstellar medium and a precursor." In: *Astronomy & Astrophysics* 694, A319.
- Krause, M., E. Pueschel, and G. Maier (2017). "Improved γ /hadron separation for the detection of faint γ -ray sources using boosted decision trees." In: *Astroparticle Physics* 89, pp. 1–9. DOI: 10.1016/j.astropartphys.2017.01.004. arXiv: 1701.06928 [astro-ph.IM].
- Kraushaar, W. L. et al. (1972). "High-Energy Cosmic Gamma-Ray Observations from the OSO-3 Satellite." In: *ApJ* 177, p. 341. DOI: 10.1086/151713.
- Krauss, M. I. et al. (2012). "Expanded Very Large Array Observations of the Radio Evolution of SN 2011dh." In: *ApJ* 750.2, p. L40. DOI: 10.1088/2041-8205/750/2/L40. arXiv: 1201.0770 [astro-ph.HE].
- Krawczynski, H. et al. (2006). "Gamma hadron separation methods for the VERITAS array of four imaging atmospheric Cherenkov telescopes." In: *Astroparticle Physics* 25.6, pp. 380–390. DOI: 10.1016/j.astropartphys.2006.03.011. arXiv: astro-ph/0604508 [astro-ph].
- Kumar, P. and B. Zhang (2015). "The physics of gamma-ray bursts & relativistic jets." In: *Phys. Rep.* 561, pp. 1–109. DOI: 10.1016/j.physrep.2014.09.008. arXiv: 1410.0679 [astro-ph.HE].
- Kurahashi, N., K. Murase, and M. Santander (2022). "High-Energy Extragalactic Neutrino Astrophysics." In: *Annual Review of Nuclear and Particle Science* 72, pp. 365–387. DOI: 10.1146/annurev-nucl-011122-061547. arXiv: 2203.11936 [astro-ph.HE].
- LHAASO Collaboration (2024). "An ultrahigh-energy γ -ray bubble powered by a super PeVatron." In: *Science Bulletin* 69.4, pp. 449–457. DOI: 10.1016/j.scib.2023. 12.040. arXiv: 2310.10100 [astro-ph.HE].
- LHAASO Collaboration et al. (2023). "A tera-electron volt afterglow from a narrow jet in an extremely bright gamma-ray burst." In: *Science* 380.6652, pp. 1390–1396. DOI: 10.1126/science.adg9328. arXiv: 2306.06372 [astro-ph.HE].
- LHAASO Collaboration, T. (2023). "Very high-energy gamma-ray emission beyond 10 TeV from GRB 221009A." In: *Science Advances* 9.46, eadj2778. DOI: 10.1126/sciadv.adj2778. eprint: https://www.science.org/doi/pdf/10.1126/sciadv.adj2778. URL: https://www.science.org/doi/abs/10.1126/sciadv.adj2778.
- LHAASO collaboration (2021). "Performance of LHAASO-WCDA and Observation of Crab Nebula as a Standard Candle." In: *arXiv e-prints*, arXiv:2101.03508. DOI: 10.48550/arXiv.2101.03508. arXiv: 2101.03508 [astro-ph.IM].
- Landau, L. D. and E. M. Lifshitz (1984). *Electrodynamics of Continuous Media*. 2nd revised and enlarged edition. Vol. 8. Course of Theoretical Physics. Oxford: Pergamon.
- Laskar, T. et al. (2023). "The Radio to GeV Afterglow of GRB 221009A." In: *ApJ* 946.1, p. L23. DOI: 10.3847/2041-8213/acbfad. arXiv: 2302.04388 [astro-ph.HE].
- Lemoine, M. and G. Pelletier (2015). "On the origin of very-high-energy photons in astrophysics: A short introduction to acceleration and radiation physics." In: *Comptes Rendus Physique* 16.6-7, pp. 628–640. DOI: 10.1016/j.crhy.2015.08.012.
- Lesage, S. et al. (2022). "GRB 221009A: Fermi GBM observation." In: *GRB Coordinates Network* 32642, p. 1.

- Lesage, S. et al. (2023). "Fermi-GBM Discovery of GRB 221009A: An Extraordinarily Bright GRB from Onset to Afterglow." In: *ApJ* 952.2, p. L42. DOI: 10.3847/2041-8213/ace5b4. arXiv: 2303.14172 [astro-ph.HE].
- Lessard, R. W. et al. (2001). "A new analysis method for reconstructing the arrival direction of TeV gamma rays using a single imaging atmospheric Cherenkov telescope." In: *Astroparticle Physics* 15.1, pp. 1–18. DOI: https://doi.org/10.1016/S0927-6505(00)00133-X. URL: https://www.sciencedirect.com/science/article/pii/S092765050000133X.
- Lessard, R. W. et al. (2002). "Wavelet imaging cleaning method for atmospheric Cherenkov telescopes." In: *Astroparticle Physics* 17.4, pp. 427–440. DOI: 10.1016/S0927-6505(01)00173-6. arXiv: astro-ph/0110033 [astro-ph].
- Li, K.-L. (2021). "Fermi-LAT Detection of TCP J18573095+1653396 (=Nova Her 2021)." In: *The Astronomer's Telegram* 14705, p. 1.
- Li, S. et al. (2024). "Fermi-LAT discovery of the GeV emission of the superluminous supernovae SN 2017egm." In: *arXiv preprint arXiv:2407.05968*.
- Li, T. P. and Y. Q. Ma (1983). "Analysis methods for results in gamma-ray astronomy." In: *ApJ* 272, pp. 317–324. DOI: 10.1086/161295.
- Linford, J. D. et al. (2017). "The Peculiar Multiwavelength Evolution Of V1535 Sco." In: *ApJ* 842.2, p. 73. DOI: 10.3847/1538-4357/aa7512. arXiv: 1703.03333 [astro-ph.HE].
- Linhoff, M. et al. (2023). "ctapipe Prototype Open Event Reconstruction Pipeline for the Cherenkov Telescope Array." In: *PoS* ICRC2023, p. 703. DOI: 10.22323/1.444.0703.
- Liu, J. C. et al. (2022). "GRB 221009A: HEBS detection." In: *GRB Coordinates Network* 32751, p. 1.
- Longair, M. S. (2011). High Energy Astrophysics.
- López-Coto, R. et al. (2022). "Istchain: An Analysis Pipeline for LST-1, the First Prototype Large-Sized Telescope of CTA." In: *Astronomical Society of the Pacific Conference Series*. Ed. by J. E. Ruiz, F. Pierfedereci, and P. Teuben. Vol. 532. Astronomical Society of the Pacific Conference Series, p. 357.
- Luna, G. J. M. et al. (2020). "Increasing Activity in T CrB Suggests Nova Eruption Is Impending." In: *ApJ* 902.1, p. L14. DOI: 10.3847/2041-8213/abbb2c. arXiv: 2009.11902 [astro-ph.SR].
- Lyman, J. D. et al. (2016). "Bolometric light curves and explosion parameters of 38 stripped-envelope core-collapse supernovae." In: *MNRAS* 457.1, pp. 328–350. DOI: 10.1093/mnras/stv2983. arXiv: 1406.3667 [astro-ph.SR].
- López-Coto, R. et al. (2023). cta-observatory/cta-lstchain: v0.10.5 2023-12-01. Version v0.10.5. DOI: 10.5281/zenodo.10245571. URL: https://doi.org/10.5281/zenodo.10245571.
- López-Coto, R. et al. (2024). cta-observatory/cta-lstchain: v0.10.7 2024-02-01. Version v0.10.7. DOI: 10.5281/zenodo.10604579. URL: https://doi.org/10.5281/zenodo.10604579.
- MAGIC Collaboration et al. (2019a). "A fast, very-high-energy γ -ray flare from BL Lacertae during a period of multi-wavelength activity in June 2015." In: A&A 623, A175. DOI: 10.1051/0004-6361/201834010. arXiv: 1901.01733 [astro-ph.HE].

- MAGIC Collaboration et al. (2019b). "Teraelectronvolt emission from the γ -ray burst GRB 190114C." In: *Nature* 575.7783, pp. 455–458. DOI: 10.1038/s41586-019-1750-x. arXiv: 2006.07249 [astro-ph.HE].
- Maehara, H. et al. (2021). "Spectroscopic classification of PNV J23244760+6111140 as a classical nova." In: *The Astronomer's Telegram* 14471, p. 1.
- Maier, G. and J. Holder (2017). "Eventdisplay: An Analysis and Reconstruction Package for Ground-based Gamma-ray Astronomy." In: *35th International Cosmic Ray Conference (ICRC2017)*. Vol. 301. International Cosmic Ray Conference, p. 747. DOI: 10.22323/1.301.0747. arXiv: 1708.04048 [astro-ph.IM].
- Maier, G. and J. Knapp (2007). "Cosmic-ray events as background in imaging atmospheric Cherenkov telescopes." In: *Astroparticle Physics* 28.1, pp. 72–81. DOI: 10.1016/j.astropartphys.2007.04.009. arXiv: 0704.3567 [astro-ph].
- Marcaide, J. M. et al. (1995a). "Discovery of shell-like radio-structure in SN1993J." In: *Nature* 373.6509, pp. 44–45. DOI: 10.1038/373044a0.
- Marcaide, J. M. et al. (1995b). "Expansion of SN 1993J." In: *Science* 270.5241, pp. 1475–1478. DOI: 10.1126/science.270.5241.1475.
- Marcowith, A. et al. (2014). "Cosmic-ray acceleration and gamma-ray signals from radio supernovæ." In: *Nuclear Physics B Proceedings Supplements* 256, pp. 94–100. DOI: 10.1016/j.nuclphysbps.2014.10.011. arXiv: 1409.3670 [astro-ph.HE].
- Margutti, R. and R. Chornock (2021). "First Multimessenger Observations of a Neutron Star Merger." In: *ARA&A* 59, pp. 155–202. DOI: 10.1146/annurev-astro-112420-030742. arXiv: 2012.04810 [astro-ph.HE].
- Martí-Devesa, G. et al. (2024). "Early-time γ -ray constraints on cosmic-ray acceleration in the core-collapse SN 2023ixf with the Fermi Large Area Telescope." In: A&A 686, A254. DOI: 10 . 1051/0004 6361/202349061. arXiv: 2404 . 10487 [astro-ph.HE].
- Martin, P. and G. Dubus (2013). "Particle acceleration and non-thermal emission during the V407 Cygni nova outburst." In: *A&A* 551, A37. DOI: 10.1051/0004-6361/201220289. arXiv: 1209.0625 [astro-ph.HE].
- Martin, P. et al. (2018). "Gamma-ray emission from internal shocks in novae." In: *A&A* 612, A38. DOI: 10.1051/0004-6361/201731692. arXiv: 1710.05515 [astro-ph.HE].
- Mas-Aguilar, A. (2025). "Search for very high energy emission from pulsars with the LST-1 telescope." PhD thesis. Universidad Complutense de Madrid.
- Mason, E. (2011). "U Scorpii 2010 outburst: observational evidence of an underlying ONeMg white dwarf." In: A&A 532, p. L11. DOI: 10.1051/0004-6361/201117440. arXiv: 1107.4013 [astro-ph.SR].
- Masuda, S. et al. (2015). "Development of the photomultiplier tube readout system for the first Large-Sized Telescope of the Cherenkov Telescope Array." In: 34th International Cosmic Ray Conference (ICRC2015). Vol. 34. International Cosmic Ray Conference, p. 1003. DOI: 10.22323/1.236.1003. arXiv: 1509.00548 [astro-ph.IM].
- Matthews, D. et al. (2023). "Radio Detection of SN2023ixf at 10 GHz." In: *The Astronomer's Telegram* 16091, p. 1.
- Mauron, N. and E. Josselin (2011). "The mass-loss rates of red supergiants and the de Jager prescription." In: A&A 526, A156. DOI: 10.1051/0004-6361/201013993. arXiv: 1010.5369 [astro-ph.SR].

- McBreen, B. et al. (1973). "Pulsed high-energy gamma rays from the Crab nebula." In: *ApJ* 184, pp. 571–580. DOI: 10.1086/152350.
- Meegan, C. A. et al. (1992). "Spatial distribution of γ -ray bursts observed by BATSE." In: *Nature* 355.6356, pp. 143–145. DOI: 10.1038/355143a0.
- Mészáros, P. (2002). "Theories of Gamma-Ray Bursts." In: *ARA&A* 40, pp. 137–169. DOI: 10.1146/annurev.astro.40.060401.093821. arXiv: astro-ph/0111170 [astro-ph].
- Mészáros, P. and M. J. Rees (1997). "Optical and Long-Wavelength Afterglow from Gamma-Ray Bursts." In: *ApJ* 476.1, pp. 232–237. DOI: 10.1086/303625. arXiv: astro-ph/9606043 [astro-ph].
- Mészáros, P., M. J. Rees, and H. Papathanassiou (1994). "Spectral properties of blast-wave models of gamma-ray burst sources." In: *ApJ* 432, pp. 181–193. DOI: 10.1086/174559. eprint: astro-ph/9311071.
- Mészáros, P., M. J. Rees, and R. A. M. J. Wijers (1998). "Viewing Angle and Environment Effects in Gamma-Ray Bursts: Sources of Afterglow Diversity." In: *ApJ* 499.1, pp. 301–308. DOI: 10.1086/305635. arXiv: astro-ph/9709273 [astro-ph].
- Metzger, B. D. et al. (2014). "Shocks in nova outflows I. Thermal emission." In: *Monthly Notices of the Royal Astronomical Society* 442.1, pp. 713–731. DOI: 10.1093/mnras/stu844. eprint: https://academic.oup.com/mnras/article-pdf/442/1/713/4065336/stu844.pdf. URL: https://doi.org/10.1093/mnras/stu844.
- Metzger, B. D. et al. (2016). "Novae as Tevatrons: prospects for CTA and IceCube." In: MNRAS 457.2, pp. 1786–1795. DOI: 10.1093/mnras/stw123. arXiv: 1510.07639 [astro-ph.HE].
- Miceli, D. and L. Nava (2022). "Gamma-Ray Bursts Afterglow Physics and the VHE Domain." In: *Galaxies* 10.3, p. 66. DOI: 10.3390/galaxies10030066. arXiv: 2205.12146 [astro-ph.HE].
- Mirzoyan, R. (1997). "On the Calibration Accuracy of Light Sensors in Atmospheric Cherenkov Fluorescence and Neutrino Experiments." In: *International Cosmic Ray Conference*. Vol. 7. International Cosmic Ray Conference, p. 265.
- Mirzoyan, R. (2023). "The Development of Ground-Based Gamma-Ray Astronomy: A Historical Overview of the Pioneering Experiments." In: *Handbook of X-ray and Gamma-ray Astrophysics*, p. 153. DOI: 10.1007/978-981-16-4544-0_62-1.
- Mizuta, A. and K. Ioka (2013). "Opening angles of collapsar jets." In: *ApJ* 777.2, p. 162. DOI: 10.1088/0004-637x/777/2/162. URL: http://dx.doi.org/10.1088/0004-637X/777/2/162.
- Moderski, R. et al. (2005). "Klein-Nishina effects in the spectra of non-thermal sources immersed in external radiation fields." In: *MNRAS* 363.3, pp. 954–966. DOI: 10.1111/j.1365-2966.2005.09494.x. arXiv: astro-ph/0504388 [astro-ph].
- Modjaz, M., C. P. Gutiérrez, and I. Arcavi (2019). "New regimes in the observation of core-collapse supernovae." In: *Nature Astronomy* 3, pp. 717–724. DOI: 10.1038/s41550-019-0856-2. arXiv: 1908.02476 [astro-ph.HE].
- Molina, I. et al. (2024). "The symbiotic recurrent nova V745 Sco at radio wavelengths." In: *MNRAS* 534.2, pp. 1227–1246. DOI: 10.1093/mnras/stae2093.
- Mooley, K. P. et al. (2018). "Superluminal motion of a relativistic jet in the neutron-star merger GW170817." In: *Nature* 561.7723, pp. 355–359. DOI: 10.1038/s41586-018-0486-3. arXiv: 1806.09693 [astro-ph.HE].

- Moralejo Olaizola, A. (2000). "Búsqueda de fuentes cósmicas de radiación gamma de muy alta energía con el detector airobicc." PhD thesis. Universidad Complutense de Madrid.
- Moralejo, A. (2021). "LST-1, the Large-Sized Telescope prototype of CTA. Status and first observations." In: *Journal of Physics: Conference Series* 2156.1, p. 012089. DOI: 10.1088/1742-6596/2156/1/012089. URL: https://dx.doi.org/10.1088/1742-6596/2156/1/012089.
- Moralejo, A. et al. (2025). cta-observatory/cta-lstchain: v0.11.0.post1. Version v0.11.0.post1. DOI: 10.5281/zenodo.15311559. URL: https://doi.org/10.5281/zenodo.15311559.
- Moriya, T. J. (2023). "On the nature of slowly rising interaction-powered supernovae." In: *MNRAS* 524.4, pp. 5309–5313. DOI: 10.1093/mnras/stad2197. arXiv: 2307.10553 [astro-ph.HE].
- Moriyama, M. (2022). "U Sco outburst!!" In: VSNET-alert 26798, p. 1. URL: http://ooruri.kusastro.kyoto-u.ac.jp/mailarchive/vsnet-alert/26798.
- Morris, P. J. et al. (2016). "Gamma-ray novae: rare or nearby?" In: Monthly Notices of the Royal Astronomical Society 465.1, pp. 1218–1226. DOI: 10.1093/mnras/stw2776. eprint: https://academic.oup.com/mnras/article-pdf/465/1/1218/8593826/stw2776.pdf. URL: https://doi.org/10.1093/mnras/stw2776.
- Morsony, B. J., D. Lazzati, and M. C. Begelman (2007). "Temporal and Angular Properties of Gamma-Ray Burst Jets Emerging from Massive Stars." In: *ApJ* 665.1, pp. 569–598. DOI: 10.1086/519483. arXiv: astro-ph/0609254 [astro-ph].
- Munar-Adrover, P. et al. (2013). "Studying the non-thermal lobes of IRAS 16547-4247 through a multi-wavelength approach." In: A&A 559, A13. DOI: 10.1051/0004-6361/201321959. arXiv: 1309.6559 [astro-ph.HE].
- Munari, U., P. Valisa, and S. Dallaporta (2021a). "Spectroscopic classification of TCP J18573095+1653396 as a nova bordering naked-eye brightness." In: *The Astronomer's Telegram* 14704, p. 1.
- Munari, U. et al. (2021b). "High ionization conditions finally emerge as Nova Cas 2021 (V1405 Cas) ends the plateau and embraces a steady decline." In: *The Astronomer's Telegram* 15093, p. 1.
- Munari, U. et al. (2022). "Radio interferometric imaging of RS Oph bipolar ejecta for the 2021 nova outburst." In: *A&A* 666, p. L6. DOI: 10.1051/0004-6361/202244821. arXiv: 2209.12794 [astro-ph.SR].
- Murach, T., M. Gajdus, and R. D. Parsons (2015). "A Neural Network-Based Monoscopic Reconstruction Algorithm for H.E.S.S. II." In: *arXiv e-prints*, arXiv:1509.00794. DOI: 10.48550/arXiv.1509.00794. arXiv:1509.00794. [astro-ph.IM].
- Murase, K. et al. (2011). "New class of high-energy transients from crashes of supernova ejecta with massive circumstellar material shells." In: *Phys. Rev. D* 84.4, p. 043003. DOI: 10.1103/PhysRevD.84.043003. arXiv: 1012.2834 [astro-ph.HE].
- Nava, L. (2018). "High-energy emission from gamma-ray bursts." In: *International Journal of Modern Physics D* 27.13, p. 1842003. DOI: 10.1142/s0218271818420038. URL: http://dx.doi.org/10.1142/S0218271818420038.
- Nava, L. (2021). "Gamma-ray Bursts at the Highest Energies." In: *Universe* 7.12. DOI: 10.3390/universe7120503. URL: https://www.mdpi.com/2218-1997/7/12/503.

- Navas, S. et al. (2024). "Review of particle physics*." In: *Phys. Rev. D* 110.3, p. 030001. DOI: 10.1103/PhysRevD.110.030001.
- Nayana, A. et al. (2024). "Dinosaur in a Haystack: X-ray View of the Entrails of SN 2023ixf and the Radio Afterglow of Its Interaction with the Medium Spawned by the Progenitor Star (Paper 1)." In: *arXiv preprint arXiv:2411.02647*.
- Neshpor, Y. I. et al. (2001). "BL Lac: A New Ultrahigh-Energy Gamma-Ray Source." In: *Astronomy Reports* 45.4, pp. 249–254. DOI: 10.1134/1.1361316. arXiv: astro-ph/0111448 [astro-ph].
- Niedzielski, A. and W. Skorzynski (2002). "Kinematical Structure of Wolf-Rayet Winds. I.Terminal Wind Velocity." In: *Acta Astron.* 52, pp. 81–104.
- Nigro, C. et al. (2019). "Towards open and reproducible multi-instrument analysis in gamma-ray astronomy." In: A&A 625, A10. DOI: 10.1051/0004-6361/201834938. arXiv: 1903.06621 [astro-ph.HE].
- Noda, K. and R. D. Parsons (2022). "Gamma-Ray Bursts at TeV Energies: Observational Status." In: *Galaxies* 10.1, p. 7. DOI: 10.3390/galaxies10010007.
- Nozaki, S et al. (2020). "The readout system based on the ultra-fast waveform sampler DRS4 for the Large-Sized Telescope of the Cherenkov Telescope Array." In: *Journal of Physics: Conference Series* 1468.1, p. 012104. DOI: 10.1088/1742-6596/1468/1/012104. URL: https://dx.doi.org/10.1088/1742-6596/1468/1/012104.
- Nozaki, S. et al. (2023). "LST-1 observations of an enormous flare of BL Lacertae in 2021." In: *arXiv e-prints*, arXiv:2309.09715. DOI: 10.48550/arXiv.2309.09715. arXiv: 2309.09715 [astro-ph.HE].
- Nugis, T. and H. J. G. L. M. Lamers (2000). "Mass-loss rates of Wolf-Rayet stars as a function of stellar parameters." In: *A&A* 360, pp. 227–244.
- Nyamai, M. M. et al. (2023). "Synchrotron emission from double-peaked radio light curves of the symbiotic recurrent nova V3890 Sagitarii." In: *MNRAS* 523.2, pp. 1661–1675. DOI: 10.1093/mnras/stad1534. arXiv: 2301.09116 [astro-ph.HE].
- Nyholm, A. et al. (2020). "Type IIn supernova light-curve properties measured from an untargeted survey sample." In: *A&A* 637, A73. DOI: 10.1051/0004-6361/201936097. arXiv: 1906.05812 [astro-ph.SR].
- O'Brien, T. J. et al. (2006). "An asymmetric shock wave in the 2006 outburst of the recurrent nova RS Ophiuchi." In: *Nature* 442.7100, pp. 279–281. DOI: 10.1038/nature04949. arXiv: astro-ph/0606224 [astro-ph].
- O'Connor, B. et al. (2023). "A structured jet explains the extreme GRB 221009A." In: *Science Advances* 9.23, eadi1405. DOI: 10.1126/sciadv.adi1405. arXiv: 2302.07906 [astro-ph.HE].
- Ofek, E. O. et al. (2013a). "An outburst from a massive star 40 days before a supernova explosion." In: *Nature* 494.7435, pp. 65–67. DOI: 10.1038/nature11877. arXiv: 1302.2633 [astro-ph.HE].
- Ofek, E. O. et al. (2013b). "X-Ray Emission from Supernovae in Dense Circumstellar Matter Environments: A Search for Collisionless Shocks." In: *ApJ* 763.1, p. 42. DOI: 10.1088/0004-637X/763/1/42. arXiv: 1206.0748 [astro-ph.HE].
- Ohm, S., C. van Eldik, and K. Egberts (2009). " γ /hadron separation in very-high-energy γ -ray astronomy using a multivariate analysis method." In: *Astroparticle Physics* 31.5, pp. 383–391. DOI: 10.1016/j.astropartphys.2009.04.001. arXiv: 0904.1136 [astro-ph.IM].

- Ohm, S. and S. Wagner (2023). "Current status and operation of the H.E.S.S. array of imaging atmospheric Cherenkov telescopes." In: Nuclear Instruments and Methods in Physics Research Section A: Accelerators, Spectrometers, Detectors and Associated Equipment 1055, p. 168442. DOI: https://doi.org/10.1016/j.nima. 2023.168442. URL: https://www.sciencedirect.com/science/article/pii/S0168900223004321.
- Ohm, S., S. Wagner, and H. E. S. S. Collaboration (2023). "Current status and operation of the H.E.S.S. array of imaging atmospheric Cherenkov telescopes." In: *Nuclear Instruments and Methods in Physics Research A* 1055, p. 168442. DOI: 10.1016/j.nima.2023.168442. arXiv: 2306.02716 [astro-ph.IM].
- Orlando, S., J. J. Drake, and M. Miceli (2017). "Origin of asymmetries in X-ray emission lines from the blast wave of the 2014 outburst of nova V745 Sco." In: MNRAS 464.4, pp. 5003–5017. DOI: 10.1093/mnras/stw2718. arXiv: 1610.05692 [astro-ph.HE].
- Oser, S. et al. (2001). "High-Energy Gamma-Ray Observations of the Crab Nebula and Pulsar with the Solar Tower Atmospheric Cerenkov Effect Experiment." In: *ApJ* 547.2, pp. 949–958. DOI: 10.1086/318415. arXiv: astro-ph/0006304 [astro-ph].
- Pacholczyk, A. G. (1970). Radio astrophysics. Nonthermal processes in galactic and extragalactic sources.
- Page, K. L. et al. (2022). "The 2021 outburst of the recurrent nova RS Ophiuchi observed in X-rays by the Neil Gehrels Swift Observatory: a comparative study." In: MNRAS 514.2, pp. 1557–1574. DOI: 10.1093/mnras/stac1295. arXiv: 2205.03232 [astro-ph.HE].
- Palatiello, M. et al. (2019). "Performance of the INFN Camera calibration device of the first Large Size Telescope in the Cherenkov Telescope Array." In: *arXiv e-prints*, arXiv:1909.08475. DOI: 10.48550/arXiv.1909.08475. arXiv: 1909.08475 [astro-ph.IM].
- Panjkov, S. et al. (2024). "Probing the soft X-ray properties and multi-wavelength variability of SN2023ixf and its progenitor." In: *PASA* 41, e059. DOI: 10.1017/pasa.2024.66. arXiv: 2308.13101 [astro-ph.HE].
- Parsons, R. D. and J. A. Hinton (2014). "A Monte Carlo template based analysis for air-Cherenkov arrays." In: *Astroparticle Physics* 56, pp. 26–34. DOI: 10.1016/j.astropartphys.2014.03.002. arXiv: 1403.2993 [astro-ph.IM].
- Pastorello, A. et al. (2007). "A giant outburst two years before the core-collapse of a massive star." In: *Nature* 447.7146, pp. 829–832. DOI: 10.1038/nature05825. arXiv: astro-ph/0703663 [astro-ph].
- Pillera, R. et al. (2022). "GRB 221009A: Fermi-LAT refined analysis." In: *GRB Coordinates Network* 32658, p. 1.
- Piran, T. (2004). "The physics of gamma-ray bursts." In: *Reviews of Modern Physics* 76.4, pp. 1143–1210. DOI: 10.1103/RevModPhys.76.1143. arXiv: astro-ph/0405503 [astro-ph].
- Piran, T. and E. Nakar (2010). "On the External Shock Synchrotron Model for Gamma-ray Bursts' GeV Emission." In: *ApJ* 718.2, pp. L63–L67. DOI: 10.1088/2041-8205/718/2/L63. arXiv: 1003.5919 [astro-ph.HE].
- Piron, F. et al. (2001). "Temporal and spectral gamma-ray properties of Mkn 421 above 250 GeV from CAT observations between 1996 and 2000." In: *A&A* 374,

- pp. 895-906. DOI: 10.1051/0004-6361:20010798. arXiv: astro-ph/0106196 [astro-ph].
- Pledger, J. L. and M. M. Shara (2023). "Possible Detection of the Progenitor of the Type II Supernova SN 2023ixf." In: *ApJ* 953.1, p. L14. DOI: 10.3847/2041-8213/ace88b. arXiv: 2305.14447 [astro-ph.SR].
- Podsiadlowski, P. (1992). "The Progenitor of SN 1987A." In: *PASP* 104, p. 717. DOI: 10.1086/133043.
- Prokhorov, D., A. Moraghan, and J. Vink (2021). "Search for gamma rays from SNe with a variable-size sliding-time-window analysis of the Fermi-LAT data." In: *Monthly Notices of the Royal Astronomical Society* 505.1, pp. 1413–1421.
- Protheroe, R. J. (1999). "Acceleration and interaction of ultra high energy cosmic rays." In: *Topics in Cosmic-Ray Astrophysics*. Ed. by M. A. Duvernois. Vol. 230, p. 247. DOI: 10.48550/arXiv.astro-ph/9812055. arXiv: astro-ph/9812055 [astro-ph].
- Rao, M. V. S. and S. Sinha (1988). "The origin of the hump in the Cerenkov lateral distribution in gamma-ray showers and a possible means of separating them from proton showers." In: *Journal of Physics G Nuclear Physics* 14.6, pp. 811–827. DOI: 10.1088/0305-4616/14/6/022.
- Ravasio, M. E. et al. (2024). "A mega–electron volt emission line in the spectrum of a gamma-ray burst." In: *Science* 385.6707, adj3638. DOI: 10.1126/science.adj3638.
- Rector, T. A. et al. (2022). "The Rate and Spatial Distribution of Novae in M31 as Determined by a 20 Year Survey." In: *ApJ* 936.2, p. 117. DOI: 10.3847/1538-4357/ac87ad. arXiv: 2207.05689 [astro-ph.GA].
- Rees, M. J. and P. Mészáros (1992). "Relativistic fireballs Energy conversion and time-scales." In: *MNRAS* 258, p. 41. DOI: 10.1093/mnras/258.1.41P.
- Rees, M. J. and P. Mészáros (1994). "Unsteady Outflow Models for Cosmological Gamma-Ray Bursts." In: *ApJ* 430, p. L93. DOI: 10.1086/187446. arXiv: astro-ph/9404038 [astro-ph].
- Ren, J., Y. Wang, and Z.-G. Dai (2024). "Jet Structure and Burst Environment of GRB 221009A." In: *ApJ* 962.2, p. 115. DOI: 10.3847/1538-4357/ad1bcd. arXiv: 2310.15886 [astro-ph.HE].
- Renzo, M. et al. (2017). "Systematic survey of the effects of wind mass loss algorithms on the evolution of single massive stars." In: A&A 603, A118. DOI: 10.1051/0004-6361/201730698. arXiv: 1703.09705 [astro-ph.SR].
- Rhoads, J. E. (1999). "The Dynamics and Light Curves of Beamed Gamma-Ray Burst Afterglows." In: *ApJ* 525.2, pp. 737–749. DOI: 10.1086/307907. arXiv: astro-ph/9903399 [astro-ph].
- Rhodes, L. et al. (2024). "Rocking the BOAT: the ups and downs of the long-term radio light curve for GRB 221009A." In: MNRAS 533.4, pp. 4435–4449. DOI: 10.1093/mnras/stae2050. arXiv: 2408.16637 [astro-ph.HE].
- Rieger, F. M. (2019). "An Introduction to Particle Acceleration in Shearing Flows." In: *Galaxies* 7.3, p. 78. DOI: 10.3390/galaxies7030078. arXiv: 1909.07237 [astro-ph.HE].
- Rieger, F. M., V. Bosch-Ramon, and P. Duffy (2007). "Fermi acceleration in astrophysical jets." In: *Ap&SS* 309.1-4, pp. 119–125. DOI: 10.1007/s10509-007-9466-z. arXiv: astro-ph/0610141 [astro-ph].

- Rieger, F. M. and F. Volpe (2010). "Short-term VHE variability in blazars: PKS 2155-304." In: *A&A* 520, A23. DOI: 10.1051/0004-6361/201014273. arXiv: 1007.4879 [astro-ph.HE].
- Riess, A. G. et al. (2022). "A Comprehensive Measurement of the Local Value of the Hubble Constant with 1 km s⁻¹ Mpc⁻¹ Uncertainty from the Hubble Space Telescope and the SH0ES Team." In: ApJ 934.1, p. L7. DOI: 10.3847/2041-8213/ac5c5b. arXiv: 2112.04510 [astro-ph.C0].
- Rossi, E., D. Lazzati, and M. J. Rees (2002). "Afterglow light curves, viewing angle and the jet structure of gamma-ray bursts." In: *MNRAS* 332.4, 945–950. DOI: 10.1046/j.1365-8711.2002.05363.x. URL: http://dx.doi.org/10.1046/j.1365-8711.2002.05363.x.
- Rybicki, G. B. and A. P. Lightman (1979). Radiative processes in astrophysics.
- Saito, T. et al. (2021). "Commissioning of the camera of the first Large Size Telescope of the Cherenkov Telescope Array." In: *arXiv e-prints*, arXiv:2108.01920. DOI: 10.48550/arXiv.2108.01920. arXiv: 2108.01920 [astro-ph.IM].
- Sari, R., T. Piran, and J. P. Halpern (1999). "Jets in Gamma-Ray Bursts." In: *ApJ* 519.1, pp. L17–L20. DOI: 10.1086/312109. arXiv: astro-ph/9903339 [astro-ph].
- Sari, R., T. Piran, and R. Narayan (1998). "Spectra and Light Curves of Gamma-Ray Burst Afterglows." In: *ApJ* 497.1, pp. L17–L20. DOI: 10.1086/311269. arXiv: astro-ph/9712005 [astro-ph].
- Sarkar, A. D. et al. (2023). "Lepto-hadronic Interpretation of 2021 RS Ophiuchi Nova Outburst." In: *The Astrophysical Journal* 951.1, p. 62. DOI: 10.3847/1538-4357/acd6ed. URL: https://dx.doi.org/10.3847/1538-4357/acd6ed.
- Sato, Y. et al. (2023a). "Synchrotron self-compton emission in the two-component jet model for gamma-ray bursts." In: *Journal of High Energy Astrophysics* 37, pp. 51–61. DOI: 10.1016/j.jheap.2022.12.004. arXiv: 2208.13987 [astro-ph.HE].
- Sato, Y. et al. (2023b). "Two-component jet model for multiwavelength afterglow emission of the extremely energetic burst GRB 221009A." In: *MNRAS* 522.1, pp. L56–L60. DOI: 10.1093/mnrasl/slad038. arXiv: 2212.09266 [astro-ph.HE].
- Schaefer, B. E. (2009). "Orbital Periods for Three Recurrent Novae." In: *ApJ* 697.1, pp. 721–729. DOI: 10.1088/0004-637X/697/1/721. arXiv: 0903.1349 [astro-ph.SR].
- Schaefer, B. E. (2010). "Comprehensive Photometric Histories of All Known Galactic Recurrent Novae." In: *ApJS* 187.2, pp. 275–373. DOI: 10.1088/0067-0049/187/2/275. arXiv: 0912.4426 [astro-ph.SR].
- Schaefer, B. E. (2023). "The B & V light curves for recurrent nova T CrB from 1842-2022, the unique pre- and post-eruption high-states, the complex period changes, and the upcoming eruption in 2025.5 \pm 1.3." In: *MNRAS* 524.2, pp. 3146–3165. DOI: 10.1093/mnras/stad735. arXiv: 2303.04933 [astro-ph.SR].
- Schaefer, B. E. et al. (2023). "Recurrent nova T CrB has just started its Pre-eruption Dip in March/April 2023, so the eruption should occur around 2024.4 +- 0.3." In: *The Astronomer's Telegram* 16107, p. 1.
- Schlegel, E. M. (1990). "A new subclass of type II supernovae?" In: MNRAS 244, pp. 269–271.
- Shafter, A. W. (2017). "The Galactic Nova Rate Revisited." In: *ApJ* 834.2, p. 196. DOI: 10.3847/1538-4357/834/2/196. arXiv: 1606.02358 [astro-ph.SR].

- Sharan Salafia, O. and G. Ghirlanda (2022). "The Structure of Gamma Ray Burst Jets." In: *arXiv e-prints*, arXiv:2206.11088. DOI: 10.48550/arXiv.2206.11088. arXiv: 2206.11088 [astro-ph.HE].
- Shilon, I. et al. (2019). "Application of deep learning methods to analysis of imaging atmospheric Cherenkov telescopes data." In: *Astroparticle Physics* 105, pp. 44–53. DOI: 10.1016/j.astropartphys.2018.10.003. arXiv: 1803.10698 [astro-ph.IM].
- Shivvers, I. et al. (2017). "Revisiting the Lick Observatory Supernova Search Volume-limited Sample: Updated Classifications and Revised Stripped-envelope Supernova Fractions." In: *PASP* 129.975, p. 054201. DOI: 10.1088/1538-3873/aa54a6. arXiv: 1609.02922 [astro-ph.HE].
- Siegert, T., D. Horan, and G. Kanbach (2022). "Telescope Concepts in Gamma-Ray Astronomy." In: *Handbook of X-ray and Gamma-ray Astrophysics*. Ed. by C. Bambi and A. Sangangelo, p. 80. DOI: 10.1007/978-981-16-4544-0_43-1.
- Sitarek, J. (2022). "TeV Instrumentation: Current and Future." In: *Galaxies* 10.1, p. 21. DOI: 10.3390/galaxies10010021. arXiv: 2201.08611 [astro-ph.IM].
- Sitarek, J. et al. (2013). "Analysis techniques and performance of the Domino Ring Sampler version 4 based readout for the MAGIC telescopes." In: *Nuclear Instruments and Methods in Physics Research A* 723, pp. 109–120. DOI: 10.1016/j.nima.2013.05.014. arXiv: 1305.1007 [astro-ph.IM].
- Sitarek, J. et al. (2018). "Nature of the low-energy, γ -like background for the Cherenkov Telescope Array." In: *Astroparticle Physics* 97, pp. 1–9. DOI: 10.1016/j.astropartphys.2017.10.005. arXiv: 1710.06980 [astro-ph.IM].
- Smartt, S. J. et al. (2009). "The death of massive stars I. Observational constraints on the progenitors of Type II-P supernovae." In: *MNRAS* 395.3, pp. 1409–1437. DOI: 10.1111/j.1365-2966.2009.14506.x. arXiv: 0809.0403 [astro-ph].
- Smartt, S. J. (2009). "Progenitors of Core-Collapse Supernovae." In: *ARA&A* 47.1, pp. 63–106. DOI: 10.1146/annurev-astro-082708-101737. arXiv: 0908.0700 [astro-ph.SR].
- Smith, N. (2014). "Mass Loss: Its Effect on the Evolution and Fate of High-Mass Stars." In: *ARA&A* 52, pp. 487–528. DOI: 10.1146/annurev-astro-081913-040025. arXiv: 1402.1237 [astro-ph.SR].
- Smith, N. (2017). "Luminous blue variables and the fates of very massive stars." In: *Philosophical Transactions of the Royal Society of London Series A* 375.2105, p. 20160268. DOI: 10.1098/rsta.2016.0268.
- Smith, N. et al. (2008). "SN 2006tf: Precursor Eruptions and the Optically Thick Regime of Extremely Luminous Type IIn Supernovae." In: *ApJ* 686.1, pp. 467–484. DOI: 10.1086/591021. arXiv: 0804.0042 [astro-ph].
- Smith, N. et al. (2023). "High-resolution spectroscopy of SN 2023ixf's first week: engulfing the asymmetric circumstellar material." In: *The Astrophysical Journal* 956.1, p. 46.
- Sokolovsky, K. V. et al. (2023). "The multiwavelength view of shocks in the fastest nova V1674 Her." In: *MNRAS* 521.4, pp. 5453–5472. DOI: 10.1093/mnras/stad887. arXiv: 2302.03043 [astro-ph.HE].
- Somero, A., P. Hakala, and G. A. Wynn (2017). "High-resolution optical spectroscopy of RS Ophiuchi during 2008-2009." In: *MNRAS* 464.3, pp. 2784–2795. DOI: 10.1093/mnras/stw2551. arXiv: 1610.00914 [astro-ph.SR].
- Sprott, D. (2000). Statistical Inference in Science. DOI: 10.1007/b98955.

- Stathakis, R. A. and E. M. Sadler (1991). "What was supernova 1988Z?" In: *MNRAS* 250, p. 786. DOI: 10.1093/mnras/250.4.786.
- Stecker, F. W. (1971). Cosmic gamma rays. Vol. 249.
- Strotjohann, N. L. et al. (2021). "Bright, Months-long Stellar Outbursts Announce the Explosion of Interaction-powered Supernovae." In: *ApJ* 907.2, p. 99. DOI: 10.3847/1538-4357/abd032. arXiv: 2010.11196 [astro-ph.HE].
- Svirski, G., E. Nakar, and R. Sari (2012). "Optical to X-Ray Supernova Light Curves Following Shock Breakout through a Thick Wind." In: *The Astrophysical Journal* 759.2, p. 108. DOI: 10.1088/0004-637X/759/2/108. URL: https://dx.doi.org/10.1088/0004-637X/759/2/108.
- Swanenburg, B. N. et al. (1981). "Second COS-B catalogue of high-energy gamma-ray sources." In: *ApJ* 243, pp. L69–L73. DOI: 10.1086/183445.
- Szanecki, M. et al. (2013). "Influence of the geomagnetic field on the IACT detection technique for possible sites of CTA observatories." In: *Astroparticle Physics* 45, pp. 1–12. DOI: 10.1016/j.astropartphys.2013.02.002. arXiv: 1302.6387 [astro-ph.IM].
- Tan, W. J. et al. (2022). "Insight-HXMT observation of GRB221009A/Swift J1913.1+1946." In: *The Astronomer's Telegram* 15660, p. 1.
- Tartaglia, L. et al. (2020). "The long-lived Type IIn SN 2015da: Infrared echoes and strong interaction within an extended massive shell." In: *A&A* 635, A39. DOI: 10.1051/0004-6361/201936553. arXiv: 1908.08580 [astro-ph.HE].
- Tartaglia, L. et al. (2024). "Signatures of anti-social mass-loss in the ordinary Type II SN 2024bch A non-interacting supernova with early high-ionisation features." In: arXiv e-prints, arXiv:2409.15431. arXiv: 2409.15431 [astro-ph.HE].
- Tatischeff, V. (2009). "Radio emission and nonlinear diffusive shock acceleration of cosmic rays in the supernova SN 1993J." In: *A&A* 499.1, pp. 191–213. DOI: 10.1051/0004-6361/200811511. arXiv: 0903.2944 [astro-ph.HE].
- Tatischeff, V. and M. Hernanz (2007). "Evidence for Nonlinear Diffusive Shock Acceleration of Cosmic Rays in the 2006 Outburst of the Recurrent Nova RS Ophiuchi." In: *ApJ* 663.2, pp. L101–L104. DOI: 10.1086/520049. arXiv: 0705.4422 [astro-ph].
- Tavani, M. et al. (2008). "The AGILE space mission." In: *Nuclear Instruments and Methods in Physics Research A* 588.1-2, pp. 52–62. DOI: 10.1016/j.nima.2008.01.
- Tavani, M. et al. (2023). "AGILE Gamma-ray Detection of the Exceptional GRB 221009A." In: *The Astrophysical Journal Letters* 956.1, p. L23.
- Tavernier, S. (2010). *Experimental Techniques in Nuclear and Particle Physics*. Springer Nature. DOI: 10.1007/978-3-642-00829-0.
- Teja, R. S. et al. (2023). "Far-ultraviolet to Near-infrared Observations of SN 2023ixf: A High-energy Explosion Engulfed in Complex Circumstellar Material." In: *ApJ* 954.1, p. L12. DOI: 10.3847/2041-8213/acef20. arXiv: 2306.10284 [astro-ph.HE].
- Thompson, D. J. (2008). "Gamma ray astrophysics: the EGRET results." In: *Reports on Progress in Physics* 71.11, p. 116901. DOI: 10.1088/0034-4885/71/11/116901. arXiv: 0811.0738 [astro-ph].

- Thompson, D. J. (2015). "Space detectors for gamma rays (100 MeV-100 GeV): From EGRET to Fermi LAT." In: *Comptes Rendus Physique* 16.6-7, pp. 600–609. DOI: 10.1016/j.crhy.2015.07.002. arXiv: 1506.07733 [astro-ph.IM].
- Thompson, D. J. et al. (1974). "SAS-2 Observations of the High-Energy Gamma Radiation from the VELA Region." In: *ApJ* 190, p. L51. DOI: 10.1086/181502.
- Thompson, D. J. et al. (1977). "Final SAS-2 gamma-ray results on sources in the galactic anticenter region." In: *ApJ* 213, pp. 252–262. DOI: 10.1086/155152.
- Thompson, D. J. et al. (1995). "The Second EGRET Catalog of High-Energy Gamma-Ray Sources." In: *ApJS* 101, p. 259. DOI: 10.1086/192240.
- Thompson, D. J. et al. (1996). "Supplement to the Second EGRET Catalog of High-Energy Gamma-Ray Sources." In: *ApJS* 107, p. 227. DOI: 10.1086/192362.
- Tully, R. B., H. M. Courtois, and J. G. Sorce (2016). "Cosmicflows-3." In: *AJ* 152.2, p. 50. DOI: 10.3847/0004-6256/152/2/50. arXiv: 1605.01765 [astro-ph.C0].
- Valisa, P. et al. (2023). "Atlas of photometric and spectroscopic daily monitoring of the very slow Nova Cas 2021 (=V1405 Cas) during the first 660 days of its outburst." In: *arXiv e-prints*, arXiv:2302.04656. DOI: 10.48550/arXiv.2302.04656. arXiv: 2302.04656 [astro-ph.SR].
- van Loon, J. T. et al. (2005). "An empirical formula for the mass-loss rates of dust-enshrouded red supergiants and oxygen-rich Asymptotic Giant Branch stars." In: *A&A* 438.1, pp. 273–289. DOI: 10.1051/0004-6361:20042555. arXiv: astro-ph/0504379 [astro-ph].
- van Paradijs, J., C. Kouveliotou, and R. A. M. J. Wijers (2000). "Gamma-Ray Burst Afterglows." In: *ARA&A* 38, pp. 379–425. doi: 10.1146/annurev.astro.38.1.379.
- Vollmann, (2024). Observations from the AAVSO International Database. https://www.aavso.org. Accessed 2024.
- Wagner, R. M. (2006). "Measurement of Very High Energy Gamma-Ray Emission from Four Blazars Using the MAGIC Telescope and a Comparative Blazar Study." PhD thesis. Munich, Tech. U.
- Wakely, S. P. and D. Horan (2008). "TeVCat: An online catalog for Very High Energy Gamma-Ray Astronomy." In: *International Cosmic Ray Conference* 3, pp. 1341–1344.
- Waxman, E. and B. Katz (2017). "Shock Breakout Theory." In: *Handbook of Supernovae*. Ed. by A. W. Alsabti and P. Murdin, p. 967. DOI: 10.1007/978-3-319-21846-5_33.
- Weekes, T. C. (1973). "A Survey of Gamma-Ray Sources in the Galactic Plane at Energies of 10¹¹ to 10¹² eV." In: *International Cosmic Ray Conference*. Vol. 1. International Cosmic Ray Conference, p. 446.
- Weekes, T. C. et al. (1989). "Observation of TeV Gamma Rays from the Crab Nebula Using the Atmospheric Cerenkov Imaging Technique." In: *ApJ* 342, p. 379. DOI: 10.1086/167599.
- Wehrle, A. E. et al. (1998). "Multiwavelength Observations of a Dramatic High-Energy Flare in the Blazar 3C 279." In: *ApJ* 497.1, pp. 178–187. DOI: 10.1086/ 305461. arXiv: astro-ph/9711243 [astro-ph].
- Weis, K. and D. J. Bomans (2020). "Luminous Blue Variables." In: *Galaxies* 8.1, p. 20. DOI: 10.3390/galaxies8010020. arXiv: 2009.03144 [astro-ph.SR].
- Weston, J. H. S. et al. (2016). "Non-thermal radio emission from colliding flows in classical nova V1723 Aql." In: MNRAS 457.1, pp. 887–901. DOI: 10.1093/mnras/stv3019. arXiv: 1505.05879 [astro-ph.SR].

- Wiggins, P. (2024). "Transient Discovery Report for 2024-01-29." In: *Transient Name Server Discovery Report* 2024-281, p. 1.
- Williams, M. A. et al. (2023). "GRB 221009A: Discovery of an Exceptionally Rare Nearby and Energetic Gamma-Ray Burst." In: *ApJ* 946.1, p. L24. DOI: 10.3847/2041-8213/acbcd1. arXiv: 2302.03642 [astro-ph.HE].
- Wood, M. et al. (2017). "Fermipy: An open-source Python package for analysis of Fermi-LAT Data." In: 35th International Cosmic Ray Conference (ICRC2017). Vol. 301. International Cosmic Ray Conference, p. 824. DOI: 10.22323/1.301.0824. arXiv: 1707.09551 [astro-ph.IM].
- Woodward, C. E. et al. (2021). "Near-infrared Studies of Nova V1674 Herculis: A Shocking Record Breaker." In: *ApJ* 922.1, p. L10. DOI: 10.3847/2041-8213/ac3518. arXiv: 2110.13053 [astro-ph.SR].
- Woosley, S. E. and J. S. Bloom (2006). "The Supernova Gamma-Ray Burst Connection." In: *ARA&A* 44.1, pp. 507–556. DOI: 10.1146/annurev.astro.43.072103. 150558. arXiv: astro-ph/0609142 [astro-ph].
- Woosley, S. E., A. Heger, and T. A. Weaver (2002). "The evolution and explosion of massive stars." In: *Reviews of Modern Physics* 74.4, pp. 1015–1071. DOI: 10.1103/RevModPhys.74.1015.
- Woosley, S. E., N. Langer, and T. A. Weaver (1993). "The Evolution of Massive Stars Including Mass Loss: Presupernova Models and Explosion." In: *ApJ* 411, p. 823. DOI: 10.1086/172886.
- Woosley, S. E. et al. (1987). "Supernova 1987A in the Large Magellanic Cloud: The Explosion of a approximately 20 M_{sun} Star Which Has Experienced Mass Loss?" In: *ApJ* 318, p. 664. DOI: 10.1086/165402.
- Xi, S.-Q. et al. (2020). "A Serendipitous Discovery of GeV Gamma-Ray Emission from Supernova 2004dj in a Survey of Nearby Star-forming Galaxies with Fermi-LAT." In: *ApJ* 896.2, p. L33. DOI: 10.3847/2041-8213/ab982c. arXiv: 2003.04795 [astro-ph.HE].
- Yaron, O. et al. (2005). "An Extended Grid of Nova Models. II. The Parameter Space of Nova Outbursts." In: *ApJ* 623.1, pp. 398–410. doi: 10.1086/428435. arXiv: astro-ph/0503143 [astro-ph].
- Yaron, O. et al. (2017). "Confined dense circumstellar material surrounding a regular type II supernova." In: *Nature Physics* 13.5, pp. 510–517. DOI: 10.1038/nphys4025. arXiv: 1701.02596 [astro-ph.HE].
- Yuan, Q. et al. (2018). "Fermi Large Area Telescope Detection of Gamma-Ray Emission from the Direction of Supernova iPTF14hls." In: *ApJ* 854.2, p. L18. DOI: 10.3847/2041-8213/aaacc9. arXiv: 1712.01043 [astro-ph.HE].
- Zabalza, V. (2015). "Naima: a Python package for inference of particle distribution properties from nonthermal spectra." In: 34th International Cosmic Ray Conference (ICRC2015). Vol. 34. International Cosmic Ray Conference, p. 922. DOI: 10.22323/1.236.0922. arXiv: 1509.03319 [astro-ph.HE].
- Zhang, B. T. et al. (2025). "The origin of very-high-energy gamma-rays from GRB 221009A: Implications for reverse shock proton synchrotron emission." In: *Journal of High Energy Astrophysics* 45, pp. 392–408. DOI: 10.1016/j.jheap.2025.01.007. arXiv: 2311.13671 [astro-ph.HE].

- Zhang, B. and P. Mészáros (2001). "High-Energy Spectral Components in Gamma-Ray Burst Afterglows." In: *ApJ* 559, pp. 110–122. DOI: 10.1086/322400. eprint: astro-ph/0103229.
- Zhang, B. and P. Mészáros (2002). "Gamma-Ray Burst Beaming: A Universal Configuration with a Standard Energy Reservoir?" In: *ApJ* 571.2, 876–879. DOI: 10.1086/339981. URL: http://dx.doi.org/10.1086/339981.
- Zhang, B., X.-Y. Wang, and J.-H. Zheng (2024). "The BOAT GRB 221009A: A Poynting-flux-dominated narrow jet surrounded by a matter-dominated structured jet wing." In: *Journal of High Energy Astrophysics* 41, pp. 42–53. DOI: 10.1016/j.jheap.2024.01.002. arXiv: 2311.14180 [astro-ph.HE].
- Zhang, S. et al. (2024). "Large Array of imaging atmospheric Cherenkov Telescopes (LACT): status and future plans." In: *Proceedings of 38th International Cosmic Ray Conference PoS(ICRC2023)*. Vol. 444, p. 808. DOI: 10.22323/1.444.0808.
- Zheng, J.-H. et al. (2022). "Interpretation of the light curve of gamma-ray emission from the 2021 outburst of the recurrent nova RS Ophiuchi." In: *Phys. Rev. D* 106.10, p. 103011. DOI: 10.1103/PhysRevD.106.103011. arXiv: 2203.16404 [astro-ph.HE].
- Zheng, J.-H. et al. (2024). "A Narrow Uniform Core with a Wide Structured Wing: Modeling the TeV and Multiwavelength Afterglows of GRB 221009A." In: *ApJ* 966.1, p. 141. DOI: 10.3847/1538-4357/ad3949. arXiv: 2310.12856 [astro-ph.HE].
- Zimmerman, E. A. et al. (2024). "The complex circumstellar environment of supernova 2023ixf." In: *Nature* 627.8005, pp. 759–762. DOI: 10.1038/s41586-024-07116-6. arXiv: 2310.10727 [astro-ph.HE].
- Zuckerman, L. et al. (2023). "Rapidly evolving Galactic plane outbursts in NEOWISE: revisiting the Galactic nova rate with the first all-sky search in the mid-infrared." In: *MNRAS* 523.3, pp. 3555–3568. DOI: 10.1093/mnras/stad1625. arXiv: 2303.08795 [astro-ph.SR].

LIST OF FIGURES

Figure 1.1	Cumulative number of gamma-ray sources. 2				
Figure 3.1	Schematic view of LAT. 22				
Figure 3.2	Schematic view of gamma-ray and CR induced EAS. 23				
Figure 3.3	Schematic view of the Cherenkov emission. 25				
Figure 3.4	Angular distribution of Cherenkov photons. 26				
Figure 3.5	Sketch of the stereoscopic view of a gamma-ray EAS. 28				
Figure 3.6	The MAGIC telescopes. 29				
Figure 3.7	Layout of telescopes of CTAO. 30				
Figure 3.8	CTAO differential flux sensitivity vs energy. 31				
Figure 3.9	CTAO differential flux sensitivity vs time. 32				
Figure 3.10	LST-1 in April 2024. 33				
Figure 4.1	Pixel charge and trigger time of an MC gamma ray. 38				
Figure 4.2	Pixel charge for an MC gamma ray and proton. 39				
Figure 4.3	Pixel charge with image moments superimposed. 40				
Figure 4.4	Geometric reconstruction of the EAS parameters. 41				
Figure 4.5	Schematic view of the <i>disp</i> method. 42				
Figure 4.6	Gammaness distribution at <i>E</i> above and below 0.5 TeV. 43				
Figure 4.7	Aeff (left) and edisp matrix. 45				
Figure 4.8	Schematic view of the wobble mode. 47				
Figure 4.9	Comparison of the DRS4 electric noise correction. 50				
Figure 4.10	Charge integration algorithms applied to waveforms. 53				
Figure 4.11	Picture threshold values using the pedestal cleaning. 54				
Figure 4.12	Definition of image and reconstructed parameters. 55				
Figure 4.13	Distribution of training and testing MC nodes. 57				
Figure 5.1	RS Oph daily SEDs at VHE gamma rays. 66				
Figure 5.2	SED at VHE gamma rays obtained with LST-1 and MAGIC				
	for the first four days. 67				
Figure 5.3	Light curve at $E > 100 \text{GeV}$ for LST-1 and MAGIC. 68				
Figure 5.4 RS Oph daily SEDs from HE to VHE gamma rays v					
	the best-fit leptonic and hadronic models without systemat-				
	ics. 69				
Figure 5.5	Same SEDs as Fig. 5.4 but for the lepto-hadronic				
	model. 73				
Figure 5.6	Corner plot of the best-fit $\Gamma_{e,1}$ for observation day 1 and the				
	associated χ^2 fit value. 78				
Figure 5.7	Derived systematic energy scaling factors for LST-1, MAGIC				
	and H.E.S.S. 79				
Figure 5.8	RS Oph daily SEDs from HE to VHE gamma rays with the				
	best-fit hadronic models with systematics. 81				
Figure 5.9	Comparison between the best-fit SED models for novae and				
	the sensitivity for LST-1 and 4 LSTs. 86				

Figure 5.10	Logarithmic integral flux-to-CTAO-sensitivity ratio for CTAO-N and CTAO-S. 88					
Figure 5.11	Daily statistical detection significance from 1-hour simulated observation of RS Oph with CTAO-N and CTAO-S. 90					
Figure 5.12	Simulated VHE gamma-ray SED of RS Oph after 1 day since the eruption with CTAO-N. 91					
Figure 6.1	SED of SN 2023ixf. 100					
Figure 6.2	Light curve of SN 2023ixf obtained with MAGIC and LST-1 100					
Figure 6.3	SED obtained using all the LST-1 observations on SN 2024bch. 102					
Figure 6.4	Light curve of SN 2024bch with LST-1. 103					
Figure 7.1	θ^2 plot using observations recorded at $T_0 + 1.33$ d. 116					
Figure 7.2	Same as Fig. 7.1, but displaying the α distributions.					
Figure 7.3	Intrinsic SED of GRB 221009A for 10, 12 and between 15 and					
	27 October 2022. 118					
Figure 7.4	Comparison of SEDs between source-independent and					
	source-dependent approaches. 119					
Figure 7.5	MWL intrinsic light curve of GRB 221009A corrected for EBL					
O	attenuation. 120					
Figure 7.6	Comparison of intrinsic light curves (0.3–5 TeV) between					
O	source-independent and source-dependent. 121					
Figure 7.7	Comparison of model parameters for Ren et al. (2024), Zheng					
O	et al. (2024), and Zhang et al. (2025). 124					
Figure A.1	Flowchart of the TRETS algorithm. 130					
Figure A.2	Simulated RS Oph light curve using TRETS. 132					
Figure A.3	BL Lac light curve on 9 Aug. 2021 using TRETS and other					
O	methods. 133					
Figure A.4	Comparison between observations-wise and weighted-average light curve from TRETS. 134					
Figure A.5	Comparison between 5-min and weighted-average light					
118416 11.0	curve from TRETS. 135					
Figure A.6	Distribution of flux time intervals with TRETS. 135					
Figure A.7	Median time-bin distribution vs detection statistical signifi-					
118416 11.7	cance. 136					
Figure B.1	Optical light curve of V1405 Cas, V1674 Her, and U Sco					
118410 2.1	2022. 141					
Figure B.2	Light curve above 100 MeV and gamma-ray SED for V1405					
	Cas. 145					
Figure B.3	Light curve above 100 MeV and gamma-ray SED for V1674					
8	Her. 146					
Figure B.4	Light curve above 100 MeV and gamma-ray SED for U Sco					
	2022. 147					

LIST OF TABLES

Table 4.1	Charge integration settings used in LST-1 for each event					
	type. 52					
Table 5.1	Observation campaign of RS Oph with LST-1 62					
Table 5.2	Nova parameters used to model the RS Oph gamma-ray					
	SED. 64					
Table 5.3	Best-fit power-law spectral parameter values and statistical					
	detection significances (Sig.) using LST-1 data. 65					
Table 5.4	Model-fit results without and with systematic uncertainties					
	using the leptonic and hadronic modelling for observation					
	days $t - t_0 \sim 1 d$, 2 d, and 4 d. 70					
Table 5.5	Model-fit results of the lepto-hadronic modelling for obser-					
	vation days $t - t_0 \sim 1 \mathrm{d}$, 2 d and 4 d. 74					
Table 5.6	Information criteria measures for the models used to model					
	the HE-VHE gamma-ray emission of RS Oph. 74					
Table 5.7	Set of input reference parameter values assumed for the					
	hadronic and leptonic model for each observation day.					
Table 5.8	Median and IQR statistics for the best-fit parameter distribu-					
	tions. 77					
Table 5.9	Daily parameter values of the log-parabola spectral models					
	used to simulate RS Oph. 90					
Table 6.1	Observation campaign of SN 2023ixf with simultaneous					
	MAGIC+LST-1 observations. 98					
Table 6.2	Observation campaign of SN 2024bch with LST-1. 101					
Table 6.3	ULs on $\dot{M}/v_{\rm w}$ of SN2023ixf and SN 2024bch. 105					
Table 7.1	Observations of GRB 221009A with LST-1 in Oct. 2022. 112					
Table A.1	TRETS parameters for the numerical simulations of RS					
	Oph. 132					
Table A.2	TRETS parameters considered for LST-1 data taken on BL					
	Lac. 134					
Table B.1	Observation summary for the novae observed with					
	LST-1. 140					
Table C.1	Issue and pull request numbers opened in each repository. 149					

The publications in large collaborations such as the CTAO, LST, or MAGIC Collaborations are signed by all the authors of the collaboration in alphabetical order. If there are external authors, they are placed at the end. The corresponding authorship acknowledges primary roles of the publication and the specific tasks are provided in the acknowledgement section or author contribution. At the time of the Thesis deposit, I signed a total of 24 published large-collaboration articles.

The peer-reviewed publications listed here have been developed as part of my doctoral Thesis.

The content of this Thesis has been included in the following published or submitted articles:

- Abe, K. et al. (including A. Aguasca-Cabot as corresponding author) (2025). "Detection of RS Oph with LST-1 and modelling of its HE/VHE gamma-ray emission." In: *A&A* 695, A152, A152. DOI: 10.1051/0004-6361/202452447.
- Abe, K et al. (including A. Aguasca-Cabot as main author) (2025). "Galactic transient sources with the Cherenkov Telescope Array Observatory." In: *MNRAS*, staf655. Manuscript in press. DOI: 10.1093/mnras/staf655.
- Abe, K. et al. (including A. Aguasca-Cabot as corresponding author) (2025). "GRB 221009A: Observations with LST-1 of CTAO and implications for structured jets in long gamma-ray bursts." Manuscript submitted to *ApJL*.
- Abe, K. et al. (including A. Aguasca-Cabot as corresponding author) (2025). "Constraining the TeV gamma-ray emission of SN 2024bch: a possible type IIn-L from a RSG progenitor." Manuscript submitted to A&A.

Other published articles related to this Thesis, but not directly included:

• Donath, A., R. Terrier, Q. Remy, A. Sinha, C. Nigro, F. Pintore, B. Khélifi, L. Olivera-Nieto, J. E. Ruiz, K. Brügge, M. Linhoff, J. L. Contreras, F. Acero, A. Aguasca-Cabot, D. Berge, P. Bhattacharjee, J. Buchner, C. Boisson, D. C. Fidalgo, A. Chen, M. de Bony de Lavergne, J. V. de Miranda Cardoso, C. Deil, M. Füßling, S. Funk, L. Giunti, J. Hinton, L. Jouvin, J. King, J. Lefaucheur, M. Lemoine-Goumard, J.-P. Lenain, R. López-Coto, L. Mohrmann, D. Morcuende, S. Panny, M. Regeard, L. Saha, H. Siejkowski, A. Siemiginowska, B. M. Sipőcz, T. Unbehaun, C. van Eldik, T. Vuillaume and R. Zanin (2023). "Gammapy: A Python package for gamma-ray astronomy." In: A&A 678, A157, A157. DOI: 10.1051/0004-6361/202346488.

The content of this Thesis has been included in the following conference proceedings:

- Abe, K. et al. (including A. Aguasca-Cabot as corresponding author) (2025).
 "LST-1 follow-up of the exceptionally bright gamma-ray burst GRB 221009A."
 Manuscript submitted to Memorie della Società Astronomica Italiana (Proceedings of 8th Heidelberg International Symposium on High-Energy Gamma-Ray Astronomy).
- **Aguasca-Cabot, A.** et al. (2025). "Novae at gamma rays with the LSTs of CTAO: present and future." In: *Highlights on Spanish Astrophysics XII*. Ed. by M. Manteiga et al., p. 161. DOI: 2025hsa..conf..161A.
- Abe, K. et al. (including A. Aguasca-Cabot as corresponding author) (2024). "GRB 221009A observations with LST-1 at VHE gamma rays." In: *Proceedings of High Energy Phenomena in Relativistic Outflows VIII PoS(HEPROVIII)*. Vol. 461, p. 058. DOI: 10.22323/1.461.0058.
- Abe, K. et al. (including A. Aguasca-Cabot as corresponding author) (2023). "Detection of the 2021 Outburst of RS Ophiuchi with the LST-1." In: *Proceedings of 38th International Cosmic Ray Conference PoS(ICRC2023)*. Vol. 444, p. 677. DOI: 10.22323/1.444.0677.
- **Aguasca-Cabot, A.**, P. Bordas, and M. Ribó (2023). "Temporal resolution of transient sources with LST-1: application to BL Lacertae." In: *Highlights on Spanish Astrophysics XI*. Ed. by M. Manteiga et al., p. 129. DOI: 2023hsa..conf..129A.
- Abe, H. et al. (including A. Aguasca-Cabot as corresponding author) (2024). "RS Ophiuchi nova outburst detection by the LST-1." In: *Proceedings of 7th Heidelberg International Symposium on High-Energy Gamma-Ray Astronomy PoS(Gamma2022)*. Vol. 417, p. 055. DOI: 10.22323/1.417.0055.

MEMBERSHIP IN COLLABORATIONS

This Thesis has been undertaken as a member of the LST-1, MAGIC, and CTAO Collaborations, in which I actively participated in several tasks and activities. These contributions include:

- Lead the coordination of the LST-1 paper «Detection of RS Oph with LST-1 and modelling of its HE/VHE gamma-ray emission»,
- Leading the coordination of the LST-1 project about «GRB 221009A»,
- Main author of the CTAO paper «Galactic transient sources with the Cherenkov Telescope Array Observatory », in which I participated in the novae subsection,
- Data-taking shifts at the Roque de los Muchachos Observatory. I have completed 80 observing nights in four observing shifts with progressive responsibilities:

LST-1

- Operator (support astronomer). 22 nights. February 2022.
- Deputy Shift Leader. 15 nights. January 2024.

MAGIC

- Operator (support astronomer). 27 nights. March 2024.
- Shift Leader. 16 nights. January 2025.
- Responsible for follow-up observations of novae of the «Target of Opportunity observations of Galactic Transient sources» observing proposal, with a total of 50 hours granted with the highest priority and during three different cycles between 2023 and 2025.
- Fast offline analysis coordinator of LST-1. 2025. This position coordinates the fast analysis of target of opportunity observations or critical observations for the commissioning of LST-1.
- **Burst Advocate** of LST-1 for four observing shifts between 2022 and 2025 of about 28 days each. The responsibilities of this position are to set up an observation strategy to follow up transient sources such as GRBs, high-energy neutrinos, GWs, fast radio bursts, etc., and ensure a smooth observation of the transient followed-up alerts.
- **Gravitational Wave Expert on Call** of MAGIC for 13 weeks between 2023 and 2024. The responsibilities of this position are to set up the observation strategy to follow up and ensure a smooth observation of GWs.
- Research stay at the Max-Planck-Institut für Physik for two weeks in October 2024 to work on several projects related to CTAO/LST-1 with Dr. David Green and collaborators.

- Participation in LST-1, MAGIC, and CTAO Collaboration meetings.
 - LST
 - LST Collaboration Meeting Autumn 2021. 17–26 Nov., 2021. Online.
 Contributed talk.
 - LST Collaboration Meeting Spring 2022. 20–29 May, 2022. Online. Contributed talk.
 - LST Collaboration Meeting Autumn 2022. 19–23 May, 2022. Bellaterra, Spain. Two contributed talks.
 - LST Collaboration Meeting Spring 2023. 19–23 May, 2023. Munich, Germany. Three contributed talks.
 - LST Collaboration Meeting Autumn 2023. 06–10 Nov., 2023. Online. Two contributed talks.
 - LST Collaboration Meeting Spring 2024. 20–24 May, 2024. Prague, Czech Republic. Contributed talk.
 - LST Collaboration Meeting Autumn 2024. 11–15 Nov., 2024. Online. Two contributed talks.
 - LST Collaboration Meeting Spring 2025. 19–23 May, 2025. Madrid, Spain.
 Contributed talk.

MAGIC

 20 MAGIC Years Conference & Symposium. 2–6 October, 2023. La Palma, Spain.

CTAO

- CTAO Organisation and Consortium Meeting Autumn 2022. 14–18 Nov., 2022. Naples, Italy. Contributed talk.
- Actively participating in the **Physics Working Group on galactic and transient sources** of the three collaborations, including monthly remote meetings.
- Actively participating in the **Analysis and Reconstruction Working Group** of LST-1, including the remote meetings every two weeks.
- Contribution with comments in the **internal review processes** of the articles closest to my field in the three collaborations.

I want to thank everyone I have worked with and shared time with during these years.

Firstly, I thank my supervisors, Pol Bordas and Marc Ribó, for their guidance, support and trust over the years. It has been a privilege to perform this Thesis under their supervision. Secondly, I want to express my gratitude to the High Energy Astrophysics group at the Universitat de Barcelona, with whom I have been honoured to work and belong.

This Thesis was carried out in the framework of large international collaborations, including LST, MAGIC, and CTAO. I had a wonderful time participating in collaboration meetings, workshops, hardware and software schools, and remote calls. I am grateful to everyone at the LST, MAGIC, and CTAO Collaborations with whom I have cooperated, their help, and the insightful discussions over the years. I also thank the people with whom I shared time at conferences and in La Palma during the data-taking shift with the MAGIC and the LST-1 telescopes.

I also want to thank all the colleagues and friends with whom I had an enjoyable time inside and outside the office, and who helped me with many doubts and questions. Finally, I would like to thank my parents, family, and Berta for all their support and love, not only throughout these years, but always.

COLOPHON

This research has been conducted at the Departament de Física Quàntica i Astrofísica and Institut de Ciències del Cosmos, Universitat de Barcelona.

This research has made use of NASA's Astrophysics Data System. This research has made use of the SIMBAD database, operated at CDS, Strasbourg, France.

We thank the staff at the Observatorio del Roque de los Muchachos for their assistance during the time of observations in the data-taking shifts with MAGIC and LST-1.

We acknowledge with thanks the variable star observations from the AAVSO International Database contributed by observers worldwide and used in this research.

This research used Python programming language. This work made use of the open-source libraries Gammapy, cta-lstchain, ctapipe, naima, astropy, pandas, scikit-learn, matplotlib, numpy, scipy, iminuit, and corner.

The LST and MAGIC Collaboration are acknowledged for allowing the use of proprietary observational data. Some of the LST and MAGIC results presented in this Thesis have not undergone the internal review procedure of LST and/or MAGIC publications.

This document was typeset using the typographical look-and-feel classicthesis developed by André Miede and Ivo Pletikosić. The style was inspired by Robert Bringhurst's seminal book on typography *The Elements of Typographic Style*. The classicthesis template is available for both LATEX and LAX at https://bitbucket.org/amiede/classicthesis/.

Final Version as of June 20, 2025 (classicthesis v4.6).

ACKNOWLEDGEMENT OF FUNDING

The author acknowledges financial support from the Spanish Ministerio de Ciencia e Innovación (MICINN) with funding from European Union NextGenerationEU and by Generalitat de Catalunya under grant PRTR-C17.I1. This Thesis is also supported by MICINN under grants PID2019-105510GB-C31, PID2019-104114RB-C33, PID2022-136828NB-C41, and PID2022-138172NB-C43, with partial support by the European Regional Development Fund (ERDF/FEDER) and by the Departament de Recerca i Universitats of the Generalitat de Catalunya through grant 2021SGR00679. The author also acknowledges support by the Spanish Unidad de Excelencia "María de Maeztu" through grant CEX2019-000918-M.